이학박사 학위논문

Pressure-induced changes in local electronic structures of crystalline and noncrystalline SiO_2 and $MgSiO_3$ phases in Earth's interior : Insights from *ab initio* calculations of x-ray Raman scattering spectrum

X-선 Raman 산란 스펙트럼 양자계산을 이용한
지구내부에서의 압력 증가에 의한
결정질과 비결정질 SiO_2 및 $MgSiO_3$ 물질의
국소전자구조 변화에 대한 연구

A dissertation in partial fulfillment of the requirements for the degree of Doctor of Philosophy.

2017 년 8 월

서울대학교 대학원
자연과학대학 지구환경과학부

이 유 수

Abstract

The potential presence of high-density SiO_2- and $MgSiO_3$-rich silicate melts has been suggested to be one of the origins of the ultralow velocity zones (ULVZ) at the lowermost mantle region. The pressure dependences of the transverse acoustic wave velocities of SiO_2 and $MgSiO_3$ glasses have been explored up to ~207 GPa to understand the elastic properties of SiO_2- and $MgSiO_3$-rich silicate melts in Earth's interior. They have been suggested to be correlated with the coordination transition of Si atoms upon compression. However, because the elastic properties of amorphous oxides are determined from the short-range structures and associated electronic structures, the correlation between the densification processes of SiO_2 and $MgSiO_3$ glasses and associated changes in the electronic structures, as well as their elastic properties, should be discussed more precisely. The *in situ* high-pressure x-ray Raman scattering (XRS) experiments can probe the element-specific electronic bonding structures and associated local atomic structures around the target element of Earth materials at high pressures. Thus, it has been used to explore the structural changes around O atoms of SiO_2 and $MgSiO_3$ glasses from upon compression from the pressure-induced bonding transitions. Despite the efforts in the previous studies, establishing the direct correlation between the structural changes around O atoms and the evolution in O *K*-edge XRS features of SiO_2 and $MgSiO_3$ glasses has been experimentally challenging because of the intrinsic structural disorder in the amorphous oxides. Recent

advances in the *ab initio* calculations have provided the opportunity to explore the electronic structures and XRS features of Earth materials at extremely high pressure that cannot be easily achieved in the current *in* situ high-pressure XRS experiments.

Here, the *l*-resolved partial density of states (PDOS) and O *K*-edge XRS features of the SiO_2 and $MgSiO_3$ high-pressure polymorphs and the high-density noncrystalline $MgSiO_3$ melts in a pressure range from ~0 to ~131 GPa were systematically calculated using the *ab initio* calculations. The pressure-induced changes in O *K*-edge XRS features of SiO_2 and $MgSiO_3$ high-pressure polymorphs, including an emergence of double-peak-like features of the SiO_2 high-pressure polymorphs, are revealed to be correlated with the enhanced proximity between neighboring O atoms. In addition, the significant changes in O *K*-edge XRS features of $MgSiO_3$ melts upon compression seem to be correlated with the decreases in interatomic distances around O atoms, primarily the O-O distances. Therefore, the pressure-induced changes in O *K*-edge XRS spectra of amorphous SiO_2 and $MgSiO_3$ glasses, from the *in situ* high-pressure XRS experiments, might be indicative of the decreases in interatomic distances around O atoms, particularly the O-O distances, rather than the coordination transition of Si and O atoms. These results suggest that the electronic structures of the crystalline and noncrystalline SiO_2 and $MgSiO_3$ phases at high pressures are strongly affected by changes in the O-O distances upon compression. Because changes in the elastic properties of amorphous oxides are induced from the short-range structural changes and associated changes in their electronic structures, the pressure dependences of transverse wave acoustic wave velocities of SiO_2 and $MgSiO_3$ glasses should be explained with

changes in the nearest neighboring O-O distances rather than changes in the Si coordination environment. In further, I expect that the current study can be applied to future studies of the pressure-induced bonding transition of a wide range of crystalline and noncrystalline oxides at extremely high pressures.

Key words : crystalline and noncrystalline SiO_2 and $MgSiO_3$ phases, *in situ* high-pressure x-ray Raman scattering experiments, core-level spectroscopy, energy-loss near-edge structure, *ab initio* calculations

Student Number : 2010-30106

Table of Contents

List of Figures

1.8686 Å) and an edge-sharing oxygen atom, [6]Si-O2-2[6]Si (O2, average [6]Si-O2: 1.7123 Å, average O2-O2 distance: 2.4213 Å).

Figure 4-2. Crystal densities (i.e., the total atomic mass divided by unit cell volume) of the SiO_2 (*a*-quartz, coesite, and stishovite) and $MgSiO_3$ [enstatite, ilmenite-type $MgSiO_3$, bridgmanite (BR), and post-bridgmanite (PBR)] high-pressure phases with respect to average Si-O bond lengths (A) and average O-O distances (B); average O-O distances (C), and average Si-O bond lengths (D) of SiO_2 and $MgSiO_3$ high-pressure phases with increasing pressure. The black line refers to the trend for all the phases studied here, whereas a blue trend line is for the bridgmanite phase only. The linear relationship between average O-O distances and pressures for all the phases is described as $d_{O\text{-}O}$(Å) = -0.0021×P(GPa)+2.59 (R^2=0.81). The linear relationship between average Si-O bond lengths and pressures for the bridgmanite phase is described as $d_{Si\text{-}O}$(Å) = -0.0013×P(GPa)+1.80 (R^2=0.99).

Figure 4-3. *l*-resolved oxygen PDOS (for unoccupied states) of O1 (A) and O2 (B) for $MgSiO_3$ bridgmanite (BR) and post-bridgmanite (PBR) with varying pressure. The Gaussian broadening FWHM for PDOS is 0.02 Ry (red solid, oxygen *s*-state; blue solid, oxygen *p*-state; green solid, oxygen *d*-state; black solid, total DOS of oxygen).

Figure 4-4. DOS threshold energy for oxygen *s*-state (red), oxygen *p*-state (blue), and oxygen *d*-state (green) for O1 (A) and O2 sites (B) in $MgSiO_3$ bridgmanite (BR; closed circle) and post-bridgmanite (PBR; open circle),

with varying average O-O distance. (C) The linear trend lines for the *s*- (red), *p*- (blue), and *d*- (green) states of both O1 and O2 atoms in the bridgmanite phase are shown.

Figure 4-5. Band gap of the SiO_2 (*a*-quartz, coesite, and stishovite) and $MgSiO_3$ [enstatite, ilmenite-type $MgSiO_3$, bridgmanite (BR), and post-bridgmanite (PBR)] high-pressure phases, with varying average O-O distance (A) and pressure (B).

Figure 4-6. (A) Site-resolved and total O *K*-edge XRS spectra [blue solid, O1, apical corner-sharing oxygen; red solid, O2, planar corner-sharing oxygen; black solid, total (O1:O2=1:2)] for bridgmanite (BR) at 25 GPa. (B) *l*-resolved O-DOSs of each orbital (red solid, *s*-state; blue solid, *p*-state; green solid, *d*-state; black solid, total O-DOS) for bridgmanite at 25 GPa. (C) Site-resolved and total O *K*-edge XRS spectra [blue solid, O1, apical corner-sharing oxygen; red solid, O2, planar corner-sharing oxygen; black solid, total (O1:O2=1:2)] for bridgmanite at 120 GPa. (D) *l*-resolved O-DOSs of each orbital (red solid, *s*-state; blue solid, *p*-state; green solid, *d*-state; black solid, total O-DOS) for bridgmanite at 120 GPa. The Gaussian broadening FWHM for PDOSs and O *K*-edge XRS spectra are 0.02 Ry and 0.5 eV, respectively. The experimental O *K*-edge XRS spectra of bridgmanite (open black circles with a black solid line) [1] was compared with the calculated O *K*-edge XRS spectra for the bridgmanite at 25 GPa.

Figure 4-7. Site-resolved (A) and total (B) O *K*-edge XRS spectra of high-pressure $MgSiO_3$ [enstatite, ilmenite-type $MgSiO_3$, bridgmanite (BR), and post-bridgmanite (PBR)] polymorphs. Those for crystallographically inequivalent oxygen sites [O1 (black), O2 (red), and O3 (blue)] are shown. The spectra of the enstatite and ilmenite-type $MgSiO_3$ are from a previous study [3]. The Gaussian broadening FWHM for O *K*-edge XRS spectra is 0.5 eV. (C) Direct comparison of the calculated O *K*-edge XRS pattern for bridgmanite and post-bridgmanite at 120 GPa.

Figure 4-8. Absorption threshold energies in the O *K*-edge XRS of SiO_2 phases (*a*-quartz, coesite, and stishovite) and $MgSiO_3$ [enstatite, ilmenite-type $MgSiO_3$, bridgmanite (BR), and post-bridgmanite (PBR)] polymorphs with varying crystal density (A), average Si-O bond lengths (B), and average O-O distance (C). The black line refers to the trend for all the phases studied here, whereas a blue trend line is for the bridgmanite phase only. The absorption threshold for SiO_2 phases, enstatite, and ilmenite-type $MgSiO_3$ phases were obtained from a previous study [3] and that for the result of SiO_2 coesite will be presented in a future contribution.

Figure 4-9. Calculated O *K*-edge XRS spectra for the bridgmanite (BR) structures with the O *K*-edge XRS features of bridgmanite and $MgSiO_3$ glasses [1]. The black and red solid lines with open circles indicate the experimental O *K*-edge XRS features of the $MgSiO_3$ glasses at 1 atm and 39 GPa respectively, and the blue solid line with open circles indicates the O *K*-edge XRS features of the bridgmanite. The black, blue, and red

solid lines at the bottom of the figure refer to the calculated O *K*-edge XRS spectra for the bridgmanite structures at 25, 79, and 120 GPa, respectively.

Figure 4-A1. Distortion of SiO_6 octahedra in bridgmanite with increasing pressure from 25 and 120 GPa. (See details in Tab. 1) The transparent molecular structure refers to the atoms in the bridgmanite at 25 GPa, and the opaque structure refers to atoms in the bridgmanite at 120 GPa. The displacements of oxygen atoms in bridgmanite at 25 GPa are represented with black arrows.

Figure 4-A2. Calculated total and PDOS (*s*-, *p*-, and *d*-states of Mg, Si, O1, and O2 atoms) for bridgmanite (BR) at 25 (A) and bridgmanite at 120 GPa (B), without applying the core-hole effect on the target oxygen atoms. (C) The O *p*-DOSs of crystallographically inequivalent oxygen O1 and O2 atoms in the bridgmanite structures at 25 and 120 GPa are directly compared. The Gaussian broadening FWHM for PDOS is 0.02 Ry.

Figure 4-A3. Comparison of the calculated O *K*-edge XRS spectra for post-bridgmanite (PBR) structures based on XRD refinement (top) [4] and *ab initio* calculations (bottom) [5].

Figure 5-1. Populations of Si ($^{[4]}$Si, $^{[5]}$Si, and $^{[6]}$Si) and O [$^{[1]}$O (nonbridging O atoms; NBO), $^{[2]}$O (bridging O atoms; BO), and $^{[3]}$O (O tricluster)] species in the $MgSiO_3$ melts at high pressures. The $^{[3]}$Si and $^{[0]}$O atoms are not presented. See details in Tab. A2 and A4 in the appendix [6].

Figure 5-2. Total (a) and partial radial distribution functions of Mg-O (b), Si-O (c), and O-O (d) pairs in the $MgSiO_3$ melts at high pressures.

Figure 5-3. (a) Pressure dependences of the short-range interatomic distances (open circles) and the average atomic coordination numbers (closed circles) of the $MgSiO_3$ melts. The average atomic coordination numbers of Si (n_{Si}) and O (n_O) atoms were determined from Fig. 1. The average Si-O bond lengths ($d_{Si\text{-}O}$), the average neighboring Mg-O ($d_{Mg\text{-}O}$) and O-O ($d_{O\text{-}O}$) distances each were determined from the corresponding radial distribution functions in Fig. 2(b), 2(c), and 2(d) respectively, i.e. the center of mass of the peak at the first-coordination shells. The n_{Si}, n_O, $d_{Si\text{-}O}$, $d_{Mg\text{-}O}$, and $d_{O\text{-}O}$ were normalized with their values at ~0 GPa (n_{Si} = 4.00, n_O = 1.31, $d_{Si\text{-}O}$ = 1.6390 Å, $d_{Mg\text{-}O}$ = 2.0460 Å, and $d_{O\text{-}O}$ = 2.7340 Å). (b) A relationship between the average atomic coordination numbers of Si (n_{Si}) and O (n_O) atoms [$n_O = 0.36n_{Si} - 0.12$ (R^2=1.00)]. (c) Pressure dependences of the extent of polymerization of $MgSiO_3$ melts: the number of nonbridging O (NBO) atoms with respect to either the number of total Si atoms (Si_{Tot}) or the number of total O atoms (O_{Tot}) in the unit cells. (d) Pressure dependences of the full-width at half-maximum (FWHM) of the radial distribution function for the Si-O bond length ($\sigma_{Si\text{-}O}$) and the topological entropy [ΔS_{Top}(Si-O)] of the $MgSiO_3$ melts.

Figure 5-4. Calculated *l*-resolved (*s*, *p*, and *d* states) partial and total density of states (DOS) for the $MgSiO_3$ melts at high pressures: the partial DOS of Mg (a, b), Si (c), and O (d, e) and the total DOS (f).

Figure 5-5. (a) The total and site-resolved (O1, O2, and O3) O *K*-edge XRS spectra of the crystalline $MgSiO_3$ phases [enstatite (1 atm), ilmenite-type $MgSiO_3$ (22 GPa), bridgmanite (25, 79, and 120 GPa)] referred from the previous studies [3,7]. (b) The O *K*-edge XRS spectra of the SiO_2 and $MgSiO_3$ glasses at 1 atm [1] and the calculated O *K*-edge XRS spectrum for the $MgSiO_3$ melt at ~0 GPa. (c) The calculated O *K*-edge XRS spectra for the $MgSiO_3$ melts at high pressures. The calculated O *K*-edge XRS features for the $MgSiO_3$ melts at high pressures were shifted by 532.24 eV to compare with experiments.

Figure 5-6. (a) Pressure dependence of the O *K*-edge absorption threshold energies (E_A) of the $MgSiO_3$ melts. (b) Correlations between the E_A and the short-range topological changes around O atoms of $MgSiO_3$ melts upon compression. The closed and open circles refer to the average atomic coordination numbers of Si (n_{Si}) and O (n_O) atoms and the average interatomic distances in the short-range order [the Si-O bond length (d_{Si-O}), and the neighboring Mg-O (d_{Mg-O}) and O-O (d_{O-O}) distances], respectively. The n_{Si}, n_O, d_{Si-O}, d_{Mg-O}, and d_{O-O} were normalized with their values at ~0 GPa (n_{Si} = 4.00, n_O = 1.31, d_{Si-O} = 1.6390 Å, d_{Mg-O} = 2.0460 Å, and d_{O-O} = 2.7340 Å).

Figure 5-7. The O *K*-edge XRS spectra of the $MgSiO_3$ glasses at high pressures (top) [1] and the calculated O *K*-edge XRS spectra for the $MgSiO_3$ melts at ~0, ~51, and ~131 GPa (bottom). The calculated O *K*-edge XRS spectra for the $MgSiO_3$ melts at ~0 GPa and different

temperatures (i.e., 2000 and 3000 K) are compared with the O *K*-edge XRS spectrum of the $MgSiO_3$ glass at the ambient pressure (center) [1]. The calculated O *K*-edge features for $MgSiO_3$ melts at high pressures were shifted by 532.24 eV to compare with the experiments.

Figure 5-A1. Pressure dependence of the densities of the $MgSiO_3$ melts calculated in this study using the GGA method (black circles) and the result from the previous study using the LDA method [8].

Figure 5-A2. Mean square displacement (MSD) of atoms in SiO_2 and $MgSiO_3$ melts with respect to the simulation time lengths in log scales. Short and thick black dashed lines refer to the slope of MSD corresponding to the ballistic ($\sim t^2$), truncated ($\sim t^{0.4}$), and diffusion ($\sim t$) regimes as labelled.

Figure 5-A3. Total (a) and partial radial distribution functions of Mg-O (a), Si-O (c), and O-O (d) pairs in SiO_2 and $MgSiO_3$ melts at ~0 GPa and different temperatures (at 2000 and 3000 K).

Figure 5-A4. The velocity auto-correlation functions (VACF) of the SiO_2 and $MgSiO_3$ melt configurations. The VACFs presented here each were calculated from the last 1 ps of the *ab initio* molecular dynamic simulations (i.e., the last 1000 configurations) for the SiO_2 and $MgSiO_3$ melts which were clearly in the diffusion regime (Fig. A2).

Figure 5-A5. Calculated total density of states for the $MgSiO_3$ melts at high pressures. The empirical correction term (Δ) of 9.0 eV was applied (see text for the details).

Figure 5-A6. The total and site-resolved (O1, O2, and O3) O *K*-edge XRS spectra of the crystalline $MgSiO_3$ phases [enstatite (1 atm), ilmenite-type $MgSiO_3$ (22 GPa), bridgmanite (25, 79, and 120 GPa)] referred from our previous studies [3,7].

Figure 5-A7. Pressure dependences of average Si coordination numbers. The results of $MgSiO_3$ glasses are referred from the previous study [8]

Figure 6-1. Crystal structures of (a) α-quartz, (b) β-quartz, (c) α-cristobalite, (d) coesite (O1~O5), (e) hp-cristobalite, (f) penta-SiO_2 (O1 and O2), (g) stishovite, (h) $CaCl_2$-type, (i) α-PbO_2-type, and (j) pyrite-type structures. Details of crystal structures are summarized in Tab. 6-1.

Figure 6-2. Pressure dependences of the average Si-O bond lengths (a) and average O-O distances (b) of the SiO_2 high-pressure polymorphs (α-quartz, β-quartz, α-cristobalite, coesite, hp-cristobalite, penta-SiO_2, stishovite, $CaCl_2$-type, α-PbO_2-type, and pyrite-type structures) and densities of SiO_2 polymorphs with respect to the average Si-O bond lengths (c) and average O-O distances (d). The black dashed lines refer to the trend for the SiO_2 polymorphs explored here with the corresponding *linear* relationships. See details in the manuscript.

Figure 6-3. (a) Calculated *l*-resolved partial density of states (PDOS), for unoccupied states, of O atoms for the SiO_2 high-pressure polymorphs (α-quartz, β-quartz, α-cristobalite, coesite, hp-cristobalite, penta-SiO_2, stishovite, $CaCl_2$-type, α-PbO_2-type, and pyrite-type structures). The Gaussian-broadening full-width at half-maximum (FWHM) for PDOS is 0.02 Ry. Red, blue, and green solid lines refer to the unoccupied O *s*, *p*, and *d* states, respectively. The maximum PDOS intensity of each SiO_2 polymorph is presented at the left side of the figure. (b) Calculated O *K*-edge XRS spectra for the SiO_2 high-pressure polymorphs. The Gaussian-broadening FWHM for O *K*-edge XRS features is 0.5 eV. Site-resolved l-resolved PDOSs and O *K*-edge XRS features for the coesite and penta-SiO_2 structures are presented in Fig. A2.

Figure 6-4. Band gap of the SiO_2 high-pressure polymorphs (α-quartz, β-quartz, α-cristobalite, coesite, hp-cristobalite, penta-SiO_2, stishovite, $CaCl_2$-type, α-PbO_2-type, and pyrite-type structures) with respect to the average Si-O bond lengths (a) and average O-O distances (b). Absorption threshold energies in the O *K*-edge XRS features of the SiO_2 high-pressure polymorphs with respect to the average Si-O bond lengths (c) and average O-O distances (d). The black dashed lines refer to the trend for all the SiO_2 polymorphs with the corresponding *linear* relationships. See details in the manuscript.

Figure 6-5. Densities of the SiO_2 high-pressure polymorphs (α-quartz, β-quartz, α-cristobalite, coesite, hp-cristobalite, penta-SiO_2, stishovite, $CaCl_2$-type, α-PbO_2-type, and pyrite-type structures) with respect to the

absorption threshold energies in their O *K*-edge XRS features. The black dashed line refers to the trend for all the SiO_2 polymorphs, whereas the red dashed line is for the higher-pressure polymorphs only (hp-cristobalite, penta-SiO_2, stishovite, $CaCl_2$-type, α-PbO_2-type, and pyrite-type structures) with the corresponding *linear* relationships. See details in the manuscript.

Figure 6-A1. Calculated *l*-resolved partial density of states (PDOS) for the SiO_2 high-pressure polymorphs as labelled: (a)α-quartz, (b) β-quartz, (c) α-cristobalite, (d) coesite, (e) hp-cristobalite, (f) penta-SiO_2, (g) stishovite at ~9.26 GPa, (h) stishovite at ~29.1 GPa, (i) $CaCl_2$-type, (j) α-PbO_2-type, and (k) pyrite-type structures. These results are calculated without applying the core-hole effects.

Figure 6-A2. Site-resolved O PDOSs (a) and O *K*-edge XRS spectra (b) of the coesite (O1~O5 distinct oxygen sites) and penta-SiO_2 (O1~O2 distinct oxygen sites) structures. The total O PDOSs and O *K*-edge XRS features obtained by taking into consideration the ratio of O atoms in the unit cell are presented in the top of each figure.

Figure 6-A3. Densities of the SiO_2 high-pressure polymorphs (α-quartz, β-quartz, α-cristobalite, coesite, hp-cristobalite, penta-SiO_2, stishovite, $CaCl_2$-type, α-PbO_2-type, and pyrite-type structures) with respect to the pressure conditions. The black dashed line refers to the trend for all the SiO_2 polymorphs with the corresponding *linear* relationship.

Figure 6-A4. Spatial distributions of Si-O and O-O pairs (partial radial distribution function) of the SiO_2 high-pressure polymorphs (α-quartz, β-quartz, α-cristobalite, coesite, hp-cristobalite, penta-SiO_2, stishovite, $CaCl_2$-type, α-PbO_2-type, and pyrite-type structures).

Figure 6-A5. The correlation between the absorption threshold energies in O *K*-edge XRS features and the band gap energies of the SiO_2 high-pressure polymorphs (α-quartz, β-quartz, α-cristobalite, coesite, hp-cristobalite, penta-SiO_2, stishovite, $CaCl_2$-type, α-PbO_2-type, and pyrite-type structures). The black dashed line refers to the trend for all the SiO_2 polymorphs with the corresponding *linear* relationship.

Figure 7-1. The Fe spin-state transition of FeO wustite structures with decreasing the volume of unit cell, from $1.0V_0$ to $0.5V_0$ as labelled. The Hubbard *U* parameters of 6.0, 5.0, 3.5, 2.5, 1.5 and 0.0 eV were used also as labelled.

Figure 7-2. The pressure-volume relationship of FeO wustite structures explored in this study. The Hubbard *U* parameters of 6.0, 5.0, 3.5, 2.5, 1.5 and 0.0 eV were used as labelled.

Figure 7-3. The pressure dependence of the Fe spin state of FeO wustite structures. The Hubbard *U* parameters of 6.0, 5.0, 3.5, 2.5, 1.5 and 0.0 eV were used as labelled.

List of Tables

Chapter 1.

Introduction

Since the Earth's interior could not be observed directly, the seismic wave velocity distribution, such as the preliminary reference Earth model (PREM) [9] and SAW642ANb [10], have been used to probe the Earth's internal structures [11-14]. The structural changes of crystalline SiO_2 and $MgSiO_3$ polymorphs and associated changes in their elastic properties have been suggested to be one of the atomistic accounts of seismic heterogeneities, anisotropies, and discontinuities in the Earth's interior [11,15]. The high-pressure mineralogy in the Earth's interior has been well summarized in the previous study [16], and the Mg-silicate is revealed to be the most abundant in the Earth's mantle. Thus, the elastic properties of Mg-silicates at high pressures, primarily in Mg_2SiO_3 and $MgSiO_3$ composition, have been explored to understand the origins of seismic discontinuities in the Earth's mantle [11,15]. Changes in the elastic properties associated with the phase transition from olivine (Mg_2SiO_4) to wadsleyite (Mg_2SiO_4) [17] and the phase transition from ringwoodite (Mg_2SiO_4) to bridgmanite ($MgSiO_3$) and periclase (MgO) [18] have been suggested to contribute to the P and S wave velocity discontinuities at the mantle transition zone at ~410 (~14 GPa) and ~660 km (~24 GPa). The phase transition between the bridgmanite ($MgSiO_3$) to post-bridgmanite ($MgSiO_3$) has been proposed to account for the seismic anomalies in the D'' region above the core-mantle boundary (CMB) at ~2850 km (~130 GPa), such as the D'' discontinuity, S wave anisotropy, and bulk sound velocity [19,20].

While the Mg-silicates are known to be the most abundant materials in the Earth's interior [16,21,22], the potential presence of free silica (SiO_2) in the Earth's deep interior, i.e. the SiO_2 high-pressure

polymorphs [23-27] and the SiO_2-rich partial melts [28], has been suggested in the previous studies. The free SiO_2 in the crystalline phases can be formed the chemical reaction between the $MgSiO_3$ polymorphs and liquid Fe ($Mg_{0.9}Fe_{0.1}SiO_3$+0.15Fe = 0.90$MgSiO_3$+0.20FeO+0.05FeSi+0.05SiO_2) near the core-mantle boundary (CMB) [26]. The crystallization of SiO_2 from the liquid Fe-Si-O ternary alloy has been confirmed in the Earth's outermost-core pressure and temperature condition (~133-145 GPa and ~4000 K) [27]. The phase transitions of SiO_2 high-pressure polymorphs have been suggested to accounts for the seismic heterogeneities in the Earth's interior. The phase transition from stishovite to $CaCl_2$-type structures at ~47-55 GPa has been suggested to be correlated with the seismically reflective features in the lower mantle at ~1200-1500 km [29-33]. The structural transition from $CaCl_2$-type to α-PbO_2-type structures at ~98-121 GPa may be associated with the shear wave velocity anomalies at ~2600-2900 km near the core-mantle boundary (CMB) [30,34]. The high-pressure SiO_2 structure has been revealed to undergo the further phase transition from α-PbO_2-type to pyrite-type structures at ~226-268 GPa [35]. This phase transition at extremely high pressure can provide further insights into the atomic and electronic structures of SiO_2 high-pressure polymorphs in the Earth's uppermost-core region as well as in the super-Earth's interior [27,30,35,36].

The seismic explorations have revealed the presence of ultralow velocity zones (ULVZ) just above the core-mantle boundary (CMB), in the very limited lowermost mantle region (i.e., ~40-km-thick and ~100-km-wide region), with the 10-30% of seismic velocity reduction [37-39]. The $MgSiO_3$ bridgmanite structure is stable at the pressure region (just below the D'' region) and the (Mg,Fe)O does not present a significant phase

transition [39]. Thus, the presence of partial melts was suggested to account for the sudden reduction of seismic wave velocity in the ULVZ [39]. In the recent studies, thanks to the advances in the *in situ* high-pressure experiments, the presence of high-density SiO_2- [28] and $MgSiO_3$-rich [40-43] silicate melts in the Earth's deep interior, i.e. the pressure and temperature conditions of ULVZ, has been proposed. The previous studies have tried probe whether the high-density SiO_2- and $MgSiO_3$-rich silicate melts can exist near the CMB or not [28,41]. The high-density SiO_2- and $MgSiO_3$-rich silicate melts at the CMB are revealed to be gravitationally stable, and, thus, they can exist in the lowermost mantle region surrounded by coexisting crystalline materials [28,41].

Changes in the transverse acoustic wave velocity of SiO_2 [44] and $MgSiO_3$ [41] glasses have been explored up to ~207 GPa using the *in situ* high-pressure Brillouin scattering experiments to understand the pressure-induced changes in elastic properties of SiO_2- and $MgSiO_3$-rich silicate melts in the Earth's deep interior. In those studies, the coordination transition of Si atoms has been suggested to explain the changes in pressure dependences (slope) of transverse wave velocities of SiO_2 and $MgSiO_3$ glasses. However, it has been suggested referred from the results of previous studies, i.e. the coordination transition of Si atoms in high-density noncrystalline SiO_2 [45] and $MgSiO_3$ [46] phases at high pressures, without the further discussion about the atomistic accounts to changes in their elastic properties. Thus, it should be discussed more in detail. The elastic properties of noncrystalline oxides are determined from the short-range structures and associated electronic structures [47,48]. In addition, in contrast to the SiO_2 and $MgSiO_3$ high-pressure polymorphs, the

noncrystalline oxides undergo the spontaneous structural changes with increasing pressure. Thus, establishing the correlations between the changes in atomic and electronic structures and associated changes in elastic properties is essential to improve our understanding about the changes in elastic properties of SiO_2- and $MgSiO_3$-rich partial melts upon compression.

Despite the difficulties in the *in situ* high-pressure experiments, there have been lots of previous studies to understand the atomistic structures of amorphous SiO_2 and $MgSiO_3$ glasses at high pressures. The pressure-induced changes in interatomic distances, that is, changes in the radial distribution functions (RDF), of prototypical SiO_2 and GeO_2 glasses have been explored: the in situ high-pressure x-ray diffraction (XRD) experiments for the SiO_2 glasses up to ~42 GPa [49] and ~100 GPa [50] and the *ex situ* high-pressure XRD experiments for the SiO_2 and GeO_2 glasses synthesized at high pressures up to ~18 GPa [51]. The neutron diffraction experiments also have been used to probe the atomic structures of SiO_2 glass at ambient condition [52] and changes in the RDFs of SiO_2 glasses associated with the permanent densification at high pressures up to ~16 GPa [53]. The pressure-induced changes in interatomic distances, those are, the Mg-O, Si-O and O-O pairs, of Mg-silicate glasses (MgO-SiO_2 join glasses) have been reported up to ~8.6 GPa using the *in situ* high-pressure neutron scattering experiments [54]. In addition, the previous study has tried to probe the densification process of $MgSiO_3$ glasses at high pressures up to ~30 GPa, particularly changes in the RDFs, with the extended x-ray absorption fine structures (EXAFS) from the *in situ* high-pressure hard x-ray experiments (the synchrotron light source) [55]. Despite these efforts in

the previous studies, the detailed densification processes of SiO_2 and $MgSiO_3$ glasses upon extreme compression up to near the core-mantle boundary condition could not be directly probe. This is because the XRS, neutron diffraction, and EXAFS experiments only can provide the interatomic distances and structural disorder [56,57].

On the other hand, the short-range structural changes, those are, changes in the cation coordination environments (e.g., $^{[4]}$Al and $^{[4]}$Si) and local O configurations (e.g., $^{[4]}$Si-O-$^{[4]}$Al and Na-O-$^{[4]}$Si), of diverse silicate glasses at high pressures, e.g. Na silicate, Na-Al silicate, and Ca-Na-Al silicate glasses, have been explored up to ~8 GPa using the *ex situ* high-pressures solid-state nuclear magnetic resonance (NMR) experiments: the ^{17}O, ^{27}Al, and ^{29}Si 1D magic-angle-spinning (MAS) and 2D 3QMAS experiments [58-61]. The presence of highly coordinated Si atoms (i.e., $^{[5]}$Si and $^{[6]}$Si) in the compressed $MgSiO_3$ glasses at high pressures, up to ~10 GPa, also has been reported from the solid-state NMR experiments: the ^{29}Si 1D MAS experiment [62]. These studies have presented the direct evidence of network polymerization of diverse silicate glasses at high pressures. However, the results have been reported in a limited pressure range, up to ~10 GPa, because of the difficulties of synthesizing sufficient amounts of high-pressure vitreous oxide sample for the solid-state NMR experiments [61,63]. In addition, the atomic structures of oxide glass samples, used in the *ex situ* high-pressure solid-state NMR experiments, represent those of oxide melts undergoing the glass transitions at high pressures. Therefore, the other, appropriate, *in situ* high-pressure experimental techniques need to be applied to improve the understanding about the pressure-induced

changes in atomic and electronic structures of noncrystalline silicate and Mg-silicate melts and glasses over a wide pressure ranges.

The *in situ* high-pressure x-ray Raman scattering (XRS) spectroscopy has been a unique experimental technique that can directly probe the element-specific electronic bonding structures and corresponding short-range structures of both crystalline and noncrystalline Earth materials over a wide pressure range (currently up to ~50 GPa) [64,65]. Thus, the pressure-induced changes in O *K*-edge XRS features of diverse crystalline and noncrystalline low-*z* oxides, which are mostly associated with the electronic transition from the occupied O 1*s* to unoccupied O 2*p* state (O 1*s*-2*p** transition), have been used to probe changes in the short- to medium-range structures around O atoms upon compression [65]. Whereas the XRS experiment provides almost similar excitation features compared with the results from the conventional x-ray absorption spectroscopy (XAS), the XAS experiment is not appropriate for the *in situ* high-pressure experiments using the diamond anvil cell or multi anvil press. Details about the differences between the XRS and XAS, and which is more suitable for the *in* situ high-pressure experiments, are summarized in Chapter 2, i.e. Non-resonant x-ray Raman scattering (XRS) spectroscopy (Why XRS?).

Details about probing the core-level excitation features of Earth materials at high pressures, using the *in situ* high-pressure XRS experiments, are summarized in the previous review [64-66]. The previous studies of low-*z* oxides are briefly summarized in Chapter 3, Chapter 4, Chapter 5, and Chapter 6, those are, the studies of crystalline and noncrystalline SiO_2 and $MgSiO_3$ phases at high pressures, and the previous

studies of Fe including oxides are summarized in Chapter 7, that is, the study of Fe-including oxides at high pressures. Here, I briefly summarize the results of previous studies exploring the O *K*-edge XRS features of SiO_2 and $MgSiO_3$ glasses at high pressures. The structural transition similar to that of stishovite with 6-coordinated Si atoms ($^{[6]}$Si) [2], the formation of highly coordinated Si atoms ($^{[5]}$Si and $^{[6]}$Si) [67], and the changes in Si-O-Si bond angle [68] have been suggested to explain the emergence of stishovite-like double-peak O *K*-edge XRS features of crystalline and amorphous SiO_2 at high pressures (i.e., the characteristic high-energy features at ~538 and ~544 eV). In the previous study for $MgSiO_3$ glasses, the formation of O triclusters [triply coordinated O atoms ($^{[3]}$O) like 2$^{[4]}$Si-$^{[3]}$O-$^{[5]}$Si] and associated structural changes in the medium-range order has been proposed to be the atomistic origins of the changes in O *K*-edge XRS spectra of $MgSiO_3$ glasses with increasing pressure up to ~39 GPa (i.e., the emergence of *K*-edge XRS features ~544-545 eV) [1]. Despite of these previous studies, the atomistic accounts of changes in O *K*-edge XRS features of SiO_2 and $MgSiO_3$ glasses are still controversial, and, thus, it has not been clear what kind of structural changes upon compression facilitate such changes in O *K*-edge XRS features. This is because probing the origins of pressure-induced changes in O *K*-edge XRS features of amorphous oxides has been experimentally challenging due to the intrinsic overlaps of excitation features stemming from symmetrically inequivalent sites as well as limitations of the *in situ* high-pressure XRS experiments [65].

Probing the atomic and electronic structures of crystalline and noncrystalline oxides at high pressures is one of the fundamental and challenging subjects in the Earth sciences as well as the condensed matter

physics. The *in situ* high-pressure x-ray Raman scattering (XRS) experiment has been a unique experimental method that helps us to probe the electronic bonding structures around the target low-*z* elements, such as O, B, Li, and C atoms, of both crystalline and noncrystalline oxides at high pressures. Thus, the pressure-induced changes in O *K*-edge XRS features of diverse oxides have been used to reveal the electronic bonding transitions of O atoms upon compression [64,65,69-71]. The earlier efforts to investigate the O *K*-edge XRS features of crystalline and noncrystalline silica and other diverse oxides are well summarized in the previous review [65]. Despite of those previous studies, determining the direct correlation between the topological changes around O atoms and the evolution in O *K*-edge XRS features of crystalline and noncrystalline oxides, particularly at extremely high pressures, has been experimentally challenging because of the limitation of *in situ* high-pressure XRS experiments and the difficulties in resolving site-specific structural information [64,65].

Recent advances in theoretical methods using the *ab initio* calculations allow us to explore the electronic bonding structures and corresponding XRS features, such as O *K*-edge and Si *K*- and $L_{2,3}$-edge excitation features, of both crystalline and amorphous oxides at high pressures beyond the experimental limitations [3,7,65,67,68,72,73]. Thus, the aim of this study is establishing the direct correlation between the short-range structural changes around O atoms and the evolution in O *K*-edge XRS features of crystalline SiO_2 and $MgSiO_3$ polymorphs and their amorphous phases with increasing pressure using the *ab initio* calculations. To achieve this purpose, the *l*-resolved partial density of states (PDOS) and the O *K*-edge XRS features of the diverse SiO_2 and $MgSiO_3$ polymorphs [α-

quartz (1 atm), stishovite (~15 GPa), enstatite (1 atm), ilmenite-type (~22 GPa), bridgmanite (~25 GPa), and post-bridgmanite (~120 GPa)], the $MgSiO_3$ high-pressures polymorphs [bridgmanite (from ~25 to ~120 GPa) and post-bridgmanite (~120 GPa)], the high-density $MgSiO_3$ melt configurations (from ~0 to ~131 GPa), and the SiO_2 high-pressure polymorphs [α-quartz (1 atm), β-quartz (1 atm), α-cristobalite (1 atm), coesite (~3.8 GPa), hp-cristobalite (~20 GPa), penta-SiO_2 (~16 GPa), stishovite (~9.3 and ~29.1 GPa), $CaCl_2$-type (~63 GPa), α-PbO_2-type (~120 GPa), and pyrite-type (~271 GPa)] were calculated systematically to establish the correlation between the local atomic structures around O atoms and the characteristic O *K*-edge XRS features. Details of each study are summarized in each section. The results of this study could improve our understanding about the structural information that could affect to the electronic structures of the crystalline and noncrystalline SiO2 phases under high pressures more precisely, as well as their elastic properties. In addition, we expect that the current study can be applied to probe the atomistic accounts of electronic bonding transition of diverse crystalline and noncrystalline Earth materials under high pressures.

Chapter 2.

Summary of this study

Chapter 3 presents the calculated *l*-resolved PDOS and site-resolved O *K*-edge XRS features for the crystalline SiO_2 [i.e., *a*-quartz (1 atm) and stishovite (~15 GPa)] and $MgSiO_3$ [i.e., enstatite (1 atm), ilmenite-type $MgSiO_3$ (22 GPa), bridgmanite (25 GPa), and post-bridgmanite (120 GPa)] phases. The electronic structures and O *K*-edge XRS features have been calculated using the *ab initio* calculations based on the full-potential linearized augmented plane wave + local orbitals (FP-LAPW+lo) method, i.e. WIEN2k [74]. The site-resolved O *K*-edge XRS features of these SiO_2 and $MgSiO_3$ polymorphs have been presented at the *first* time. In further, I have tried to probe the atomistic origins of pressure-induced changes in the O *K*-edge XRS spectra of $MgSiO_3$ glasses, which were obtained from the previous *in situ* high-pressure XRS experiments [1], through the comparison between the O *K*-edge XRS features of the bridgmanite at ~25 GPa and post-bridgmanite at ~120 GPa. Thus, the pressure-induced changes in O *K*-edge XRS features of $MgSiO_3$ glasses have been suggested to be indicative of the enhanced proximity between neighboring O atoms, rather than changes in the Si coordination environments. Despite the efforts in this study, the direct correlation between the structural changes around O atoms, in the short- to medium-range order, and changes in the O *K*-edge XRS features of $MgSiO_3$ glasses could not be determined systematically, since the O *K*-edge XRS features of crystalline polymorphs within different symmetry groups (bridgmanite at ~25 GPa and post-bridgmanite at ~120 GPa), and at different pressure conditions, have been compared. The results of this study were already published [3].

Chapter 4 presents the calculated PDOSs and O *K*-edge XRS features for the $MgSiO_3$ high-pressure polymorphs: bridgmanite (from ~25

to ~120 GPa) and post-bridgmanite (at ~120 GPa). These results also have been calculated using WIEN2k [74]. The results of Chapter 3 are combined to determine the general relationship between the short-range topological changes around O atoms and associated changes in the electronic structures, as well as O *K*-edge XRS features, of the crystalline SiO_2 and $MgSiO_3$ polymorphs. The results have been used to reveal the relationship between the short- to medium-range structural changes around O atoms and changes in the band gap energies and O *K*-edge XRS features of the SiO_2 and $MgSiO_3$ high-pressure polymorphs. The enhanced proximity between neighboring O atoms seems to be strongly correlated with changes in the absorption threshold energies in O K-edge XRS features, and the band gap energies, of the crystalline SiO_2 and $MgSiO_3$ polymorphs, while the characteristic O *K*-edge XRS features result from the distinctive local atomic configurations around O atoms. In further, I have tried to probe the atomistic origins of pressure-induced changes in O *K*-edge XRS features of $MgSiO_3$ glasses [1], through the comparison with changes in the O *K*-edge XRS features of bridgmanite structures with increasing pressure from ~25 to ~120 GPa. Though the detailed densification process of $MgSiO_3$ glass could not been determined, the results presented here reveal that the enhanced proximity between neighboring O atoms, even without the coordination transition of Si atoms, can facilitate the significant changes in O *K*-edge XRS features with an emergence of high-energy excitation features above ~540 eV. The results of this study were published in the paper [7].

Chapter 5 presents the electronic structures and O *K*-edge XRS features of highly disordered $MgSiO_3$ melts at high pressures from ~0 to

~131 GPa. Since the potential presence of high-density $MgSiO_3$-rich partial melts has been suggested as one of the origins of seismic heterogeneities in the Earth's interior [1,41-43], the atomic and electronic structures, and associated elastic properties, of highly disordered Mg-silicates at high pressures have been highlighted. However, the pressure-induced changes in the electronic structures and corresponding changes in the core-level excitation features of amorphous Mg-silicates have not been systematically established yet, since previous studies have focused on their structural and elastic properties [8,75-77]. The atomic configurations of high-density $MgSiO_3$ melts at high pressures were obtained using the *ab initio* molecular dynamic (AIMD) simulations based in the projected augmented wave (PAW) type pseudopotential method, i.e. CASTEP [78]. The O *K*-edge XRS features of $MgSiO_3$ melts also have been calculated using CASTEP [78]. On the other hand, the PDOSs of high-density $MgSiO_3$ melts were calculated using WIEN2k [74]. The calculated PDOSs and O *K*-edge XRS features for $MgSiO_3$ melts at high pressures present significant changes upon compression, particularly above ~18 GPa. The band gap energies of $MgSiO_3$ melts significantly increase while the pressure increases from ~16 to ~131 GPa, and the O *K*-edge XRS features also shift to a higher-energy region, i.e. an emergence of the high-energy features above ~540 eV. Because the decreases in the short-range interatomic distance, such as the Si-O bond length, neighboring Mg-O and O-O distances, seem to be more associated with the densification of MgSiO3 melts in a higher-pressure region from ~18 to ~131 GPa, changes in the PDOSs and O *K*-edge XRS features of the $MgSiO_3$ melts might be due to the decreases in the short-range interatomic distances around O atoms. In further, the atomistic origins of the pressure-

induced changes in the O *K*-edge XRS features of the $MgSiO_3$ glasses have been determined more precisely, because it is obvious that the calculated O *K*-edge XRS features for the $MgSiO_3$ melts are more helpful than the results in the previous chapters. The results of this study suggest that the pressure-induced changes in O *K*-edge XRS features of the $MgSiO_3$ glasses with increasing pressure are due primarily to the decreases in the short-range interatomic distances around O atoms, and, thus, it cannot directly indicate the presence of highly coordinated Si and O atoms. However, the pressure-induced changes in the O *K*-edge XRS features of the $MgSiO_3$ glasses can, indirectly, suggest the presence of highly coordinated Si and O atoms, as well as the O triclusters (e.g., $^{[5]}$Si-$^{[3]}$O-2$^{[4]}$Si), because the decreases in the interatomic distances in the short-range order present moderate correlations with the increases in average atomic coordination numbers of Si and O atoms, in a higher-pressure region above ~18 GPa. The results presented here, along with the results in Chapter 1 and Chapter 2, could improve our knowledge about the densification process of high-density $MgSiO_3$-rich partial melts. Furthermore, I have discussed that changes in the band gap energies of the crystalline and noncrystalline SiO_2 and $MgSiO_3$ phases with the enhanced proximity between neighboring O atoms at high pressures can be used to extended our knowledge about the band gap engineering of the perovskite-type photovoltaics and the quantum dot materials in the perovskite matrix [79-81].

Chapter 6 presents the calculated PDOSs and O *K*-edge XRS features of the SiO_2 high-pressure polymorphs [α-quartz (1 atm), β-quartz (1 atm), α-cristobalite (1 atm), coesite (~3.8 GPa), hp-cristobalite (~20 GPa), penta-SiO_2 (~16 GPa), stishovite (~9.3 and ~29.1 GPa), $CaCl_2$-type (~63

GPa), α-PbO_2-type (~120 GPa), and pyrite-type (~271 GPa)] to determine the atomistic accounts of the pressure-induced changes in O *K*-edge XRS features of SiO_2 glasses with an emergence of double-peak-like excitation features at ~538 and ~544 eV. The previous studies have suggested that the emergence of double-peak-like O *K*-edge XRS features may be attributed in part to the presence of $^{[6]}$Si atom with the stishovite-like structural transition [2], the formation of highly coordinated Si atoms ($^{[5]}$Si, $^{[6]}$Si, and $^{[6+]}$Si) [44,67], and the changes in Si-O-Si bond angle with Si-O bond elongation [73]. However, the results of this study suggests that the emergence of double-peak-like O *K*-edge XRS features might be indicative of the enhanced proximity of neighboring O atoms, in a distance of less than ~2.5 Å, rather than the coordination transition of Si atoms at high pressures, since the O *K*-edge XRS spectra of hp-cristobalite ($^{[4]}$Si), penta-SiO_2 ($^{[5]}$Si), and stishovite ($^{[6]}$Si) structures exhibit similar double-peak-like excitation features. In further, both the band gap energies and the absorption threshold energies in O *K*-edge XRS features of the SiO_2 high-pressure polymorphs present strong correlations with the nearest neighboring O-O distances, as well as their densities. Whereas this study could improve our understanding about the atomistic accounts of the pressure-induced changes in O *K*-edge XRS features of SiO_2 glasses along with the origins of the emergence of double-peak-like excitation features, the further theoretical studies of noncrystalline SiO_2 melts and glasses are expected because of the continuous and complicated structural changes in the noncrystalline network structures of SiO_2 melts and glasses.

Chapter 7 presents the spin-state transition of Fe atoms in FeO wustite structures upon compression as well as changes in their Fe $L_{2,3}$-edge

XRS features. Fe-oxides and Fe-including oxides at high pressures, originated from the dissolution of Fe atoms from the outer core, also have enormous geophysical implications near the core-mantle boundary, as the high-density $MgSiO_3$-rich lower-mantle melts, and, thus, they have been explored in many previous studies [82,83]. Probing the atomic and electronic structures of the simple Fe oxides under extremely high pressures would be helpful to interpret and predict the atomistic accounts of the core-level excitation features, such as the Fe $L_{2,3}$-edge XRS excitation features, of the diverse crystalline and noncrystalline Fe-including oxides under high pressures. In the previous studies, the Fe $L_{2,3}$-edge XRS features have been used to determine the Fe oxidation state quantitatively [84]. Therefore, the atomistic accounts of pressure-induced changes in Fe $L_{2,3}$-edge XRS features have not been studied systematically yet. Thus, the aim of this study is probing the direct correlation between the topological changes around Fe atoms and the changes in Fe $L_{2,3}$-edge XRS features systematically, along with the effects of spin-state transition. To do this, the electronic structures, spin-state transition of Fe atoms, and Fe $L_{2,3}$-edge XRS features of FeO wustite structures have been calculated in a wide range of pressure (from ~19 to ~378 GPa) using the *ab initio* calculations based on the PAW-type pseudopotential method, i.e. CASTEP [78].

Chapter 8 presents the calculated nuclear magnetic resonance (NMR) parameters for the multi-component environmental minerals, i.e. the lepidolite structures, whereas most of previous Chapters have focused on calculating the XRS features of crystalline and noncrystalline oxides at high pressures. Lepidolite $[K(Li,Al)_3(Al,Si)_4O_{10}(F,OH)_2]$ is one of the most-abundant Li-bearing minerals [85]. Two lepidolite structures (1M-type and

$2M_2$-type), referred from the previous study [86], have been used to calculated the NMR chemical shielding and electric field gradient (EFG) tensors of the substituted Li atoms. The NMR parameters have been calculated using the *ab initio* calculations based on the gauge including projector augmented wave (GIPAW) method implemented in CASTEP [78,87]. The calculated NMR parameters for the Li atoms at the symmetrically inequivalent sites in the lepidolite 1M and $2M_2$ structures present considerable differences. Thus, the results of this study suggest that the Li atoms at the symmetrically inequivalent sites in the lepidolite structures would be resolved through the ^{7}Li 2D multiple-quantum magic-angle-spinning (MQMAS) and the ^{7}Li-^{7}Li homonuclear correlation MAS NMR experiments.

Chapter 3.

Pressure-induced changes in local electronic structures of SiO_2 and $MgSiO_3$ polymorphs: Insights from *ab initio* calculations of O *K*-edge energy-loss near-edge structure spectroscopy

Yoo Soo Yi and Sung Keun Lee

Published in *American Mineralogist*, 2012, v. 97, 897-909

Since this study is extended from my previous thesis of M. Sc., parts of this study are not included here. The results of this study were published on American Mineralogist at 2012 [3].

Abstract

Despite its important geophysical implications, direct probing of the local electronic structure of mantle minerals, such as $MgSiO_3$ perovskite and post-perovskite is experimentally challenging. Recent advances in ab initio calculations have allowed us to explore the details of the local electronic bonding structure around oxygen in $MgSiO_3$ polymorphs in Earth's interior. Here, I calculate the O *K*-edge energy-loss near-edge structure (ELNES) spectra for SiO_2 and $MgSiO_3$ polymorphs (i.e., α-quartz, stishovite, enstatite, ilmenite-type $MgSiO_3$, $MgSiO_3$ perovskite, and post-perovskite) using *ab initio* calculations based on the full-potential linearized planewave (FP-LAPW) method. The calculated O *K*-edge ELNES spectra for SiO_2 and $MgSiO_3$ polymorphs show characteristic oxygen *K*-edge features caused by distinctive local atomic configurations and topology around oxygen, and are in good agreement with previous experimental O *K*-edge X□ray Raman scattering (XRS) results. The O *K*-edge ELNES spectra for α-quartz and enstatite show similar edge features at ~538 eV, which is characteristic of corner-sharing oxygen sites ($^{[4]}$Si-O-$^{[4]}$Si). The spectra for stishovite and ilmenite-type $MgSiO_3$ show edge features with double peaks at ~537–538 and ~541–543 eV due to an electronic excitation from an oxygen in edge-sharing topology. The spectrum for $MgSiO_3$ perovskite shows a broad peak spanning from ~538 to ~543 eV, which results from corner-sharing oxygen with two six-coordinated silicon ($^{[6]}$Si-O-$^{[6]}$Si). The calculated O *K*-edge ELNES spectrum for $MgSiO_3$ post-perovskite shows a predicted main feature at ~543–545 eV, approximately 3 eV higher than that of $MgSiO_3$ perovskite. These O *K*-edge features

systematically shift to higher energy with increasing degree of densification in atomic arrangement in the polymorphs (from enstatite, ilmenite, perovskite, to post-perovskite), indicating an increase in the energy of unoccupied oxygen 2*p*-state with pressure. The calculated O *K*-edge spectra also show the effect of densification on the changes in the edge features for the crystallographically distinct oxygen sites: the features for the corner-sharing oxygen move to higher energy from enstatite, perovskite, to post-perovskite. A drastic peak shift for edge-sharing O atoms in ilmenite-$MgSiO_3$ and post-perovskite is also observed. These results confirm that the oxygen *K*-edge features at ~540–550 eV for $MgSiO_3$ glass at pressures above ~20 GPa can be due to densification of the atomic configurations around oxygen in melt networks associated with enhanced proximity between oxygen atoms. The current methods also shed light on a unique opportunity to probe the pressure-induced electronic bonding transitions and topology in diverse simple and complex oxides in Earth's interior using *ab initio* calculations of O *K*-edge ELNES spectra.

Introduction

The knowledge of the electronic and atomic structure of $MgSiO_3$ polymorphs is essential to understand their elasticity, thermodynamic, and transport properties and to provide atomistic origins of the evolution and dynamics of the mantle in the Earth's interior (e.g., [88,89] and references therein). Advances in *in-situ* high-pressure high-temperature experimental techniques combined with brilliant synchrotron x-ray radiation and theoretical calculations have allowed us to explore details of the atomic structures of crystalline $MgSiO_3$ polymorphs at high pressure (e.g., [14,19,82,90-102] and references therein). For instance, the phase transition between $MgSiO_3$ perovskite (Pv) and post-perovskite (PPv) near the core-mantle boundary at ~125 GPa provides atomistic constraints on the structure and heterogeneity in the D" layer and ultra-low velocity zones (ULVZ) at core-mantle boundary [see [4,14,15,19,20,94] and references therein]. Although the atomic structures of $MgSiO_3$ phases at high pressure are well understood, *direct* probing of the detailed electronic bonding structure (e.g., partial local electronic density of states) of these polymorphs, particularly PPv at ~125 GPa, are experimentally challenging.

Local electronic structure can be obtained by probing energy-loss near-edge structure (ELNES), which is one of the effective tools for unveiling element-specific electronic bonding environments (i.e., local atomic structures and chemical environments) around atoms of interests with their characteristic absorption edge features from an excitation of core electron to unbound states. It can be traditionally obtained through x-ray absorption spectroscopy [XAS, particularly x-ray absorption near-edge

structure (XANES)] and electron energy loss spectroscopy (EELS) operated using transmission electron microscopy (TEM) (e.g., see [103-106] and references therein). Whereas simple correlations between the atomic structures and edge features are difficult to establish, previous O *K*-edge studies have shown that the O *K*-edge features for oxides depend on the local structures, chemical composition, and overall topology around oxygen (e.g., Si-O and O-O bond lengths and Si-O-Si bond angles) (e.g., [107]). The O *K*-edge features including peak position can be dominated by the spatial configuration of oxygens around target oxygen, while the detailed edge features (from sub eV to a few eV) can also be strongly affected by the distribution of cations around the oxygen atoms [108].

Often the changes in the O *K*-edge features are rather subtle, and, thus, comparison with predicted XANES features based on theoretical analysis is necessary to confirm the changes [108]: the O *K*-edge ELNES spectra for relatively simple oxides such as MgO, ZnO, SiO_2, Al_2O_3, TiO_2, and GeO_2 have been calculated to elucidate the atomistic origins of experimental O *K*-edge features and have successfully reproduced experimental results [68,107-117]. While the local electronic bonding natures of low-*z* crystalline amorphous oxides at ambient pressures have been studied using earlier XANES spectroscopy using soft x-rays and/or EELS (e.g., [118-121]), conventional synchrotron XAS is not suitable for probing low-*z* oxides at high pressures due to the inability of the soft x-rays to penetrate the sample environments to sustain its high pressure condition (e.g., Be gasket of a diamond anvil cell, etc.) (e.g., [122]). EELS technique has similar limitation in its *in-situ* application to materials under compression.

X-ray Raman scattering (XRS) is an element-specific, *in-situ* experimental probe of bulk oxides with low-*z* elements at extreme conditions (and at ambient pressure) using hard x-rays yet provides the sensitivity of soft x-rays; therefore, it allows us to probe the detailed local bonding nature of low-*z* elements in oxides at high pressures [1,2,64,68,70,72,122-129]. Under the dipole transition selection rule, its transition matrix is identical to an x-ray absorption cross section (see [70] for the review). In particular, previous oxygen *K*-edge XRS studies have revealed pressure-induced changes in the electron bonding transitions in SiO_2, $MgSiO_3$ glass, H_2O, and O_2 phases at high pressures [1,72,129-131]. For instance, the pressure-induced changes in the O *K*-edge features of $MgSiO_3$ glass above ~20 GPa is characterized by an increase in the edge features at 544–545 eV, which was suggested to be due to the formation of triply coordinated oxygen (i.e., oxygen tricluster and thus the transition of the local oxygen configuration from $^{[4]}$Si-O-$^{[4]}$Si to $^{[5]}$Si-O-2$^{[4]}$Si) through comparison of the O *K*-edge features of diverse SiO_2 and $MgSiO_3$ polymorphs [1]. An O *K*-edge XRS study revealed that $(O_2)_4$ molecular clusters in the ε-phase at high pressure show characteristic pressure-induced changes in O *K*-edge features; specifically, the energy for π^* ($1s$-$1\pi_g^*$)- and σ^*($1s$-$3\sigma_u^*$)-transitions increases with increasing pressure from 10 GPa to 47 GPa, indicating a pressure-induced increase in the intermolecular interactions [72]. O K-edge XRS experiments for liquid water probed the molecular arrangement in the intermediate-range of liquid water [129]. Additionally, O *K*-edge XRS experiments for ice phases reveal characteristic O *K*-edge features due to their distinctive local configurations [127,130-132].

These studies proved that XRS experiments can probe crystalline and amorphous oxides at pressure up to ~70 GPa (e.g., 50 GPa for the O *K*-edge of SiO_2 glass [2], ~39 GPa for the O K-edge of $MgSiO_3$ glass [1], ~74 GPa for the Si *L*-edge of SiO_2 glass [73], ~25 GPa for the B *K*-edge of B_2O_3 glass [128], and ~34 GPa for the O *K*-edge of O_2 molecules [72]). These observed trends in pressure-induced changes in O *K*-edge features for molecules and amorphous oxides contribute to the understanding of the atomistic origins of electronic bonding transitions in mantle minerals. Indeed, a previous O K-edge study on silica and Mg-silicate showed that the O *K*-edge is potentially useful for probing bonding transitions in oxide at high pressures [1]. However, the current pressure limit of approximately ~40–70 GPa for XRS experiments (mostly due to x-ray beam size and scattering geometry with DAC) does not allow us to probe the direct bonding changes in diverse oxide polymorphs that are stable above 70 GPa. These limitations pose a great challenge to probing the detailed bonding environments in $MgSiO_3$ PPv near the core-mantle boundary at a pressure of ~120-135 GPa and high temperature: the local electronic bonding structure of $MgSiO_3$ PPv cannot be probed using the current *in-situ* high-pressure XRS experiments. The potential results would provide improved insights into the atomistic origins of the local electronic bonding structure of amorphous Mg-silicate at high pressures.

The ELNES spectra for crystalline oxides can be alternatively predicted using *ab initio* calculations to overcome the inherent difficulties of *in-situ* high-pressure experiments [2,68,72,133]. The ELNES spectra for amorphous and crystalline oxides and transition metals have been calculated using the multiple scattering theory (mostly for high-*z* elements

such as transition metals) [134-140], and using the *ab initio* theory (mostly for low-*z* elements such as silicate oxides) with either molecular orbital calculations [141-144] or full electronic structure calculations [68,145-148]. The calculation based on the multiple scattering theory has met with limited success for calculations of spectra involving low-*z* elements (e.g., [103,140] and references therein). Molecular orbital calculations can yield ELNES spectra for compounds involving low-*z* elements from the photo-absorption cross-section (PACS) combined with the time-dependent density functional theory [142,144,149-152]. The band structure methods estimate the ELNES spectra for materials from the site-projected partial density of states (PDOS) of target elements calculated from the full electronic structure for crystalline materials with varying types of basis sets. A recent study showed that the O *K*-edge XRS experiments for SiO_2 polymorphs are well-reproduced by the oxygen 2*p*-projected electronic PDOS (e.g., [68] and references therein). Note that calculated site-projected PDOS cannot include the quantitative contributions of the monopole and other higher order multipole transitions to the ELNES spectrum [68,70,116,145,148]. These progress and advances in the *ab initio* calculations enable us to more efficiently provide accurate estimation of the ELENES spectra for materials of interest. Particularly, the theoretical implementation of full-potential linearized augmented plane wave (FP-LAPW) methods have been successful in reproducing experimental ELNES or PODS spectra for various materials with low-*z* elements such as Mg, MgO, Si, and SiO_2 phases. [68,74,116,117] where the ELNES spectra for materials can be calculated from the relativistic double differential scattering cross section (DDSCS) expanded in spherical harmonics, taking

into consideration the dipole transition and other higher order multipole transitions [116,117,153]. While these advances can potentially be applied to explore the bonding nature of oxides at high pressures, few studies have been carried out on the theoretical calculations of O *K*-edge ELNES spectra for important oxides (e.g., $MgSiO_3$) with geophysical implications in the Earth's interior. Systematic relationship between topology around oxygen atoms and O *K*-edge features in Mg-silicates has not yet been established.

In this study, I report the O *K*-edge ELNES spectra for SiO_2 and $MgSiO_3$ high-pressure polymorphs using *ab initio* calculations based on the density functional theory to achieve improved insights into the origins of distinctive O *K*-edge features for $MgSiO_3$ polymorphs from their short-range structures and topology. I present the first O *K*-edge ELNES spectrum for $MgSiO_3$ Pv and PPv, the latter is not currently achievable using XRS experiments. I also present oxygen site specific analyses of the ELNES spectra of these polymorphs at high pressure to establish a systematic link between pressure-induced changes in atomic configurations in silicates and the corresponding edge features. I finally discuss the atomistic origins of O *K*-edge XRS spectra for $MgSiO_3$ glass at pressures above ~20 GPa based on the comparison with those of their crystalline analogs.

Calculations

Silica and Mg-silicate polymorphs

The SiO_2 polymorphs explored here include *a*-quartz, stishovite; those for $MgSiO_3$ polymorphs are ortho-enstatite, ilmenite-type $MgSiO_3$, $MgSiO_3$ perovskite, and $MgSiO_3$ post-perovskite. The crystal structures, lattice parameters, and atomic coordinates in the unit cells for these polymorphs were obtained from previous x-ray diffraction experiments and theoretical *ab initio* calculations [4,154-158]. The space groups, lattice parameters, and internal variables (bond angles and lengths) for these polymorphs are given in Table 1.

Electronic structure calculations

Quantum chemical calculations were performed to establish the relationship between O K-edge features, partial electronic density of states, and atomic configurations around oxygen atoms in the SiO_2 and $MgSiO_3$ polymorphs using the Wien2k code, which utilizes a full-potential linear augmented plane wave plus local orbital methods (FP-LAPW + lo) [74]. The exchange and correlation interactions are described by the generalized gradient approximation (GGA), and the exchange-correlation functional, Perdew-Burke-Ernzerhof (PBE96), was used for phases studied here. The Muffin-Tin radius (R_{MT}) of Si and O were ~1.44–1.62 Å and the R_{MT} of Mg was ~1.67–1.81 Å. A cut-off energy separating the core and valence states of the electron of -7.1 Ry was used, which allows us to include the Si 2*p*-orbital as a valence state during self-consistent field (SCF) calculations. The product of the smallest value of all atomic radii (R_{MT}) and a plane wave cut-

off parameter (K_{MAX}) (RK_{MAX}) of 5.0 was used: all the calculated silicate polymorphs consist of *sp*-orbital elements (O-$1s^2 2s^2 2p^4$, Si-[Ne] $3s^2 3p^2$, and Mg-[Ne] $3s^2$). A magnitude of the largest vector in the Fourier expansion of charge density (G_{MAX}) of 12.0 was used. The number of *k*-points used for the calculation of the electronic structure in the reciprocal lattice was ~30–50 for the SiO_2 and $MgSiO_3$ polymorphs depending on the number of atoms in each unit cell. The electronic structures of the ground states for the SiO_2 and $MgSiO_3$ polymorphs were refined using SCF convergence criteria of total energy fluctuation of 10^{-4} Ry and charge density fluctuation of 10^{-4} e.

Calculation of PDOS and ELNES spectra

The O *K*-edge ELNES spectra were calculated ~0–30 eV from the absorption edge (i.e., at 538.25 eV) under both dipole-allowed transitions along with other monopole and multipole transitions (i.e., quadrupole and octopole). The ELNES spectra were calculated from the transition matrix of relativistic DDSCS, which incorporate a transition from an initial state of the core electron (ground state of the target electron) into the final state occupied by the target electron in the conduction band [153]. The calculated O K-edge ELNES spectra were broadened with a Gaussian broadening (g) of 0, 0.5, and 1 eV (full-width at half-maximum; FWHM) to obtain good visual similarity in the features between the calculated and experimental results. The PDOS for each orbital of the oxygen atoms were also calculated to analyze the origins of the O *K*-edge ELNES spectra. The calculated PDOS were broadened with a Gaussian broadening with a FWHM of 0.04 Ry. The O *K*-edge ELNES spectra and PDOS for each orbital of the oxygen atoms in $MgSiO_3$ ortho-enstatite and PPv were calculated by taking into account the

relative fraction of the crystallographically distinct oxygen sites in the lattice. Furthermore, the core-hole effect from the 1*s*-orbital of oxygen was considered for the calculations of the O *K*-edge ELNES spectra as the core-hole effect on the overall *K*-edge features of diverse crystalline silicates is known to be significant [99,116,117,142,159,160]. The core-hole effect on the oxygen 1*s*-orbital was imposed on the target atom using the final state approximation methods, thereby reconstructing the change from the initial state of the oxygen orbital (i.e., fully occupied) into the final state after interaction (i.e., single 1*s* electron transferred to the conduction band) [112,117]. Then, the SCF calculations were performed to obtain the electronic structure in which the core-hole was left by the excited oxygen 1*s*-electron, which contributes to the locally changed electronic structure. The ELNES spectrum and PDOS of oxygen were calculated after removing the extra valence charge. The calculated O *K*-edge ELNES spectra for SiO_2 and $MgSiO_3$ polymorphs were shifted to reproduce the O *K*-edge features of the corresponding experimental XRS spectra. The O *K*-absorption edge for SiO_2 α-quartz, stishovite, and $MgSiO_3$ ortho-enstatite was set to 530 eV, and the absorption edge for ilmenite-type $MgSiO_3$, $MgSiO_3$ Pv, and PPv was set to 529 eV.

Results and discussion

Calculated O *K*-edge ELNES spectra for SiO_2 and $MgSiO_3$ polymorphs

Figure 1A shows the calculated O *K*-edge ELNES spectrum for α-quartz with a corner-sharing oxygen ($^{[4]}$Si-O-$^{[4]}$Si, average $^{[4]}$Si-O bond length: 1.6086 Å, $^{[4]}$Si-O-$^{[4]}$Si bond angle: 143.60°, Table 1). The calculated ELNES spectrum presents a broad feature at ~538 eV with a shoulder at higher energy region, and a small feature at ~545 eV. The features at ~538 eV are due to an excitation of a core electron from the oxygen 1*s*-state into unoccupied oxygen 2*p*-states that are hybridized with the silicon 3*s*- and 3*p*-states of two four-coordinated Si atoms in corner-sharing SiO_4 tetrahedra (σ^* transition) [1,2]. The ~545 eV feature stems from the long-range periodicity of corner-sharing SiO_4 tetrahedra; this feature does not depend on the variation of the local bond angles and bond lengths and it becomes more significant for the larger silicate clusters with multiple coordination shells in multiple scattering simulations [161]. The overall O *K*-edge features are consistent with earlier theoretical and experimental XRS, EELS, and XAS studies [1,2,68,120,161]. Figure 1B shows the calculated PDOS for the *s*-, *p*-, and *d*-states of the oxygen atoms in α-quartz, which show that the calculated O *K*-edge ELNES spectrum mainly arises from the contribution of the oxygen 2*p*-state [1,68].

Figure 2 presents the calculated O *K*-edge ELNES spectrum (Figure 2A) and PDOS (Figure 2B) for SiO_2 stishovite with edge-sharing oxygen (2$^{[6]}$Si-O- $^{[6]}$Si, $^{[6]}$Si-O bond length: 1.7753 Å, Table 1). The calculated O *K*-edge ELNES spectrum shows a distinct double peak feature with intense peaks at ~537 and ~542 eV, which is consistent with previous experimental and calculated XRS and EELS studies [2,68,120,121,162,163]. These features are reported to stem from the transition of an oxygen core electron from the 1*s*-state into the oxygen *p*-*p* hybridized state of two neighboring oxygen

atoms in edge-sharing SiO_6 octahedron [1,2]. An excitation of a core electron from the oxygen 1*s*-state to the oxygen 2*p*-state hybridized with the silicon 3*s*- and 3*p*-state leads to an additional contribution to the features at ~537 eV [1,2,164]. Figure 2B also shows the PDOS for each orbital component of oxygen in stishovite indicating that the calculated O K-edge ELNES spectrum for SiO_2 stishovite is due to a contribution from the oxygen 2*p*-state.

Figure 3A presents the total O *K*-edge ELNES spectrum for $MgSiO_3$ ortho-enstatite. The calculated spectrum shows a peak at ~ 538 eV and is in good agreement with the features from previous XRS spectrum. [1]. This O *K*-edge ELNES spectrum was calculated taking into consideration the equal fractions of three crystallographically distinct oxygen sites (Figure 3B): these oxygen sites include non-bridging apical oxygen (O1, 2$^{[6]}$Mg-O1-$^{[6]}$Mg, average $^{[4]}$Si-O1 bond length: 1.6159 Å, average $^{[6]}$Mg-O1 bond length: 2.1371 Å), non-bridging basal oxygen (O2, $^{[6]}$Mg-O2-$^{[4]}$Si, average $^{[4]}$Si-O2: 1.5869 Å, average $^{[6]}$Mg-O2: 1.9640 Å), and corner-sharing bridging oxygen (O3, $^{[4]}$Si-O3-$^{[4]}$Si, average $^{[4]}$Si-O3: 1.6663 Å, average $^{[4]}$Si-O3-$^{[4]}$Si angle: 131.15°, Table 1). In figure 3C, the corner-sharing oxygen (O3) in $MgSiO_3$ ortho-enstatite yields O K-edge features that are similar to those for *a*-quartz and due to the excitation of an oxygen 1*s*-state core electron into the *sp*-hybridized state between the oxygen 2*p*-state and the silicon 3*s*- and 3*p*-state. The non-bridging apical (O1) and basal (O2) oxygen atoms show distinct O *K*-edge features with two partially separated peaks at ~536 and 541 eV. The slight difference between the calculated O K-edge spectrum and the XRS spectrum for $MgSiO_3$ ortho-enstatite (~541 eV) may be due to the uncertainty in the experimental XRS spectrum stemming from the relatively low signal to background ratio and low resolution (> ~1 eV). Figure 3D shows the PDOS for each state of oxygen in $MgSiO_3$ ortho-

enstatite, thereby confirming a major contribution from the oxygen 2*p*-state to the O *K*-edge ELNES spectrum.

Figure 4A shows the O *K*-edge ELNES spectrum for ilmenite-type $MgSiO_3$ in which peculiar O K-edge features with two peaks at ~538 eV and ~542 eV are observed, which is consistent with previous experimental results [1]. Note that all the oxygen in the polymorph are edge-sharing oxygen ($^{[6]}$Si-O-$^{[6]}$Si, average $^{[6]}$Si-O bond length: 1.7989 Å, O-O bond length: 2.3316 Å, average Mg-O distance: 2.0765 Å). The O *K*-edge features with characteristic double peaks are somewhat similar to those of stishovite, indicating that the edge-sharing oxygen may yield similar O *K*-edge features. Figure 4B presents the PDOS for each state of oxygen, which again reveals the remarkable similarity between the O *K*-edge features of ilmenite-type $MgSiO_3$ and the oxygen 2*p*-state PDOS.

Figure 5A shows the calculated O *K*-edge ELNES spectrum for $MgSiO_3$ Pv. There are two crystallographically distinct oxygen sites in $MgSiO_3$ Pv (Figure 5B): an apical oxygen atom, $^{[6]}$Si-O1-$^{[6]}$Si [O1, $^{[6]}$Si-O1: 1.8001 Å, $^{[6]}$Si-O1-$^{[6]}$Si angle: 146.51°, average Mg-O1: 2.0551 Å]; and a planar oxygen atom, $^{[6]}$Si-O2-$^{[6]}$Si [O2, $^{[6]}$Si-O2: ~1.7825–1.7960 Å, $^{[6]}$Si-O2-$^{[6]}$Si angle: 147.04°, average O2-O2 distance: 2.5304 Å, average Mg-O2: 2.2523 Å]. The ratio of O1 to O2 fraction is 1:2. The calculated O *K*-edge ELNES spectrum for $MgSiO_3$ Pv shows broad peaks centered at ~540.5 eV with fine features at 537 eV, 539 eV and ~542 eV. The broad features at ~ 540 eV is thus characteristic of oxygen atoms linking two $^{[6]}$Si atoms (corner-sharing $^{[6]}$Si-O-$^{[6]}$Si). The peak position and the overall shape are also consistent with the previous experimental result, while the energy resolution and signal-to-background ratio of the *in-situ* high-pressure XRS spectrum for $MgSiO_3$ Pv may not be sufficient to resolve the fine features in the O *K*-edge spectrum [1]. This result indicates that the O *K*-edge features for $MgSiO_3$ polymorphs could be affected by the silicon coordination

environments [2]. Figure 5C shows the O *K*-edge ELNES spectra for the O1 and O2 sites in the $MgSiO_3$ Pv. These oxygen sites show similar spectral features because of their similarity in atomic environments. Figure 5D shows the PDOS for each electronic state of oxygen in $MgSiO_3$ Pv, which confirms that the oxygen 2*p*-state is the main contributor to the O *K*-edge ELNES spectrum for $MgSiO_3$ Pv.

Figure 6A represents the O *K*-edge ELNES spectrum for $MgSiO_3$ PPv where broad and complicated features are observed spanning from the ~540 to 550 eV region. The spectrum is also calculated by taking into account the two crystallographically distinct oxygen sites of $MgSiO_3$ PPv shown in Figure 6B, which is a corner-sharing oxygen atom, $^{[6]}$Si-O1-$^{[6]}$Si [O1, $^{[6]}$Si-O1: 1.6443 Å, $^{[6]}$Si-O1-$^{[6]}$Si angle: 135.75°, Mg-O1: 1.8377 Å] and an edge-sharing oxygen atom, $^{[6]}$Si-O2-$^{[6]}$Si [O2, $^{[6]}$Si-O2: 1.6643 Å, average O2-O2 distance: 2.3514 Å]. The proportion of O1 to O2 is 1:2. Both the O1 and O2 sites of $MgSiO_3$ PPv yield distinctive O *K*-edge features as shown in Figure 6C: the O1 site shows a broad feature ranging from ~ 538 eV to ~548 eV region and the O2 site shows two characteristic peaks at ~540 and ~542.5 eV. Note that the O K-edge feature for corner-sharing oxygen atoms (O1, $^{[6]}$Si-O-$^{[6]}$Si) in $MgSiO_3$ PPv shifts to higher energy (~ 3 eV) than those in other $MgSiO_3$ polymorphs. The double peak features for the O2 site (edge-sharing oxygen) is also distinct from the features for edge-sharing oxygen in ilmenite-type $MgSiO_3$, implying that O *K*-edge features $MgSiO_3$ polymorphs could depend on the local oxygen configuration and topology beyond the short-range structures (see below for further discussion). Figure 6D presents the calculated PDOS for oxygen in $MgSiO_3$ PPv, which confirms the major contribution of the oxygen 2*p*-state component to the O *K*-edge ELNES spectrum for $MgSiO_3$ PPv.

Site-resolved O *K*-edge features of SiO_2 and $MgSiO_3$ polymorphs

Figure 3-1A shows the calculated O *K*-edge ELNES spectra for SiO_2 and $MgSiO_3$ polymorphs. The calculated spectra are generally consistent with the experimental O *K*-edge XRS spectra [1,2], resolving changes in the local oxygen configuration and topology in these crystals. The overall similarity between experimental and calculated spectra suggests that the current method is useful for the reproduction of O *K*-edge features for crystalline oxides at both ambient and high pressure. On the basis of the similarity between the calculated ELNES patterns and the experimental XRS spectra for the minerals studied here, the predicted O *K*-edge ELNES spectrum for $MgSiO_3$ PPv is also expected to be correct. The differences between the O *K*-edge features for $MgSiO_3$ Pv and PPv stem from their different local atomic configurations and topology around the oxygen atoms: the latter has the shorter Si-O, and O-O bond lengths, and the Mg-O distances (Table 1) [4,5]. These changes were also shown in the calculated PDOS for valence bands for PPv and Pv phases (see appendix) [165]. The total Si PDOS/O PDOS ratio of valence bands increases from Pv (16.5) to PPv (17.8), indicating an pressure-induced increase in charge transfer (i.e., iconicity) from Si and O. Future XRS experimental confirmation for $MgSiO_3$ PPv with improved x-ray optics and photon flux remain to be explored.

Figure 3-1B shows the calculated O *K*-edge ELNES spectra for $MgSiO_3$ polymorphs only. Whereas the fine features (> ~0.5 eV) depend on the topology of atomic configurations around oxygens in these crystals as previously discussed, it is clear that O *K*-edge features shift to higher energy (~ 3-4 eV) with increasing degree of densification in atomic arrangement in $MgSiO_3$ polymorphs (from enstatite, ilmenite, Pv, to PPv).

The calculated O *K*-edge spectra for the SiO_2 and $MgSiO_3$ polymorphs show characteristic O *K*-edge features for the crystallographically distinct oxygen sites in each polymorph. For instance, O *K*-edge ELNES spectrum shows that the features for the bridging oxygen moves to higher energy from enstatite (1atm), Pv (27 GPa), to PPv (121 GPa) (Figure 7C). The features are mainly affected by the silicon coordination environment and Si-O bond lengths. A drastic and peak shift for edge-sharing oxygens in ilmenite-$MgSiO_3$ and PPv is also observed (Figure 7D). I note that the shift of the σ^* features observed for the polymorphs is consistent with the trend observed for both π^* and σ^* peaks in $(O_2)_4$ cluster in the ε-phase with increasing pressure [72]. A similar trend in pressure-induced edge energy shift has been reported for simple elements (e.g., O, Ne, and Cl) where pressure-induced increase in mean excitation energy is reported [166].

Pressure-induced changes in O *K*-edge XRS spectra of $MgSiO_3$ glasses

The presence of Mg-silicate melts at the core-mantle boundary has been suggested and discussed [1,39,46,167-171]. Whereas the atomic structures of high-density melts at the core-mantle boundary have not been well understood, the current results yield insights into the atomistic origins of pressure-induced changes in the local electronic bonding structures of $MgSiO_3$ glass at high pressures [1]. Figure 8 shows the O *K*-edge XRS spectra for $MgSiO_3$ glass at 1 atm and 39 GPa compared with the calculated O K-edge features for $MgSiO_3$ Pv and PPv. The O *K*-edge XRS spectrum for $MgSiO_3$ glass at ~39 GPa shows features at ~543–545 eV [1]. This trend is comparable to the changes in the O *K*-edge features of $MgSiO_3$ Pv and PPv. I previously suggested that the feature at ~545 eV is due to the formation of

oxygen triclusters and the associated changes in the medium-range structures [1]. The formation of oxygen triclusters $MgSiO_3$ melts at high pressure can enhance melt viscosity and lead to a decrease in the crystal-melt partitioning coefficient of the element [1]. While it is yet difficult to confirm the presence of oxygen triclusters based on the results presented here alone, on the basis of the differences between the local oxygen configurations of $MgSiO_3$ Pv and PPv and the corresponding changes in the O *K*-edge features, the current results show that a densification of crystalline silicates (formation of highly coordinated Si and enhanced proximity between oxygen atoms) in the unit cell lead to a shift of edge features into higher energy region. The atomistic origins of pressure-induced O *K*-edge features for $MgSiO_3$ glass above ~20 GPa could therefore be due to the densification of the atomic configurations around oxygen atoms. Additionally, the enhanced oxygen proximity and highly coordinated Si associated with the formation of a tricluster can lead to similar changes in the O *K*-edge features in the silicate glass at high pressures [1] and may account for the densification mechanism for high-density Mg silicate melts near the core-mantle boundary, although the effect of temperature on $MgSiO_3$-rich melts at high pressures remains to be clarified.

The O *K*-edge ELNES features of SiO_2 and $MgSiO_3$ polymorphs provide the electronic bonding structure around oxygen from the information of the unoccupied oxygen 2*p*-state (i.e., the lowest unoccupied molecular orbital of the oxygen atoms, LUMO). The calculated O *K*-edge features for $MgSiO_3$ PPv shift to higher energy (~3 eV) compared with that of $MgSiO_3$ Pv, which implies a higher oxygen unoccupied 2*p*-state in

$MgSiO_3$ PPv. Because the chemical reactivity of oxides is often related to their electronic structure in the LUMO, the chemical reactivity in SiO_2 and $MgSiO_3$ polymorphs can be estimated from the unoccupied 2*p*-state of oxygen. The current results thus suggest distinctive reactivity of $MgSiO_3$ PPv and Pv. The current methods can also be applicable to predicting the ELNES spectra for crystalline oxides polymorphs that are experimentally difficult (and/or impossible) to achieve using current high-pressure in *in situ* experimental techniques. I finally note that the current theoretical calculations are useful to predict and/or interpret O *K*-edge features for complex and multi-component oxides and/or metal oxides with cation defects [60,172]. Despite the importance of studying the O *K*-edge absorption features for natural, multi-component Earth materials, it is difficult to yield the detailed atomistic origins of ELNES spectral features from current XRS experimental techniques due to overlap among the edge features that are intrinsic to multi-component oxides. The current theoretical approach could yield the atomistic origins of complicated spectral features for multi-component oxides and complex natural metal oxides from their atomic structures and site-specific contributions to the ELNES and XRS spectra.

Appendix

Figure A1 presents total and partial density of states (PDOS) for valence bands for $MgSiO_3$ Pv and PPv phases. The detailed calculation conditions and convergence criteria used for the calculations are identical to those summarized above. The results for valence bands were obtained without considering the core-hole effect. The calculated PDOS for valence bands are similar to the previous results [165] where the decreases in peak values of DOS in the valence bands were observed, suggesting an increase in the overlap of Si(*p*,*s*)-O*p* orbitals (see text).

Table and Figures

Table 3-1. Space groups, and lattice parameters, and internal variables of SiO_2 and $MgSiO_3$ polymorphs.

(1) α-quartz, 2×2×1 super cell (36 atoms), [158]

(2) Stishovite, 2×2×1 super cell (48 atoms), synthesized at 15 GPa and 1920 K [156]

(3) Ortho-enstatite, single cell (80 atoms), [155]

(4) Ilmenite, single cell (80 atoms), synthesized at 22 GPa and 1820 K [157]

(5) Perovskite, 2×1×1 super cell (40 atoms), synthesized at 27 GPa and 2100 K (XRD experiment was performed at ambient condition) [154]

(6) Post-perovskite, 2×1×1 super cell (40 atoms), Pressure cycled at ~124-134 GPa and ~2500-2600 K (*in-situ* XRD experiment was performed at 121 GPa and 300 K) [4]

Name	α-Quartz[1]	Stishovite[2]	Enstatite[3]	Ilmenite $MgSiO_3$[4]	$MgSiO_3$ Pv[5]	$MgSiO_3$ PPv[6]
System	Trigonal	Tetragonal	Orthorhombic	Rhombohedral	Orthorhombic	Rhombohedral
Space group (number)	$P3_132$ (152)	$P4_2/mnm$ (136)	Pbca (61)	R-3 (148)	Pbnm (62)	Cmcm (63)
Cell parameters (Å)						
a	4.9213	4.1801	18.225	4.7284	4.7754	2.4560
b	4.9213	4.1801	8.8130	4.7284	4.9292	8.0420
c	5.4039	2.6678	5.1800	13.5591	6.8969	6.0930
Bond length (Å)						
Si-O	1.6086	1.7753	1.6159 (O1) 1.5869 (O2) 1.6663 (O3)	1.7989	1.8006 (O1) 1.7893 (O2)	1.6443 (O1) 1.6643 (O2)
Average Si-O	1.6086	1.7753	1.6339	1.7989	1.7930	1.6576
O-O edge (Å)		2.2761 2.5243		2.3316	2.5304 (O2-O2) 2.5335 (O1-O2)	2.3514 (O2-O2) 2.3395 (O1-O2)
Average O-O		2.4416		2.3316	2.5325	2.3434
Mg-O (Å)			2.1371 (O1) 1.9640 (O2) 2.3660 (O3)	2.0765	2.0551 (O1) 2.2523 (O2)	1.8377 (O1) 2.0014 (O2)
Average Mg-O			2.1175	2.0765	2.2030	1.9604
Bond angle (°)						
$^{[4]}$Si-O-$^{[4]}$Si	143.60		131.15			
$^{[6]}$Si-O-$^{[6]}$Si				99.23	146.51 (O1) 147.04 (O2)	135.75 (O1) 95.10 (O2)
$2^{[6]}$Si-O-$^{[6]}$Si		98.83 130.59				
Polyhedral volume ($Å^3$)						
SiO_4	2.1356		2.2147			
SiO_6		7.9396		7.5919	7.6808	6.0458

Only the most important figure, i.e. Fig. 3-1, is presented here. Fig. 3-1 refers to Figure 7 in the published version of this Chapter [3]. Other figures can be found in the published version of this Chapter [3].

Figure 3-1. (A) Calculated O *K*-edge ELNES spectra (black solid line) for SiO_2 (α-quartz, stishovite) and $MgSiO_3$ (ortho-enstatite, ilmenite, perovskite, and post-perovskite) polymorphs with the corresponding x-ray Raman scattering experimental results (open red circles with red solid line) from previous works [1,2]. (B) Calculated O *K*-edge ELNES spectra for $MgSiO_3$ high pressure polymorphs as labeled. (C) Calculated O *K*-edge ELNES spectra for corner-sharing oxygen sites in $MgSiO_3$ high pressure polymorphs as labeled. (D) Calculated O *K*-edge ELNES spectra for edge-sharing oxygen site in SiO_2 and $MgSiO_3$ polymorphs as labeled. The spectrometer broadening parameter (g) of Gaussian broadening FWHM for calculated O K-edge ELNES spectra is 1.0 eV.

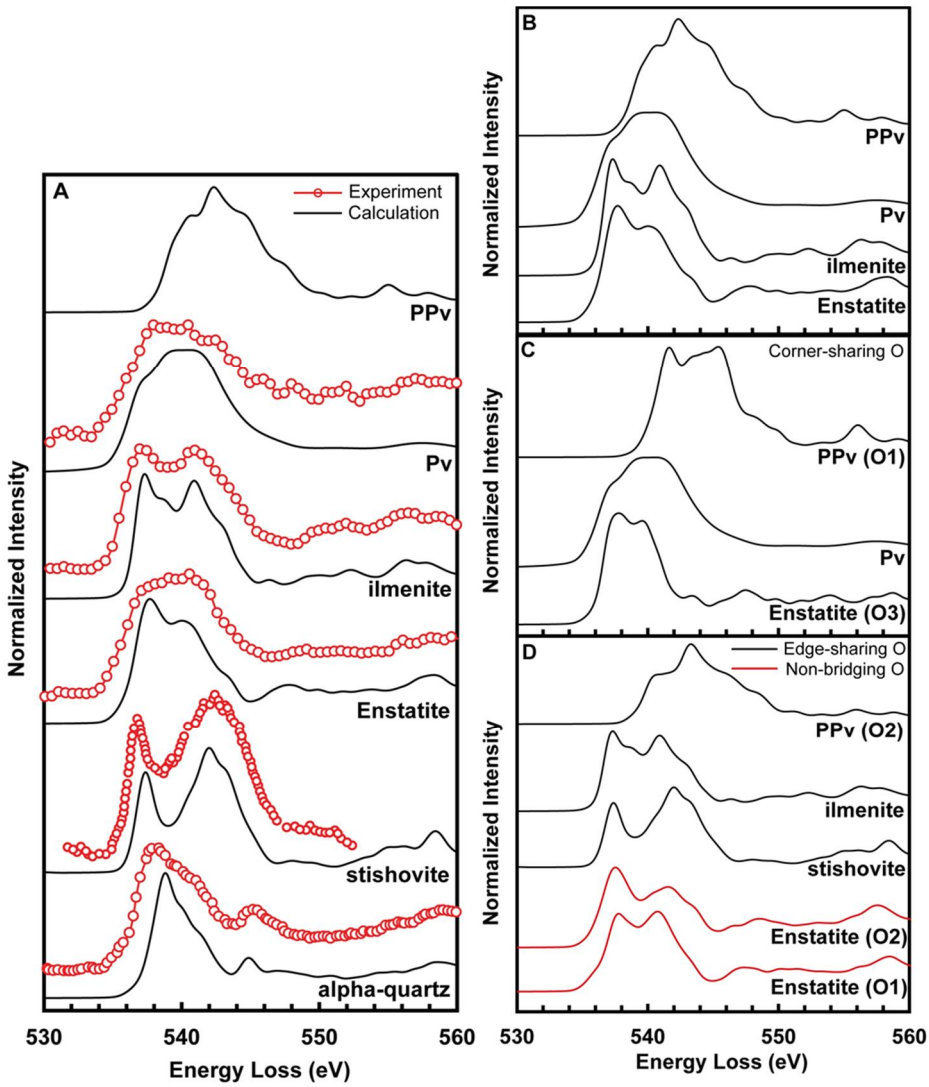
A
Experiment
Calculation
PPv
Pv
ilmenite
Enstatite
stishovite
alpha-quartz
Normalized Intensity
530
540
550
560
Energy Loss (eV)
B
PPv
Pv
ilmenite
Enstatite
C
Corner-sharing O
PPv (O1)
Pv
Enstatite (O3)
D
Edge-sharing O
Non-bridging O
PPv (O2)
ilmenite
stishovite
Enstatite (O2)
Enstatite (O1)

Chapter 4.

Atomistic origins of pressure-induced changes in the O *K*-edge x-ray Raman scattering features of $MgSiO_3$ high-pressure polymorphs: Insights from *ab initio* calculations

Yoo Soo Yi and Sung Keun Lee

Published in *Physical Review B*, 2016, v. 94, 094110

Abstract

Despite its fundamental importance in condensed matter physics and geophysical implications, establishing the systematic and direct link between the pressure-induced structural changes in crystalline and non-crystalline low-*z* oxides and their corresponding evolution in O *K*-edge core-electron excitation features under extreme compression has been challenging. Here I calculated the site-resolved partial density of states (PDOS) and O *K*-edge X-ray Raman scattering (XRS) spectra for two of the important oxide phases in the Earth's lower mantle, $MgSiO_3$ bridgmanite and post-bridgmanite up to 120 GPa using *ab initio* calculations, revealing the electronic origins of the O *K*-edge features for oxides under compression. The absorption threshold (E_A) and band gap increase *linearly* with a decrease in the O-O distance in diverse SiO_2 and $MgSiO_3$ high-pressure phases [E_A(eV) ≈ -10.9×$d_{O\text{-}O}$(Å)+34.4], providing the first predictive relationship between the E_A and the O-O distances in the oxide at high pressure. Despite densification, upon isobaric phase transition from bridgmanite to post-bridgmanite at 120 GPa, a decrease in band gap results in a decrease in edge energy because of an increase in O-O distance. The oxygen proximity is a useful structural proxy of oxide densification upon compression, as it explains the pressure-induced changes in O *K*-edge XRS features of crystalline and amorphous SiO_2 and $MgSiO_3$ at high pressures. These results can be applied to studies of the pressure-bonding transitions in a wide range of oxides under extreme compression that is not achievable with current experimental XRS techniques.

Introduction

Direct probing of the detailed bonding nature of crystalline and non-crystalline oxides at high pressure are among the fundamental and challenging questions in condensed matter physics. Particularly, the pressure-induced changes in atomic configurations in SiO_2 and $MgSiO_3$ at high pressures are critical in clarifying the chemical and physical evolution of the Earth's crust and mantle [15,22,173] and the atomistic origins of the seismic heterogeneities near the core-mantle boundary at a depth of ~2850 km [11,14,19-21,41]. *In situ* high-pressure synchrotron X-ray Raman scattering (XRS) is a unique experimental method that probes the element-specific local electronic structures around low-*z* elements (e.g., O, B, Li, and C) and that has been used to explore the direct electronic bonding transitions of low-*z* oxides and silicates under extreme compression [64,65,69-71]. In particular, O *K*-edge XRS has provided insights into the changes in the bonding transitions of SiO_2 [67,68], GeO_2 [174], B_2O_3 [122], alkali borate [124,128,175] glasses, diverse silicate glasses such as $MgSiO_3$ [1,3], $CaMgSi_2O_6$ [176], and multi-component glasses [177], as well as molecular solids and fluids, such as H_2O [123,129-131,178], and solid O_2 [72] phases at ambient and high pressure up to ~ 70 GPa. In addition to the first excitation shell (i.e., *K*-edge) for low-*z* elements, *L*- and *M*-edge XRS processes for high-*z* elements (e.g., Fe $M_{2,3}$-edge XRS) have also been used to probe the pressure-induced changes in electron spin transition, oxidation states, and local coordination in FeO, Fe_2O_3, and FeS [179,180].

While a detailed review of the previous experimental efforts to explore the O *K*-edge feature of crystalline and non-crystalline silica and

silicates can be found elsewhere [65], a brief summary of these efforts is called for. The XRS experiment on SiO_2 glasses at high pressures up to ~51 GPa revealed the pressure-induced changes in the O *K*-edge XRS spectra [2]. A comparison of *a*-quartz (consisting of 6-coordinated Si atom, $^{[4]}$Si) and stishovite (high pressure polymorph, consisting of $^{[6]}$Si) with the characteristic O *K*-edge XRS spectra attributed the formation of $^{[6]}$Si to the emergence of stishovite-like excitation features (at ~544 eV) of the O *K*-edge XRS spectra of the SiO_2 glasses at high pressures [2]. Oxygen triclusters ($^{[3]}$O; triply coordinated O atoms) have been suggested as the structural origin of the formation of ~544-545 eV features in the earlier O *K*-edge XRS spectrum for the densified $MgSiO_3$ glasses up to 39 GPa [1]. Though minor, pressure-induced shift in O *K*-edge energy was observed in the XRS spectrum for shock-compressed multi-component quaternary oxide glasses [177]. A recent O *K*-edge XRS study of $CaMgSi_2O_6$ glasses under compression up to~ 20 GPa reported the formation of a similar feature at ~544-545 eV. The formation of $^{[6]}$Si has been attributed to the structural origin of the feature [176].

Despite these experimental efforts, establishing the direct link between the changes in the XRS features observed in extreme high pressure conditions and the corresponding local atomic configurations of crystalline and non-crystalline materials has been experimentally challenging because of the limitations of *in situ* high-pressure XRS experiments (with current pressure limit of ~ 70 GPa) and the difficulties in resolving crystallographically distinct and, thus, site-specific structural information [64,65]. Consequently, the electronic bonding nature of two of the important oxide phases in the Earth's lower mantle, $MgSiO_3$ bridgmanite

(stable up to 130 GPa) and post-bridgmanite (stable near the core-mantle boundary) at a pressure of ~120-135 GPa [4,5,14,181], cannot be directly probed using current *in situ* high-pressure XRS experiments. Inputs from theoretical calculations are indeed necessary for the analysis of XRS features in order to interpret XRS edge features properly [3,65,67,68,72]. *Ab initio* calculations have been effective in predicting the core-electron excitation spectrum, including XRS, electron energy loss spectroscopy (EELS), and X-ray absorption near-edge structure (XANES) for low-*z* oxides and silicates [116,117,182]. Particularly, *ab initio* calculations of O *K*-edge XRS spectra for oxides at high pressure overcome the current difficulties of *in situ* high-pressure experiments, providing insight into the pressure-induced structural transitions in oxides under compression [3,64,65]. For example, the calculated O p^*-DOS and Si s^*- and d^*-DOSs were also used to account for the O *K*-edge (due to O 1s-2p^* transition) and Si $L_{2,3}$-edge (due to Si 2p-3s^* and -3d^* transitions) XRS spectra of diverse SiO_2 high-pressure phases [3,65,68]. Successive phase transitions and corresponding structural changes around oxygen in diverse crystalline oxides leads to pressure-induced changes in the calculated O *K*-edge XRS features [3]. A recent theoretical study explored the pressure-induced changes in the O *K*-edge features of amorphous SiO_2, where the formation of highly coordinated Si atoms has been suggested to be the emergence of the high-pressure XRS features at ~544 eV [67].

Whereas the aforementioned advances and progress shed light on unknown details of the pressure-induced bonding transitions in oxide, there are several fundamental unsolved questions in the origin of O *K*-edge XRS features in both crystalline and amorphous oxides upon compression.

First, although the simple short-range structure [coordination number and local structures, non-bridging oxygen (NBO) and bridging oxygen (BO)] in oxide glasses has been linked to observed peaks and features [1,2,65,67,68,72,73,174], those XRS features in the O *K*-edge are often broad and span ~20-30 eV. The interpretation is further complicated by the overlaps among the XRS features that are due to multiple crystallographic sites and their long-range topological variations. Consequently, the origin of 544-545eV features in the O *K*-edge XRS spectra for oxide glasses at high pressure has been controversial: previous experimental and theoretical studies have provided distinct structural origins for the emergence of the high-pressure feature in the O *K*-edge XRS spectra for oxides, formation of $^{[6]}$Si [2,67], formation of $^{[3]}$O and related changes in the medium-range order [1], and overall topological variation (Si-O, Mg-O, O-O, bond angle, etc.), similar to pressure-induced structural transitions in crystalline oxides [3]. Therefore, further theoretical confirmation has been anticipated. Second, the quantitative and systematic relationships between the local oxygen configurations and O *K*-edge XRS features (edge-energy) in both crystalline and non-crystalline oxides remain to be established. While it has been previously confirmed that an increase in structural densification upon phase transition leads to a systematic increase in O *K*-edge energy [3], the comparison has been made between polymorphs at their corresponding pressure condition at the onset of phase transition (e.g., bridgmanite at 25 GPa and post-bridgmanite at 120 GPa). Therefore, remaining fundamental question includes whether structural densification within a stability field of a single phase can result in pressure-induced changes in O *K*-edge XRS spectra. Furthermore, the effect of onset of isobaric phase transition on O *K*-

edge XRS features (i.e., $MgSiO_3$ bridgmanite at 120 GPa and coexisting post-bridgmanite at 120 GPa) is not known. Third, it is expected that band gap may increase with increasing pressure, contributing to changes in O *K*-edge feature of oxides upon compression. Indeed, the effect of Si-O bond on the band gap in SiO_2 polymorphs (*a*-quartz, *β*-quartz, *β*-tridymite, *a*-cristobalite, *β*-cristobalite, keatite, coesite, and stishovite) up to ~10 GPa has been reported [183]. However, the systematic effect of pressure and topological changes, such as Si-O, and O-O distance in silicate crystals on the band gap and its effect on O *K*-edge XRS features up to pressure ranges that are relevant to the core-mantle boundary (~120-130 GPa) have not been explored. The novel information from XRS on densification-induced changes in electronic bonding nature has fundamental implications in condensed matter physics and it could highlight the utility of O *K*-edge XRS as unique structural probe of the electronic structure of diverse oxides at high pressure.

Recent advances in *ab initio* calculations provide an opportunity to calculate the site-specific XRS spectra of crystalline oxides at high pressures [3,175], which are difficult or impossible to achieve with current experimental XRS techniques [64,65]. Therefore, this study's objectives are to reveal the atomistic and electronic origins of the O *K*-edge features for oxides using *ab initio* calculations and to further determine the general relationship between the densification in oxygen environments and the O *K*-edge energy features of diverse oxides under extreme compression. Specifically, I calculate the site-resolved partial density of states (PDOS) and the O *K*-edge XRS spectra for bridgmanite and post-bridgmanite $MgSiO_3$ high-pressure phases based on the full-potential linearized

augmented plane wave + local orbitals (FP-LAPW + lo) method [74], and examine the atomistic origins for the pressure-induced changes in the calculated results. In particular, I explore the effect of pressure-induced changes in the band gap on the O *K*-edge XRS features. The $MgSiO_3$ bridgmanite has a significantly wide range of stability, from ~25 GPa to ~120 GPa [14,181,184], and it provides a rare opportunity to reveal the unknown effect of pressure-induced changes in structural densification in the same phase. Based on the results calculated in the present study and the results from a previous study [3], I also seek to find simple structural and spectroscopic proxy to the densification around the oxygen atoms in low-*z* oxide glasses and crystals under extreme compression.

Calculations

Crystal structures

The crystal structures of the bridgmanite and post-bridgmanite $MgSiO_3$ high-pressure phases used in this study were obtained from previous experimental and theoretical studies (bridgmanite synthesized at ~25 GPa [181], bridgmanite at 45 GPa [185], 79 GPa [186], 90 GPa [185], 120 GPa [5], and a post-bridgmanite phase at 120 GPa [5], or 121 GPa [4]). The crystal structures of the bridgmanite and post-bridgmanite phases at 120 GPa were obtained from a theoretical study [5]. The structures of bridgmanite at 45 and 90 GPa were rescaled from bridgmanite at 79 GPa according to the lattice compressibility of bridgmanite [185], thus they have the same fractional atomic coordinates. Table 4-1 provides details of the crystal structures, including the lattice parameters, bond lengths, interatomic distances, and bond angles. The crystal structures of the bridgmanite and post-bridgmanite were visualized using the VESTA [187]. The electronic structures and corresponding O *K*-edge XRS spectra of the bridgmanite and post-bridgmanite under high pressure were calculated without additional optimization of lattice structure. Both the bridgmanite and post-bridgmanite phases contain crystallographically inequivalent oxygen atoms—those are, O1 and O2 atoms. The oxygen atoms have only corner-sharing topologies in bridgmanite as apical corner-sharing O1 atoms ($^{[6]}$Si-O1-$^{[6]}$Si) and planar corner-sharing O2 atoms ($^{[6]}$Si-O2-$^{[6]}$Si) connecting the SiO_6 octahedra, while the post-bridgmanite phase exhibits both corner- and edge-sharing topologies as corner-sharing O1 atoms ($^{[6]}$Si-O1-$^{[6]}$Si) and edge-sharing O2 atoms ($^{[6]}$Si-O2-2$^{[6]}$Si), as shown in the Figure 4-1. Here, I

attempt to calculate O *K*-edge spectra for these crystallographically distinct oxygen sites in the crystals. While the site-specific O *K*-edge XRS calculations have only been utilized for a few previous studies (e.g., [3,175]), a similar calculation of site-specific information has been used for the other element specific experimental probes including ^{17}O NMR where the previously unknown details of oxygen environments (e.g., corner-sharing oxygen: $^{[4,5,6]}$Si-O-$^{[4]}$Si, $^{[4,5,6]}$Al-O-$^{[4]}$Si, $^{[4,5,6]}$Al-O-$^{[4]}$Si, non-bridging oxygen: Mg-O-$^{[4]}$Si, and metal-bridging oxygen: Pb-O-Pb) in a range of amorphous oxides at ambient and high pressure were revealed [60,188-193].

Calculating electronic structures and the O *K*-edge XRS spectra

The PDOSs and O *K*-edge XRS spectra of the bridgmanite and post-bridgmanite at high pressures were calculated using the WIEN2k based on the FP-LAPW + lo method [74]. Because the FP-LAPW + lo method describes all the electronic states without additional approximations of the core orbitals, it is suitable for calculating the core-level spectroscopy [116,147,182]. In the FP-LAPW + lo method, the electronic states of an atom are classified into three regions (core states, valence states, and semi-core states). These distinct electronic states are calculated using different basis sets to improve the efficiency of the self-consistent field (SCF) calculations. The Perdew-Berke-Ernzerhof for the solid (PBESOL) scheme based on the generalized gradient approximation (GGA) method was used as the exchange-correlation functional to describe the short-range electronic interactions [194]. The Muffin-Tin radii (R_{MT}) for Mg, Si, and O were 1.7-1.9 Å, 1.54-1.67 Å, and 1.54-1.67 Å, respectively. The cut-off energy for the separation of the core and valence states (E_{CUT}) was set to -7.0 Ry, and the Si

2*p*-state was included in the valence state. The E_{CUT} value was chosen to prevent leakage of core electrons from the Muffin-Tin spheres because the leaked core electrons generate semi-core states that increase the convergence time for the SCF calculations. However, negligible differences were observed between the calculated PDOSs with varying E_{CUT} values (i.e., -6.0 and -7.0 Ry). Including Si 2*p*-state in the core state does not lead to a significant change in the PDOS pattern. RK_{MAX} [the scalar product of the minimum value of R_{MT} and the largest plane wave cut-off vector (K_{MAX})] for the bridgmanite and post-bridgmanite is 5.0, which is suitable for describing *sp*-orbital elements from the Mg, Si, and O atoms in the unit cell. The G_{MAX}, (i.e., the magnitude of the largest vector in the Fourier expansion of the charge density) was set to 12.0. The number of *k*-points in the irreducible Brillouin zone for calculating the PDOSs and O *K*-edge XRS spectra was set to 18 and 36, respectively, while the *Γ*-point calculation (the center of the Brillouin zone) was sufficient for silicates and oxides [68,116]. The SCF calculations were carried out using the convergence criteria of 10^{-4} Ry for the total energy and 10^{-3} e for the charge [3]. The PDOSs of the bridgmanite and post-bridgmanite were calculated taking into consideration the core-hole effects with a 2×1×1 supercell (see below for additional details of core-hole effect). The site-resolved PDOSs of the oxygen atoms were obtained from each crystallographically inequivalent oxygen atom (O1 and O2) in each unit cell. Calculated PDOSs for the Mg, Si, and O atoms are also resolved by the angular momentum of each electronic state (*l*-resolved PDOS). The calculated *l*-resolved PDOSs are presented from -30 to 30 eV with respect to the Fermi energy and are broadened with the full-width at half-maximum (FHWM) Gaussian broadening factors of

0.02 Ry. The O *K*-edge XRS spectra for a series of bridgmanite and post-bridgmanite phases were calculated for the crystallographically inequivalent O1 and O2 atoms. In XRS processes, the O 1*s*-electron is excited to the unoccupied states by incident X-ray photons, and the local electronic structures around the oxygen atoms are affected to an extent by this partially empty O 1*s*-state [64,117,147,182]. This core-hole effect is significant in low-*z* elements, but it is less critical in high-*z* elements because the sufficient number of outer electrons in high *z*-element can mitigate the effect of the partially empty core states [116,117,139]. Therefore, the core hole is applied to the target oxygen atom to obtain reliable O *K*-edge XRS spectra for both the bridgmanite and the post-bridgmanite phases. A single 1*s*-core electron of the target oxygen atom is excited to the valence states as an extra background charge to preserve the total charge in the unit cell. This adjustment of the electronic occupation mimics the final state of the electronic transition because of the XRS process [116,182]. The O *K*-edge XRS spectra of the bridgmanite and post-bridgmanite were calculated with a 2×1×1 supercell using the Wien2K from the transition matrix of relativistic double differential scattering cross section (DDSCS) under dipole-allowed transitions as well as monopole, quadrupole, and octopole-allowed transitions [74,139,153]. The calculated O *K*-edge XRS spectra are presented up to 45 eV above the absorption O *K*-edge energy of 528.25 eV. Here the values for energy loss (i.e., energy of scattered photon–elastic energy) in the calculated O *K*-edge features are estimated by adding 528.25 eV to $E\text{-}E_F$ (where E_F is the highest occupied energy state for oxygen). All the calculated O *K*-edge XRS spectra were broadened with 0.5 eV of the

FWHM Gaussian-broadening factors so they are visually similar to the experimental XRS spectra.

Results and Discussion

Pressure-induced structural changes in $MgSiO_3$ polymorphs

Table 4-1 lists the lattice parameters and internal variables of the bridgmanite and post-bridgmanite. The interatomic distances of the bridgmanite change significantly with increasing pressure from 25 to 120 GPa: the average Si-O1 bond length decreases by 6.9% (from 1.7725 Å to 1.6500 Å), and the average Si-O2 bond length decreases by 6.6% (from 1.7681 Å to 1.6508 Å). The average O1-O2 and O2-O2 distances also decrease by 7.3% (from 2.5035 Å to 2.3340 Å) and 7.11% (from 2.5005 Å to 2.3345 Å), respectively (Fig. 4-A1) [5,181]. Figure 4-2 presents the crystal densities (i.e., the total atomic mass with respect to the unit cell volume) of the SiO_2 and $MgSiO_3$ high-pressure phases with respect to the Si-O bond lengths and O-O distances. The Si-O bond lengths of the SiO_2 and $MgSiO_3$ high-pressure phases (consisting of SiO_6 octahedron, $^{[6]}Si$) were negatively correlated with the crystal density (Fig. 4-2A). A strong negative and *linear* correlation between the crystal densities and O-O distances of the SiO_2 and $MgSiO_3$ high-pressure phases was observed, regardless of the Si coordination numbers ($^{[4]}Si$ and $^{[6]}Si$) (Fig. 4-2B), indicating that the O-O distance can describe the pressure-induced densification of the SiO_2 and $MgSiO_3$ phases well.

Pressure-induced changes in PDOSs of $MgSiO_3$ polymorphs

Because the O *K*-edge XRS features arise primarily from the O 1*s*-2*p** transition [64], the unoccupied O PDOSs of the crystallographically

distinct O1 and O2 atoms in the $MgSiO_3$ phases with increasing pressure are calculated to account for the atomistic origins of the changes in O *K*-edge spectra. Figure 4-3 shows the *l*-resolved O PDOSs (for unoccupied states) of O1 (A) and O2 (B) for $MgSiO_3$ bridgmanite and post-bridgmanite, where the systematic pressure-induced changes in the PDOS is demonstrated. Note that pressure-induced broadening in O PDOS in the empty states is prevalent primarily in *d*- states, whereas the pressure-induced broadening is not clearly demonstrated for *s*- and *p*- states. Figure 4-4 also shows the DOS threshold energy in unoccupied states for the oxygen *s*-state, *p*-state, and *d*-state for O1 and O2 in the $MgSiO_3$ bridgmanite with varying average O-O distance. Here, the DOS threshold of each *l*-resolved DOS was estimated from the energy transfer value with the largest change in slop near the absorption edge of the spectrum. This threshold energy increases *linearly* with an increase in pressure and, thus, a decrease in O-O distance. A decrease O PDOS threshold is also observed upon phase transition from bridgmanite to post-bridgmanite at 120 GPa.

The systematic changes in O PDOS indicates an increase in band gap with O-O distance and/or pressure. Figure 4-5A presents the changes in the band gap (E_G) of the SiO_2 and $MgSiO_3$ high-pressure phases with respect to the O-O distance [see appendix for the total and PDOS of bridgmanite phase for valence state with which the band gap were estimated (Fig. 4-A2)] [3]. The band gaps of the diverse SiO_2 and $MgSiO_3$ high-pressure phases decrease *linearly* with decreasing O-O distance ($d_{O\text{-}O}$), regardless of phases or the Si coordination number [i.e., E_G (eV) ≈ -14.1×$d_{O\text{-}O}$(Å)+42.6]. The pressure-induced decrease in the E_G of the bridgmanite phase alone can also be well-described with the relationship, E_G (eV) ≈ -

22.7×$d_{O\text{-}O}$(Å)+63.9. Note that the E_G does not correlate strongly with the Si-O bond length. Figure 4-5B also shows the changes in the E_G of the SiO_2 and $MgSiO_3$ high-pressure phases with increasing pressure. The E_G of $MgSiO_3$ bridgmanite increases with increasing pressure up to 120 GPa, which is consistent with previous theoretical studies for the $MgSiO_3$ enstatite at relatively low pressures up to 2 GPa, where a positive correlation between the E_G and pressures is demonstrated [195]. Upon phase transition between the bridgmanite and post-bridgmanite, at ~120 GPa the E_G decreases from 11 to 8.3 eV, as expected from a decrease in O PDOS (Figs. 4-3 & 4-4), consistent with earlier PDOS calculation of bridgmanite and post-bridgmanite without applying the core-hole effects on target oxygen atoms [165]. This result indicates that short-range electronic repulsion is mitigated upon phase transition in $MgSiO_3$ (from bridgmanite to post-bridgmanite), while overall electronic interaction should increase with increasing pressure. This observed change in the calculated XRS confirms that the overall densification in medium- to larger-length scale beyond the first coordination environments also contributes to the changes in O *K*-edge spectra.

Calculated O *K*-edge XRS spectra for $MgSiO_3$ polymorphs

Figure 4-6 shows the calculated O *K*-edge XRS spectra and the *l*-resolved PDOSs for the unoccupied states of the oxygen atoms in bridgmanite at 25 and 120 GPa. Figure 4-6A shows the O *K*-edge XRS spectra for the O1 and O2 sites in the $MgSiO_3$ bridgmanite at 25 GPa, where broad peaks centered at ~540 eV, which is characteristic of oxygen atoms linking two $^{[6]}$Si atoms (i.e. corner-sharing $^{[6]}$Si-O-$^{[6]}$Si), with fine features at

~537.5, ~539.5, and ~541.4 eV. Figure 4-6B shows their site-resolved PDOSs for the unoccupied *s*-, *p*-, and *d*-states of the oxygen atoms at 25 GPa. Figure 4-6C shows the calculated O *K*-edge XRS spectrum for $MgSiO_3$ bridgmanite at 120 GPa, where the features at ~539.6, ~541.9, and ~544.2 eV are observed. Note that there are systematic pressure-induced shifts in the overall features (~ 2-4 eV) from 25 GPa to 120 GPa. Furthermore, there is a noticeable change in the overall spectral pattern with increasing pressure, indicating that a small change in topology with a fixed crystal symmetry contribute the changes in XRS pattern in the phase. Figure 4-6D shows the site-resolved PDOSs for the oxygen atoms in the bridgmanite at 120 GPa, where the positive peak shifts that are due to enhanced electronic interactions are demonstrated. These results confirm that the calculated O *K*-edge XRS spectra arise primarily from the contribution of the unoccupied oxygen 2*p*-state of PDOS.

Figure 4-7 shows the pressure-induced changes in the calculated O *K*-edge XRS spectra for $MgSiO_3$ polymorphs [enstatite (at 1 atm), ilmenite-type $MgSiO_3$ (i.e., akimotoite, at 22 GPa), bridgmanite (from 25 to 120 GPa), and post-bridgmanite (at 120 GPa)]. The site-resolved O *K*-edge XRS spectra of the crystallographically inequivalent oxygen atoms (e.g., O1, O2 and O3) (Fig. 4-7A) and the total O *K*-edge XRS spectra (Fig. 4-7B) are shown. The calculated O *K*-edge XRS spectra for the enstatite and ilmenite-type $MgSiO_3$ were from our previous study [3]. Previous experimental and theoretical studies have confirmed that the main feature of enstatite at ~538 eV (σ^* transition) is due to the transition of core electrons to unoccupied 2*p*-state in oxygen atoms, hybridized with neighboring $^{[4]}$Si atoms [1,3]. The distinct non-bridging apical oxygen (O1, 3$^{[6]}$Mg-$^{[4]}$O1-$^{[4]}$Si), non-bridging

basal oxygen (O2, 2[6]Mg-[3]O2-[4]Si), and corner-sharing bridging oxygen (O3, [4]Si-[3]O3-[4]Si[6]Mg) in the crystal show characteristic patterns that arise from distinct short-to medium-range structures around the oxygen [3]. Peculiar features with two peaks at ~536.4 and ~540.1 eV are observed in the O *K*-edge XRS spectrum for ilmenite-type $MgSiO_3$, which is consistent with previous experimental results [1]. These double-like features are characteristic of the edge-sharing oxygen ([6]Mg[6]Si-[4]O-[6]Mg[6]Si, with the average [6]Si-O bond length of 1.7989 Å, the [6]Si-[4]O-[6]Si bond angle of 99.23°, the O-O bond length of 2.3316 Å, and the average Mg-O distance of 2.0765 Å) [1,3]. The O *K*-edge XRS spectrum of bridgmanite at 120 GPa shows the characteristic feature near 541.7 eV, which is mostly from the O2 atom, and the other features at ~539.9 and ~543.9 eV are from both the O1 and O2 atoms. Those features shift to a higher energy region with increasing pressure from 25 GPa to 120 GPa. The O *K*-edge XRS spectrum for $MgSiO_3$ post-bridgmanite at 120 GPa shows complex features that span from the ~8 to ~20 eV and are due to a corner-sharing oxygen atom, [6]Si-O1-[6]Si, and an edge-sharing oxygen atom, [6]Si-O2-2[6]Si. For example, the spectrum for O2 site shows two characteristic peaks at ~537.8 and 540.5 eV, similar to the double-peak features for that for edge-sharing oxygen in ilmenite-type $MgSiO_3$.

The results calculated here provide previously unknown details about the effect of the bonding nature around oxygen on the O *K*-edge XRS features. For example, the characteristic features at ~536.7 eV in the total O *K*-edge XRS spectrum of bridgmanite at 25 GPa are caused primarily by the contribution of O1 atom. The significant increase in the relative peak intensity of ~541.5 eV in the O *K*-edge features of bridgmanite at 120 GPa is

due primarily to the contribution from the atomic configurations around the O2 atom. Although the features can be related to the certain structural units, they are overall broad and span 10-20 eV, so a care should be taken to assign the narrow features to specific atomic environments (e.g., NBO and BO), as has often been done in analyses of the XANES spectra for the oxide glasses (see [110,196] for the review of XANES analysis of glasses). Finally, a similar systematic shift of the σ^* features in the O *K*-edge XRS spectra for the $MgSiO_3$ polymorphs has been observed for both π^* and σ^* in the $(O_2)_4$ cluster in the ε-phase [72]. A similar trend in the pressure-induced edge energy shift has been reported for simple elements (e.g., O, Ne, and Cl), suggesting a pressure-induced increase in mean excitation energy [166] (see below for further discussion).

Figure 4-7C shows the calculated O *K*-edge XRS spectra for bridgmanite and post-bridgmanite structures at 120 GPa. The differences between the O *K*-edge features for $MgSiO_3$ bridgmanite and post-bridgmanite stem from their differing local atomic configurations—packing of the SiO_6 octahedra with the emergence of an edge-shared topology for the bridgmanite and coexisting post-bridgmanite at 120 GPa: the latter has the longer average Si-O bond lengths (1.6505 Å *vs.* 1.6853 Å), longer average O-O distances (2.3342 Å *vs.* 2.3835 Å), a larger volume of SiO_6 octahedra (5.9938 $Å^3$ *vs.* 6.3675 $Å^3$), shorter average Mg-O distances (1.9811 Å *vs.* 1.9496 Å), and shorter Si-Si distances [the Si-Si distance in the Si-O1-Si direction (an apical corner-sharing oxygen atom in bridgmanite, and a c-axis direction in the unit cell) decreases from 3.1320 Å to 3.0495 Å, and Si-Si distances in the Si-O2-Si direction (planar corner-sharing and edge-sharing oxygen atoms in bridgmanite and post-bridgmanite, respectively—a- and

b-axis directions in the unit cell) decrease from 3.1290 Å to 2.4550 Å]. Thus, there is a higher overall density in the post-bridgmanite (from 3.2802 amu/Å^3 to 3.3315 amu/Å^3). The significant differences in absorption thresholds, in particular—a decrease in edge energy at 120 GPa upon phase transition—indicates less electronic repulsion between the Si and O atoms in Si-O bond in post-bridgmanite than in bridgmanite, as expected from the longer Si-O bond length and O-O distances even with the shorter Mg-O and Si-Si distances (particularly in the direction of SiO_6 polyhedra constructing the edge-sharing topology in post-bridgmanite—a- and b-axis directions in the unit cells). In contrast to previous study, which have revealed a systematic increase in edge energy features upon phase transition [3], an isobaric phase transition can result in a negative shift in the absorption threshold (mainly because of a decrease in band gap upon densification).

The calculated O *K*-edge spectra for the SiO_2 and $MgSiO_3$ polymorphs show the effects of densification on the O *K*-edge features for the crystallographically distinct oxygen sites [3]. A similar trend in pressure-induced edge energy shift has been reported for solid oxygen and archetypal single-component oxide glasses [65,67,72]. The changes in the O *K*-edge features upon phase transitions suggest that a densification of crystalline silicates (*via* formation of highly coordinated Si and enhanced proximity between oxygen atoms) shifts edge features into a higher energy region [3]. Furthermore, the current results reveal that, without significant changes in topology and coordination number, there is systematic shift to a higher energy with pressure, which is due in part to a pressure-induced increase in band gap. A slight difference in the crystal structure of post-

bridgmanite from *ab initio* calculations [5] and experiments [4] results in a slight but non-negligible change in the XRS features, indicating that the XRS features at high pressure are sensitive to the small changes in topology and crystal symmetry (see appendix, Fig. 4-A3).

Figure 4-8 presents the absorption threshold of the O *K*-edge XRS spectra of diverse SiO_2 and $MgSiO_3$ high-pressure phases with respect to the Si-O bond lengths, crystal densities, and O-O distances. Each absorption threshold of the calculated O *K*-edge XRS spectrum was determined from the energy at which the O *K*-edge feature increases most rapidly (i.e., from the slope of calculated O *K*-edge XRS spectrum). The absorption threshold energies of the diverse SiO_2 and $MgSiO_3$ high-pressure phases may not be closely correlated with either the Si-O bond lengths or Si coordination numbers (Fig. 4-8A), but there is a moderate degree of correlation between the absorption threshold energies and the crystal densities (Fig. 4-8B). In the Fig. 4-8C, the absorption threshold energies (E_A) are correlated *linearly* with the O-O distances (d_{O-O}), regardless of the chemical compositions (SiO_2 and $MgSiO_3$) and Si coordination numbers ($^{[4]}$Si and $^{[6]}$Si). This result can be represented by the simple relationship, $E_A(eV) \approx -10.5 \times d_{O-O}(Å) + 33.7$. This correlation reveals a similar trend to that between the band gap and the O-O distance shown in the Fig. 4-3, so the absorption threshold and the band gap energies are *linearly* correlated ($E_G \approx -1.2 \times E_A - 1.4$). The results presented here provide a quantitative relationship between the structural parameter and the changes in the O *K*-edge XRS features of the diverse SiO_2 and $MgSiO_3$ high-pressure phases. The oxygen proximity is a useful structural indicator of oxide densification upon compression, explaining the pressure-induced changes

in the O *K*-edge XRS features of crystalline and amorphous SiO_2 and $MgSiO_3$ at high pressures.

Pressure-induced changes in O *K*-edge XRS spectra of $MgSiO_3$ glasses

It has been shown that the characteristic O *K*-edge XRS features of crystalline and amorphous SiO_2 at high pressures can be explained in part by the formation of highly coordinated Si atoms with increasing pressure [2,67]. Because the formation of highly coordinated Si atoms in the fully-polymerized SiO_2 glasses is associated with the formation of $^{[3]}$O (e.g., $^{[4]}$Si-$^{[3]}$O-2$^{[4]}$Si) and the topological changes around O atoms, the change could be due to the formation of $^{[3]}$O, as suggested by the O *K*–edge XRS spectra for $MgSiO_3$ glass at high pressure [1]. The current study and previous studies have also shown that the O *K*-edge XRS features of SiO_2 and $MgSiO_3$ polymorphs depend on the local oxygen and topology beyond the short-range structures [1,3]. It is also clear that successive phase transitions lead to changes in the O *K*-edge XRS features with pressure, resulting in a shift in edge-energy features (and the absorption threshold) [3]. The current study of bridgmanite (from 25 to 120 GPa) adds additional insights into the origin of the O *K*-edge features in that, even without phase transition (and, thus, within identical crystal symmetry, topology, and cation and anion coordination environments), densification in the crystal can lead to significant changes (mainly systematic peak energy shifts) in the O *K*-edge XRS spectrum, resulting primarily from an increase in band gap with pressure. These results can help to clarify the atomistic origins of pressure-induced changes in diverse O *K*-edge features for complex oxide glasses. Figure 4-9 presents the calculated O *K*-edge XRS features for bridgmanite

and the experimental O *K*-edge XRS spectra of $MgSiO_3$ glasses and bridgmanite [1]. While the calculations reproduce most of the features, the calculated XRS intensity above ~550 eV (i.e., ~15-20 eV from the E_F) was underestimated to a degree: although the FP-LAPW +lo method typically calculates the ground state density of electrons well, the intensity of unoccupied states far from the Fermi level may not be properly estimated because of the insufficient basis sets in these unoccupied state regions [116,117,182,197]. The underestimated XRS cross section can be improved using the additional basis sets for the high energy regions far from the Fermi level [197]. Figure 4-9 also shows the O *K*-edge XRS features of the $MgSiO_3$ glasses, where significant changes in the XRS features with increasing pressure are prevalent. Distinct spectral features at ~545 eV appear at 39 GPa, whereas overall spectral features shift with a broadening of FWHM to a higher-energy region. While the O *K*-edge XRS of the non-crystalline $MgSiO_3$ at high pressures remains to be calculated, in our previous experimental study of the O *K*-edge XRS of $MgSiO_3$ glass at high pressure (up to 40 GPa), it has been suggested that the formation of oxygen triclusters (oxygen coordinated with three Si frameworks; $^{[3]}$O) and changes in the short- to medium-range structures that are associated with the formation of $^{[3]}$O upon densification can contribute significantly to the formation of the ~545 eV feature [1]. Recent *ab initio* MD simulation of cold-compressed $MgSiO_3$ glasses confirms the presence of a considerable fraction of oxygen triclusters at high pressure ~40 GPa [8], indicating that the formation of the $^{[3]}$O can partly contribute to the emergence of the high-pressure O *K*-edge feature. Nevertheless, the O *K*-edge XRS spectra of the bridgmanite are also comparable to those in the O *K*-edge XRS features of

the $MgSiO_3$ glasses with increasing pressure. Therefore, while the formation of $^{[3]}O$ and the associated decrease in O-O distance can explain the emergence of ~545 eV features in the spectra, the current results suggest that the formation of $^{[3]}O$ in the glasses may not be uniquely attributed the formation of the 545 eV features. The current study shows that densification with no cation and anion coordination transformation can explain the feature at 545 eV. Therefore, the observed changes in the 545 eV features can be primarily due to a reduction in O-O distance. The formation of $^{[3]}O$, the Si coordination number, and the shortening of the Mg-O distance leads to a decreases in the O-O distance in silicates and the emergence of high-pressure features in the O *K*-edge XRS spectra.

Crystalline and non-crystalline $MgSiO_3$ at high pressure have strong geophysical and geochemical implications for the mantle minerals and melts in Earth's and other planets' interiors [19,22,88,92]. The band gap and absorption threshold energies of the SiO_2 and $MgSiO_3$ high-pressure phases (Fig. 4-5A and 4-8C) show a *linear* negative relationship with the O-O distances, including the bridgmanite and post-bridgmanite $MgSiO_3$ high-pressure phases that exist near the core-mantle boundary. These changes result from the topological changes around the oxygen atoms from short- to medium-range structures (i.e., the Si-O bond lengths, the O-O and Mg-O distances, and the Si coordination numbers). These results suggest changes in the chemical reactivity of the SiO_2 and $MgSiO_3$ high-pressure phases because chemical reactions that include electron transfer are assessed in terms of their relative differences in energy between the highest occupied molecular orbital (HOMO) and the lowest unoccupied molecular orbital (LUMO). Although the changes in the chemical reactivity of the SiO_2 and

$MgSiO_3$ high-pressure phases are difficult to comprehend fully from the current results, the smaller band gap of post-bridgmanite suggests more efficient electron transfer than bridgmanite at 120 GPa and, thus, higher chemical reactivity.

Conclusion

Despite earlier efforts to reveal the atomistic origins of the O *K*-edge XRS features, the relationship between the structures (e.g., the formation of highly coordinated Si atoms, the formation of oxygen triclusters and associated changes in medium-range structures, and the enhanced oxygen proximity) and the emergence of high energy features in the O *K*-edge XRS spectra have not been fully explained because of the intrinsic overlaps of O *K*-edge features in the crystalline and non-crystalline network structures and the current experimental limitations of synchrotron XRS up to 60-70 GPa [65]. The present study carried out quantitative analysis of the O *K*-edge XRS spectra of the diverse SiO_2 and $MgSiO_3$ high-pressure phases up to 120 GPa to determine the relationship between the changes in electronic structures and the topological changes in the short- to medium-range structures around oxygen atoms. The study determined the *linear* relationships between the O-O distances and the absorption threshold and band gap of the SiO_2 and $MgSiO_3$ high-pressure phases, along with their simple predictive models. The oxygen proximity is a useful structural proxy of oxide densification upon compression, as it explains the pressure-induced changes in O *K*-edge XRS features of crystalline and amorphous

SiO_2 and $MgSiO_3$ at high pressures. This study can be applied to efforts to unravel the pressure-induced bonding transitions in more complex, multi-component non-crystalline materials under compression *via* O *K*-edge XRS experiments, thus providing insight into the atomistic account of the structural heterogeneity in lower mantle melts.

Table and Figures

Table 4-1. Space groups, lattice parameters, and internal variables of $MgSiO_3$ bridgmanite and post-bridgmanite.

A 2×1×1 super cell (total 40 atoms) was used in the XRS calculations for the bridgmanite and post-bridgmanite phases.

(1)XRD at 15 GPa, from Sugahara, Yoshiasa, Komatsu, Yamanaka, Bolfan-Casanova, Nakatsuka, Sasaki and Tanaka [181]

(2)modified from the bridgmanite at 79.7 GPa in Fiquet, Dewaele, Andrault, Kunz and Le Bihan [186] by rescaling its lattice parameters according to the lattice compressibility suggested by Fiquet, Andrault, Dewaele, Charpin, Kunz and Hausermann [185]

(3)*in situ* XRD experiments using the *in situ* high-temperature DAC at 79.7 GPa and 1681 K, Fiquet, Dewaele, Andrault, Kunz and Le Bihan [186]

(4)modified from the bridgmanite at 79.7 GPa in Fiquet, Dewaele, Andrault, Kunz and Le Bihan [186] by modifying its lattice parameters according to the lattice compressibility suggested by Fiquet, Andrault, Dewaele, Charpin, Kunz and Hausermann [185]

(5)*ab initio* calculations, Iitaka, Hirose, Kawamura and Murakami [5]

(6)*ab initio* calculations, Iitaka, Hirose, Kawamura and Murakami [5]

(7)Murakami, Hirose, Kawamura, Sata and Ohishi [4]

Name	Bridgmanite					Post-bridgmanite	
	25 GPa[1]	45 GPa[2]	79 GPa[3]	90 GPa[4]	120 GPa[5]	120 GPa[6]	121 GPa[7]
System	Orthorhombic					Rhombohedral	
Space group	*Pbnm* (62)					*Cmcm* (63)	
Cell parameters (Å)							
a	4.7019	4.5659	4.4449	4.3552	4.2890	2.4550	2.4560
b	4.8704	4.7903	4.6648	4.6528	4.5570	8.0510	8.0420
c	6.7827	6.6288	6.4544	6.3619	6.2640	6.0990	6.0930
Si-O bond lengths (Å)							
Avg. Si-O	1.7695	1.7430	1.6971	1.6762	1.6505	1.6853	1.6576
Si-O1 (×2)	1.7725	1.7316	1.6860	1.6611	1.6500	1.6312	1.6443
Si-O2 (×4)	1.7681	1.7488	1.7027	1.6837	1.6508	1.7123	1.6643
O-O distances (Å)							
Avg. O-O	2.5025	2.4648	2.3999	2.3703	2.3342	2.3835	2.3434
O1-O2 (×8)	2.5035	2.4607	2.3959	2.3649	2.3340	2.3646	2.3395
O2-O2 (×4)	2.5005	2.4731	2.4080	2.3812	2.3345	2.4213	2.3514
Mg-O distances (Å)							
Avg. Mg-O	2.1669	2.0977	2.0424	2.0168	1.9811	1.9496	1.9604
Avg. Mg-O1	2.0382	1.9583	1.9067	1.9032	1.8484	1.8686	1.8377
Avg. Mg-O2	2.2098	2.1441	2.0877	2.0547	2.0253	1.9766	2.0014
Si-O-Si bond angles (°)							
$^{[6]}$Si-O1-$^{[6]}$Si	146.1407	146.2943	146.3000	146.4572	143.2781	138.3689	135.7544
$^{[6]}$Si-O2-$^{[6]}$Si	146.3562	142.1901	142.1896	142.2701	142.7830	91.5940	95.0964
Volume of the SiO_6 (Å^3)							
SiO_6	7.3849	7.0535	6.5108	6.2719	5.9938	6.3675	6.0458
Crystal densities (amu/ Å^3)							
ρ	2.5856	2.7700	3.0008	3.1152	3.2802	3.3315	3.3371

Figure 4-1. Crystal structures of (A) bridgmanite at 25 GPa and (B) post-bridgmanite at 120 GP. Crystallographically inequivalent oxygen atoms in the unit cells are labeled O1 and O2. There are two crystallographically distinct oxygen sites in $MgSiO_3$ bridgmanite at 25 GPa: an apical oxygen atom, $^{[6]}$Si-O1-$^{[6]}$Si (O1, $^{[6]}$Si-O1: 1.7725 Å, $^{[6]}$Si-O1-$^{[6]}$Si angle: 146.1407°, average Mg-O1: 2.0382 Å), and a planar oxygen atom, $^{[6]}$Si-O2-$^{[6]}$Si (O2, average $^{[6]}$Si-O2: 1.7681 Å, $^{[6]}$Si-O2-$^{[6]}$Si angle: 146.3562°, average O2-O2 distance: 2.5005 Å, average Mg-O2: 2.2098 Å). The oxygen environments in post-bridgmanite at 120 GPa include a corner-sharing oxygen atom, $^{[6]}$Si-O1-$^{[6]}$Si (O1, $^{[6]}$Si-O1: 1.6312 Å, $^{[6]}$Si-O1-$^{[6]}$Si angle: 138.3689°, Mg-O1: 1.8686 Å) and an edge-sharing oxygen atom, $^{[6]}$Si-O2-2$^{[6]}$Si (O2, average $^{[6]}$Si-O2: 1.7123 Å, average O2-O2 distance: 2.4213 Å).

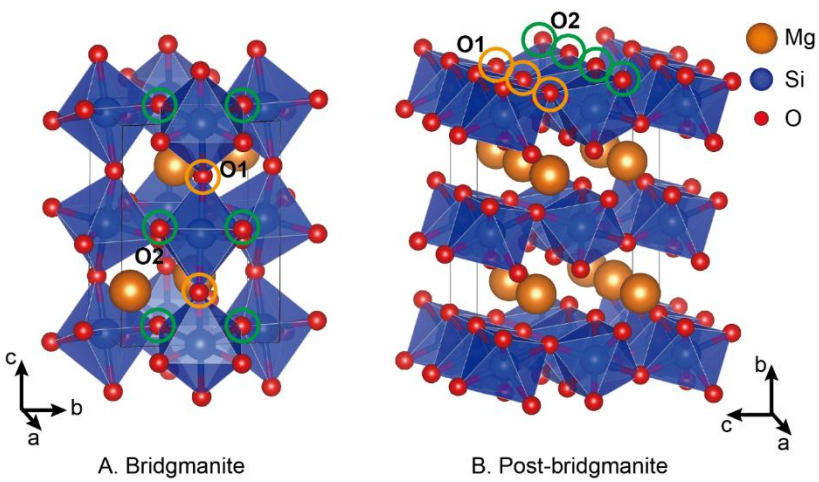

Figure 4-2. Crystal densities (i.e., the total atomic mass divided by unit cell volume) of the SiO_2 (*a*-quartz, coesite, and stishovite) and $MgSiO_3$ [enstatite, ilmenite-type $MgSiO_3$, bridgmanite (BR), and post-bridgmanite (PBR)] high-pressure phases with respect to average Si-O bond lengths (A) and average O-O distances (B); average O-O distances (C), and average Si-O bond lengths (D) of SiO_2 and $MgSiO_3$ high-pressure phases with increasing pressure. The black line refers to the trend for all the phases studied here, whereas a blue trend line is for the bridgmanite phase only. The linear relationship between average O-O distances and pressures for all the phases is described as $d_{O\text{-}O}$(Å) = -0.0021×P(GPa)+2.59 (R^2=0.81). The linear relationship between average Si-O bond lengths and pressures for the bridgmanite phase is described as $d_{Si\text{-}O}$(Å) = -0.0013×P(GPa)+1.80 (R^2=0.99).

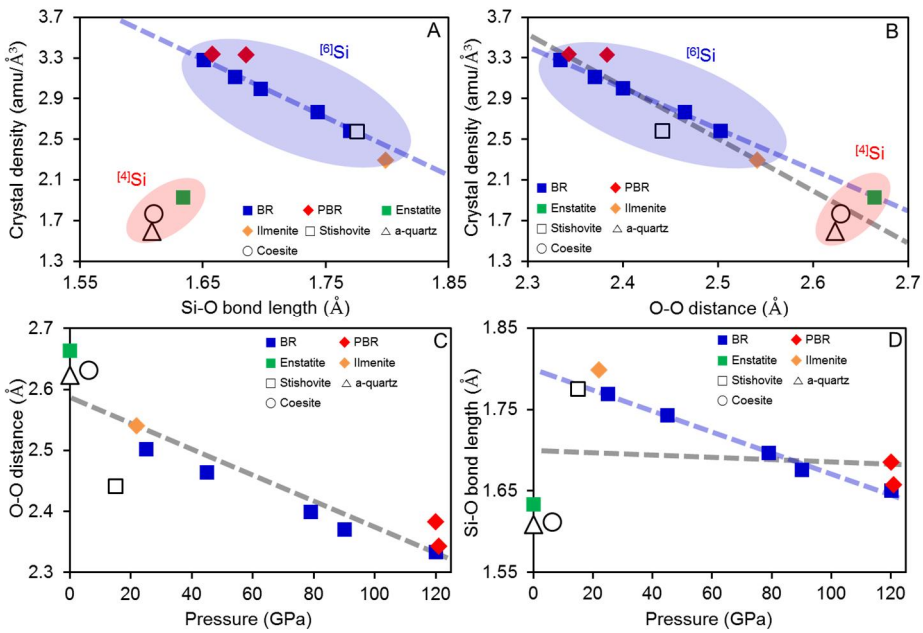

Figure 4-3. *l*-resolved oxygen PDOS (for unoccupied states) of O1 (A) and O2 (B) for $MgSiO_3$ bridgmanite (BR) and post-bridgmanite (PBR) with varying pressure. The Gaussian broadening FWHM for PDOS is 0.02 Ry (red solid, oxygen *s*-state; blue solid, oxygen *p*-state; green solid, oxygen *d*-state; black solid, total DOS of oxygen).

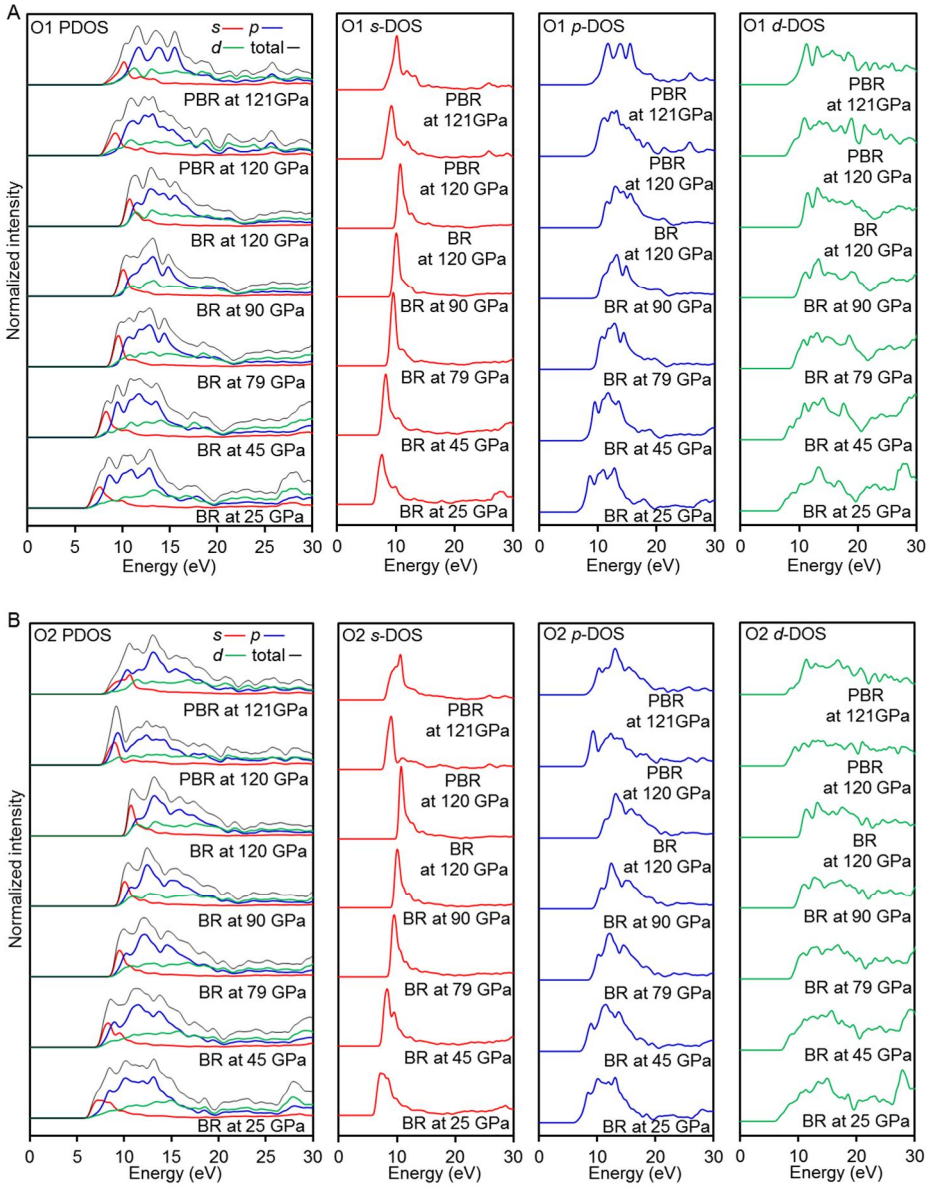
A
O1 PDOS
s
p
d
total
O1 s-DOS
O1 p-DOS
O1 d-DOS
PBR at 121GPa
PBR at 120 GPa
BR at 120 GPa
BR at 90 GPa
BR at 79 GPa
BR at 45 GPa
BR at 25 GPa
Normalized intensity
Energy (eV)
B
O2 PDOS
O2 s-DOS
O2 p-DOS
O2 d-DOS

Figure 4-4. DOS threshold energy for oxygen *s*-state (red), oxygen *p*-state (blue), and oxygen *d*-state (green) for O1 (A) and O2 sites (B) in $MgSiO_3$ bridgmanite (BR; closed circle) and post-bridgmanite (PBR; open circle), with varying average O-O distance. (C) The linear trend lines for the *s*- (red), *p*- (blue), and *d*- (green) states of both O1 and O2 atoms in the bridgmanite phase are shown.

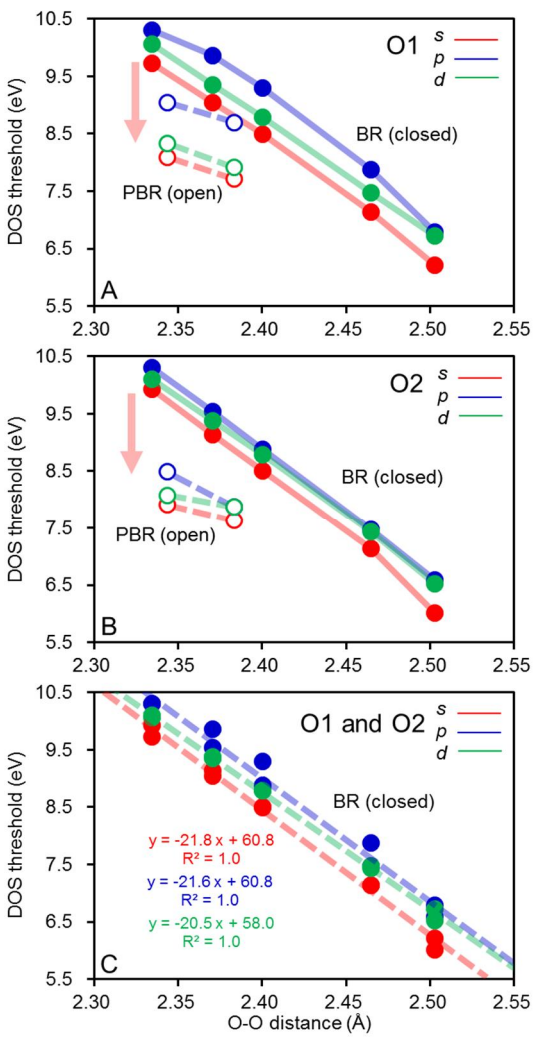

Figure 4-5. Band gap of the SiO_2 (*a*-quartz, coesite, and stishovite) and $MgSiO_3$ [enstatite, ilmenite-type $MgSiO_3$, bridgmanite (BR), and post-bridgmanite (PBR)] high-pressure phases, with varying average O-O distance (A) and pressure (B).

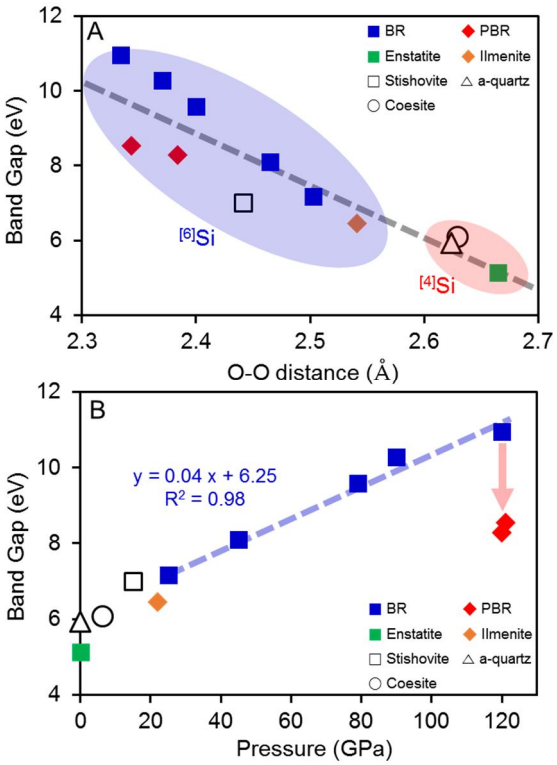

Figure 4-6. (A) Site-resolved and total O *K*-edge XRS spectra [blue solid, O1, apical corner-sharing oxygen; red solid, O2, planar corner-sharing oxygen; black solid, total (O1:O2=1:2)] for bridgmanite (BR) at 25 GPa. (B) *l*-resolved O-DOSs of each orbital (red solid, *s*-state; blue solid, *p*-state; green solid, *d*-state; black solid, total O-DOS) for bridgmanite at 25 GPa. (C) Site-resolved and total O *K*-edge XRS spectra [blue solid, O1, apical corner-sharing oxygen; red solid, O2, planar corner-sharing oxygen; black solid, total (O1:O2=1:2)] for bridgmanite at 120 GPa. (D) *l*-resolved O-DOSs of each orbital (red solid, *s*-state; blue solid, *p*-state; green solid, *d*-state; black solid, total O-DOS) for bridgmanite at 120 GPa. The Gaussian broadening FWHM for PDOSs and O *K*-edge XRS spectra are 0.02 Ry and 0.5 eV, respectively. The experimental O *K*-edge XRS spectra of bridgmanite (open black circles with a black solid line) [1] was compared with the calculated O *K*-edge XRS spectra for the bridgmanite at 25 GPa.

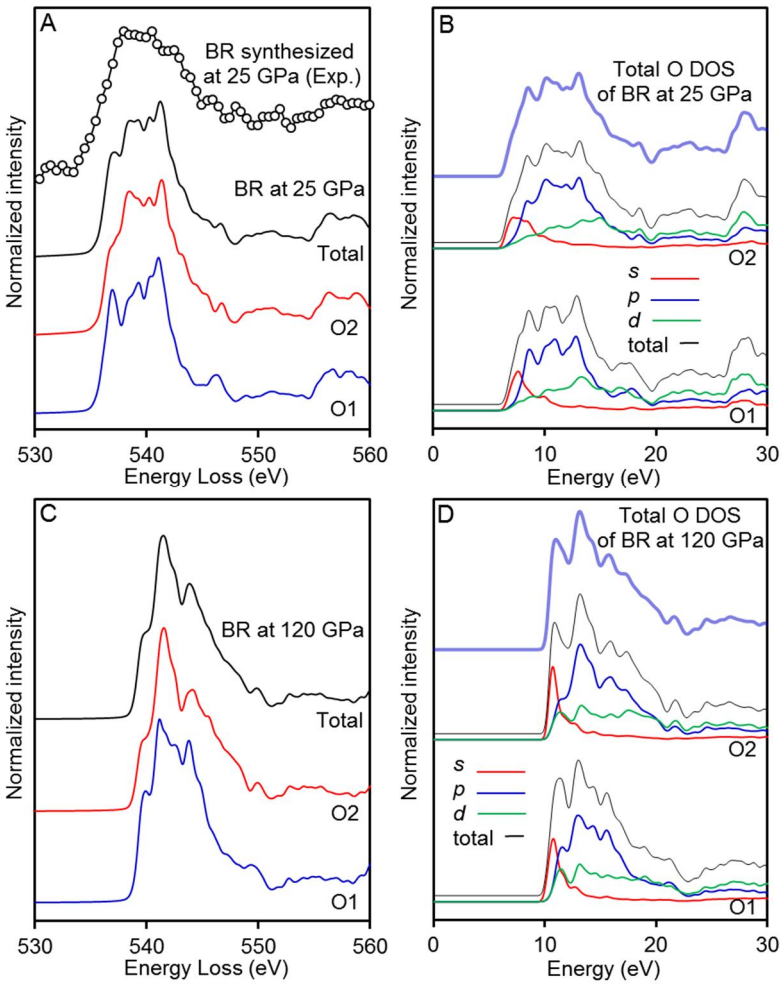
A
BR synthesized
at 25 GPa (Exp.)
BR at 25 GPa
Total
O2
O1
Normalized intensity
530
540
550
560
Energy Loss (eV)
B
Total O DOS
of BR at 25 GPa
O2
s
p
d
total
O1
Normalized intensity
0
10
20
30
Energy (eV)
C
BR at 120 GPa
Total
O2
O1
Normalized intensity
530
540
550
560
Energy Loss (eV)
D
Total O DOS
of BR at 120 GPa
O2
s
p
d
total
O1
Normalized intensity
0
10
20
30
Energy (eV)

Figure 4-7. Site-resolved (A) and total (B) O *K*-edge XRS spectra of high-pressure $MgSiO_3$ [enstatite, ilmenite-type $MgSiO_3$, bridgmanite (BR), and post-bridgmanite (PBR)] polymorphs. Those for crystallographically inequivalent oxygen sites [O1 (black), O2 (red), and O3 (blue)] are shown. The spectra of the enstatite and ilmenite-type $MgSiO_3$ are from a previous study [3]. The Gaussian broadening FWHM for O *K*-edge XRS spectra is 0.5 eV. (C) Direct comparison of the calculated O *K*-edge XRS pattern for bridgmanite and post-bridgmanite at 120 GPa.

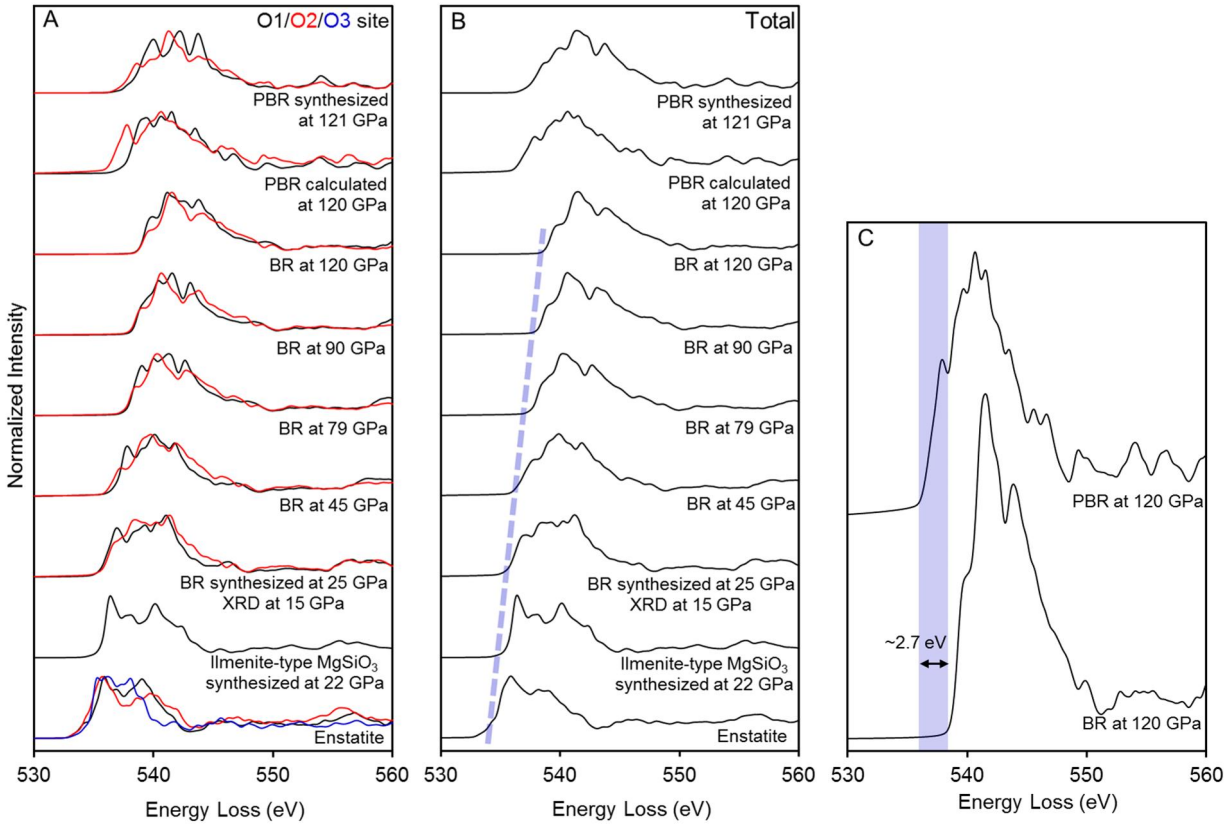
A
O1/O2/O3 site
PBR synthesized at 121 GPa
PBR calculated at 120 GPa
BR at 120 GPa
BR at 90 GPa
BR at 79 GPa
BR at 45 GPa
BR synthesized at 25 GPa XRD at 15 GPa
Ilmenite-type MgSiO3 synthesized at 22 GPa
Enstatite
Normalized Intensity
530
540
550
560
Energy Loss (eV)
B
Total
PBR synthesized at 121 GPa
PBR calculated at 120 GPa
BR at 120 GPa
BR at 90 GPa
BR at 79 GPa
BR at 45 GPa
BR synthesized at 25 GPa XRD at 15 GPa
Ilmenite-type MgSiO3 synthesized at 22 GPa
Enstatite
530
540
550
560
Energy Loss (eV)
C
PBR at 120 GPa
~2.7 eV
BR at 120 GPa
530
540
550
560
Energy Loss (eV)

Figure 4-8. Absorption threshold energies in the O *K*-edge XRS of SiO_2 phases (*a*-quartz, coesite, and stishovite) and $MgSiO_3$ [enstatite, ilmenite-type $MgSiO_3$, bridgmanite (BR), and post-bridgmanite (PBR)] polymorphs with varying crystal density (A), average Si-O bond lengths (B), and average O-O distance (C). The black line refers to the trend for all the phases studied here, whereas a blue trend line is for the bridgmanite phase only. The absorption threshold for SiO_2 phases, enstatite, and ilmenite-type $MgSiO_3$ phases were obtained from a previous study [3] and that for the result of SiO_2 coesite will be presented in a future contribution.

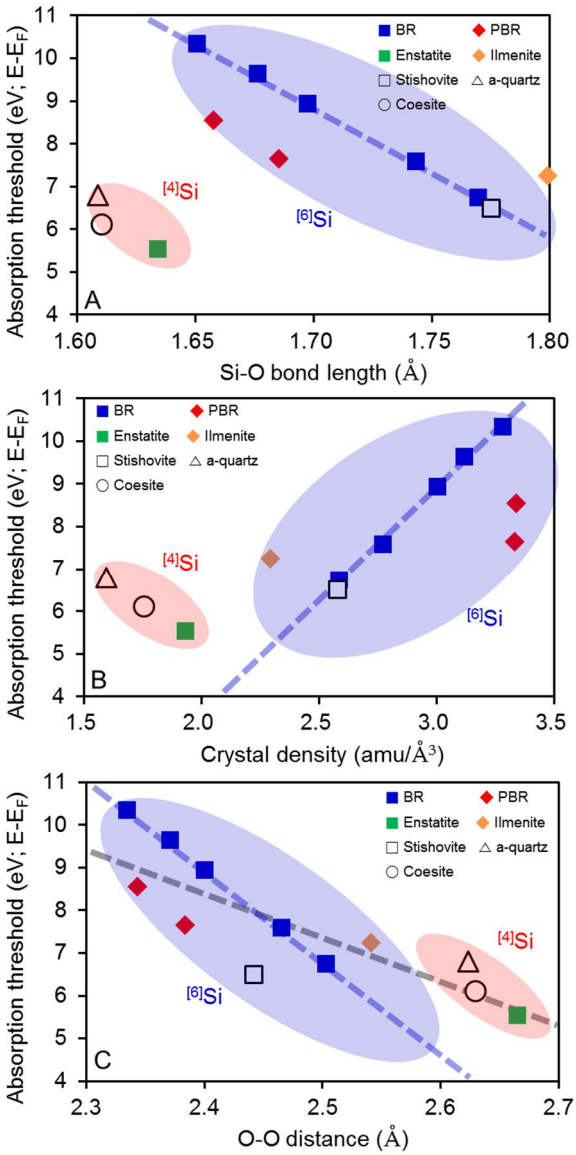
BR
PBR
Enstatite
Ilmenite
Stishovite
a-quartz
Coesite
[4]Si
[6]Si
A
Absorption threshold (eV; E-E$_F$)
Si-O bond length (Å)
B
Crystal density (amu/Å^3)
C
O-O distance (Å)

Figure 4-9. Calculated O *K*-edge XRS spectra for the bridgmanite (BR) structures with the O *K*-edge XRS features of bridgmanite and $MgSiO_3$ glasses [1]. The black and red solid lines with open circles indicate the experimental O *K*-edge XRS features of the $MgSiO_3$ glasses at 1 atm and 39 GPa respectively, and the blue solid line with open circles indicates the O *K*-edge XRS features of the bridgmanite. The black, blue, and red solid lines at the bottom of the figure refer to the calculated O *K*-edge XRS spectra for the bridgmanite structures at 25, 79, and 120 GPa, respectively.

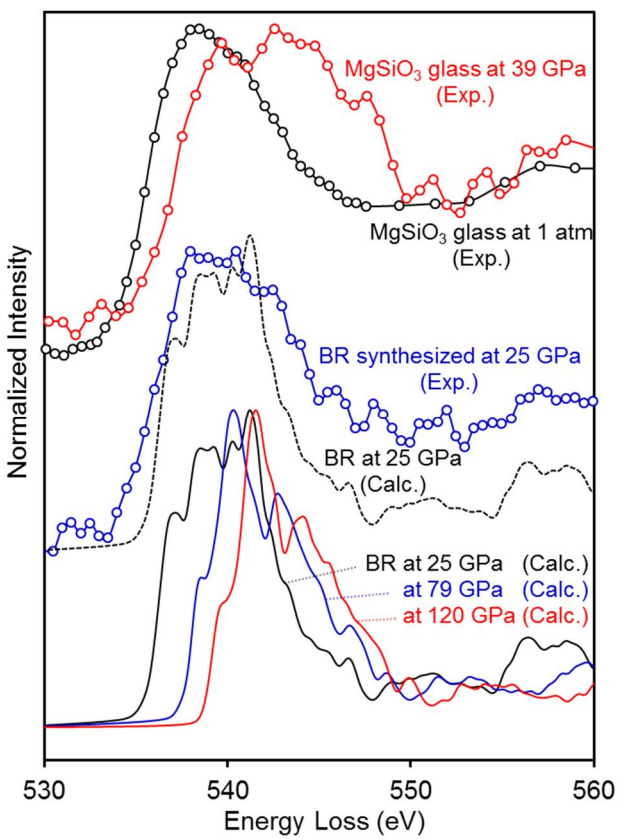

Appendix

Pressure-induced topological changes in the $MgSiO_3$ bridgmanite

Earlier x-ray and theoretical studies have shown that distortion of the SiO_6 octahedra in bridgmanite increases with increasing pressure [181,198] (Fig. 4-A1): the quadratic elongation of a SiO_6 octahedron in bridgmanite (the ratio of the Si-O bond length in the SiO_6 octahedron with respect to the center-to-vertex distance of a regular octahedron of the same volume) decreases from 1.0005 to 1.0002 with increasing pressure. These small changes in local oxygen configurations and the degree of octahedral distortion can also lead to the changes in the local electronic structures and O *K*-edge XRS spectra for the $MgSiO_3$ bridgmanite at high pressures.

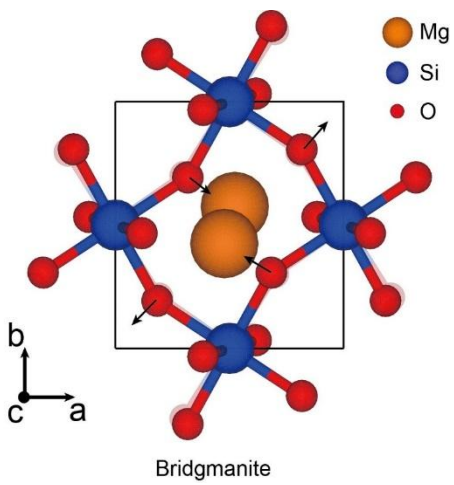

Figure 4-A1. Distortion of SiO_6 octahedra in bridgmanite with increasing pressure from 25 and 120 GPa. (See details in Tab. 1) The transparent molecular structure refers to the atoms in the bridgmanite at 25 GPa, and the opaque structure refers to atoms in the bridgmanite at 120 GPa. The

displacements of oxygen atoms in bridgmanite at 25 GPa are represented with black arrows.

Partial DOS of the bridgmanite with varying pressure

Figure 4-A2 presents the total and PDOS for valence bands for $MgSiO_3$ bridgmanite at 25 and 120 GPa. The results for valence bands were obtained without considering the core-hole effect. The calculated PDOS for valence bands are similar to those in the previous results [165], where the decreases in peak values of DOS in the valence bands were observed, suggesting an increase in the overlap of Si(*p*,*s*)-O *p*-state (see text). The electronic structure of the bridgmanite and post-bridgmanite in the pressure range of 0-86 GPa are reported [165]. An increase in band gap with increasing pressure is caused by a shift in the conduction band to a higher-energy region and the delocalizations of electronic states of Mg, Si, and O atoms. Fig. 4-A2(A) and 4-A2(B) present the calculated PDOSs for Mg, Si, and crystallographically inequivalent O1 and O2 oxygen atoms in bridgmanite at 25 and 120 GPa, respectively. The calculated DOSs of the bridgmanite up to 120 GPa show good agreements with previous results [165]. The delocalization of Si- and O-PDOSs indicates an increase in the probability that an electron will be in Si and O atoms simultaneously. Hence, the covalent character of Si-O bonds and the electron-electron interactions increase, resulting in a decrease in polarizability and ionicity [199-204] and an almost 100 GPa (from 25 to 120 GPa) increase in pressure. Fig. 4-A2(C) presents the differences in site-resolved O *p*-states of the bridgmanite structures at 25 and 120 GPa. The peak intensities around 0 eV

of the O *p*-states for the O1 and O2 atoms in bridgmanite at 25 GPa decrease significantly with increasing electronic density in the lower-energy regions.

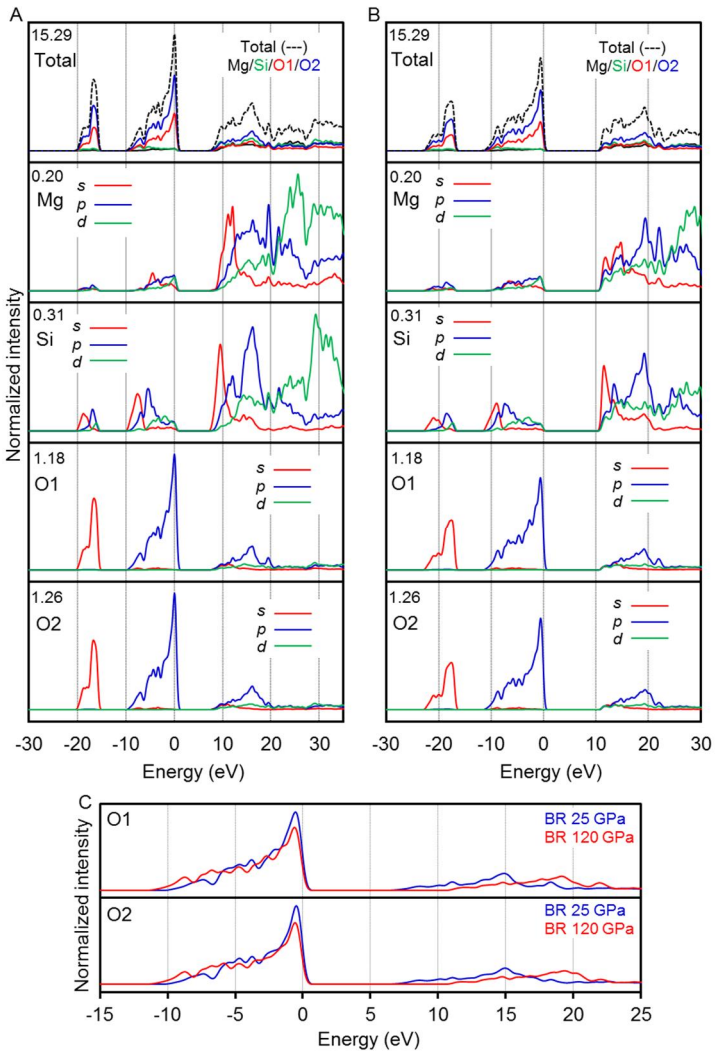

Figure 4-A2. Calculated total and PDOS (*s*-, *p*-, and *d*-states of Mg, Si, O1, and O2 atoms) for bridgmanite (BR) at 25 (A) and bridgmanite at 120 GPa (B), without applying the core-hole effect on the target oxygen atoms.

(C) The O *p*-DOSs of crystallographically inequivalent oxygen O1 and O2 atoms in the bridgmanite structures at 25 and 120 GPa are directly compared. The Gaussian broadening FWHM for PDOS is 0.02 Ry.

Calculated O *K*-edge XRS spectra for post-bridgmanite

There is a slight difference in the crystal structure of post-bridgmanite from *ab initio* calculations and experiments (XRD) [4,5]. Post-bridgmanite at 120 GPa (from *ab initio* calculations) consists of a corner-sharing oxygen atom, $^{[6]}$Si-O1-$^{[6]}$Si (O1, $^{[6]}$Si-O1: 1.6312 Å, $^{[6]}$Si-O1-$^{[6]}$Si angle: 138.3689°, Mg-O1: 1.8686 Å), and an edge-sharing oxygen atom, $^{[6]}$Si-O2-2$^{[6]}$Si (O2, average $^{[6]}$Si-O2: 1.7123 Å, $^{[6]}$Si-O2-$^{[6]}$Si angle: 91.5940°, average O2-O2 distance: 2.4213 Å, Mg-O2: 1.9766 Å) [5]. The atoms of $MgSiO_3$ post-bridgmanite at 121 GPa (from XRD) consist of a corner-sharing oxygen atom, $^{[6]}$Si-O1-$^{[6]}$Si (O1, $^{[6]}$Si-O1: 1.6443 Å, $^{[6]}$Si-O1-$^{[6]}$Si angle: 135.7544°, Mg-O1: 1.8377 Å), and an edge-sharing oxygen atom, $^{[6]}$Si-O2-2$^{[6]}$Si (O2, average $^{[6]}$Si-O2: 1.6643 Å, $^{[6]}$Si-O2-$^{[6]}$Si angle: 95.0964° average O2-O2 distance: 2.3514 Å, Mg-O2: 2.0014 Å) [4]. The proportion of O1 to O2 is 1:2. This change results in a slight but noticeable change in the XRS features (Fig. 4-A3).

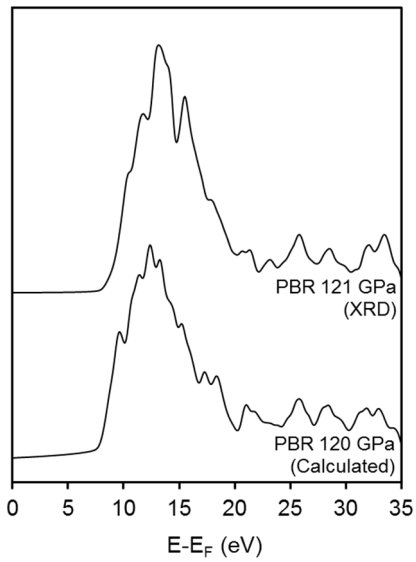

Figure 4-A3. Comparison of the calculated O *K*-edge XRS spectra for post-bridgmanite (PBR) structures based on XRD refinement (top) [4] and *ab initio* calculations (bottom) [5]

Chapter 5.

Pressure-induced bonding transitions in $MgSiO_3$ melts: Insights from *ab initio* calculations of oxygen *K*-edge x-ray Raman scattering spectrum

Yoo Soo Yi and Sung Keun Lee

It will be submitted to *American Mineralogist*

Abstract

The potential presence of high-density $MgSiO_3$-rich melts has been suggested as one of the atomistic accounts of the seismic heterogeneity near the core-mantle boundary (~2850 km) in the Earth's interior, but their elastic properties, as well as the atomic and electronic structures, have not been fully understood. The *in situ* high-pressure x-ray Raman scattering (XRS) spectroscopy can directly probe the element-specific electronic bonding structures of low-*z* oxides at high pressures. Despite its essential roles in geophysical implications and condensed matter physics, establishing the direct link between the topological changes around O atoms and the evolution in the O *K*-edge excitation features of noncrystalline low-*z* oxides under high pressures has been experimentally challenging. Recent advances in the *ab initio* calculations allow us to explore the electronic bonding structures and corresponding element-specific core-level excitation features, e.g. *K*- and $L_{2,3}$-edge, of crystalline and noncrystalline low-*z* oxides at extremely high pressures that cannot be achievable in the current XRS experiments.

Here, I report the direct link between the short- to medium-range topological changes around O atoms and the evolutions in O *K*-edge XRS features, as well as the density of states, of one of the important phases in the Earth's lower mantle, i.e. $MgSiO_3$, under high pressures up to ~131 GPa using the *ab initio* calculations. Despite the topological transformation associated with the coordination transition of Si and O atoms, the band gap energies and O *K*-edge XRS features of $MgSiO_3$ melts do not present considerable changes in a lower-pressure region from ~0 to ~18 GPa.

However, they start to change considerably in a higher-pressure region from ~18 to ~131 GPa with the significant decreases in the short-range interatomic distances around O atoms. The pressure-induced changes in the O *K*-edge XRS spectra of $MgSiO_3$ melts thus are revealed to be attributed in part to the enhanced electronic interactions associated with the decreases in the short-range interatomic distances around O atoms. The O *K*-edge absorption threshold energies (E_A) of $MgSiO_3$ melts, in a pressure range from ~18 to ~131 GPa, present *linear* relationships with the average interatomic distances between neighboring Mg-O ($d_{Mg\text{-}O}$) and O-O ($d_{O\text{-}O}$) distances [E_A (eV) = -12.68$d_{Mg\text{-}O}$ (Å) + 557.52 (R^2 = 0.77) and E_A (eV) = -6.12$d_{O\text{-}O}$ (Å) + 547.67 (R^2 = 0.86)]. The atomistic accounts of the pressure-induced changes in the O *K*-edge excitation features, as well as the detailed densification mechanism, of the $MgSiO_3$ melts under high pressures can provide the further insights into the pressure dependences of the elastic properties of the high-density $MgSiO_3$-rich melts and, thus, the origins of the seismic heterogeneity near the core-mantle boundary in the Earth's interior. In addition, I expect that the current study can shed light on the future studies for exploring the pressure-induced electronic bonding transitions, along with the evolution in core-level excitation features, in a wide range of crystalline and noncrystalline oxides under extremely high pressures.

Introduction

Probing the atomistic account of the pressure-induced changes in the characteristics of Earth materials is essential to understand the evolution of the Earth's interior. The seismic wave velocity distribution, such as the preliminary references Earth model (PREM) [9], is one of the most important exploration data that directly unveils the Earth's inside. It can provide the elastic properties, and thus the prediction of the pressure dependences of the atomic structures [11], of Earth materials in the Earth's deep interior, particularly $(Mg,Fe)_2SiO_4$ in the upper mantle (forsterite) and mantle transition zone (wadsleyite, ringwoodite) but separated into the $(Mg,Fe)SiO_3$ (bridgmanite) and (Mg,Fe)O (magnesiowüstite) in the lower mantle below ~660 km those are most abundant materials in the Earth's mantle [13,15,22]. The presence of the seismic heterogeneity near the core-mantle boundary (CMB) in the Earth's interior (at ~2850 km), i.e. the intermittently detected ultra-low velocity zone (ULVZ) at the D'' layer [21], has provided further insights into the phase stability of Mg-silicates at extremely high pressures and temperatures (~130 GPa and ~2500-3000 K near the CMB [9,12]). The previous studies thus have tried to probe and predict the characteristic of Mg-silicates at high pressures as well as their atomistic accounts to the characteristics of seismic wave propagation. The phase transition between the bridgmanite ($MgSiO_3$ perovskite [205]) to post-bridgmanite and associated changes in their elastic properties have been suggested as the origins of the seismic heterogeneity near the CMB [4,11,14,15,19,20]. The potential presence of high-density Mg-silicate melts, primarily in $MgSiO_3$ composition, also has been proposed as one of the

origins of those seismic heterogeneity [1,41-43]. However, the atomic and electronic structures, as well as the elastic properties, of noncrystalline silicates and Mg-silicates at extremely high pressures have not been fully understood because of the lack of suitable experimental techniques.

The x-ray Raman scattering (XRS) spectroscopy presents the core-level excitation features induced from the electron transition from the core states to the corresponding unoccupied states, e.g. most of the O *K*-edge XRS features stem from the electronic transition from the occupied O 1*s* state to the unoccupied O 2*p* state (O 1*s*-2*p** transition) [64]. The *in situ* high-pressure XRS spectroscopy thus have been a unique experimental technique that can directly probe the element-specific electronic bonding structures and corresponding short-range atomic structures of crystalline and noncrystalline materials at high pressures [64,65]. The O *K*-edge XRS features of low-*z* oxides under high pressures have provided insights into the atomistic account of the pressure-induced bonding transitions in H_2O [129-132,178] and $(O_2)_4$ [72] molecular solids, SiO_2 [2,66-68], GeO_2 [174], borate glasses [122,124,128,175], $MgSiO_3$, [1,3,7,55] and multi-component silicate glasses [58,176] at high pressures up to ~70 GPa. In addition, the *L*- and *M*-edge XRS features of low- and high-*z* elements, e.g. Si $L_{2,3}$-edge, Fe $L_{2,3}$-edge, and Fe $M_{2,3}$-edge, have been used to probe the changes in the local coordination environments, oxidation states, and the electron-spin-state of Si [206], SiO_2 [73], Fe oxides [179,180], $FeCO_3$ [66], and FeS [66,207] under high pressures.

A detailed review of the previous studies for exploring the core-level excitation features of crystalline and noncrystalline Earth materials at high pressures, e.g. *K*-edge features for low-*z* oxides such as SiO_2, $MgSiO_3$,

GeO_2, B_2O_3, and alkali borate under high pressures, can be found in elsewhere [65]. The previous experimental studies for amorphous SiO_2 and $MgSiO_3$ glasses have tried to probe the atomistic origins of the pressure-induced changes in the O *K*-edge XRS features of SiO_2 and $MgSiO_3$ glasses through the comparison between the O *K*-edge features of well-known low- and high-pressure crystalline phases [1,2]. It has been experimentally challenging because of the intrinsic overlaps of excitation features from O atoms at symmetrically distinct sites (difficulties in resolved the site-specific information) and the limitations of the *in situ* high-pressure XRS experiments (the current pressure limit is ~70 GPa) [65]. The presence of 6-coordinated Si ($^{[6]}$Si) atoms have been suggested as the structural indicator of the emergence of the stishovite-like double-peak O *K*-edge features of amorphous SiO_2 glasses under high pressures up to ~51 GPa (the characteristic high-energy features at ~538 and ~544 eV), though it was known to stem from the *p-p* hybridization between the neighboring O atoms [2]. This is because the formation of highly coordinated network forming cations in the fully polymerized prototypical simple oxides (SiO_2, GeO_2, and B_2O_3) is directly associated with the topological changes around O atoms, such as the coordination environment of O atoms, the O-O distances, and the Si-O-Si bond angles [65]. On the contrary, the formation of O triclusters [triply coordinated O atoms ($^{[3]}$O) such as 2$^{[4]}$Si-$^{[3]}$O-$^{[5]}$Si] and associated structural changes in the medium-range order has been proposed as the atomistic origins of the pressure-induced changes in the O *K*-edge XRS spectra of $MgSiO_3$ glasses (the emergence of ~544-545 eV features) with increasing pressure up to ~39 GPa [1]. Despite of these efforts in the previous experiments, the general relationship between the

structural changes around O atoms and the changes in O *K*-edge XRS features of the amorphous low-*z* oxides glasses, particularly silicates and Mg-silicates, could not be established. Therefore, the theoretical studies using the *ab initio* calculations indeed have been required for the precise interpretation of XRS edge features of crystalline and noncrystalline materials at high pressures.

Recent advances in the theoretical methods using the *ab initio* calculations allow us to explore the electronic bonding structures and corresponding XRS edge features, e.g. O *K*-edge and Si *K*- and $L_{2,3}$-edge, of crystalline and noncrystalline low-*z* oxides at extremely high pressures [3,7,65,67,68,72,73]. While the structural transition similar to that of stishovite with $^{[6]}$Si atoms has been suggested to be associated with the changes in O *K*-edge XRS features of amorphous SiO_2 glasses under high pressures [2], the theoretical study using the *ab initio* calculations has proposed the formation of highly coordinated Si atoms ($^{[5]}$Si and $^{[6]}$Si) to explain the emergence of stishovite-like O *K*-edge excitation features of SiO_2 glasses at high pressures up to ~150 GPa [67]. The calculated *l*-resolved partial density of states (PDOS) for Si (the unoccupied Si *s* and *d* states for Si $L_{2,3}$-edge features; Si 2*p*-3*s** and -3*d** transitions) and O (the unoccupied O *p* state for O *K*-edge features; O 1*s*-2*p** transition) atoms of crystalline SiO_2 phases (*a*-quartz, *β*-quartz, *a*-cristobalite, coesite, hp-cristobalite, penta-SiO_2, stishovite, $CaCl_2$-type, pyrite-type) have been used to probe the atomistic account of the XRS features of crystalline SiO_2 phases [68] and SiO_2 glasses at high pressures (up to ~74 GPa) [73]. In these studies, the Si-O-Si bond angle, not the Si coordination environments [2,67], has

been proposed to explain the characteristic XRS features of crystalline and amorphous SiO_2 at high pressures [68,73].

In our recent theoretical studies, the calculated O *K*-edge XRS features and the *l*-resolved PDOSs for crystalline SiO_2 [*a*-quartz (1 atm), coesite (6.5 GPa), and stishovite (~15 GPa)] and $MgSiO_3$ [enstatite (1 atm), ilmenite-type $MgSiO_3$ (22 GPa), bridgmanite (from 25 to 120 GPa), and post-bridgmanite (120 GPa)] phases have been used to establish the general relationship between the short-range structures around O atoms and the O *K*-edge XRS features of silicates and Mg-silicates [3,7]. The absorption threshold energies of O *K*-edge XRS features, as well as the band gap energies, of these crystalline SiO_2 and $MgSiO_3$ phases present strong negative correlations with the interatomic distances between neighboring O atoms [3,7]. This implies that the changes in O *K*-edge XRS features and *l*-resolved PDOSs of crystalline SiO_2 and $MgSiO_3$ phases are attributed in part to the enhanced proximity between neighboring O atoms and the associated increase in the short-range electronic interactions such as O *p*-*p* hybridization [3,7]. In addition, these results have been used to explain the changes in the O *K*-edge XRS spectra of $MgSiO_3$ glasses with increasing pressure up to ~39 GPa obtained in the previous *in situ* high-pressure XRS experiments [1].

Whereas the advances and progress in these previous studies shed light on the details of the pressure-induced bonding transitions, and associated changes in XRS features, of low-*z* oxides under high pressures, there remain several fundamental problems that should be resolved. First, since the previous theoretical studies for Mg-silicates, particularly $MgSiO_3$ and Mg_2SiO_4 glasses, have focused on the structural, transport, and elastic

properties under high pressures [8,75,77,208,209], the changes in the electronic structures of noncrystalline $MgSiO_3$ with increasing pressure up to near the core-mantle boundary condition (~130 GPa at ~2850 km) have not been explored systematically. Second, the atomistic account of the origins of high-energy O *K*-edge XRS features (at ~544-545 eV) of crystalline and noncrystalline SiO_2 and $MgSiO_3$ have been controversial. As mentioned above, the formation of highly coordinated Si atoms [67], as well as the structural transition similar to that of stishovite with $^{[6]}$Si [2], the formation of O triclusters ($^{[3]}$O) and associated changes in the medium-range order [1], the changes in the Si-O-Si bond angle [68], and the enhanced proximity between neighboring O atoms [3,7] have been proposed to explain the changes in O *K*-edge XRS features of crystalline and noncrystalline SiO_2 and $MgSiO_3$ under high pressures. The direct link, and thus the quantitative and predictive relationship, between the topological changes around O atoms, e.g. the formation of highly coordinated Si and O atoms and decreases in the short- to medium-range interatomic distances, and the pressure-induced changes in O *K*-edge XRS features of crystalline and noncrystalline SiO_2 and $MgSiO_3$ phases remains to be established. Consequently, further theoretical studies for exploring the atomistic account of the XRS features of noncrystalline SiO_2 and $MgSiO_3$ melts under high pressures have been expected.

The aim of this study is thus establishing the direct link between the topological changes around O atoms and the changes in electronic structures, and thus the evolution in O *K*-edge XRS features, of noncrystalline $MgSiO_3$ under high pressures. For this purpose, the noncrystalline $MgSiO_3$ melt configurations at high pressures, up to ~130

GPa, were simulated using the *ab initio* molecular dynamics. Then, the *l*-resolved PDOSs and O *K*-edge XRS spectra of these simulated $MgSiO_3$ melt configurations at high pressures were calculated using the *ab initio* calculations. See the following section for details about how to calculate the *l*-resolved PDOSs and O *K*-edge XRS features of $MgSiO_3$ melts at high pressures. The calculated electronic structures for $MgSiO_3$ melts at high pressures provide the evolution in the element-specific *l*-resolved electronic states upon compression, i.e. the pressure-induced changes in Mg *s*, *p*, and *d* states, Si *s*, *p*, and *d* states, and O *s*, *p*, and *d* states. The simulated $MgSiO_3$ melt configurations at high pressures and their O *K*-edge XRS spectra calculated here can provide the direct link between the structural changes around O atoms in the short- to medium-range order and associated changes in the O *K*-edge XRS features of noncrystalline $MgSiO_3$ melts upon compression. In addition, these results can be used to probe the atomistic origins of the pressure-induced changes in the O *K*-edge XRS spectra of $MgSiO_3$ glasses, which were obtained in the previous *in situ* high-pressure XRS experiments [1]. The results of this study can provide the further insights into the detailed densification mechanism of the high-density $MgSiO_3$-rich melts and associated changes in the electronic structures, as well as the atomistic account of the seismic heterogeneity near the core-mantle boundary [15,21,22]. In further, I expect that the current study, along with the results of our previous studies [3,7], can be applied to interpret and predict the XRS features of crystalline and noncrystalline low-*z* oxides at extremely high pressures, and thus it can be the guideline for the future *in situ* high-pressure XRS experiments.

Calculations

In this study, the noncrystalline $MgSiO_3$ melt configurations at high pressures up to ~131 GPa were obtained using the *ab initio* molecular dynamic (AIMD) simulations based on the projector augmented wave (PAW) type pseudopotential method, i.e. CASTEP [78]. The electronic structures of $MgSiO_3$ melts at high pressures were calculated using the conventional *ab initio* calculations based on the full-potential linearized augmented plane wave with local orbitals (FP-LAPW+lo) method, i.e. WIEN2k [74]. Though the FP-LAPW+lo method is more favorable for calculating the core-electron excitation features of low-*z* elements with applying the core-hole effects (see details in references) [116,147], the O *K*-edge XRS spectra of $MgSiO_3$ melts at high pressures were calculated using the *ab initio* calculations based on the PAW-type pseudopotential method for the efficiency of calculations. I have noted that the calculated O *K*-edge XRS features for the SiO_2 *a*-quartz using both the FP-LAPW+lo and PAW-type pseudopotential method presents almost identical excitation features near the absorption thresholds.

$MgSiO_3$ melt configurations at high pressures

The noncrystalline $MgSiO_3$ melt configurations at high pressures were obtained from the AIMD simulations based on the PAW-type pseudopotential method, i.e. CASTEP [78]. The electronic structures, and the electrostatic potential landscapes, for estimating the interatomic forces among atoms in the unit cells were calculated as following. The Perdew-Berke-Ernzerhof (PBE) scheme based on the generalized gradient

approximation was used as the exchange-correlation functional to describe the very short-range on-site electronic interactions [210]. The PAW-type ultrasoft pseudopotential was used to describe the electronic interactions among atoms in the unit cells. The plane-wave-cutoff energy, which determines a level of describing electronic orbitals, was set to 310 eV. The single Γ point was used for the self-consistent-field (SCF) calculations, since the single Γ point in the irreducible Brillouin zone have been reported to be sufficient for calculating simple insulating materials such as silicates and Mg-silicates [68]. The parameters for empty band, which determines the number of additional bands included in the SCF calculations as a percentage of the number of occupied band, and smearing, which refers to the broadening width for the occupied electronic states, each were set to 20% and 0.2 eV respectively to enhance the convergency of SCF calculations. The SCF convergence criterion for the total energy was set to 2×10^{-6} eV/atom.

The AIMD simulations for obtaining the $MgSiO_3$ melt configurations at high pressures each were performed with the NVT ensemble, i.e. the Nosé-Hoover-Langevin thermostat [211]. The time-step for the AIMD simulations was set to 1 fs. The initial configuration for $MgSiO_3$ melts was generated from the bridgmanite ($MgSiO_3$ perovskite) at 25 GPa referred from the x-ray diffraction experiments [181]. The bridgmanite structure was extended to a 2×2×2 supercell (i.e., the volume is defined as 1.0 V_0 containing 32 Mg, 32 Si, and 96 O atoms) to reduce the boundary effects induced from the periodic boundary condition. The volume of this extended bridgmanite supercell was expanded isotropically from $1.0V_0$ to $1.6V_0$ to decrease its density to 2.56 g/cm^3 that is comparable

to the density of amorphous $MgSiO_3$ at the ambient condition (~2.6 g/cm^3) [8]. Then, the long-range periodicity, i.e. the crystallinity, of the bridgmanite structure of $1.6V_0$ was removed by melting at 6000 K for 4 ps. The noncrystalline $MgSiO_3$ configuration of $1.6V_0$ (2.56 g/cm^3) at 6000 K was annealed at 3000 K for 3 ps to obtain the reliable $MgSiO_3$ melt configuration of $1.6V_0$ at 3000 K. The $MgSiO_3$ melt configuration of $1.6V_0$ at 3000 K was isotropically compressed, and then they each were annealed at 3000 K for 3-4 ps (i.e., the hot compression) to obtain the equilibrated $MgSiO_3$ melt configurations at high pressures: $1.4V_0$ (2.93 g/cm^3), $1.2V_0$ (3.42 g/cm^3), $1.0V_0$ (4.10 g/cm^3), and $0.8V_0$ (5.13 g/cm^3) at 3000 K. The pressure conditions of compressed $MgSiO_3$ melt configurations each were estimated as ~0 GPa ($1.6V_0$), ~7 GPa ($1.4V_0$), ~18 GPa ($1.2V_0$), ~51 GPa ($1.0V_0$), and ~131 GPa ($0.8V_0$), respectively. The temperature and maximum pressure conditions of $MgSiO_3$ melts, i.e. 3000 K and ~131 GPa, were determined based on the geotherm and pressure near the core-mantle boundary in the Earth's interior, i.e. ~2500-3000 K and ~130 GPa at ~2850 km [9,12]. See the appendix (Tab. A1 and Fig. 5-A1) for details about the pressure estimation for the compressed $MgSiO_3$ melt configurations [6]. I have confirmed that all the $MgSiO_3$ melt configurations at high pressures were sufficiently equilibrated, and thus they can be used to obtain the reliable structural and transport properties. See the appendix for the mean square displacement of simulated $MgSiO_3$ melt configurations (Fig. 5-A2) [6].

Calculating PDOSs and O *K*-edge XRS spectra

The *l*-resolved partial density of states (PDOS), i.e. Mg *s*, *p*, *d* states, Si *s*, *p*, *d* states and O *s*, *p*, *d* states, of $MgSiO_3$ melts at high pressures were calculated using the *ab initio* calculations based on the FP-LAPW+lo method, i.e. WIEN2k [74]. The calculated PDOSs each were broadened with the full-width at half-maximum (FWHM) Gaussian broadening factor of 0.02 Ry, and they were presented in an energy range from -30 to 30 eV. The GGA-PBE scheme was used as the exchange-correlation functional for describing the on-site electron-electron interactions [210]. The Muffin-Tin radii (R_{MT}) for Mg, Si, and O atoms in $MgSiO_3$ melts at high pressures each were set to 1.7-1.9 Å, 1.54-1.67 Å, and 1.54-1.67 Å, respectively. The cutoff energy (E_{CUT}) for the separation between the core and valence states was set to -6.0 Ry. The single Γ point in the irreducible Brillouin zone was used for the SCF calculations. The RK_{MAX}, which refers to the scalar product of the minimum value of R_{MT} and the largest plane wave cutoff vector of K_{MAX}, was set to 7.0. The G_{MAX}, which refers to the magnitude of the largest vector in the Fourier expansion of the charge density, was set to 12.0. The convergence criteria for the SCF calculations were set to 10^{-4} Ry for the total energy and 10^{-3} e for the charge distance. See our previous studies [3,7], and other references [116,117], for the detailed descriptions of these parameters.

I should note that the partially empty core-states due to the inelastically scattered x-ray photons, i.e. the x-ray Raman scattering (XRS), significantly affect to the local electronic structures, and thus the core-excitation features, of target elements, particularly for the low-*z* elements [64]. This is the so-called core-hole effect. The core-hole effect thus should be accounted for calculating the reliable O *K*-edge XRS features of

crystalline and noncrystalline low-*z* oxides [116,117] (also see our previous studies [3,7]). The FP-LAPW+lo method is more favorable for calculating the core-level spectroscopy of low-*z* oxides, because it can easily apply the core-hole effect on target elements without approximating the electronic structures of core-level states [117,147]. However, in this study, the PAW-type pseudopotential with on the fly scheme, i.e. calculating the pseudopotential for each SCF calculation step, was used to calculate the O *K*-edge XRS features of $MgSiO_3$ melts at high pressures with applying the core-hole effect on target O atoms for the efficiently of calculations. The O *K*-edge XRS spectra of $MgSiO_3$ melts at high pressures were calculated by taking into consideration the contributions of each excitation features stemmed from the symmetrically inequivalent O atoms in the unit cells, i.e. total 96 O atoms. The GGA-PBE scheme was used as the exchange-correlation functional [210]. The plane-wave-cutoff energy of 310 eV was used. The number of *k* points in the irreducible Brillouin zone, for calculating the electronic structures and O *K*-edge XRS spectra of $MgSiO_3$ melts at high pressures, was set to 6. The parameters for empty band and smearing each were set to 20% and 0.2 eV. The SCF convergence criterion was set to 10^{-6} eV/atom for the total energy.

Results and Discussion

Populations of Si and O species of $MgSiO_3$ melts at high pressures

Figure 5-1 presents the populations of Si ($^{[4]}$Si, $^{[5]}$Si, and $^{[6]}$Si) and O [$^{[1]}$O (nonbridging O; NBO), $^{[2]}$O (bridging O; BO), and $^{[3]}$O (tricluster)] species in $MgSiO_3$ melts at high pressures: 32 Mg, 32 Si, and 96 O atoms are in the unit cells. The $^{[3]}$Si and $^{[0]}$O, of which the populations are relatively small, are not included in Fig. 5-1 (see Tab. A1-A5 in the appendix [6]). The populations of Si and O species in $MgSiO_3$ melts at each pressure conditions were determined from the sufficiently annealed $MgSiO_3$ melt configurations (see Fig. 5-A2 in the appendix [6]). The proportions of highly coordinated Si atoms increase (i.e.,$^{[5]}$Si from 2 to 16 and $^{[6]}$Si from 0 to 6) at the expense of NBO atoms (i.e., $^{[1]}$O from 60 to 40), while the pressure increases from ~0 to ~131 GPa. The presence of O triclusters ($^{[3]}$O) in $MgSiO_3$ melts have been confirmed above ~7 GPa, and its population gradually increases (from 0 to 8) with increasing pressure up to ~131 GPa, and it implies the short-range topological changes around O atoms under high pressures. I note that the presence of O triclusters in the highly depolymerized amorphous Mg-silicates at high pressures, particularly $MgSiO_3$ and Mg_2SiO_4 glasses, have been suggested and predicted in previous experimental and theoretical studies [1,8,65,77]. The result presented here thus is consistent in part with these previous studies. The populations of BO atoms ($^{[2]}$O) reached to its maximum value at ~51 GPa, and then it starts to decrease above ~51 GPa with the significant increase in the populations of O triclusters ($^{[3]}$O). Pressure dependences of the coordination transitions of both Si and O atoms seem to decrease above ~18

GPa, and thus they present *nonlinear* relationships with a pressure. The pressure dependences of the proportion of highly coordinated Si and O atoms will be discussed more precisely in the following section (Fig. 5-3).

Partial radial distribution functions of $MgSiO_3$ melts at high pressures

Figure 5-2 presents the total and partial radial distribution functions (RDF) of $MgSiO_3$ melts at high pressures. The presented RDFs each were obtained by averaging the RDF of $MgSiO_3$ melt configurations in the last 1 ps of AIMD simulations (i.e., 1000 $MgSiO_3$ melt configurations) which were sufficiently annealed and thus in the diffusion regime (see details in Fig. **5-**A2 in the appendix [6]). The total RDFs in Fig. 5-2(a) presents significant changes in the interatomic distances from the short- to medium-range order with increasing pressure. The changes in RDFs around 1.4-2.0 Å are induced from changes in the interatomic distances between Si-O [Fig. 5-2(c)] and Mg-O [Fig. 5-2(b)] pairs in the first-coordination shell, and the changes around 2.0-3.0 Å are due primarily to the decrease in the neighboring O-O distances [Fig. 5-2(d)]. The changes beyond ~3.0 Å are due primarily to the decreases in the O-O distances beyond the first-coordination shell [Fig. 5-2(d)] and in part to the decreases in the Si-O [Fig. 5-2(c)] and Mg-O [Fig. 5-2(d)] distances beyond the first-coordination shell.

The Mg-O RDFs of $MgSiO_3$ melts at high pressures in Fig. 5-2(b) do not change considerably at a relatively lower-pressure region, but they start to significantly shift to a lower radial region above ~18 GPa, in both the first- and second-coordination shells. These changes in Mg-O distances in the short- to medium-range order above ~18 GPa imply their contribution

to the densification of high-density $MgSiO_3$ melts at a higher-pressure region. The Si-O RDFs in Fig. 5-2(c) present the relatively weaker relevance between the Si-O bond lengths and the densification of $MgSiO_3$ melts upon compression due to the rigidity of the Si-O covalent bonds. A gradual decrease in the Si-O distances beyond the first-coordination shell (i.e., beyond ~2.6 Å) indicates decreases in the medium-range interatomic distances and, thus, the enhanced proximity among network building Si polyhedra in $MgSiO_3$ melts, such as a SiO_4 tetrahedron, under high pressures. The O-O RDFs in Fig. 5-2(d) present gradual decreases in the O-O distances in the short- (i.e., in the first-coordination shell; ~1.6-3.0 Å) to medium-range (i.e., in the second-coordination shell; ~3.0-5.0 Å) order with increasing pressure. The decrease in the O-O distances in the first-coordination shell seems to be associated in part with the formation of the highly coordinated Si polyhedra, such as the SiO_6 octahedron [see details in Fig. 5-3(a) in the following section]. The decrease in the O-O distances in the second-coordination shell [Fig. 5-2(d)], along with the decrease in the Si-O distances beyond the first-coordination shell (i.e., beyond ~2.6 Å) [Fig. 5-2(c)], implies changes in the packing of network building Si polyhedra in the $MgSiO_3$ melts upon compression.

Topological changes of $MgSiO_3$ melts upon compression

Since the pressure-induced structural changes of $MgSiO_3$ melts have been reported in Fig. 5-1 and 5-2, the quantitative determination of topological changes around O atoms can be established precisely. Figure 5-3 presents the topological changes around O atoms in the short-range order (i.e., the coordination transition of Si and O atoms and the changes in the

short-range interatomic distances) [Fig. 5-3(a) and 5-3(b)], the changes in the extent of polymerization [Fig. 5-3(c)], and the changes in topological disorder [Fig. 5-3(d)] of $MgSiO_3$ melts upon compression. The pressure dependence of the densities of $MgSiO_3$ melts is presented in Fig. 5-A1 in the appendix [6]. Fig. 5-3(a) presents the pressure dependences of the average atomic coordination numbers of Si (n_{Si}) and O (n_O) atoms and the average Si-O bond lengths (d_{Si-O}) and the average neighboring Mg-O (d_{Mg-O}) and O-O (d_{O-O}) distances. The values presented in Fig. 5-3(a) were normalized with their values at ~0 GPa (n_{Si} = 4.00, n_O = 1.31, d_{Si-O} = 1.6390 Å, d_{Mg-O} = 2.0460 Å, and d_{O-O} = 2.7340 Å) to show the short-range topological changes around O atoms upon compression more clearly. The n_{Si} (from 4.00 to 4.88) and n_O (1.31 to 1.63) of $MgSiO_3$ melts increase with increasing pressure implying the formation of highly coordinated Si and O atoms at the expense of NBO atoms and, thus, an increase in the extent of polymerization [Fig. 5-3(c)] upon compression. The pressure dependences of n_{Si} and n_O decrease with increasing pressure, particularly above ~18 GPa, showing the *nonlinear* relationships with the pressure.

The d_{Mg-O} does not present considerable changes at a relatively lower-pressure region (from 2.0460 to 2.0360 Å), but it starts to decrease significantly in a pressure region from ~18 to ~131 GPa (from 2.0360 to 1.9080 Å). The Mg-O distances beyond the first-coordination shell also present the considerable shift in this relatively higher-pressure region [Fig. 5-2(b)]. The d_{Si-O} seems not to be strongly correlated with the pressure-induced densification of $MgSiO_3$ melts because of its relatively small changes upon compression (from 1.6390 to 1.6500 Å), while the d_{Si-O} is slightly associated with the formation of highly coordinated Si polyhedra.

The $d_{Si\text{-}O}$ slightly increases (from 1.6390 to 1.6660 Å) with the formation of highly coordinated Si atoms, but it starts to decrease at a higher-pressure region from ~51 to ~131 GPa (from 1.6660 to 1.6500 Å) implying the presence of compressed highly coordinated Si polyhedra in $MgSiO_3$ melts under extremely high pressures. The gradual decreases in the $d_{O\text{-}O}$ in a pressure range from ~0 to ~131 GPa (from 2.7340 to 2.3420 Å) is associated in part with the increase in the n_{Si} upon compression due primarily to the geometrical differences among Si polyhedra with distinct Si coordination environments (i.e., slightly longer Si-O bond lengths and shorter O-O distances in the highly coordinated Si polyhedra). The decrease in the $d_{O\text{-}O}$ thus can be indicative of the formation of highly coordinated Si atoms under high pressures. However, I should note that the decrease in the $d_{O\text{-}O}$ in a higher-pressure region, which are partly associated with the presence of compressed highly coordinated Si polyhedra, imply implies the decrease in the short-range interatomic distances around O atoms. The decrease in the $d_{O\text{-}O}$ and associated changes in the electronic structures, as well as XRS features, of $MgSiO_3$ melts under high pressures will be precisely discussed in the following section. The decrease in O-O distances beyond the first-coordination shell [Fig. 5-2(d)] starts to decrease above ~7 GPa implying the denser packing of the network building Si polyhedra in $MgSiO_3$ melts with decreasing the interatomic distances in the medium-range order.

The detailed densification mechanism of $MgSiO_3$ melts under high pressures can be determined more systematically. The $d_{Si\text{-}O}$, $d_{Mg\text{-}O}$, and $d_{O\text{-}O}$ do not present considerable changes in a pressure range from ~0 to ~18 GPa regardless of the increases in the n_{Si} and n_O with increasing pressure. This result implies that, in this relatively lower-pressure region, the

formation of highly coordinated Si and O atoms has a primary role in the topological densification of $MgSiO_3$ melts under high pressures with an increase in the extent of polymerization of the highly depolymerized network structures. In contrast, in a relatively higher-pressure region, from ~18 to ~131 GPa, the contribution of the decreases in the interatomic distances in the short- to medium-range order to the densification of $MgSiO_3$ melts become more significant: the decreases in the Mg-O distances in the first- ($d_{Mg\text{-}O}$) and second-coordination shells [Fig. 5-2(b)], the decrease in the Si-O distances beyond the first-coordination shell [Fig. 5-2(c)], and the decreases in the O-O distances in the first- ($d_{O\text{-}O}$) and second-coordination shells [Fig. 5-2(d)], as well as the decreases in the pressure dependences of the n_{Si} and n_O with increasing pressure [Fig. 5-3(a)].

In previous studies, the formation of highly coordinated O atoms in the fully polymerized prototypical noncrystalline oxides, such as SiO_2, GeO_2, and B_2O_3 glasses, under high pressures have been revealed to be directly associated with the formation of highly coordinated network forming cations, i.e. Si, Ge, and B atoms [65]. Fig. 5-3(b) presents the strong correlation between the n_{Si} and n_O in the highly depolymerized $MgSiO_3$ melts under high pressures with the simple *linear* relationship: $n_O = 0.36n_{Si} - 0.12$ (R^2=1.00). The *linearity* between the n_{Si} and n_O implies that the presence of highly coordinated Si atoms in $MgSiO_3$ melts at high pressures indicates the presence of highly coordinated O atoms such as O triclusters ($^{[3]}O$) and vice versa. The proportional constant of this *linear* relationship might be smaller than that of the fully polymerized noncrystalline SiO_2 because the formation of highly coordinated O atoms can be hindered from the

presence of network modifying cation in the highly depolymerized $MgSiO_3$ melts.

Fig. 5-3(c) presents the pressure dependence of the extent of polymerization of $MgSiO_3$ melts. The extent of polymerization of $MgSiO_3$ melts can be determined quantitatively from the ratio of NBO atoms with respect to either the number of total Si (NBO/Si_{Tot}) or total O (NBO/O_{Tot}) atoms in the unit cells. Both NBO/Si_{Tot} (from 1.88 to 1.25) and NBO/O_{Tot} (from 0.65 to 0.43) decrease with increasing pressure implying an increase in the extent of polymerization of the highly depolymerized $MgSiO_3$ melts associated with the coordination transition of Si and O atoms under high pressures. The pressure dependences of NBO/S_{Tot} and NBO/O_{Tot} decrease with increasing pressure as revealed in Fig. 5-1 and 5-3(a). This result is consistent with that the contribution of the coordination transition of Si and O atoms to the topological densification of $MgSiO_3$ melts become less significant at a higher-pressure region, i.e. the contribution of the decreases in the interatomic distances in the short- to medium-range order become more significant at a higher-pressure region, as revealed in Fig. 5-3(a). However, the ratio of NBO atoms with respect to the number of SiO_4 tetrahedra (NBO/T), which has been commonly used to describe the extent of polymerization of noncrystalline silicates at the ambient condition [58], increases from 2.14 to 4.00 in a pressure region from ~0 to ~131 GPa implying the decrease in the extent of polymerization of $MgSiO_3$ melts with increasing pressure. This failure of NBO/T is due to the more rapid decrease in the proportion of $^{[4]}$Si atoms (decreases by ~64.3%; from 28 to 10) compared with that of NBO atoms (decreases by ~33.3%; from 60 to 40) in $MgSiO_3$ melts under high pressures as revealed in Fig. 5-1.

The pressure-induced topological disorder is one of the inherent aspects to determine the structural changes in $MgSiO_3$ melts under high pressures. The topological entropy stemmed from the Si-O bond length distribution [S_{Top}(Si-O)] can be used to quantitatively determine the topological disorder in $MgSiO_3$ melt network structures upon compression. This has been discussed in a previous study for Na-Al silicate glasses [212]. The changes in S_{Top}(Si-O) can be estimated from the changes in the full-width at half-maximum (FWHM) of the Si-O RDFs ($\sigma_{Si\text{-}O}$) in Fig. 5-2(c). Fig. 5-3(d) presents changes in the $\sigma_{Si\text{-}O}$ and associated changes in the ΔS_{Top}(Si-O) of $MgSiO_3$ melts with increasing pressure. Since the AIMD simulations for $MgSiO_3$ melts have been performed with the NVT ensemble, the entropy difference between the $MgSiO_3$ melts at different pressures can be established with the following relationship: $\Delta S(J/K) = S_2 - S_1 = k_B \cdot \ln[Q_2/Q_1] + (E_2 - E_1)/T$, where the Q_i and E_i refer to the partition function and energy at different pressures and the k_B and T refer to the Boltzmann constant and temperature, respectively. This relationship can be approximated as the simulated $MgSiO_3$ melts were obtained from the NVE ensemble by assuming the sufficient number of atoms in the unit cells ($\Delta E/E \sim 1/N^{½}$, where N refers to the number of atoms in the unit cells): $\Delta S(J/K) = S_2 - S_1 = k_B \cdot \ln[Q_2/Q_1]$ [212]. Consequently, the ΔS_{Top}(Si-O) of $MgSiO_3$ melts with increasing pressure can be estimated as following: $\Delta S_{Top}(Si\text{-}O)\ (J/K) = S_2 - S_1 = k_B \cdot \ln(\sigma_2/\sigma_1)$ where σ_i refers to the FWHM of the Si-O RDF at different pressures. The $\sigma_{Si\text{-}O}$ increases in a pressure range from ~0 to ~51 GPa due primarily to the presence of diverse Si polyhedra within different coordination states [Fig. 5-1 and 5-3(a)]. Thus, the ΔS_{Top}(Si-O), in this pressure region, present positive values implying the increase in the

topological disorder in $MgSiO_3$ melts under compression. The $\sigma_{Si\text{-}O}$ starts to decrease above ~51 GPa implying the decrease in the Si-O bond length distribution associated with the presence of the compressed Si polyhedra at extremely high pressures as revealed in the decrease in the $d_{Si\text{-}O}$ in Fig. 5-3(a). The ΔS_{Top}(Si-O), in the extremely high pressures above ~51 GPa, thus presents a negative value. Therefore, the S_{Top}(Si-O) increases by 6.1561×10^{-24} J/K with increasing pressure from ~0 to ~131 GPa. The Si-O-Si bond angle distribution in the $MgSiO_3$ melts would increase with the structural transformation associated with the formation of highly coordinated Si and O atoms under high pressures, i.e. due to the geometrical differences in the Si polyhedra with distinctive coordination environments as well as their connected network structures. Therefore, though the contribution of the Si-O-Si bond angle distribution to the topological entropy could be accounted here, the topological disorder of the $MgSiO_3$ melts would increase with increasing pressure up to ~131 GPa.

Calculated partial density of states for $MgSiO_3$ melts at high pressures

Since the previous studies for noncrystalline Mg-silicates at high pressures, e.g. $MgSiO_3$ and Mg_2SiO_4 glasses, have focused on their structural, transport, and elastic properties [8,75,77,208,209], changes in the electronic structures of noncrystalline $MgSiO_3$ melts under high pressures up to near the core-mantle boundary condition (~130 GPa at ~2850 km) have not been systematically explored yet. Figure 5-4 presents the calculated *l*-resolved partial density of states (PDOS), i.e. Mg *s*, *p*, and *d* states, Si *s*, *p*, and *d* states, and O *s*, *p*, and *d* states, and total DOS for $MgSiO_3$ melts at high pressures, and thus they can reveal the pressure-

induced changes in the electronic structures of $MgSiO_3$ melts. The results presented in Fig. 5-4 were obtained by taking into consideration the *l*-resolved PDOSs of each symmetrically inequivalent Mg, Si, and O atoms in the unit cells (32 Mg, 32 Si, and 96 O atoms). The calculated PDOSs for $MgSiO_3$ melts present broad features in contrast with those of the crystalline $MgSiO_3$ structures calculated with the same Gaussian FWHM broadening factor in our previous studies [3,7]. Thus is due to the presence of extended and localized electronic states in the highly disordered noncrystalline network structures of $MgSiO_3$ melts [213,214].

Fig. 5-4(a) and 4(b) present the calculated Mg ($1s^2$ $2s^2$ $2p^6$ $3s^2$) PDOSs for $MgSiO_3$ melts at high pressures. While the unoccupied Mg PDOSs in Fig. 5-4(a) seem not to be strongly correlated with the topological densification of $MgSiO_3$ melts under high pressures, the unoccupied Mg *s* and *p* states slightly shift to a higher-energy region above ~18 GPa. The occupied Mg PDOSs also present similar pressure dependences, they shift to a lower-energy region with delocalization with increasing pressure, particularly above ~18 GPa. This result indicates that the changes in the outermost occupied Mg *s* state stem from the increase in the short-range electronic interactions, particularly between Mg 3*s* and O 2*p* states, with the significant decrease in the $d_{Mg\text{-}O}$ above ~18 GPa revealed in Fig. 5-2(b) and 5-3(a).

Fig. 5-4(c) presents the calculated Si ($1s^2$ $2s^2$ $2p^6$ $3s^2$ $3p^2$) PDOSs for $MgSiO_3$ melts at high pressures. The unoccupied Si *p* state considerably shift to a higher-energy region with delocalizations above ~18 GPa. The occupied Si 3 *s*, *p* state at ~0 GPa is localized in a range from -11 to 0 eV, and it is hybridized with the occupied O 2*p* state constructing the 4-

coordinated Si atoms, i.e. sp^3-like hybridization. The slight changes in the Si 3*s* and 3*p* state, in a pressure range from ~0 to ~18 GPa, are associated with the formation of highly coordinated Si atoms under high pressures, since the coordination transition of Si and O atoms have a primary role in the topological densification of $MgSiO_3$ melts in a relatively lower-pressure region as revealed in Fig. 5-3(a). The empty Si 3*d* state, at similar energy range with the occupied O 2*p* state, starts to be filled with the nonbonding electrons from other adjacent O atoms, i.e. the lone pair electrons, with increasing pressure facilitating the formation of highly coordinated Si atoms [2,67]. In a higher-pressure region above ~18 GPa, the outermost occupied Si 3*s* and 3*p* states significantly shift to a lower-energy region with delocalizations upon compression. This changes in the occupied Si 3*s* and 3*p* states stem from the enhanced short-range electronic interaction associated with the presence of compressed Si-O bonds at extremely high pressures as revealed in Fig. 5-3(a).

Fig. 5-4(d) presents changes in the occupied O ($1s^2$ $2s^2$ $2p^4$) PDOSs of $MgSiO_3$ melts with increasing pressure. The outermost occupied O 2*s* and 2*p* states present slight changes with increasing pressure at a relatively lower-pressure region. These changes are associated with the formation of highly coordinated Si atoms. The occupied O 2*p* state at ~0 GPa presents sharp features in a range from -5 to 0 eV, which stem from the lone pair electrons of O atoms in the SiO_4 tetrahedron. Similar features in the occupied O 2*p* state have been presented in previous studies for the *a*-quartz and SiO_2 glasses at the ambient condition [215]. These characteristic features become negligible at high pressures above ~51 GPa. This is because of both the increase in the short-range topological disorder due to

the increase in the Si-O bond length distribution [Fig. 5-3(d)] and the expense of lone pair electrons in the occupied O 2*p* state to fill the empty Si 3*d* state facilitating the formation of highly coordinated Si atoms [Fig. 5-3(a)]. The occupied O 2*s* and 2*p* states considerably shift to a lower-pressure region with delocalizations above ~18 GPa. These changes mostly stem from the enhanced short-range electronic interaction between the neighboring Si and O atoms associated with the presence of compressed Si-O covalent bonds under extremely high pressures, consistent with the origins of pressure-induced changes in the occupied Si 3*s* and 3*p* states in Fig. 5-4(c). These changes in the occupied O 2*s* and 2*p* states in a higher-pressure region also might be associated with the decreases in the nearest-neighboring O-O distances ($d_{O\text{-}O}$), which can facilitate the *p*-*p* hybridization between the nearby O atoms. The changes in the electronic structures, as well as the O *K*-edge XRS features, of crystalline and amorphous SiO_2 [2,67], crystalline $MgSiO_3$ [7], and $(O_2)_4$ molecular solids [72] due to the *p*-*p* hybridization between neighboring O atoms have been discussed in the previous studies. Details about the contribution of the O *p*-*p* hybridization to the changes in O *K*-edge XRS features will be discussed in the following section.

Fig. 5-4(e) presents the unoccupied O PDOSs of $MgSiO_3$ melts at high pressures. The unoccupied O PDOSs of $MgSiO_3$ melts in a pressure range from ~0 to ~18 GPa, where the coordination transitions of Si and O atoms have a primary role in the topological densification of $MgSiO_3$ melts, seem not to be associated with the topological variations around O atoms under high pressures. In a higher-pressure region above ~18 GPa, the unoccupied O *p* state shift to a higher-energy region with an emergence of

high-energy features above ~10 eV, consistent with the pressure dependence of the occupied O 2*s* and 2*p* states presented in Fig. 5-4(d). The changes in the unoccupied O *p* state might be associated with the enhanced short-range electronic interactions due to the presence of compressed Si-O covalent bonds as well as the *p*-*p* hybridization between nearby O atoms due to the enhanced proximity between neighboring O atoms at extremely high pressures. I should note that the changes in the unoccupied O *p* state with increasing pressure imply the changes in the O *K*-edge XRS features of $MgSiO_3$ melts, because most of O *K*-edge XRS features stem from the electronic transition from the occupied O 1*s* state to the unoccupied O 2*p* state (the O dipole-allowed 1*s*-2*p** transition) [64].

Fig. 5-4(f) presents the calculated total DOSs for $MgSiO_3$ melts at high pressures. This result reveals the pressure-induced changes in the band gap energies, i.e. the energy difference between the highest occupied state and the lowest unoccupied state, of $MgSiO_3$ melts. I should note that the total DOSs of $MgSiO_3$ melts at a relatively lower-pressure region present the metallic-like features, i.e. the overlapped occupied and unoccupied states. However, it does not indicate that the $MgSiO_3$ melts have a metallic character at a lower-pressure region, since the band gap correction has not been applied to the results presented here. See details about the band gap correction of $MgSiO_3$ melts in Fig. 5-A5 in the appendix [6]. The band gap energies in a pressure range from ~0 to ~18 GPa present negligible changes with increasing pressure even with the topological changes in $MgSiO_3$ melts due primarily to the formation of highly coordinated Si atoms at the expense of nonbridging O atoms [Fig. 5-3(a)]. In contrast, the band gap energy increases about 3 eV in a higher-pressure

region from ~18 to ~131 GPa where the decreases in the short- to medium-range interatomic distances significantly contribute to the topological densification of $MgSiO_3$ melts [Fig. 5-3(a)]. The similar pressure dependence of the band gap energies has been reported for the GaAs in a pressure range from ~0 to ~18 GPa [216]. In a previous study, the strong negative correlation between the interatomic distances between the nearest-neighboring O atoms and the band gap energies has been reported in the crystalline SiO_2 and $MgSiO_3$ phases [7]. In addition, the Si-O bond lengths also present a strong negative correlation with the band gap energies in a single crystalline phase in a pressure range from ~25 to ~120 GPa, i.e. the $MgSiO_3$ bridgmanite consisting of the SiO_6 octahedra [7]. The result of this study, along with the results from previous studies, imply that the decreases in the short-range interatomic distances and, thus, the enhanced short-range electronic interactions and/or repulsions among the outermost electronic states of neighboring Mg, Si, and O atoms can facilitate the significant increase in the band gap energies of $MgSiO_3$ melts at extremely high pressures above ~18 GPa. I should note that the gradual decrease in the nearest-neighboring O-O distances ($d_{O\text{-}O}$) in a pressure range from ~0 to ~18 GPa presented in Fig. 5-3(a) (from 2.7340 Å to 2.6260 Å) seems not to be associated with the increase in the band gap energies of $MgSiO_3$ melts under high pressures. The decrease in the $d_{O\text{-}O}$ at a higher-pressure region above ~18 GPa (from 2.6260 Å to 2.3420 Å), however, might enhance the short-range electronic interactions between nearby O atoms, particularly *p*-*p* hybridization [72]. Details about the contribution of the O *p*-*p* hybridization to the changes in the O *K*-edge XRS features of $MgSiO_3$ melts under high pressures will be discussed in the following section.

Calculated O *K*-edge XRS spectra for $MgSiO_3$ melts at high pressures

Figure 5-5 present the calculated O *K*-edge XRS spectra for crystalline $MgSiO_3$ phases (a), the O *K*-edge XRS spectra of SiO_2 and $MgSiO_3$ glasses at the ambient condition (b), and the calculated O K-edge XRS spectra for $MgSiO_3$ melts at high pressures up to ~131 GPa (c). The calculated O *K*-edge XRS spectra for $MgSiO_3$ melts presented here were shifted by 532.24 eV to compare with the experiments, because the x-axis of the calculated XRS spectrum is the relative energy difference with respect to the Fermi level (i.e., $E-E_F$). Fig. 5-5(a) present the calculated O *K*-edge XRS spectra for crystalline $MgSiO_3$ phases (enstatite at 1 atm, ilmenite-type $MgSiO_3$ at 22 GPa, bridgmanite structures from 25 to 120 GPa) reported in our previous studies [3,7]. Details about the atomistic accounts of these characteristic O *K*-edge XRS features of the crystalline $MgSiO_3$ phases can be found in our previous studies [3,7], and thus a brief summary is presented in the appendix (Fig. 5-A6) [6]. While the calculated O *K*-edge XRS spectra for the crystalline $MgSiO_3$ phases present characteristic core-level excitation features induced from their distinctive local O configurations, these O *K*-edge features gradually shift to a higher-energy region upon compression. This pressure dependence of O *K*-edge XRS features of crystalline $MgSiO_3$ phases has been revealed to be partly attributed to the topological densification around O atoms, particularly associated with the enhanced proximity between neighboring O atoms [7].

Fig. 5-5(b) presents the O *K*-edge XRS spectra of SiO_2 and $MgSiO_3$ glasses at the ambient pressure reported in the previous XRS experiments [1] and the O *K*-edge XRS spectrum of the $MgSiO_3$ melt at ~0 GPa

calculated in this study. The O *K*-edge XRS spectra of SiO_2 and $MgSiO_3$ glasses at the ambient pressure present broad excitation features compared with those of crystalline $MgSiO_3$ phases in Fig. 5-5(a). These broad O *K*-edge features of noncrystalline silicates result from the intrinsic overlaps of the excitation features of symmetrically inequivalent O atoms attributed to the variations of the Si-O bond length, the Mg-O and O-O distances, and the Si-O-Si bond angle [1,65]. These O *K*-edge features of SiO_2 and $MgSiO_3$ glasses present similar excitation features near the absorption threshold from ~545 to ~540 eV because most of these features stem from the bridging O atoms linking SiO_4 tetrahedra, i.e. $^{[4]}$Si-O-$^{[4]}$Si [1]. The O *K*-edge XRS spectrum of $MgSiO_3$ glass present the slightly difference excitation features at a higher-energy region above ~543 eV due to the presence of nonbriding O atoms, i.e. Mg-O-$^{[4]}$Si, and, thus, the topological disorder [1]. See Fig. 5-A3 in the appendix for the discussion about the topological differences between the noncrystalline SiO_2 and $MgSiO_3$ melts due to the presence of nonbridging O atoms [6]. The calculated O *K*-edge XRS spectrum for $MgSiO_3$ melt at ~0 GPa presents similar excitation features to those of $MgSiO_3$ glass at the ambient pressure, particularly near the absorption threshold. These similar XRS features imply that the O *K*-edge XRS spectrum of $MgSiO_3$ melt at ~0 GPa calculated in this study successfully represent the complicated short- to medium-range structures around O atoms in the noncrystalline $MgSiO_3$ melt at ~0 GPa. Therefore, the results in Fig. 5-5(c) can be used to establish the direct link between the short- to medium-range structural changes around O atoms and the changes in O *K*-edge XRS features of noncrystalline $MgSiO_3$ melts under high pressures. Slight differences between the O *K*-edge XRS features of

$MgSiO_3$ glass and melt at the ambient pressure and ~0 GPa will be discussed in the following section (Fig. 5-7).

Fig. 5-5(c) presents the calculated O *K*-edge XRS spectra for $MgSiO_3$ melts at high pressures. The O *K*-edge XRS features of $MgSiO_3$ melts do not present considerable changes at a lower-pressure region from ~0 to ~18 GPa. However, they present significant changes in their peak positions and widths at a higher-pressure region above ~18 GPa: the highest peak position shifts by ~4.6 eV (from ~537.4 eV to ~ 542.0 eV) and the absorption threshold energy also shifts by ~1.7 eV (from ~532.4 eV to ~534.1 eV) with increasing pressure from ~18 to ~131 GPa. This result is consistent with the pressure induced changes in the band gap energies of $MgSiO_3$ melts presented in Fig. 5-4(f). I should note that the gradual shift in O *K*-edge XRS features of crystalline $MgSiO_3$ phases in Fig. 5-5(a) is attributed in part to the enhanced proximity between neighboring O atoms [7]. In addition, the similar changes in the O *K*-edge excitation features have been reported in a previous study for the $(O_2)_4$ molecular solid: both π^* (the O 1*s*-1π_g^* transition) and σ^* (the O 1*s*-1σ_u^* transition) peaks shift to a higher-energy region with decreasing the interatomic distances between nearby O atoms upon compression [72]. The pressure-induced changes in the O *K*-edge XRS features of $MgSiO_3$ melts presented here, therefore, also might be attributed in part to the enhanced proximity between nearby O atoms in the noncrystalline network structures. Since the changes in the atomic structures of $MgSiO_3$ melts under high pressures have been revealed in Fig. 5-3(a), the correlation between the short- to medium-range topological changes around O atoms and associated changes in the O *K*-edge XRS features of $MgSiO_3$ melts can be established precisely.

Pressure-induced changes in O K-edge XRS spectra of $MgSiO_3$ melts

Figure 5-6 presents the pressure dependence of the O *K*-edge absorption threshold energies (E_A) of $MgSiO_3$ melts (a) and the correlations between the short-range structural changes around O atoms and the E_A (b): the Si-O bond length ($d_{Si\text{-}O}$), the neighboring Mg-O ($d_{Mg\text{-}O}$) and O-O ($d_{O\text{-}O}$) distances, and the average atomic coordination numbers of Si (n_{Si}) and O (n_O) atoms revealed in Fig. 5-3(a). The E_A of $MgSiO_3$ melts at high pressures each were determined from the energy at which the O *K*-edge features increase rapidly, and thus it can be carried out from the slope of the calculated O *K*-edge XRS spectra for $MgSiO_3$ melts at high pressures. The n_{Si}, n_O, $d_{Si\text{-}O}$, $d_{Mg\text{-}O}$, and $d_{O\text{-}O}$ presented in Fig. 5-6(b) were normalized with their values at ~0 GPa (n_{Si} = 4.00, n_O = 1.31, $d_{Si\text{-}O}$ = 1.6390 Å, $d_{Mg\text{-}O}$ = 2.0460 Å, and $d_{O\text{-}O}$ = 2.7340 Å) to present their pressure dependences more clearly. Fig. 5-6(a) presents that the E_A of $MgSiO_3$ melts do not present considerable shift in a lower-pressure region from ~0 to ~18 GPa, but it significantly increases with increasing pressure above ~18 GPa. This result is consistent with the pressure dependence of band gap energies of $MgSiO_3$ melts revealed in Fig. 5-4(f) that presents the significant increase in the band gap energies of $MgSiO_3$ melts with increasing pressure from ~18 to ~131 GPa.

In a lower-pressure region from ~0 to ~18 GPa, the E_A of $MgSiO_3$ melts present negligible changes upon compression as revealed in Fig. 5-6(a). This result implies that the change in the E_A of $MgSiO_3$ melts seems not to be strongly correlated with the topological densification of $MgSiO_3$ melts primarily associated with the formation of highly coordinated Si and O atoms under high pressures. Thus, in this lower-pressure region, the

increases in the n_{Si} (4.00 to 4.38) and n_O (1.31 to 1.46) in Fig. 5-6(b) do not present the clear correlations with the changes in the O *K*-edge XRS features, as well as the E_A, of $MgSiO_3$ melts under high pressures. The gradual decreases in the $d_{O\text{-}O}$ (from 2.7340 to 2.6260 Å), in this lower-pressure region, cannot induce the considerable changes in the O *K*-edge XRS features of $MgSiO_3$ melts because of the relatively long interatomic distances between the nearby O atoms. In contrast, the E_A of $MgSiO_3$ melts presented in Fig. 5-6(a) shows a significant increase (from ~531.3 to ~533.2 eV) in a pressure range from ~18 to ~131 GPa associated with the emergence of the high-energy excitation features above ~540 eV presented in Fig. 5-5(c). The increases in the n_{Si} (from 4.38 to 4.88) and n_O (from 1.46 to 1.63) in this higher-pressure region seem to be correlated with the changes in the E_A of $MgSiO_3$ melts. However, since the coordination transitions of Si and O atoms in a lower-pressure region, without considerable decreases in the short-range interatomic distances, could not facilitate the changes in the O *K*-edge XRS features of $MgSiO_3$ melts as revealed in Fig. 5-5(c) and 5-6(b), the short-range topological changes around O atoms mostly associated with the formation of highly coordinated Si and O atoms may not have a primary role on the changes in the O *K*-edge XRS features of $MgSiO_3$ melts under high pressures.

In a higher-pressure region above ~18 GPa, the increase in the E_A of $MgSiO_3$ melts with increasing pressure is moderately correlated with the decrease in the $d_{Mg\text{-}O}$ (from 2.0360 to 1.9080 Å). This implies that the pressure-induced changes in the O *K*-edge XRS features of $MgSiO_3$ melts seem to be partly attributed to the decrease in the $d_{Mg\text{-}O}$ and, thus, the enhanced short-range electronic interaction between the Mg 3*s* and O 2*p*

states. The $d_{Si\text{-}O}$, which refers to the average bond lengths of the rigid Si-O covalent bonds, seems not to be strongly correlated with the E_A because of its relatively small changes upon compression compared with the other parameters. However, the presence of compressed Si-O bonds could contribute in part to the changes in the calculated O *K*-edge XRS spectra for $MgSiO_3$ melts under extremely high pressures due to the enhanced electronic interaction between the outermost electronic states of Si (3*s* and 3*p* states) and O (2*p* state) atoms. The similar trend, i.e. the negative correlation between the Si-O bond length and the E_A of $MgSiO_3$ bridgmanite structures, has been revealed in our previous study [7]. The $d_{Si\text{-}O}$ of the network building Si polyhedra is correlated with the interatomic distances in their edge, i.e. the neighboring O-O distances ($d_{O\text{-}O}$). Thus, the contribution of the decrease in the $d_{O\text{-}O}$ to the changes in the O *K*-edge XRS features of $MgSiO_3$ melts are discussed in the following paragraph.

The decrease in the $d_{O\text{-}O}$ (from 2.7340 to 2.6260 Å) in a pressure range from ~0 to ~18 GPa cannot facilitate the considerable changes in the O *K*-edge XRS features of $MgSiO_3$ melts upon compression as presented in Fig. 5-5(c) and 5-6(b). In contrast, the decrease in the $d_{O\text{-}O}$ (from 2.6260 to 2.3420 Å) in a higher-pressure region from ~18 to ~131 GPa would partly contribute to the changes in the O *K*-edge excitation features of $MgSiO_3$ melts, i.e. a shift to a higher-energy region with an emergence of high-energy features above ~544 eV, since the changes in the O *K*-edge features of diverse oxides under high pressures have been revealed to be associated in part with the decrease in the neighboring O-O distances [2,7,67,72]. The characteristic O *K*-edge excitation features of SiO_2 stishovite have been revealed to stem from the *p*-*p* hybridization between the nearby O atoms

(the features at both ~538 and ~544 eV), in a distance ~2.44 Å at ~15 GPa [156], and the hybridization between the Si 3*s* and O 2*p* states (the feature at ~538 eV) [2,67]. Thus, the stishovite-like O *K*-edge features of SiO_2 glasses at high pressures above ~20 GPa, which have been explained with the structural transition similar to the stishovite with $^{[6]}$Si [2] and the formation of $^{[5]}$Si and $^{[6]}$Si [67], could be attributed in part to the formation of the O *p*-*p* hybridization associated with the enhanced proximity between the nearby O atoms under high pressures. The O *K*-edge features of the $(O_2)_4$ molecular solid, reported in a previous study [72], present the characteristic excitation features stemmed from the *p*-*p* hybridization, i.e. at ~532 and ~540 eV from the 1*s*-1π_g* and 1*s*-1σ_u* transitions respectively, between the neighboring O atoms, in a distance ~2.34 Å at ~11 GPa [217]. These double-peak excitation features of the $(O_2)_4$ molecular solid, which are slightly similar to those of the stishovite [2,67], shift to a higher-energy region with decreasing the inter-cluster bond lengths upon compression from ~10 to ~47 GPa [72]. In addition, the clear negative correlation between the $d_{O\text{-}O}$, in a range from ~2.33 to ~2.66 Å, and the E_A of diverse crystalline SiO_2 and $MgSiO_3$ phases have been revealed in our previous study [7]. The changes in the calculated O *K*-edge XRS features for $MgSiO_3$ melts in a pressure range from ~18 to ~131 GPa, therefore, could be partly attributed to the O *p*-*p* hybridization associated with the enhanced proximity between the nearby O atoms upon compression (from 2.6260 to 2.3420 Å), since the sufficiently close O atoms, maybe below the ~2.44 Å, certainly can induce the O *p*-*p* hybridization and, thus, the high-energy features at ~540-545 eV.

The results presented here, along with the results from the previous studies [2,7,67,72], indeed indicate that the pressure-induced

changes in the O *K*-edge excitation features of noncrystalline $MgSiO_3$ melts are primarily attributed to the decreases in the short-range interatomic distances upon compression, not the topological transformation associated with the formation of highly coordinated Si and O atoms. The quantitative relationships between the short-range topological changes around O atoms (n_{Si}, n_O, $d_{Mg\text{-}O}$ and $d_{O\text{-}O}$) and the E_A of $MgSiO_3$ melts, in a pressure range from ~18 to ~131 GPa where the excitation features of $MgSiO_3$ melts present significant changes upon compression, can be established: E_A (eV) = -12.68$d_{Mg\text{-}O}$ (Å) + 557.52 (R^2 = 0.77) for the $d_{Mg\text{-}O}$, E_A (eV) = -6.12$d_{O\text{-}O}$ (Å) + 547.67 (R^2 = 0.86) for the $d_{O\text{-}O}$, E_A (eV) = 3.55n_{Si} + 515.83 (R^2 = 1.00) for the n_{Si}, and E_A (eV) = 10.64n_O + 515.83 (R^2 = 1.00) for the n_O, respectively. These *linear* relationships are revised in a pressure range from ~0 to ~131 GPa: E_A (eV) = -13.76$d_{Mg\text{-}O}$ (Å) + 559.62 (R^2 = 0.86) for the $d_{Mg\text{-}O}$, E_A (eV) = -5.30$d_{O\text{-}O}$ (Å) + 545.67 (R^2 = 0.90) for the $d_{O\text{-}O}$, E_A (eV) = 2.09n_{Si} + 522.76 (R^2 = 0.88) for the n_{Si}, and E_A (eV) = 5.74n_O + 523.58 (R^2 = 0.85) for the n_O, respectively. I should note that, in these relationships, while the changes in the O *K*-edge excitation features of $MgSiO_3$ melts are revealed to be primarily induced from the decreases in the short-range interatomic distances around O atoms ($d_{Si\text{-}O}$, $d_{Mg\text{-}O}$, and $d_{O\text{-}O}$), the average atomic coordination numbers of Si (n_{Si}) and O (n_O) atoms present strong correlations with the E_A of $MgSiO_3$ melts. This is because the coordination transition of Si and O atoms in the noncrystalline network structures are moderately correlated with the decreases in the short-range interatomic distances under extremely high pressures as revealed in Fig. 5-3(a). Thus, the pressure-induced changes in the O *K*-edge features of noncrystalline $MgSiO_3$ melts can imply the presence of highly coordinated Si and O atoms under high pressures

associated with the decreases in the short- to medium-range interatomic distances. The current results thus are partly consistent with the previous studies in which the structural transition similar to stishovite with $^{[6]}$Si [2], the formation of highly coordinated Si atoms ($^{[5]}$Si and $^{[6]}$Si) [67], the formation of O triclusters (e.g., $^{[5]}$Si-$^{[3]}$O-2$^{[4]}$Si) and associated structural changes in the medium-range order [1], and the enhanced proximity between neighboring O atoms [3,7] have been suggested to explain the changes in the O *K*-edge excitation features of noncrystalline SiO_2 and $MgSiO_3$ phases under high pressures. The direct link between the short-range topological changes around O atoms and the changes in the O *K*-edge excitation features of $MgSiO_3$ melts under high pressures, established here, can be used to probe the atomistic origins of the pressure-induced changes in the O *K*-edge XRS spectra of $MgSiO_3$ glasses reported in the previous *in situ* high-pressure XRS experiments [1].

Origins of the pressure-induced changes in the O *K*-edge XRS spectra of $MgSiO_3$ glasses

The atomistic accounts of the changes in the core-level excitation features of the crystalline and noncrystalline SiO_2 and $MgSiO_3$ under high pressures have been controversial even with the efforts in previous studies: the stishovite-like structural transition with $^{[6]}$Si [2], the formation of highly coordinated Si atoms ($^{[5]}$Si and $^{[6]}$Si) [67], the changes in the Si-O-Si bond angle [68,73], the formation of O triclusters and associated changes in the medium-range order [1], and the enhanced proximity between neighboring O atoms [3,7]. This has been because of the difficulties of resolving site-specific information even with the state-of-the-art XRS experimental

techniques and the intrinsic differences between the atomic structures, as well as the densification mechanisms, of the crystalline and noncrystalline oxides under high pressures [65]. It thus is obvious that the current results for the $MgSiO_3$ melts under high pressures can provide the further insights into the atomistic origins of the pressure-induced changes in the O *K*-edge excitation features of amorphous $MgSiO_3$ glasses [1]. Figure 5-7 presents the O *K*-edge XRS spectra of $MgSiO_3$ glasses at high pressures up to ~39 GPa (top) [1] and the O *K*-edge XRS spectra of $MgSiO_3$ melts at high pressures up to ~131 GPa calculated in this study (bottom). The calculated O *K*-edge XRS features for $MgSiO_3$ melts were shifted by 532.24 eV to with the O *K*-edge XRS spectra of $MgSiO_3$ glasses at high pressures. The direct link between the short-range topological changes around O atoms and associated changes in the O *K*-edge XRS features of $MgSiO_3$ melts have been established in Fig. 5-6(b). Thus, the detailed atomistic origins of the changes in the O *K*-edge XRS spectra of $MgSiO_3$ glasses under high pressures, which could not have been precisely determined in the previous studies [1,3,7], now can be revealed through the comparison between the pressure-induced changes in the O *K*-edge excitation features of $MgSiO_3$ glasses and melts.

I have noticed the slight differences between the excitation features of $MgSiO_3$ glass and melt at the similar pressure conditions in Fig. 5-5(b). In the center of Fig. 5-7, the O *K*-edge XRS spectrum of the $MgSiO_3$ glass at the ambient pressure is compared with the calculated O *K*-edge XRS spectrum for the $MgSiO_3$ melt at ~0 GPa and 3000 K. The O *K*-edge XRS spectrum of the $MgSiO_3$ melt at ~0 GPa presents similar excitation features to those of the $MgSiO_3$ glass at the ambient pressure due to the topological similarity

around O atoms, e.g. the presence of bridging ([4]Si-O-[4]Si) and nonbridging O (Mg-O-[4]Si) atoms in the highly depolymerized noncrystalline network structures. However, the slight differences between these O *K*-edge features are presented, particularly near the absorption threshold and at the higher-energy region above ~544 eV. These differences in the O *K*-edge excitation features might be due primarily to the potential presence of the high-energy, and thus highly disordered, molecular clusters in the $MgSiO_3$ melt, which are stable at a higher-temperature region (3000 K), compared with the $MgSiO_3$ glass quenched at a room temperature (~300 K). The melting and glass transition temperatures of the $MgSiO_3$ enstatite at 1 atm are ~1830 and ~1039 K, respectively [218]. The calculated O *K*-edge XRS spectrum for the $MgSiO_3$ melt at ~0 GPa and 2000 K thus are presented to confirm the effect of the thermally-induced topological disorder to the O *K*-edge excitation features. The O *K*-edge XRS features of the $MgSiO_3$ melt at ~0 GPa and 2000 K present more similar excitation features to those of $MgSiO_3$ glass at the ambient pressure, implying their closer topological similarity in the short-range order, compared to the $MgSiO_3$ melt at a higher temperature. Nonetheless, the $MgSiO_3$ melt configurations at a relatively lower-temperatures condition, i.e. at 2000 K, should not be used to simulate the high-density $MgSiO_3$ melts under extremely high pressures because the melting temperature of $MgSiO_3$ (~1830 K at 1 atm [218]) would increase under high pressures [219]. The temperature effects to the atomic structures of the noncrystalline oxide melts under high pressures and their XRS excitation features should be explored in the future study, since, in this study, I have focused on the atomistic accounts of the pressure-induced changes in the XRS excitation features of the noncrystalline Mg-silicates.

See Fig. 5-A3 in the appendix for the details about the thermally-induced topological disorder in the $MgSiO_3$ melts [6].

The O *K*-edge XRS spectra of $MgSiO_3$ glasses present significant changes with increasing pressure up to ~39 GPa, even with the insufficient resolution of the *in situ* high-pressure XRS experiments (> 1.0 eV) [64,65]. The highest peak position shifts to a higher-energy region from ~538.5 to ~542.5 eV with an emergence of the high-energy features above ~544 eV. The calculated O *K*-edge XRS features for $MgSiO_3$ melts under high pressures up to ~131 GPa present comparable changes to the pressure-induced changes in the O *K*-edge XRS spectra of $MgSiO_3$ glasses, i.e. the shift to a higher-energy region with an emergence of the high-energy features above ~544 eV, while the O *K*-edge XRS spectra of the $MgSiO_3$ melts in a relatively lower-pressure region from ~0 to ~18 GPa present negligible differences in their excitation features as revealed in Fig. 5-5(c) and 5-6(b). The pressure-induced changes in the O *K*-edge XRS spectra of $MgSiO_3$ glasses thus might be attributed to the structural changes around O atoms which resembles those in the $MgSiO_3$ melts under high pressures, particularly in a pressure range from ~18 to ~131 GPa. In Fig. 5-5(c) and 5-6(b), the changes in the O *K*-edge excitation features of $MgSiO_3$ melts under high pressures are revealed to be attributed in part to the decreases in the short-range interatomic distances around O atoms and, thus, the enhanced short-range electronic interactions, not the topological densification associated with the formation of highly coordinated Si and O atoms. The pressure-induced changes in the O *K*-edge XRS spectra of $MgSiO_3$ glasses, therefore, are indeed indicative of the decreases in the short-range interatomic distances around O atoms under high pressures. Nonetheless,

the pressure-induced changes in the O *K*-edge XRS features of $MgSiO_3$ glasses can imply the presence of highly coordinated Si and O atoms, as well as the O triclusters, under high pressures, since the decreases in the short-range interatomic distances around O atoms in the $MgSiO_3$ melts are moderately correlated with the increases in the average atomic coordination numbers of Si and O atoms as presented in Fig. 5-3(a). Based on the results so far, I now can unveil the atomistic accounts of the pressure-induced changes in the O *K*-edge XRS spectra of $MgSiO_3$ glasses that cannot be precisely determined in the previous studies: The pressure-induced changes in the O *K*-edge excitation features of $MgSiO_3$ glasses indicate the structural transition of $MgSiO_3$ glasses under high pressures associated with the decreases in the short-range interatomic distances and, also, the formation of highly coordinated Si and O atoms in the highly depolymerized noncrystalline network structures.

I note that the O *K*-edge XRS spectra of $MgSiO_3$ glasses (up to ~39 GPa) and melts (in a pressure range from ~18 to ~131 GPa) present the comparable pressure-induced changes in their excitation features, even with the significantly different pressure ranges. This is attributed to the distinctive structural rigidities of $MgSiO_3$ melts (3000 K) and glasses (~300 K) at extremely different temperatures, i.e. the resistance to the topological transformation associated with the formation of highly coordinated Si and O atoms, and, thus, the different densification mechanisms. The topological transformation associated with the coordination transition of Si and O atoms in the highly depolymerized noncrystalline network structures might be more favorable in the $MgSiO_3$ melts than the $MgSiO_3$ glasses quenched at a room temperature due to the thermally-induced, and thus

higher, degree of freedom of atoms in the $MgSiO_3$ melts at a higher temperature. The similar trend has been presented in the previous theoretical studies for $MgSiO_3$ glasses under high pressure: The $MgSiO_3$ glasses, which were compressed at 3000 K and then quenched to 300 K (i.e., the hot compression), present a more rapid increase in the average coordination numbers of Si and O atoms than the $MgSiO_3$ glasses compressed after quenching at 300 K (i.e., the cold compression) [8].

Implications

The potential presence of high-density $MgSiO_3$-rich melts [1,41] and the phase transition between the bridgmanite and post-bridgmanite [4,20] have been suggested as the atomistic accounts of the seismic heterogeneity near the core-mantle boundary (~2850 km) in the Earth's interior. The elastic properties of the crystalline oxides under high pressures, such as $MgSiO_3$ [4,20] and CO_2 [220] polymorphs, have been well established using the linear response theory implemented in the *ab initio* calculations [47]. The previous studies for the amorphous phonon scattering features of amorphous materials, however, have focused on probing the origins of differences in the thermal and vibrational properties between glasses and crystals at extremely low temperatures [221-225] to probe the remarkably different phonon-related properties, e.g. the heat capacity, thermal conductivity, and acoustic absorption, from their crystalline counterparts [48]. Thus, the atomistic accounts of the pressure-induced changes in the characteristics of the seismic wave propagation in the noncrystalline oxides under extremely high pressures have not been fully understood. I have noted that, in the recent theoretical study, the structures and elastic properties of the amorphous $MgSiO_3$ glasses at high pressures have been reported [8]. Though that study could have improved our understanding about the acoustic wave propagation in the high-density $MgSiO_3$ glasses under high pressures, there remain some deficiencies to explain the pressure dependences of the seismic wave propagation in the high-density $MgSiO_3$-rich lower mantle melts and, also, the origins of the seismic heterogeneity near the core-mantle boundary.

The phonon density of states of highly disordered materials with the extended and localized vibrational excitation features, and, thus, their vibrational properties, are essentially determined from the short-range order structures [47,48,226]. Thus, the elastic characteristics of the $MgSiO_3$ melts, as well as the high-density $MgSiO_3$-rich melts, under high pressures would present slightly or significantly different pressure dependences from those of the $MgSiO_3$ glasses [8], because of their structural differences in the short-range order due to the distinctive structural rigidities at extremely different temperatures. The acoustic wave velocities of the $MgSiO_3$ glasses compressed at different temperatures (i.e., compressed at 3000 K and quenched to ~300 K or compressed after quenching at ~300 K), reported in the previous study [8], also present slightly different pressure dependences in the same manner. The detailed densification mechanism, and associated changes in the electronic structures, of the $MgSiO_3$ melts revealed here could provide the further insights into the elastic properties of the high-density $MgSiO_3$-rich melts and, thus, the atomistic accounts of the seismic heterogeneity near the core-mantle boundary. The future phonon calculations for the $MgSiO_3$ melts under extremely high pressures, therefore, are expected.

The pressure-induced changes in the band gap energies, along with the O *K*-edge absorption threshold energies, of $MgSiO_3$ melts, which have been revealed to be attributed in part to the decreases in the short-range interatomic distances, imply the changes in the electrical conductivity of the high-density $MgSiO_3$-rich melts under high pressures with its atomistic accounts. This result also implies the changes in the chemical reactivity of the high-density $MgSiO_3$-rich melts under extremely high pressures

because the electron transfer, which facilitates the chemical reaction, is assessed from the relative energy difference between the valence and conduction bands. In addition, the pressure dependences of the band gap energies of noncrystalline $MgSiO_3$ melts, along with the increase in the band gap energies of crystalline SiO_2 and $MgSiO_3$ phases [7], could provide the further insights into the band gap engineering for the crystalline and noncrystalline oxide photovoltaics, as well as the colloidal quantum dots in a perovskite matrix [79-81].

Conclusion

Modern theoretical methods based on the *ab initio* calculations have shed light on probing the atomistic accounts of the complicated XRS features of multi-component and complex crystalline and noncrystalline oxides under high pressures. The current study reveals the direct link between the structural changes in the short- to medium-range order and the evolution in the XRS excitation features, along with their electronic structures, of noncrystalline $MgSiO_3$ melts under high pressures. The quantitative relationships between the topological changes around O atoms and the changes in the O *K*-edge XRS features thus can be established for the *first* time. The pressure-induced changes in the calculated O *K*-edge excitation features of $MgSiO_3$ melts are revealed to be attributed in part to the decreases in the short-range interatomic distances around O atoms, i.e. the Si-O bond lengths and the neighboring Mg-O and O-O distances. Nonetheless, these changes in the O *K*-edge features seem to be correlated with the formation of highly coordinated Si and O atoms because the coordination transition of Si and O atoms in the noncrystalline network structures under high pressures are associated with the decreases in the short-range interatomic distances. Consequently, I could conclude that the current results are agree in part with the previous studies in which the structural transition similar to stishovite with $^{[6]}$Si [2], the formation of highly coordinated Si atoms ($^{[5]}$Si and $^{[6]}$Si) [67], the formation of O triclusters (e.g., $^{[5]}$Si-$^{[3]}$O-2$^{[4]}$Si) and associated structural changes in the medium-range order [1], and the enhanced proximity between neighboring O atoms [3,7] have been suggested to explain the changes in the O *K*-edge

excitation features of noncrystalline SiO_2 and $MgSiO_3$ under high pressures. The slight differences between the densification mechanisms of $MgSiO_3$ melts and glasses could provide the further insights into the atomistic accounts of the pressure dependences of the seismic wave propagation in the high-density $MgSiO_3$-rich lower mantle melts at extremely high pressures and, thus, the origins of the seismic heterogeneity near the core-mantle boundary in the Earth's interior [11,20,21,41]. I further expect that the current study can be applied to interpret and predict the core-level excitation features, e.g. the O *K*-edge, Si $L_{2,3}$-edge, and Fe $L_{2,3}$-edge [64,65,207], of diverse multi-component oxides under extremely high pressures that cannot be achievable in the current *in situ* high-pressure XRS experiments. In addition, the changes in the band gap energies of crystalline and noncrystalline SiO_2 and $MgSiO_3$ phases under high pressures, presented here and our previous studies [3,7] would provide further insights into the band gap engineering of diverse oxide photovoltaics [79-81].

Figures

Figure 5-1. Populations of Si ($^{[4]}$Si, $^{[5]}$Si, and $^{[6]}$Si) and O [$^{[1]}$O (nonbridging O atoms; NBO), $^{[2]}$O (bridging O atoms; BO), and $^{[3]}$O (O tricluster)] species in the $MgSiO_3$ melts at high pressures. The $^{[3]}$Si and $^{[0]}$O atoms are not presented. See details in Tab. A2 and A4 in the appendix [6].

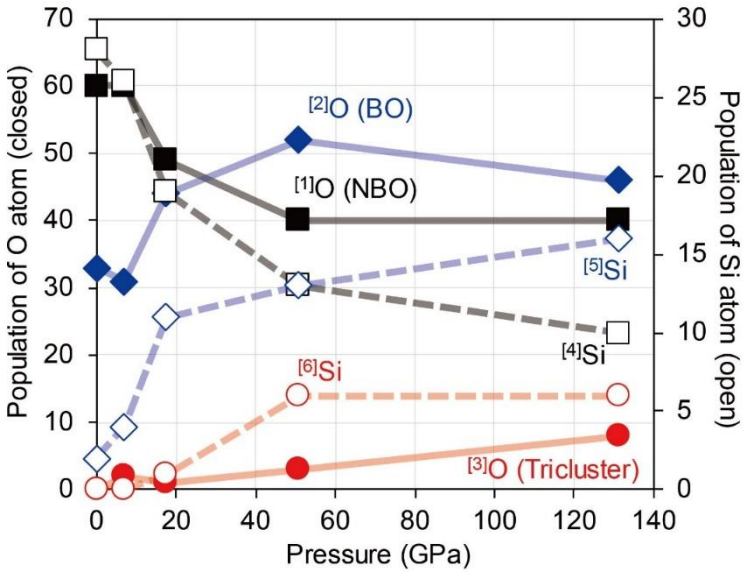

Figure 5-2. Total (a) and partial radial distribution functions of Mg-O (b), Si-O (c), and O-O (d) pairs in the $MgSiO_3$ melts at high pressures.

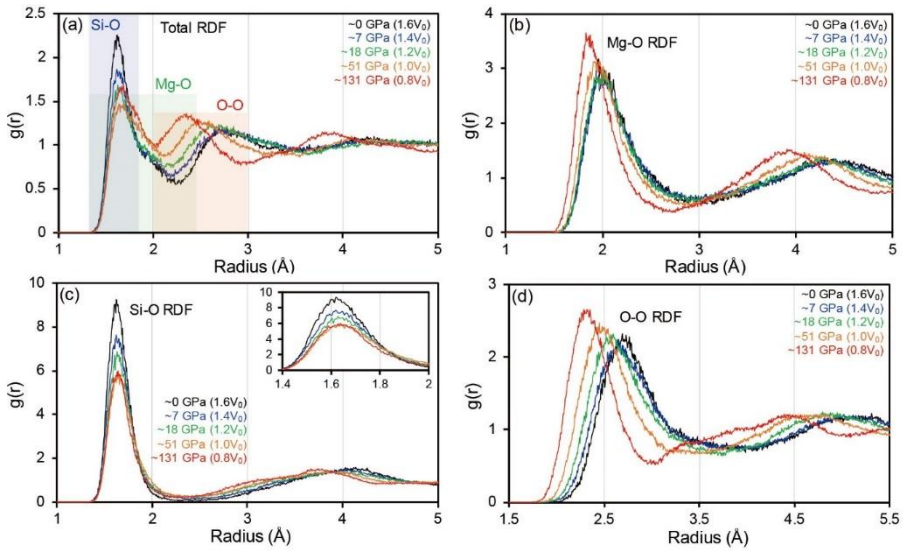

Figure 5-3. (a) Pressure dependences of the short-range interatomic distances (open circles) and the average atomic coordination numbers (closed circles) of the $MgSiO_3$ melts. The average atomic coordination numbers of Si (n_{Si}) and O (n_O) atoms were determined from Fig. 5-1. The average Si-O bond lengths ($d_{Si\text{-}O}$), the average neighboring Mg-O ($d_{Mg\text{-}O}$) and O-O ($d_{O\text{-}O}$) distances each were determined from the corresponding radial distribution functions in Fig. 5-2(b), 5-2(c), and 5-2(d) respectively, i.e. the center of mass of the peak at the first-coordination shells. The n_{Si}, n_O, $d_{Si\text{-}O}$, $d_{Mg\text{-}O}$, and $d_{O\text{-}O}$ were normalized with their values at ~0 GPa (n_{Si} = 4.00, n_O = 1.31, $d_{Si\text{-}O}$ = 1.6390 Å, $d_{Mg\text{-}O}$ = 2.0460 Å, and $d_{O\text{-}O}$ = 2.7340 Å). (b) A relationship between the average atomic coordination numbers of Si (n_{Si}) and O (n_O) atoms [$n_O = 0.36n_{Si} - 0.12$ (R^2=1.00)]. (c) Pressure dependences of the extent of polymerization of $MgSiO_3$ melts: the number of nonbridging O (NBO) atoms with respect to either the number of total Si atoms (Si_{Tot}) or the number of total O atoms (O_{Tot}) in the unit cells. (d) Pressure dependences of the full-width at half-maximum (FWHM) of the radial distribution function for the Si-O bond length ($\sigma_{Si\text{-}O}$) and the topological entropy [ΔS_{Top}(Si-O)] of the $MgSiO_3$ melts.

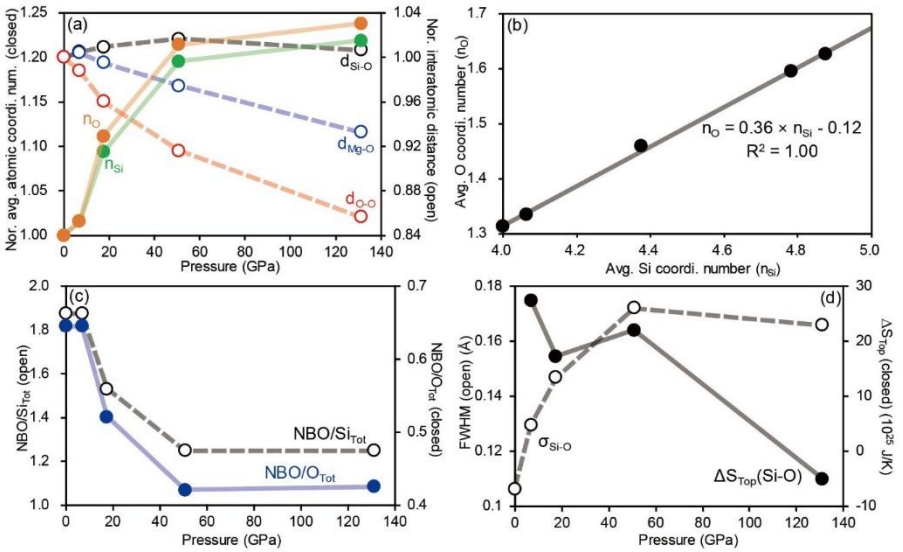
(a)
Nor. avg. atomic coordi. num. (closed)
Nor. interatomic distance (open)
Pressure (GPa)
d_{Si-O}
d_{Mg-O}
d_{O-O}
n_O
n_{Si}
(b)
Avg. O coordi. number (n_O)
Avg. Si coordi. number (n_{Si})
$n_O = 0.36 \times n_{Si} - 0.12$
$R^2 = 1.00$
(c)
NBO/Si_{Tot} (open)
NBO/O_{Tot} (closed)
Pressure (GPa)
NBO/Si_{Tot}
NBO/O_{Tot}
(d)
FWHM (open) (Å)
ΔS_{Top} (closed) (10^{25} J/K)
Pressure (GPa)
σ_{Si-O}
ΔS_{Top}(Si-O)

Figure 5-4. Calculated *l*-resolved (*s*, *p*, and *d* states) partial and total density of states (DOS) for the $MgSiO_3$ melts at high pressures: the partial DOS of Mg (a, b), Si (c), and O (d, e) and the total DOS (f).

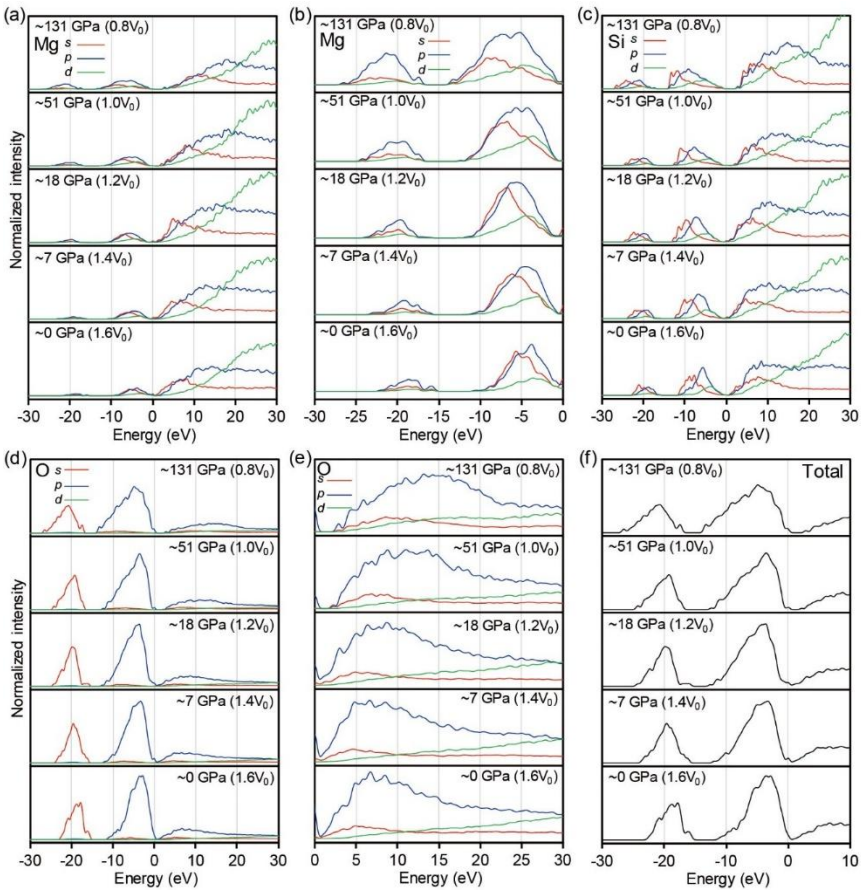

Figure 5-5. (a) The total and site-resolved (O1, O2, and O3) O *K*-edge XRS spectra of the crystalline $MgSiO_3$ phases [enstatite (1 atm), ilmenite-type $MgSiO_3$ (22 GPa), bridgmanite (25, 79, and 120 GPa)] referred from the previous studies [3,7]. (b) The O *K*-edge XRS spectra of the SiO_2 and $MgSiO_3$ glasses at 1 atm [1] and the calculated O *K*-edge XRS spectrum for the $MgSiO_3$ melt at ~0 GPa. (c) The calculated O *K*-edge XRS spectra for the $MgSiO_3$ melts at high pressures. The calculated O *K*-edge XRS features for the $MgSiO_3$ melts at high pressures were shifted by 532.24 eV to compare with experiments.

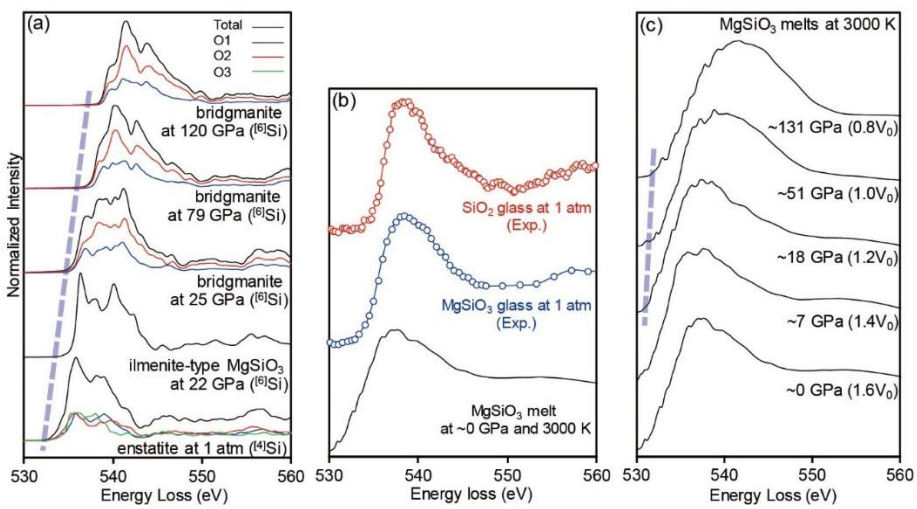

Figure 5-6. (a) Pressure dependence of the O *K*-edge absorption threshold energies (E_A) of the $MgSiO_3$ melts. (b) Correlations between the E_A and the short-range topological changes around O atoms of $MgSiO_3$ melts upon compression. The closed and open circles refer to the average atomic coordination numbers of Si (n_{Si}) and O (n_O) atoms and the average interatomic distances in the short-range order [the Si-O bond length (d_{Si-O}), and the neighboring Mg-O (d_{Mg-O}) and O-O (d_{O-O}) distances], respectively. The n_{Si}, n_O, d_{Si-O}, d_{Mg-O}, and d_{O-O} were normalized with their values at ~0 GPa (n_{Si} = 4.00, n_O = 1.31, d_{Si-O} = 1.6390 Å, d_{Mg-O} = 2.0460 Å, and d_{O-O} = 2.7340 Å).

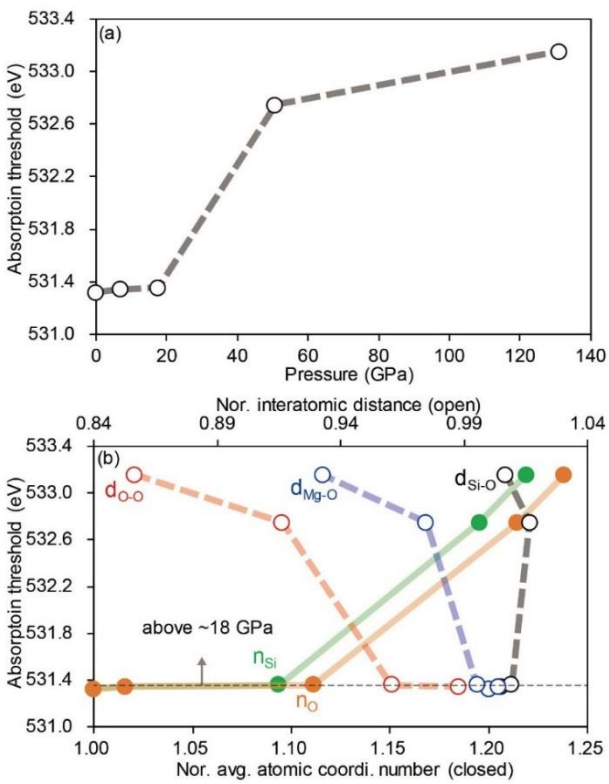

Figure 5-7. The O *K*-edge XRS spectra of the $MgSiO_3$ glasses at high pressures (top) [1] and the calculated O *K*-edge XRS spectra for the $MgSiO_3$ melts at ~0, ~51, and ~131 GPa (bottom). The calculated O *K*-edge XRS spectra for the $MgSiO_3$ melts at ~0 GPa and different temperatures (i.e., 2000 and 3000 K) are compared with the O *K*-edge XRS spectrum of the $MgSiO_3$ glass at the ambient pressure (center) [1]. The calculated O *K*-edge features for $MgSiO_3$ melts at high pressures were shifted by 532.24 eV to compare with the experiments.

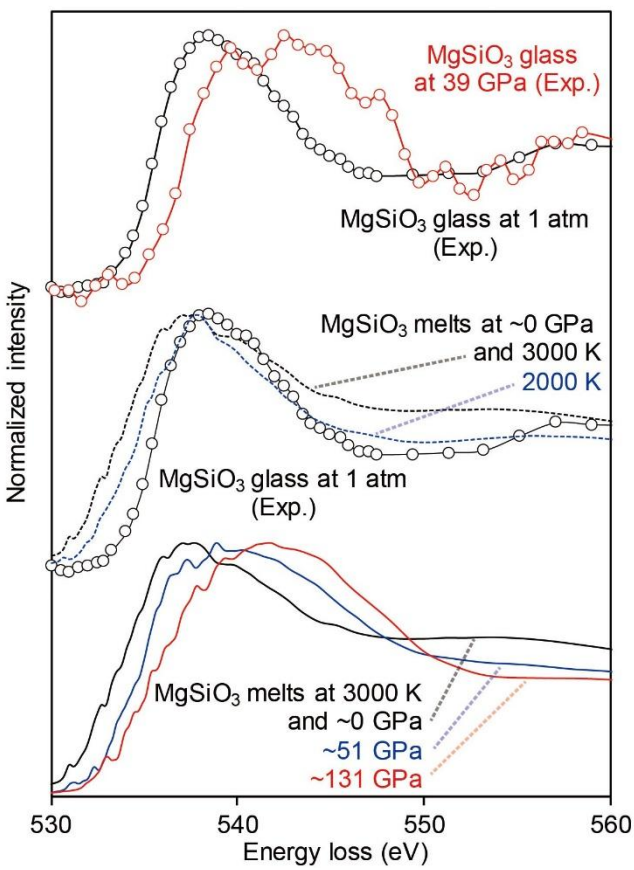

Appendix

Pressure estimation for the simulated $MgSiO_3$ melt configurations

Table **5-**A1 presents the result of the pressure estimation for the $MgSiO_3$ melts with different scaled volumes (from $0.8V_0$ to $1.6V_0$). The effective pressures (P) on the $MgSiO_3$ melts can be specified into the kinetic (P_K) and static (P_S) pressures: $P(V) = P_K(V)+P_S(V)$. The P_K and P_S can be obtained from the results of the *ab initio* molecular dynamic (AIMD) simulations, using CASTEP [78], for the $MgSiO_3$ melts at high pressures. The values of P_S each were estimated from the stress tensors of the $MgSiO_3$ melt configurations at the end of the AIMD simulations without taking into consideration of the thermally induced kinetic effects, i.e. the stress tensors were calculated at T = 0 K. The values of P_K, which stem from the thermally induced kinetic energies of atoms in the unit cells (at T = 3000 K), were estimated by averaging the kinetic pressures over the last 0.1 ps of the AIMD simulations for the $MgSiO_3$ melts, i.e. using the last 100 configurations.

The electronic structures calculated with the distinctive plane-wave-cut-off energies (E_{CUT}) usually present slightly different results and, thus, different static pressures (P_S) because of the inherent incompleteness of the electron wave functions consisting of the truncated basis sets with the different E_{CUT} values [227]. The effect of the incompleteness of the wave functions used to describe the electronic structures should be reduced to obtain the precise P_S values with applying the Pulay correction term (P_{Pulay}) that refers to the different between the static pressure values estimated with the lower and higher E_{CUT} values [75-77]. This P_{Pulay} term can be ignored with the sufficiently high and, thus, fully converged E_{CUT} values. The E_{CUT} of 600 eV has been reported to be sufficient in the previous

theoretical study for the Mg_2SiO_4 melts [77]. The static pressure values thus have been calculated, additionally, with the higher E_{CUT} = 900 eV to obtain the precise P_S values, since, in this study, the AIMD simulations have been performed with the relatively lower E_{CUT} = 310 eV. The P_S(V; E_{CUT}=900 eV) in Tab. A1 should be used to estimate the reliable values of $P(V)$.

The pressure values estimated using the local density approximation (LDA) method are usually overestimated than experiments because of the overbinding of covalent bonds. Though most of this overbinding problem are fixed in the generalized gradient approximation (GGA) method, the calculated pressure values are not sufficiently accurate, e.g. the transition pressures from experiments are usually observed between the pressure values calculated using the LDA and GGA methods. The pressure values calculated in this study, using the GGA method, thus should be arbitrary shifted to compare with the results experiments. The calculated pressure for the $MgSiO_3$ melt of $1.6V_0$ thus was shifted to ~0 GPa with the empirical correction term (P_E) because its density (2.56 g/cm^3) is similar to the density of the $MgSiO_3$ melt at the ambient condition (~2.6 g/cm^3) reported in a previous study [8]. Other calculated pressure values for the $MgSiO_3$ melts of different scaled volumes were also shifted by the same P_E value. Consequently, the pressure values of the $MgSiO_3$ melts have been estimated with the following relationship: $P(V) = P_K(V;\ E_{CUT}$=310 eV)+$P_S(V;\ E_{CUT}$=900 eV)+P_E (see details in Tab. A1). Figure 5-A1 presents the pressure dependence of the densities of the $MgSiO_3$ melt configurations simulated here, and it is compared with the result from the previous study using the LDA method [8] to confirm the reliability of the pressure values of $MgSiO_3$ melts estimated in this study. The pressure values of the $MgSiO_3$ melts estimated in this study present a similar result with the previous study using the LDA method [8], but the pressure values in a higher-pressure region above ~50 GPa are slightly overestimated.

Table 5-A1. Estimated pressure values for the simulated $MgSiO_3$ melt configurations.

Scaled volume (V_0)	Density (g/cm^3)	P_K (GPa)	P_S (E_{CUT}=310 eV) (GPa)	P_S (E_{CUT}=900 eV) (GPa)	P_{Pulay} (GPa)	P_E (GPa)	P (GPa)
1.6	2.56	3.2	3.8	1.9	-1.9		0.0
1.4	2.93	3.6	10.4	8.3	-2.1		6.9
1.2	3.42	4.2	21.7	18.4	-3.3	-5.0	17.6
1.0	4.10	5.1	53.5	50.7	-2.8		50.8
0.8	5.13	6.4	132.0	129.8	-2.2		131.2

P_K: Kinetic pressures, averaged out last 0.1 ps (100 MD steps) in the diffusion regime (E_{CUT}=310 eV)
P_S: Static pressures with specific E_{CUT} values (E_{CUT} = 310 or 900 eV)
P_{Pulay}: Pulay correction terms determined with $P_S(V; E_{CUT}=900\text{ eV}) - P_S(V; E_{CUT}=310\text{ eV})$
P_E: Empirical correction term to shift the pressure of $MgSiO_3$ 1.6V_0 to 0 GPa
$P(V) = P_K(V; E_{CUT}=310\text{ eV}) + P_S(V; E_{CUT}=310\text{ eV}) + P_{Pulay}(V) + P_E = P_K(V; E_{CUT}=310\text{ eV}) + P_S(V; E_{CUT}=900\text{ eV}) + P_E$

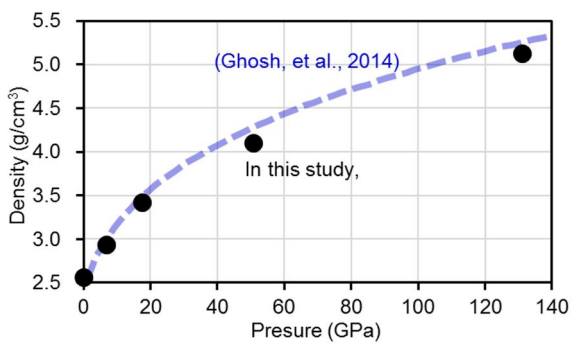

Figure 5-A1. Pressure dependence of the densities of the $MgSiO_3$ melts calculated in this study using the GGA method (black circles) and the result from the previous study using the LDA method [8].

Populations of Si and O species in the $MgSiO_3$ melts at high pressures

The pressure dependences of the populations of Si and O species, i.e. the coordination environments, in the $MgSiO_3$ melts are presented in Fig. 5-1 in the manuscript without the populations of uncommon atomic

configurations with extremely small proportion, such as the $^{[3]}$Si and $^{[0]}$O. I note that the estimation of the atomic coordination numbers of Si and O atoms and, thus, the populations of Si and O species can vary with the different bond length tolerances, i.e. the bond criteria, which are used to determine whether the Si-O covalent bonds are formed. The upper (TF_U) and lower (TF_L) bond length tolerance factors determine the largest and smallest distances between two atoms for which a covalent bond may still be formed, and the distance (D) between the atoms should be in the product between the ideal bond length, i.e. the sum of covalent radii of two atoms (R_1 and R_2), to form a covalent bond: $TF_L \times (R_1+R_2) < D < TF_U \times (R_1+R_2)$. The ideal covalent radii of Si and O atoms are ~1.11 and ~0.66 Å, respectively. Table **5-**A2 and **5-**A3 present the populations of Si species in the $MgSiO_3$ melts at high pressures estimated with the different bond length tolerances, and table **5-**A4 and **5-**A5 present the populations of O species. In Tab. A2 and A4, the TF_U and TF_L were set to 1.2 and 0.6, respectively. The numbers of highly coordinated Si and O atoms at a higher-pressure region above ~51 GPa seem to be overcounted because of the presence of the Si-O bonds with the unexpected long bond lengths over ~2.0 Å. In Tab. A3 and A5, the value of TF_U varies from 0.96 to 1.1, while the TF_L was fixed to 0.6 to remove the unrealistic Si-O bonds with the long bond lengths. Therefore, the results in Tab. A3 and A5, with the relatively lower values of TF_L, have been used to present the topological changes in the $MgSiO_3$ melts under high pressures presented in Fig. 5-1 in the manuscript. The average Si-O coordination numbers with different bond length tolerance factors are compared with the results from previous study of $MgSiO_3$ glasses at high pressures [8] in Fig. 5-A6.

Table 5-A2. Populations of Si species in the $MgSiO_3$ melts at high pressures. The upper and lower bond length tolerance factors were set to 1.2 and 0.6, respectively.

Si coordination	$1.6V_0$ ~0 GPa	$1.4V_0$ ~7 GPa	$1.2V_0$ ~18 GPa	$1.0V_0$ ~51 GPa	$0.8V_0$ ~131 GPa
$^{[3]}$Si	1	1	0	0	0
$^{[4]}$Si	31	26	16	6	0
$^{[5]}$Si	0	4	12	13	10
$^{[6]}$Si	0	1	4	13	20
$^{[7]}$Si	0	0	0	0	2
Total Si	32	32	32	32	32
Avg. coordination	3.97	4.16	4.63	5.22	5.75

Table 5-A3. Populations of Si species in the $MgSiO_3$ melts at high pressures (Fig. 5-1). The upper bond length tolerance factor varies from 0.96 to 1.1, while the lower tolerance factor was fixed to 0.6.

Si coordination	$1.6V_0$ ~0 GPa	$1.4V_0$ ~7 GPa	$1.2V_0$ ~18 GPa	$1.0V_0$ ~51 GPa	$0.8V_0$ ~131 GPa
$^{[3]}$Si	2	2	1	0	0
$^{[4]}$Si	28	26	19	13	10
$^{[5]}$Si	2	4	11	13	16
$^{[6]}$Si	0	0	1	6	6
Total Si	32	32	32	32	32
Avg. coordination	4.00	4.06	4.38	4.78	4.88

Table 5-A4. Populations of O species in the $MgSiO_3$ melts at high pressures. The upper and lower bond length tolerance factors were set to 1.2 and 0.6, respectively.

O coordination	$1.6V_0$ ~0 GPa	$1.4V_0$ ~7 GPa	$1.2V_0$ ~18 GPa	$1.0V_0$ ~51 GPa	$0.8V_0$ ~131 GPa
$^{[0]}$O	3	2	1	0	0
$^{[1]}$O	59	57	46	32	24
$^{[2]}$O	34	35	47	57	57
$^{[3]}$O	0	2	2	7	14
$^{[4]}$O	0	0	0	0	1
Total O	96	96	96	96	96

Table 5-A5. Populations of Si species in the $MgSiO_3$ melts at high pressures (Fig. 5-1). The upper bond length tolerance factor varies from 0.96 to 1.1, while the lower tolerance factor was fixed to 0.6.

O coordination	$1.6V_0$ ~0 GPa	$1.4V_0$ ~7 GPa	$1.2V_0$ ~18 GPa	$1.0V_0$ ~51 GPa	$0.8V_0$ ~131 GPa
$^{[0]}O$	3	3	2	1	2
$^{[1]}O$	60	60	49	40	40
$^{[2]}O$	33	31	44	52	46
$^{[3]}O$	0	2	1	3	8
Total O	96	96	96	96	96
Avg. coordination	1.31	1.33	1.46	1.59	1.63

Mean square displacements of atoms in the $MgSiO_3$ melts at high pressures

Figure 5-A2 presents the mean square displacements (MSD) of the $MgSiO_3$ melts at high pressures. The SiO_2 and $MgSiO_3$ melt configurations, presented in Fig. 5-A2, have been simulated sufficiently long time over 3-4 ps, i.e. 3000 to 4000 MD steps, to obtain the equilibrated states. The calculated MSDs for the SiO_2 and $MgSiO_3$ melts can be specified into three regimes with their slopes: the ballistic ($\sim t^2$, non-physical phenomena), truncated ($\sim t^{0.4}$, truncated by surrounding atoms), and diffusion ($\sim t$, physical and, thus, equilibrated phenomena) regimes. The SiO_2 and $MgSiO_3$ melt configurations, which were clearly in the diffusion regime (i.e., in the last 1.0 ps of the AIMD simulations), should be used to obtain the reliable structural and transport properties, such as the radial distribution functions (RDF) and the velocity auto-correlation functions (VACF). The MSDs of the $MgSiO_3$ melts in a lower-pressure region, with the higher degree of freedom and thus faster dynamics of atoms in the unit cells, converge to the diffusion regime easier than those in a higher-pressure region. This result

implies a decrease in the diffusivity and, thus, an increase in the viscosity of the $MgSiO_3$ melts with increasing pressure. The pressure dependence of the MSDs of the Mg_2SiO_4 melts, which presented a significant decrease in the self-diffusion coefficient upon compression, has been reported in a previous theoretical study [77].

The melting and glass transition temperatures of the $MgSiO_3$ enstatite are ~1830 and ~1039 K [218], and those of the SiO_2 *a*-quartz are ~1986 and ~1475 K [228,229], respectively. The SiO_2 and $MgSiO_3$ melt configurations at ~0 GPa with different temperatures, i.e. 2000 and 3000 K, thus have been simulated to confirm the temperature-induced topological disorder and the differences in the O *K*-edge excitation features. The $MgSiO_3$ melt configuration at ~0 GPa and 2000 K was obtained by annealing the $MgSiO_3$ melt configuration, which was simulated at ~0 GPa and 3000 K, at 2000 K for 4 ps. See the manuscript for details about the AIMD simulations for the $MgSiO_3$ melts. The SiO_2 melt configuration at ~0 GPa and at different temperatures (2000 and 3000 K) were simulated from the modified SiO_2 *a*-quartz. The crystal structure of the initial configuration is modified from the trigonal (a = b and, $\alpha = \beta = 90°$ and $\gamma = 120°$) to the orthorhombic ($\alpha = \beta = \gamma = 90°$) system with P1 symmetry, i.e. the 2×2×1 supercell. The initial configuration of SiO_2 melts thus consists of 24 Si and 48 O atoms in the unit cell. The densities of the calculated SiO_2 melt configurations at ~0 GPa were set to ~2.1922 g/cm^3 to mimic the density of amorphous SiO_2 at ambient condition (~2.20 g/cm^3) [228]. The initial configuration was melted at 6000 K for 4 ps to remove its crystallinity, and then it was annealed at 3000 and 2000 K for 4 ps to obtain the SiO_2 melt configurations with different temperatures. I note that, though the number

of atoms in the SiO_2 melt configurations seems not to be appropriate to simulate the precise and reliable melt configurations, the result of this rough calculation is sufficient to confirm the difference between the Si-O bond length distributions in the SiO_2 and $MgSiO_3$ melt configurations due to the presence of the network modifying cation, i.e. the Mg atoms.

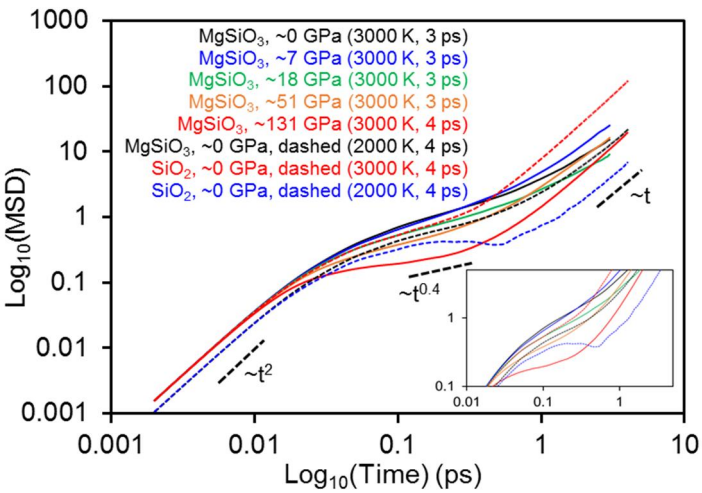

Figure 5-A2. Mean square displacement (MSD) of atoms in SiO_2 and $MgSiO_3$ melts with respect to the simulation time lengths in log scales. Short and thick black dashed lines refer to the slope of MSD corresponding to the ballistic ($\sim t^2$), truncated ($\sim t^{0.4}$), and diffusion ($\sim t$) regimes as labelled.

Partial radial distribution functions of SiO_2 and $MgSiO_3$ melts at ~0 GPa

Figure 5-A3 presents the total and partial radial distribution functions (RDF) of the SiO_2 and $MgSiO_3$ melt configurations at ~0 GPa and different temperatures (2000 and 3000 K), implying the topological disorder

due to the presence of the network modifying cation, i.e. the Mg atoms, and the temperature-induced topological disorder in the noncrystalline network structures. The partial RDFs of the $MgSiO_3$ melts, particularly the Si-O and O-O pairs, present broader features than those of the SiO_2 melts at the same temperature implying the higher topological disorder around O atoms in the highly depolymerized $MgSiO_3$ melts. This result can provide the further insights into the atomistic accounts of the differences in the O *K*-edge XRS features of the SiO_2 and $MgSiO_3$ glasses at the ambient condition presented in the Fig. 5-5(b) in the manuscript. In addition, the RDFs of the SiO_2 and $MgSiO_3$ melts at ~0 GPa and 3000 K present broad peak widths than those at the lower temperature (2000 K) due to the presence of the high-energy, and thus highly disordered, molecular clusters stable at the relatively higher temperatures. This result can explain the differences in the O *K*-edge excitation features of the $MgSiO_3$ glass and melts at the similar pressure condition presented in Fig 5-5(b) in the manuscript.

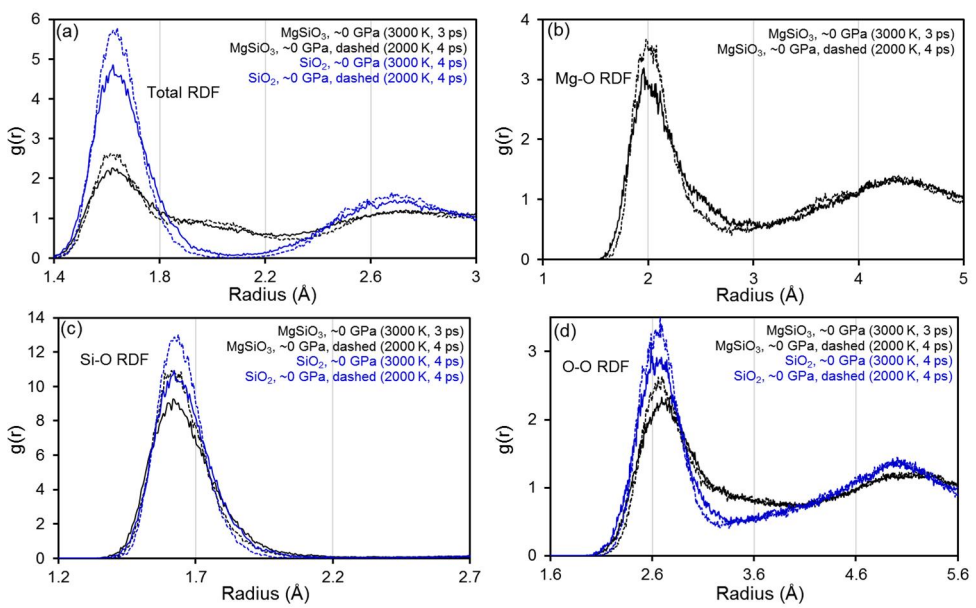

Figure 5-A3. Total (a) and partial radial distribution functions of Mg-O (a), Si-O (c), and O-O (d) pairs in SiO_2 and $MgSiO_3$ melts at ~0 GPa and different temperatures (at 2000 and 3000 K).

Velocity auto-correlation functions of the $MgSiO_3$ melts at high pressures

Figure 5-A4 presents the velocity auto-correlation functions (VSCF) of the SiO_2 and $MgSiO_3$ melts at high pressures. The VACFs presented here each were calculated using the SiO_2 and $MgSiO_3$ melt configurations in the last 1 ps of the AIMD simulations, i.e. 1000 MD steps, which are clearly in the diffusion regime. The calculated VACFs for the $MgSiO_3$ melts, particularly at 3000 K, more rapidly decay in a higher-pressure region implying the decrease in the diffusivity of the $MgSiO_3$ melts with increasing pressure. The pressure-induced decrease in the diffusivity of the noncrystalline Mg-silicates has been reported in the previous theoretical studies [77,209]. The pressure dependence of the diffusivity of the $MgSiO_3$ melts presented here seems to be correlated with the increase in the extent of polymerization associated with the formation of highly coordinated Si and O atoms, as well as the O triclusters ($^{[3]}O$), as revealed in Fig. 5-1 and 5-3(c) in the manuscript. This result is consistent with the changes in the transport properties of the noncrystalline oxides associated with the presence of O triclusters under high pressures that have been addressed in the recent review of the previous studies [65]. The VACFs of the SiO_2 melts present more rapid decays than those of the $MgSiO_3$ melts at the similar pressure conditions implying the higher viscosity in the fully polymerized

SiO_2 melts, compared to the highly depolymerized $MgSiO_3$ melts. The effects of temperature on the diffusivity of the SiO_2 and $MgSiO_3$ melts can be confirmed from the VACFs of the SiO_2 and $MgSiO_3$ melts at ~0 GPa and different temperatures (2000 and 3000 K). The VACFs of the SiO_2 and $MgSiO_3$ melts at ~0 GPa and 2000 K present more rapid decays than those of the SiO_2 and $MgSiO_3$ melts at ~0 GPa and the higher temperature implying the higher diffusivity in the SiO2 and MgSiO3 melts at the higher temperatures.

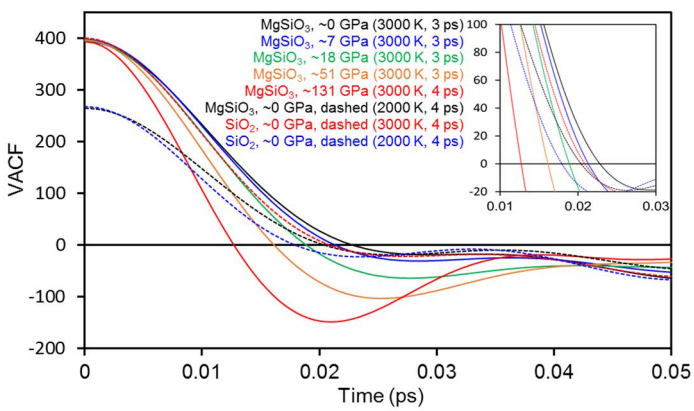

Figure 5-A4. The velocity auto-correlation functions (VACF) of the SiO_2 and $MgSiO_3$ melt configurations. The VACFs presented here each were calculated from the last 1 ps of the *ab initio* molecular dynamic simulations (i.e., the last 1000 configurations) for the SiO_2 and $MgSiO_3$ melts which were clearly in the diffusion regime (Fig. 5-A2).

Band gap correction for the density of states of the $MgSiO_3$ melts

The band gap energies, calculated using the conventional LDA and GGA methods, are usually underestimated because of the approximated non-

local exchange-correlation functionals used to describe the electronic structures [230]. The underestimated band gap energies (E_G) can be corrected (E_G*) with a shift of the conduction band to a higher-energy region with respect to the valence band, i.e. the scissors operation, with the arbitrary determined empirical correction term (Δ): $E_G^* = E_G + \Delta$ (usually, $\Delta > 0.0$ eV) [230]. This band gap correction should be applied to the result of this study to obtain the reliable band gap energies and optical properties of the $MgSiO_3$ melts [230]. The band gap correction has not been applied to the calculated density of states (DOS) for the $MgSiO_3$ melts presented in Fig. 5-4, because the objective of that calculation is just to confirm the changes in the electronic structures of the $MgSiO_3$ melts under high pressures. The DOSs of the $MgSiO_3$ melts and, thus, the band gap energies in Fig. 5-4(f) have been calculated using the FP-LAPW+lo method, i.e. WIEN2k [74]. The rigid shift of the conduction band is, however, not implemented in WIEN2k. I thus try to apply the band gap correction to the DOSs of the $MgSiO_3$ melts calculated with the PAW-type pseudopotential method implemented in CASTEP to reveal the pressure-induced changes in the band gap energies of the $MgSiO_3$ melts with a clear band gap separation. Figure 5-A5 presents the calculated DOSs for the $MgSiO_3$ melts at high pressures with applying the band gap correction. The empirical correction term (Δ) was set to 9.0 eV; this value was determined from the band gap energy of the SiO_2 glass at the ambient condition reported in the previous study [231]. The band gap separation in Fig. 5-A5 presents an identical pressure dependence with the results presented in Fig. 5-4(f) in the manuscript.

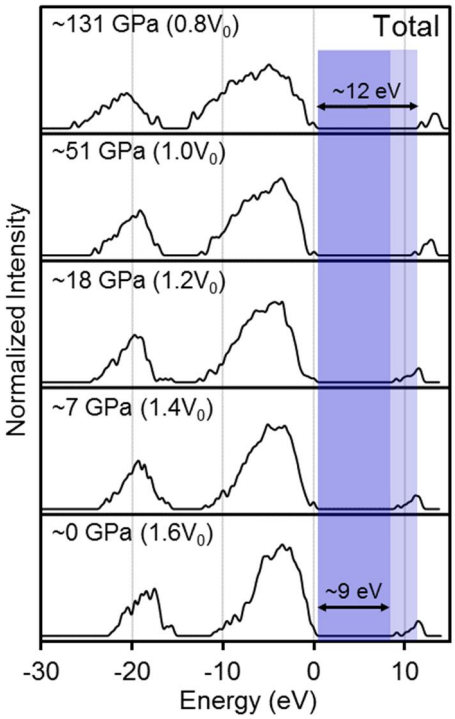

Figure 5-A5. Calculated total density of states for the $MgSiO_3$ melts at high pressures. The empirical correction term (Δ) of 9.0 eV was applied (see text for the details).

Calculated O *K*-edge XRS spectra of the crystalline $MgSiO_3$ phases

Figure 5-A6 presents the calculated O *K*-edge XRS spectra of the crystalline $MgSiO_3$ phases [enstatite (1 atm), ilmenite-type $MgSiO_3$ (22 GPa), bridgmanite (25, 79 and 120 GPa)] referred from our previous study [3,7], also presented in Fig. 5-5(a). Details about the atomistic accounts of the characteristic O *K*-edge XRS features of the crystalline $MgSiO_3$ phases have been reported in our previous studies [3,7]. They present characteristic O *K*-edge excitation features due to the distinctive local atomic configurations around O atoms in the each crystalline $MgSiO_3$ phases. These O *K*-edge XRS features each were obtained by taking into consideration of the contributions of the site-resolved excitation features of the crystallographically inequivalent O atoms [O1:O2 = 1:2 for the bridgmanite structures and O1:O2:O3 = 1:1:1 for the enstatite]. These calculated O *K*-edge XRS features for the crystalline $MgSiO_3$ phases are arbitrary shifted by 528.25 eV to compare with the experiments. The O *K*-edge XRS features of the enstatite around 533-542 eV stem from the nonbridging apical O atoms (O1, Mg-O1-$^{[4]}$Si, average $^{[4]}$Si-O1 bond length: 1.6159 Å, average Mg-O1 bond length: 2.1371 Å), the nonbridging basal O atoms (O2, Mg-O2-$^{[4]}$Si, average $^{[4]}$Si-O2: 1.5869 Å, average Mg-O2: 1.9640 Å), and the corner-sharing bridging O atoms (O3, $^{[4]}$Si-O3-$^{[4]}$Si, average $^{[4]}$Si-O3: 1.6663 Å, average $^{[4]}$Si-O3-$^{[4]}$Si angle: 131.15°). The characteristic double-peak-like excitation features in the O *K*-edge XRS spectrum of the ilmenite-type $MgSiO_3$ (at ~535.4 and ~540.2 eV) are induced from the edge-sharing O atoms linking two SiO_6 octahedra (average $^{[6]}$Si-O bond length: 1.7989 Å, $^{[6]}$Si-O-$^{[6]}$Si bond angle: 99.23°, O-O bond length: 2.3316 Å, average Mg-O distance: 2.0765 Å). The O *K*-edge XRS spectrum of the bridgmanite at 25

GPa are induced from the site-specific excitation features of the apical corner-sharing O atoms (O1, $^{[6]}$Si-O1: 1.7725 Å, $^{[6]}$Si-O1-$^{[6]}$Si angle: 146.1407°, average Mg-O1: 2.0382 Å) and the planar corner-sharing O atoms (O2, average $^{[6]}$Si-O2: 1.7681 Å, $^{[6]}$Si-O2-$^{[6]}$Si angle: 146.3562°, average O2-O2 distance: 2.5005 Å, average Mg-O2: 2.2098 Å) linking SiO_6 octahedra. The O *K*-edge XRS features of the bridgmanite significantly change with increasing pressure, in a pressure range from 25 to 120 GPa, due to the topological changes around O atoms in the short- to medium-range order: the corner-sharing O atoms (O1, $^{[6]}$Si-O1: from 1.7725 to 1.6500 Å, $^{[6]}$Si-O1-$^{[6]}$Si angle: from 146.1407° to 143.2781°, average Mg-O1: from 2.0382 to 1.8484 Å) and edge-sharing O atoms (O2, average $^{[6]}$Si-O2: from 1.7681 to 1.6508 Å, $^{[6]}$Si-O2-$^{[6]}$Si angle: from 146.3562° to 142.7830°, average O2-O2 distance: from 2.5005 to 2.3345 Å, average Mg-O2: from 2.2098 to 2.0253 Å) linking SiO_6 octahedra.

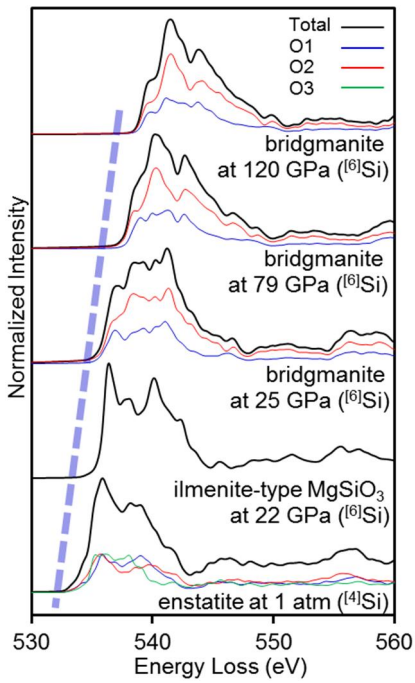

Figure 5-A6. The total and site-resolved (O1, O2, and O3) O *K*-edge XRS spectra of the crystalline $MgSiO_3$ phases [enstatite (1 atm), ilmenite-type $MgSiO_3$ (22 GPa), bridgmanite (25, 79, and 120 GPa)] referred from our previous studies [3,7].

Pressure dependence of Si-O coordination

Figure 5-A7 presents the pressure dependences of average atomic coordination numbers of Si atoms. The average Si coordination numbers calculated with different bond length tolerance factors (see Tab. A2 and Tab. A3) are compared with the results of MgSiO3 glasses referred from the previous study [8]. The results calculated in this study are relatively in good agreement with the results of $MgSiO_3$ glasses with the longer bond length tolerance factors.

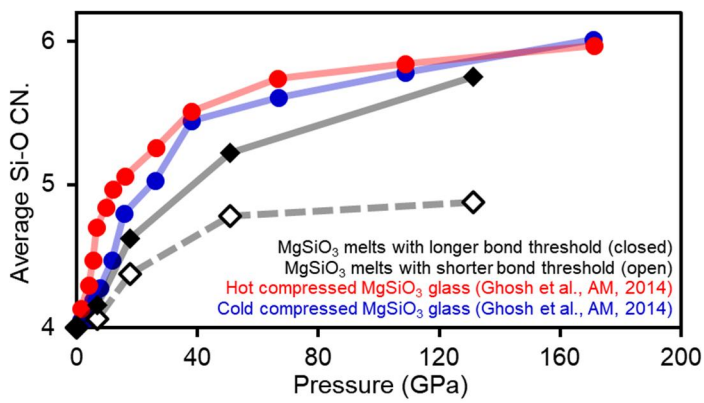

Figure 5-A7. Pressure dependences of average Si coordination numbers. The results of $MgSiO_3$ glasses are referred from the previous study [8].

Chapter 6.

Pressure-induced changes in O *K*-edge x-ray Raman scattering features of SiO_2 high-pressure polymorphs: Implication for high-density SiO_2 melt and glass in the Earth's deep interior

Yoo Soo Yi, Hoon Khim, Yong Hyun Kim and Sung Keun Lee

It will be submitted to *Geophysical Research Letter*

This study was conducted in collaboration with Hoon Khim and Yong Hyun Kim, and the results will be submitted to Geophysical Research Letters as soon as it is ready. All the manuscript was written by Yoo Soo Yi. Hoon Kim and Yong Hyun Kim contributed, in part, to the calculations of data and the drawing of figures.

Abstract

Probing the atomic and electronic structures of crystalline and noncrystalline SiO_2 phases at high pressures is essential to understand the Earth's interior, such as the atomistic accounts of the seismic heterogeneities. Here, we calculated the *l*-resolved partial density of states (PDOS) and O *K*-edge x-ray Raman scattering (XRS) features of the SiO_2 high-pressure polymorphs using the *ab initio* calculations to probe the atomistic accounts of pressure-induced changes in O *K*-edge XRS features of crystalline and amorphous SiO_2 phases, e.g. an emergence of double-peak-like excitation features at ~538 and 544 eV. The emergence of double-peak-like excitation features and changes in the absorption threshold energies of the calculated O *K*-edge XRS spectra for the SiO_2 high-pressure polymorphs have been revealed to be correlated with the enhanced proximity between neighboring O atoms, not the coordination transition of Si atoms. Therefore, the changes in O *K*-edge XRS features of SiO_2 glasses at high pressures with the emergence of double-peak-like excitation features might be correlated with the decrease in neighboring O-O distances. Thus, it cannot directly indicate the presence of highly coordinated Si atoms. In addition, the relationship between the absorption threshold energies in O *K*-edge XRS features and densities of the SiO_2 high-pressure polymorphs suggests that the densities of SiO_2 glasses at extremely high pressures could be estimated from the systematic *in situ* high-pressure XRS experiments of SiO_2 glasses. We further expect that the current study can be applied to interpret and predict the evolution in core-level excitation features of a

wide range of crystalline and noncrystalline Earth materials at high pressures.

Introduction

The potential presence of free silica (SiO_2) in the Earth's deep inside, e.g. the SiO_2 high-pressure polymorphs [23-25] and the SiO_2-rich silicate melts [28] which are differentiated from the subducted mid-ocean ridge basalt (MORB), has been suggested in the previous studies, whereas the Mg-silicates are known to be the most abundant materials in the Earth's mantle [21,22]. In the other previous study, it has been suggested that the free SiO_2 also can be generated from the chemical reaction between the bridgmanite and liquid iron ($Mg_{0.9}Fe_{0.1}SiO_3$ + 0.15Fe = 0.90$MgSiO_3$ + 0.20FeO + 0.05FeSi + 0.05SiO_2) near the core-mantle boundary (CMB) [26]. In addition, the possibility of crystallization of SiO_2 high-pressure polymorphs from the liquid Fe-Si-O ternary alloy under the Earth's uppermost-core condition (~133-145 GPa and ~4000 K) has been suggested in the recent previous study [27]. Thus, the atomic and electronic structures, and associated dynamic and elastic properties, of SiO_2 high-pressure polymorphs and high-density noncrystalline SiO_2 phases have been studied in diverse fields of geology, e.g. the mantle evolution [232], the seismic heterogeneities in the Earth's interior [11], and the prediction of super-Earth's internal structures [36,233].

The phase transitions of SiO_2 high-pressure polymorphs have been proposed to explain the seismic heterogeneities in the Earth's interior if the free SiO_2 presents in appreciable amounts. The phase transition from stishovite to $CaCl_2$-type structures at ~47-55 GPa has been suggested to be correlated with the seismic anisotropy and reflective features at ~1200-1500

km below the subduction zone [30,31,33,234,235], and the phase transition from $CaCl_2$-type to α-PbO_2-type structures at ~98-121 GPa has been expected to be associated with the seismic wave velocity anomalies at the D'' layer near ~2700 km [30,34,234,235]. The further phase transition from □-PbO_2-type to pyrite-type structures at ~226-268 GPa [30,35] has been used to predict and understand the atomic and electronic structures, and associated elastic properties, of SiO_2 high-pressure polymorphs in either the Earth's uppermost-core region or the super-Earth's interior [27,36].

On the other hand, the potential presence of high-density SiO_2-rich silicate melts has been proposed to be attributed in part to the 10-30% of seismic wave velocity reduction at the ultralow velocity zone (ULVZ) near the core-mantle boundary (CMB) at ~2870 km [28]. However, in contrast to the crystalline SiO_2 high-pressure polymorphs, the atomistic accounts of the changes in elastic properties of noncrystalline SiO_2 melts and glasses, as well as the SiO_2-rich silicate melts, have not been fully understood. Despite the difficulties of *in situ* high-pressure experiments, previous studies have explored the changes in elastic properties of noncrystalline SiO_2 and $MgSiO_3$ glasses under high pressures. Changes in the extent of network polymerization have been proposed to explain the anomalous elastic properties of SiO_2 melts and glasses in a pressure range from ~2 to ~8 GPa, i.e. violating the Birch's law [236]. In the other previous studies, the changes in Si-O coordination environments, i.e. a gradual transition from $^{[4]}Si$ to $^{[6]}Si$ (from ~0 to ~40 GPa) and a formation of $^{[6+]}Si$ atoms (above ~140 GPa), have been suggested to be correlated with changes in the pressure dependences (slopes) of the transverse acoustic wave velocities of SiO_2 and $MgSiO_3$ glasses at high pressures up to ~207 GPa [41,44]. Thanks to these

previous studies, we could improve our understanding about the atomistic accounts of the changes in the transverse acoustic wave velocities of SiO_2 and $MgSiO_3$ glasses under high pressures. However, in those studies, the results of previous studies, i.e. the coordination transition of Si atoms in high-density noncrystalline SiO_2 (pressure up to ~150 GPa) [45] and $MgSiO_3$ (pressure up to ~136 GPa) [46] phases at high pressures, have been adopted without further discussion about the correlation between the structural changes in the short-range order and the changes in transverse acoustic wave velocities.

In the recent theoretical study using the *ab initio* calculations, changes in the slope of acoustic wave velocity of SiO_2 glass also have been explained with the changes in Si coordination environments [67]. However, the correlation between the changes in atomic and electronic structures and the changes in elastic properties of amorphous SiO_2 glasses has not been discussed in detail. It has been well known that the elastic properties of highly disordered oxide melts and glasses, i.e. the phonon density of states (the extended and localized vibrational excitation features), are determined from the short-range atomic structures and associated electronic structures [47,48]. Therefore, probing the correlation between the changes in atomic and electronic structures of noncrystalline SiO_2 glass upon compression could provide further insights into the atomistic accounts of the pressure-induced changes in elastic properties of noncrystalline SiO_2 phases, as well as SiO_2-rich silicate melts in the Earth's interior. However, probing the correlation between the densification processes of highly disordered SiO_2 melts and glasses and associated changes in the electronic structures under high pressures has been experimentally challenging because of the inherent

structural disorder and the lack of suitable experimental techniques. Thus, the appropriate experimental and theoretical probes should be applied.

The *in situ* high-pressure x-ray Raman scattering (XRS) experiment can provide the element-specific electronic bonding structures of the Earth materials at high pressures, along with their short- to medium-range structures around the target element [64,65]. Thus, the O *K*-edge XRS spectra of the crystalline and noncrystalline oxides at high pressures, which mostly stem from the electronic transition from the occupied O 1*s* state to the unoccupied O 2*p* state (1*s*-2*p** transition), have been used to explore the pressure-induced bonding transitions and associated changes in the local atomic structures around O atoms, e.g. the SiO_2 polymorphs [68], SiO_2 glasses [67,237], GeO_2 polymorphs [174], borate glasses [122,175,238,239], $MgSiO_3$ glasses [1,55], and multi-component silicate glasses [176,240]. Details about probing the atomistic accounts of the O *K*-edge XRS features of diverse oxides at high pressures up to ~70 GPa have been summarized in the reviews [65,66]. Thus, the results of SiO_2 glasses at high pressures will be discussed here.

An emergence of characteristic double-peak-like O *K*-edge XRS features at ~538 and ~544 eV, which are similar to those of stishovite, has been reported in the previous study of the SiO_2 glass at high pressure [237]. The stishovite-like structural transition with the presence of 6-coordinated Si atoms ($^{[6]}Si$) [237] and the formation of highly coordinated Si atoms ($^{[5]}Si$ and $^{[6]}Si$) [67] have been suggested to be correlated with the emergence of the double-peak-like O *K*-edge XRS features of the SiO_2 glasses at high pressures above ~22 GPa, whereas it was known to be induced from the *p*-*p* hybridization between the neighboring O atoms [237]. On the other hand,

changes in the Si-O-Si bond angle and Si-O bond length elongation, regardless of the further coordination transition of Si atoms, have been proposed to explain the changes in Si $L_{2,3}$-edge XRS features of SiO_2 glass with increasing pressure up to ~74 GPa [73] and differences in O *K*-edge XRS features of diverse SiO_2 high-pressure polymorphs [68]. Despite the efforts in those previous studies, the atomistic accounts of pressure-induced changes in O *K*-edge XRS features of the SiO_2 glass, along with the emergence of double-peak-like excitation features, have been still controversial. We have noted that those studies have focused on the Si coordination environments whereas the O *K*-edge XRS features are determined from the short-range atomic structures around O atoms. In contrast, in the recent theoretical studies of SiO_2 and $MgSiO_3$ polymorphs, the enhanced proximity between the neighboring O atoms under high pressures has been suggested to be correlated with their pressure-induced changes in O *K*-edge XRS features [3,7], as well as those of $MgSiO_3$ glasses at high pressures [1]. The results of those studies suggest that the electronic structures of crystalline and noncrystalline SiO_2 and $MgSiO_3$ phases, particularly their O *K*-edge XRS features, should be explained with the short-range structures around O atoms rather than the Si coordination environments. Therefore, the atomistic accounts of pressure-induced changes in O *K*-edge XRS features of crystalline and noncrystalline SiO_2 phases, with the emergence of double-peak-like excitation features like those of the stishovite, should be discussed more systematically.

The aim of this study is establishing the correlation between the short-range structural changes around O atoms and the evolution in O *K*-edge XRS features of the crystalline and noncrystalline SiO_2 phases under

high pressures. To achieve this purpose, the *l*-resolved partial density of states (PDOS) and the O *K*-edge XRS features of the diverse SiO_2 high-pressure polymorphs were calculated systematically using the *ab initio* calculations. The atomistic accounts of the emergence of double-peak-like O *K*-edge XRS features of the SiO_2 glass at high pressure would be discussed with the systematically calculated O *K*-edge XRS features for the SiO_2 high-pressure polymorphs. The results of this study could improve our understanding about the structural information that could affect to the electronic structures of the crystalline and noncrystalline SiO_2 phases under high pressures more precisely, as well as their elastic properties. In addition, we expect that the current study can be applied to probe the atomistic accounts of electronic bonding transition of diverse crystalline and noncrystalline Earth materials under high pressures.

Calculations

Crystal structures of the SiO_2 high-pressure polymorphs

The electronic structures and O *K*-edge XRS features of the diverse SiO_2 high-pressure polymorphs were calculated using the *ab initio* calculations based on the full-potential linearized augmented plane wave with local orbitals (FP-LAPW+lo) method [74]. The SiO_2 high-pressure polymorphs were referred from the previous experimental and theoretical studies: α-quartz ($^{[4]}$Si; ~1 atm) [158], β-quartz ($^{[4]}$Si; ~1 atm) [241], α-cristobalite ($^{[4]}$Si; ~1 atm) [242], coesite ($^{[4]}$Si; ~3.8 GPa) [243], hp-cristobalite ($^{[4]}$Si; ~20 GPa) [244], penta-SiO_2 ($^{[5]}$Si; ~16 GPa) [245], stishovite ($^{[6]}$Si; ~9.3

and ~29.1 GPa) [246], $CaCl_2$-type ($^{[6]}$Si; ~63 GPa) [29], α-PbO_2-type ($^{[6]}$Si; ~120 GPa) [32], and pyrite-type ($^{[6]}$Si; ~271 GPa) structures [35]. Table 6-1 presents the structural information of these SiO_2 high-pressure polymorphs, such as the Si coordination environments, lattice parameters, average Si-O bond lengths, average O-O distances, and average Si-O-Si bond angles. The crystal structures of SiO_2 high-pressure polymorphs are presented in Figure 1, and they were visualized using VESTA [247]. The calculations of electronic structures and O *K*-edge XRS features were performed without the further structural optimization. The coesite structure has symmetrically inequivalent Si (Si1 and Si2, Si1:Si2 = 1:1) and O (O1~O5, O1:O2:O3:O4:O5 = 1:1:2:2:2) atoms at the distinct atomic sites in the unit cell. The O atoms in the coesite exhibit corner-sharing topologies connecting either symmetrically identical Si atoms ($^{[4]}$Si#-O#-$^{[4]}$Si#, # = 1,2) or symmetrically inequivalent Si atoms ($^{[4]}$Si1-O#-$^{[4]}$Si2, #=3,4,5). The penta-SiO_2 structure also has symmetrically inequivalent O atoms (O1 and O2, O1:O2 = 1:1). They exhibit both edge- ($^{[5]}$Si-O1-2$^{[5]}$Si) and corner-sharing ($^{[5]}$Si-O2-$^{[5]}$Si) topologies connecting SiO_5 polyhedra, and the edge-sharing O atom (O1) is triply coordinated by the surrounded Si atoms, i.e. the oxygen tricluster ($^{[3]}$O1). Thus, we attempt to calculate the site-specific electronic structures and O *K*-edge XRS features for the O atoms at the symmetrically inequivalent sites. Details of how to calculate the electronic structures and O *K*-edge XRS features of the SiO_2 high-pressure polymorphs are summarized in the following section.

Calculating density of states and O *K*-edge XRS spectra

The Perdew-Berke-Ernzerhof scheme for solids (PBEsol), based on the generalized gradient approximation (GGA) method, was used as the exchange-correlation functional to describe the on-site electron-electron interactions [248]. The Muffin-Tin radii (R_{MT}) of Si and O atoms each were set to 1.34-1.64 Å and 1.45-1.64 Å, respectively. The cutoff energy (E_{CUT}) for the core-valence states separation was set to -7.2~-6.0 Ry (1 Ry = 13.6 eV) to reduce the core-electron leakage as possible that can increase the self-consistent field (SCF) calculation time as the semi-core states. The RK_{MAX} value, which indicates the scalar product of the minimum value of R_{MT} and the largest plane wave cutoff vector of K_{MAX}, was set to 7.0. The G_{MAX} value, which is the magnitude of the largest vector in the Fourier expansion of the charge density, was set to 14.0. The numbers of *k* points in the irreducible Brillouin zone for the SCF calculations were set to 24-48, while the single Γ point calculation was reported to be sufficient for simple insulators such as silica [68,174,249]. The SCF convergence criteria were set to 10^{-4} Ry for the total energy and 10^{-4} e for the charge distance. The detailed descriptions of these parameters have been summarized in our previous studies [3,7], and other references [249,250].

The electrons in the O 1*s* state can be excited into the corresponding unoccupied states due to the inelastically scattered incident x-ray photons, i.e. the x-ray Raman scattering (XRS) process [64]. This partially empty core state affects to the local electronic structures around the target element, i.e. the so-called core-hole effects. The core-hole effects are particularly significant in the low-*z* elements, and, thus, it should be considered to calculate the precise XRS features of the low-*z* oxides [249].

Thus, the O *K*-edge XRS features of the SiO_2 high-pressure polymorphs should be calculated with applying the core-hole effects on the O 1*s* state. The extended supercell structures should be used to reduce the unexpected electronic interactions from the periodically repeated O atoms which contain the 1*s* core hole. The sizes of the supercell structures used for calculations are summarized in Tab. 6-1. Also, see our recent previous studies for the practical aspects of applying the core-hole effects on the target O atom [3,7]. The XRS features in the low-q limit (i.e., the small momentum transfer vector) are comparable with the core-level excitation features obtained from the x-ray absorption spectroscopy (XAS) and electron energy-loss spectroscopy (EELS) [64]. Thus, though we have calculated the O *K*-edge energy-loss near-edge structure (ELNES) features of the SiO_2 high-pressure polymorphs using WIEN2k [249], the calculated ELNES features are called as the XRS features to emphasize that they are compared with the results of *in situ* high-pressure XRS experiments.

The *l*-resolved PDOSs of O atoms in the SiO_2 high-pressure polymorphs, which were calculated with applying the core-hole effects on the target O atom, were presented in an energy range from 0 to 30 eV (in the unoccupied states) with the full-width at half-maximum (FWHM) Gaussian broadening parameter of 0.02 Ry. The unoccupied O *p* state features have been used to interpret and predict the O *K*-edge XRS features [68,73], because most of the characteristic O *K*-edge XRS features stem from the electronic transition from the occupied 1*s* state to the unoccupied 2*p* state of the O atoms (i.e., the O 1*s*-2*p** transition). The calculated *l*-resolved PDOSs for Si and O atoms, without applying the core-hole effects, were presented in the appendix (Fig. 6-A1). The O *K*-edge XRS features of the

SiO_2 high-pressure polymorphs were calculated from the transition matrix determined from the relativistic double differential scattering cross section (DDSCS), including all the possible electronic transitions, i.e. the monopole-, dipole, quadrupole-, and octopole-allowed transitions [74,249]. The calculated O *K*-edge XRS features for the SiO_2 high-pressure polymorphs were presented up to 30 eV above the Fermi level (E_F), i.e. the highest occupied energy state of O atom, with the FWHM Gaussian-broadening parameter of 0.5 eV. The calculated O *K*-edge XRS features were shifted by 530 eV to make it comparable with the results of *in situ* high-pressure XRS experiments. The O PDOSs and O *K*-edge XRS features of the coesite and penta-SiO_2 structures presented here were obtained by taking into consideration the contributions from the symmetrically inequivalent O atoms. The site-resolved O PDOSs and O *K*-edge XRS features of the coesite and penta-SiO_2 structures were presented in the appendix (Fig. 6-A2).

Results and Discussion

Structural characteristics of the SiO_2 high-pressure polymorphs

Figure 6-2 presents the pressure (P) dependences of the average Si-O bond lengths ($d_{Si\text{-}O}$) and O-O distances ($d_{O\text{-}O}$) [Fig. 6-2(a) and Fig. 6-2(b)] and the correlations between the densities (ρ) and the $d_{Si\text{-}O}$ and $d_{O\text{-}O}$ [Fig. 6-2(c) and Fig. 6-2(d)] of the SiO_2 high-pressure polymorphs. In Fig. 6-2(a), the $d_{Si\text{-}O}$ of the SiO_2 polymorphs consisting of either the corner-sharing O atoms connecting two SiO_4 tetrahedra ($^{[4]}$Si-O-$^{[4]}$Si) or the edge-sharing O atoms connecting two SiO_6 octahedra ($^{[6]}$Si-O-2$^{[6]}$Si) each gradually decrease with increasing pressure. However, within all the SiO_2 high-pressure

polymorphs, the $d_{Si\text{-}O}$ does not present a clear correlation with respect to the pressure [$d_{Si\text{-}O}$ (Å) = -0.0001P (GPa) + 1.6489 (R^2 = 0.0085)]. In contrast, the $d_{O\text{-}O}$ of the SiO_2 high-pressure polymorphs presents a strong correlation with the pressure regardless of either the Si coordination environments or the local oxygen topologies (i.e., the corner- and edge-sharing O atoms) [$d_{O\text{-}O}$ (Å) = -0.0013P (GPa) + 2.5596 (R^2 = 0.7457)].

In Fig. 6-2(c), the densities (ρ) of the SiO_2 high-pressure polymorphs do not present a strong correlation with the $d_{Si\text{-}O}$ [ρ (g/cm^3) = 7.35$d_{Si\text{-}O}$ (Å) – 8.09 (R^2 = 0.13)]. However, they seem to be positively correlated with the Si coordination numbers because the $d_{Si\text{-}O}$ increases with the structural transition to the higher-pressure SiO_2 polymorphs consisting of the highly coordinated Si atoms ($^{[5]}$Si and $^{[6]}$Si). On the other hand, within the SiO_2 polymorphs consisting of the same Si coordination numbers, the ρ presents a negative correlation with the $d_{Si\text{-}O}$ because of the decrease in the Si-O covalent bonds under high pressures. In Fig. 6-2(d), the ρ of the SiO_2 high-pressure polymorphs exhibits a strong negative correlation with the $d_{O\text{-}O}$ regardless of the Si coordination environments [ρ (g/cm^3) = -10.66$d_{O\text{-}O}$ (Å) – 30.61 (R^2 = 0.95)]. This strong *linear* relationship between the ρ and $d_{O\text{-}O}$ suggests that the average O-O distance can be used to describe the densification of the SiO_2 polymorphs than other structural parameters. The ρ of the SiO_2 high-pressure polymorphs with respect to the pressure are presented in Fig. 6-A3 [ρ (g/cm^3) = 0.01P (GPa) + 3.32 (R^2 = 0.72)]. The results presented here suggest that if the detailed densification process can be revealed from the pressure-induced changes in O *K*-edge XRS features the densities of crystalline and noncrystalline SiO_2 phases may be estimated from the *in situ* high-pressure XRS experiments.

Calculated *l*-resolved O PDOSs for the SiO_2 high-pressure polymorphs

Figure 6-3 presents the calculated *l*-resolved O PDOSs, i.e. the *s*, *p*, and *d* states of O atom, in the unoccupied states above the Fermi level (E_F) and the calculated O *K*-edge XRS spectra for the SiO_2 high-pressure polymorphs. The presented *l*-resolved O PDOSs present characteristic features stemming from the distinctive local atomic structures around O atoms of the SiO_2 high-pressure polymorphs. The presented O PDOSs, particularly the unoccupied O *p* states of the SiO_2 high-pressure polymorphs consisting of the 6-coordinated Si atoms (i.e., stishovite, $CaCl_2$-type, and α-PbO_2-type structures) present considerable broadening (delocalization) with the structural transition to the higher-pressure polymorphs upon compression, but it is not clearly demonstrated in the unoccupied O *s* and *d* states. The atomistic accounts of the characteristic O PDOSs of the SiO_2 high-pressure polymorphs, particularly the unoccupied O *p* state, will be discussed in the interpretation of calculated O *K*-edge XRS features in Fig. 6-3(b). The occupied PDOSs calculated without applying the core-hole effects are presented in Fig. 6-A1.

Calculated O *K*-edge XRS spectra for the SiO_2 high-pressure polymorphs

The calculated O *K*-edge XRS spectra for the SiO_2 high-pressure polymorphs in Fig. 6-3(b) present similar features to the corresponding unoccupied O *p* state in Fig. 6-3(a) as expected, because most of the characteristic O *K*-edge XRS features stem from the electronic transition from the unoccupied O 1*s* state to the unoccupied O 2*p* state [64]. The calculated O *K*-edge XRS spectra for the α-quartz, β-quartz, coesite, and α-cristobalite structures, which exhibit similar local atomic structures [e.g.,

the Si coordination environment ([4]Si), the corner-sharing topology of O atoms ([4]Si-O-[4]Si), the Si-O bond lengths, and the O-O distances], present almost same excitation features at ~538.7 eV with a small feature at ~545 eV. The calculated O *K*-edge XRS spectrum for the hp-cristobalite presents distinct excitation features at ~538 and ~544 eV, whereas the hp-cristobalite structure exhibits a similar topology to those of the α-quartz, β-quartz, coesite, and α-cristobalite structures. This will be discussed with the results of the hp-cristobalite, penta-SiO_2, and stishovite structures. The characteristic O *K*-edge XRS features of the α-quartz stem from the hybridization between the Si 3*s* and O 2*p* states [237]. Thus, the similar O *K*-edge XRS features of the β-quartz, coesite, and α-cristobalite structures imply the significance of the Si-O covalent bonds in the electronic structures of these low-pressure SiO_2 polymorphs. The small differences in the O *K*-edge XRS of these SiO_2 polymorphs might be originated from the slight structural differences around O atoms in the short- to medium-range order.

The calculated O *K*-edge XRS spectra for the hp-cristobalite, penta-SiO_2, and stishovite structures present similar double-peak-like excitation features at ~538 and ~544 eV, despite the significant topological differences around O atoms. The Si coordination environments and average Si-O bond lengths of the hp-cristobalite ([4]Si with 1.554 Å), penta-SiO_2 ([5]Si with 1.703 Å), and stishovite ([6]Si with 1.760 Å) structures are significantly different, whereas their average O-O distances present rather similar values in a range from ~2.487 to ~2.561 Å as presented in Fig. 6-2(c), Fig. 6-2(d), and Tab. 6-1. The double-peak-like O *K*-edge XRS features of the stishovite structures, as well as the characteristic unoccupied O *p* state, are attributed

to the hybridization between the Si 3*s* and O 2*p* states (at ~538 eV) and the *p*-*p* hybridization between the neighboring O atoms (at ~538 and ~544 eV) [68,237]. Thus, the similar O *K*-edge XRS features of these SiO_2 polymorphs suggest that the emergence of double-peak-like excitation features of the SiO_2 polymorphs, as well as the SiO_2 glass at high pressure, might be indicative of the enhanced proximity between neighboring O atoms rather than the coordination transition of Si atoms. In addition, we confirmed the spatial distribution of Si-O and O-O pairs of the SiO_2 high-pressure polymorphs (Fig. 6-A4). The Si-O distribution does not present a strong correlation with the emergence of the double-peak-like O *K*-edge XRS features, but they seem to appear where the nearest neighboring O atoms are in a distance of less than ~2.5 Å ($d_{O\text{-}O} \leq$ ~2.5 Å).

The calculated O *K*-edge XRS spectra for the stishovite (~9.3 and ~29.1 GPa), $CaCl_2$-type (~63 GPa), and α-PbO_2-type (~120 GPa) structures, of which the O atoms exhibit the stishovite-like edge-sharing topology ($^{[6]}$Si-O-2$^{[6]}$Si), present considerable changes with the structural transition to the higher-pressure polymorphs upon compression. The double-peak-like O *K*-edge XRS features, in the result of the stishovite structures, gradually shift to a higher-energy region with delocalizations due to the enhanced short-range electronic interactions associated with the decreases in the Si-O covalent bond lengths and O-O distances. The calculated O *K*-edge XRS spectrum for the α-PbO_2-type structure presents such a broad single-peak-like excitation feature as the spectral change continues. The prevalent electronic delocalizations in the Si-O covalent bonds associated with the phase transition to the higher-pressure polymorphs are well demonstrated in the occupied *s*, *p*, and *d* states of Si and O atoms calculated without

applying the core-hole effects (Fig. 6-A1). We noted that the double-peak-like O *K*-edge XRS features of the ε-phase $(O_2)_4$ molecular solid, which stem from the *p*-*p* hybridization between neighboring O atoms (at ~532 and ~540 eV from the 1*s*-π_g* and 1*s*-1σ_u* transitions, respectively), shift to a higher-energy region with decreasing the O-O distances upon compression [251]. Thus, the decrease in interatomic distance between neighboring O atoms might be significant in the shift in O *K*-edge XRS features of these SiO_2 polymorphs.

The calculated O *K*-edge XRS spectrum for the pyrite-type structure at extremely high pressure above ~271 GPa presents delocalized but somewhat stishovite-like excitation features at a higher-energy region. However, the O atoms in the pyrite-type structure exhibit the corner-sharing topology connecting two SiO_6 octahedra ($^{[6]}$Si-O-$^{[6]}$Si) in contrast to those of stishovite-like polymorphs with the edge-sharing topology ($^{[6]}$Si-O-2$^{[6]}$Si). Thus, the previous *in situ* high-pressure x-ray diffraction (XRD) experiments of the highly-densified pyrite-type structure suggested the atypical Si coordination environments, i.e. the SiO_6 octahedra with two interpolyhedral Si-O bonds (the 6+2 cation coordination) [35]. The theoretical study of the highly-densified pyrite-type structure has reported the mixed ionic-covalent character of Si-O bonds and no considerable covalent character between the neighboring O atoms [252]. In addition, the occupied *s*, *p*, and *d* states of Si and O atoms of the pyrite-type structure, which were calculated without applying the core-hole effects [Fig. 6-A1(k)], exhibit substantially distinctive electronic structures compared with those of stishovite-like SiO_2 polymorphs. The outermost occupied PDOSs of Si and O atoms present a forbidden region similar to those of the lone pair

electrons of the α-quartz [Fig. 6-A1(a)]. These results imply that the characteristic O *K*-edge XRS features, as well as the unoccupied O *p* state, of the pyrite-type structure, stem from the atypical mixed ionic-covalent character of Si-O bonds in the highly-densified structures, and, thus, it does not indicate the presence of the significant covalent character between the neighboring O atoms as in those of the stishovite-like polymorphs.

The band gap and absorption threshold energies

Figure 6-4 presents the band gap (E_G) and absorption threshold (E_A) energies of the SiO_2 high-pressure polymorphs with respect to the Si-O bond lengths (d_{Si-O}) and O-O distances (d_{O-O}). Each band gap energy of the SiO_2 polymorph was obtained from the calculated PDOS without applying the core-hole effects (Fig. 6-A1), and each absorption threshold energy was determined from the energy value at which the O *K*-edge XRS features rapidly increases. Since most of the O *K*-edge XRS features stem from the electronic transition from the occupied O 1*s* state to the unoccupied O 2*p* state, the band gap and absorption threshold energies of the SiO_2 high-pressure polymorphs present a strong relationship in Fig. 6-A5 as expected [E_A (eV) = 0.65E_G (eV) + 532.49 (R^2 = 0.85)]. The band gap [Fig. 6-4(a)] and absorption threshold energies [Fig. 6-4(c)] of the SiO_2 high-pressure polymorphs do not present strong correlations with either the Si-O bond length [E_G (eV) = 3.95d_{Si-O} (Å) + 0.64 (R^2 = 0.02) and E_A (eV) = -0.43d_{Si-O} (Å) + 537.81 (R^2 = 0.00)] or the Si coordination numbers. In Fig. 6-4(b) and Fig. 6-4(d), the band gap and absorption threshold energies present clear *linear* relationships with the O-O distances [E_G (eV) = -12.87d_{O-O} (Å) + 39.25 (R^2 = 0.88) and E_A (eV) = -7.56d_{O-O} (Å) + 555.95 (R^2 = 0.61)]. In addition, the strong

correlations between the O-O distances and the absorption threshold energies in O *K*-edge XRS features of the SiO_2 and $MgSiO_3$ polymorphs, as well as their band gap energies, have been reported in the recent previous study [7]. These results suggest that the interatomic atomic distance between neighboring O atoms can be a useful structural indicator to explain the evolution in electronic structures and O *K*-edge XRS features of the SiO_2 polymorphs associated with the structural transitions upon compression.

Implications for the densified SiO_2 glasses

The emergence of double-peak-like O *K*-edge XRS features of SiO_2 glass at high pressure have been reported in the previous studies, and it has been explained by focusing on the short-range topologies around Si atoms, either the stishovite-like structural transition with the presence of $^{[6]}$Si atoms [2] or the formation of highly coordinated Si atoms ($^{[5,6]}$Si) [67]. In contrast to the results in these previous studies, in Fig. 6-3(b), the calculated O *K*-edge XRS spectra for SiO_2 high-pressure polymorphs even consisting of the distinct Si coordination environments [hp-cristobalite ($^{[4]}$Si), penta-SiO_2 ($^{[5]}$Si), and stishovite ($^{[6]}$Si) structures] present similar double-peak-like excitation features. The double-peak-like O *K*-edge XRS features were observed in the SiO_2 polymorphs of which the nearest neighboring O atoms are in a distance of less than ~2.5 Å (Fig. 6-A4), whereas the Si coordination environments and Si-O bond length do not present clear correlations. In addition, the similar double-peak-like excitation features, which stem from the O *p*-*p* hybridization, also have been observed in the O *K*-edge XRS spectra of the $(O_2)_4$ molecular solid at high pressure [72]. Despite the

inherent structural differences between the crystalline and noncrystalline oxides, the results presented here can be applied to interpret the emergence of double-peak-like O *K*-edge XRS features of SiO_2 glass at high pressure because the O *K*-edge XRS features are determined from the short-range topology around O atom even in crystalline and noncrystalline oxides. Therefore, the emergence of double-peak-like O *K*-edge XRS features of SiO_2 glass at high pressure also might be attributed in part to the enhanced proximity between neighboring O atoms upon compression, and, thus, it may not be the direct evidence of the presence of highly coordinated Si atoms. However, since the decreases in interatomic distances of SiO_2 melts and glasses with increasing pressure were revealed to be moderately correlated with the formation of highly coordinated Si and O atoms [45,67], the emergence of double-peak-like O *K*-edge XRS features in SiO_2 glass could suggest either the presence of $^{[6]}$Si atoms or the formation of highly coordinated Si atoms, and, thus, it is partly consistent with the previous studies [2,67].

The previous studies have tried to understand the densification process of SiO_2 glass from diverse experiments, e.g. the pressure-induced changes in the Brillouin scattering features [44], O *K*-edge XRS features [2,67], and Si $L_{2,3}$-edge XRS features [73]. However, the interpretations of these previous studies are controversial: the presence of $^{[6]}$Si atom with the stishovite-like structural transition [2], formation of highly coordinated Si atoms ($^{[5]}$Si, $^{[6]}$Si, and $^{[6+]}$Si) [44,67], and changes in Si-O-Si bond angle with Si-O bond elongation [73]. This controversy of interpretations may be due to the lack of knowledge about changes in not only the short- to medium-range structural changes but also change in density of SiO_2 glass with

increasing pressure. Despite the importance on understanding the structural changes as well as changes in the acoustic wave velocities of the densified SiO_2 glasses, direct measurement of the density of SiO_2 glass at high pressure is still experimentally challenging (the current pressure limit is ~50 GPa) [253]. In this study, I have revealed that the changes in O *K*-edge XRS features of SiO_2 polymorphs are attributed in part to the enhanced proximity between neighboring O atoms [Fig. 6-4(d)] as well as the strong correlation between the densities and O-O distances of SiO_2 polymorphs [Fig. 6-2(d)]. Figure 6-5 presents the correlation between the absorption threshold energies and the densities of SiO_2 polymorphs explored in this study, and they present a relatively strong *linear* relationship [ρ (g/cm^3) = 0.81E_A (eV) – 431.59 (R^2 = 0.51)]. This quantitative and predictive relationship may be more useful in a higher-pressure region, since there is a stronger correlation in the SiO_2 polymorphs consisting of $^{[5]}$Si and $^{[6]}$Si atoms, exceptionally including hp-cristobalite (hp-cristobalite, penta-SiO_2, stishovite, $CaCl_2$-type, and α-PbO_2-type structures) [ρ (g/cm^3) = 0.65E_A (eV) – 344.57 (R^2 = 0.87)]. These results suggest that the density of other SiO_2 high-pressure polymorphs, maybe along with those of noncrystalline SiO_2 melts and glasses at high pressures, could be determined from the *in situ* high-pressure XRS experiments. However, because the noncrystalline SiO_2 melts and glasses undergo the spontaneous and complicated structural changes upon compression [45,67], the further theoretical studies for the electronic structures and XRS features of the SiO_2 melts and glasses at high pressures are expected to reveal the correlation between the densification process and the changes in O *K*-edge XRS features of SiO_2 melts and glasses with increasing pressure.

Conclusion

In this study, the correlation between the short-range order topological changes around O atoms and changes in the O *K*-edge XRS features, along with the emergence of double-peak-like excitation features, of SiO_2 high-pressure polymorphs (α-quartz, β-quartz, α-cristobalite, coesite, hp-cristobalite, penta-SiO_2, stishovite, $CaCl_2$-type, α-PbO_2-type, and pyrite-type structures) have been explored using the *ab initio* calculations. The emergence of characteristic double-peak-like excitation features and changes in absorption threshold energies of the O *K*-edge XRS spectra of these SiO_2 high-pressure polymorphs have been revealed to be associated in part with the enhanced proximity between neighboring O atoms, and, thus, the *p*-*p* hybridization between neighboring O atoms. These results have been used to probe the atomistic accounts of the emergence of double-peak-like O *K*-edge XRS features of SiO_2 glass at high pressure which are still controversial. I have concluded that the double-peak-like O *K*-edge XRS features of the SiO_2 glass at high pressure suggest the decrease in interatomic distances, particularly between neighboring O atoms maybe in a distance of less than ~2.5 Å, and, thus, it cannot directly indicate the presence of highly coordinated Si atoms. In addition, the relatively strong correlation between the pressure-induced changes in O *K*-edge XRS features, particularly the absorption threshold energies, and the densities of SiO_2 high-pressure polymorphs suggest a new possibility to estimate the density of SiO_2 glass by probing the direct link between the short-range

topologies around O atoms and the O *K*-edge XRS features. Therefore, the future experimental and theoretical studies of SiO_2 melts and glasses at high pressure are expected. I further expect that the current study can be applied to probe the atomistic origins of characteristic XRS features of the other amorphous oxides at high pressures.

Figures and Table

Table 6-1. Si coordination environments, space groups, lattice parameters, pressure conditions, and other interatomic structural parameters of SiO_2 high-pressure polymorphs.

(1)α-quartz [158], 2×2×1 supercell with 36 atoms

(2)β-quartz [241], 2×2×1 supercell with 36 atoms

(3)α-cristobalite [242], 2×2×1 supercell with 48 atoms

(4)coesite [243], 1×1×1 supercell with 48 atoms

(5)hp-cristobalite [244], 2×2×1 supercell with 48 atoms

(6)penta-SiO_2 [245], 2×1×1 supercell with 36 atoms

(7)stishovite [246], 2×2×2 supercell with 48 atoms

(8)$CaCl_2$-type SiO_2 [29], 2×2×2 supercell with 48 atoms

(9)α-PbO_2-type SiO_2 [32], 2×1×2 supercell with 48 atoms

(10)pyrite-type SiO_2 [35], 2×1×2 supercell with 48 atoms

(11)These values present distinctive Si-O-Si bond angles in the SiO_2 polymorphs.

Phase	[4]Si					[5]Si	[6]Si				
	α-qtz.[1]	β-qtz.[2]	α-crist.[3]	Coesite[4]	hp-crist.[5]	P-SiO_2[6]	Stishovite[7]		$CaCl_2$[8]	α-PbO_2[9]	Pyrite[10]
System											
	Trigonal	Hexagonal	Tetragonal	Monoclinic	Tetragonal	Trigonal	Tetragonal		Orthorhombic	Orthorhombic	Cubic
Space group											
	[152]$P3_121$	[180]$P6_222$	[92]$P4_12_12$	[15]C2/c	[92]$P4_12_12$	[154]$P3_221$	[136]$P4_2/mnm$		[58]Pnnm	[60]Pbcn	[205]Pa-3
Pressure (GPa)											
	1 atm	1 atm	1 atm	3.753	20	16	9.26	29.1	63	120	271
Lattice parameter (Å)											
a	4.912	4.997	4.969	7.020	4.355	4.414	4.134	4.044	3.897	3.711	3.923
b	4.912	4.997	4.969	12.262	4.355	4.414	4.134	4.044	4.001	4.651	3.923
c	5.404	5.457	6.926	7.126	5.960	9.358	2.654	2.619	2.566	4.159	3.923
Average Si-O bond length (Å)											
	1.608	1.588	1.603	1.605	1.554	1.703	1.760	1.729	1.694	1.649	1.605
Average O-O distance (Å)											
	2.626	2.593	2.618	2.621	2.522	2.561	2.487	2.442	2.394	2.327	2.264
Average Si-O-Si bond angle (°)											
	143.72	153.28	146.38	140.84	135.07	126.90	130.58	130.58	130.01	128.39	119.60
[11]				180.00		97.27	98.84	98.84	98.62	97.76	
Si-O polyhedral volume ($Å^3$)											
	2.1339	2.0531	2.1145	2.1202	1.8484	3.9297	7.1856	6.8067	6.4105	5.9201	5.338
Density (g/cm^3)											
	2.65	2.54	2.33	3.03	3.53	3.79	4.40	4.66	4.99	5.56	6.61

Figure 6-1. Crystal structures of (a) α-quartz, (b) β-quartz, (c) α-cristobalite, (d) coesite (O1~O5), (e) hp-cristobalite, (f) penta-SiO_2 (O1 and O2), (g) stishovite, (h) $CaCl_2$-type, (i) α-PbO_2-type, and (j) pyrite-type structures. Details of crystal structures are summarized in Tab. 6-1.

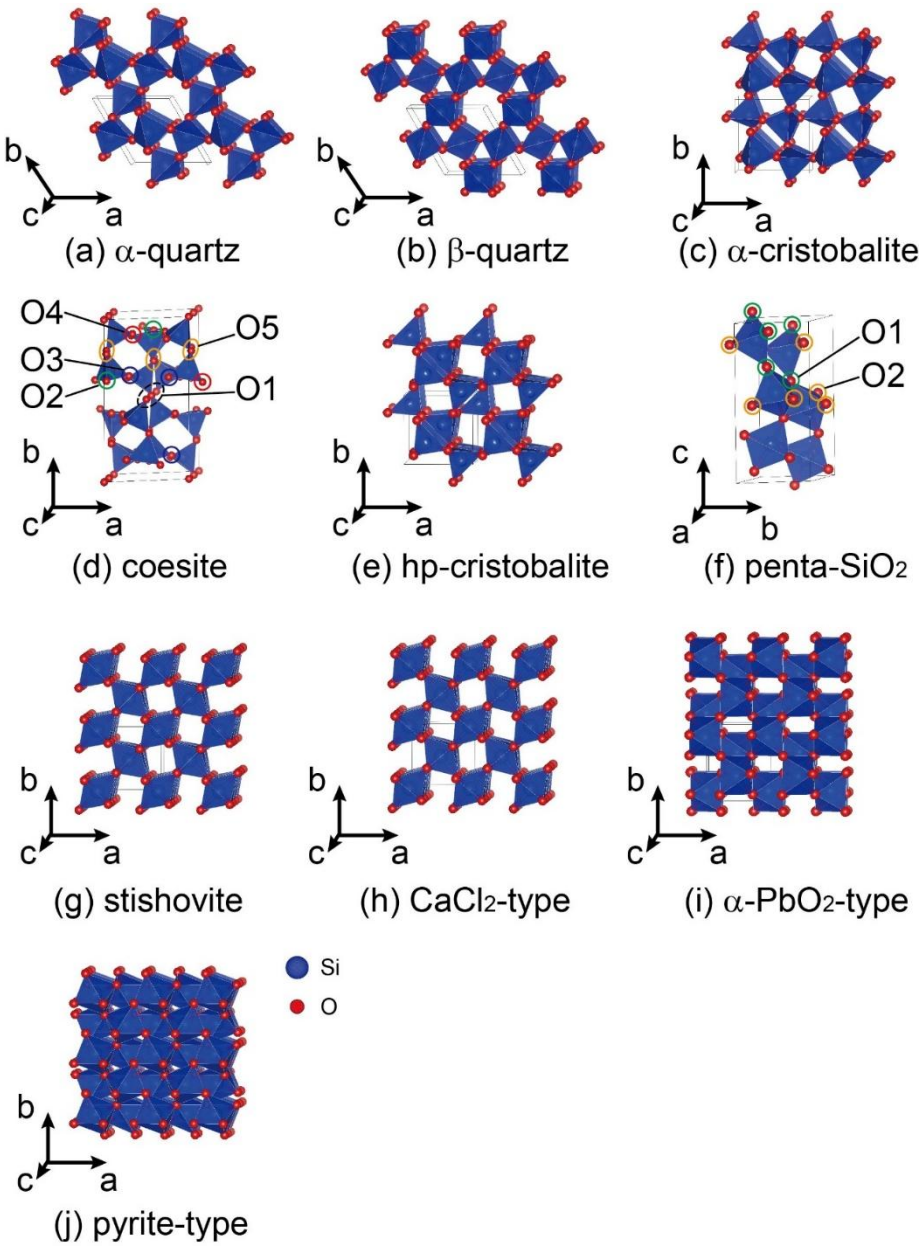

Figure 6-2. Pressure dependences of the average Si-O bond lengths (a) and average O-O distances (b) of the SiO_2 high-pressure polymorphs (α-quartz, β-quartz, α-cristobalite, coesite, hp-cristobalite, penta-SiO_2, stishovite, $CaCl_2$-type, α-PbO_2-type, and pyrite-type structures) and densities of SiO_2 polymorphs with respect to the average Si-O bond lengths (c) and average O-O distances (d). The black dashed lines refer to the trend for the SiO_2 polymorphs explored here with the corresponding *linear* relationships. See details in the manuscript.

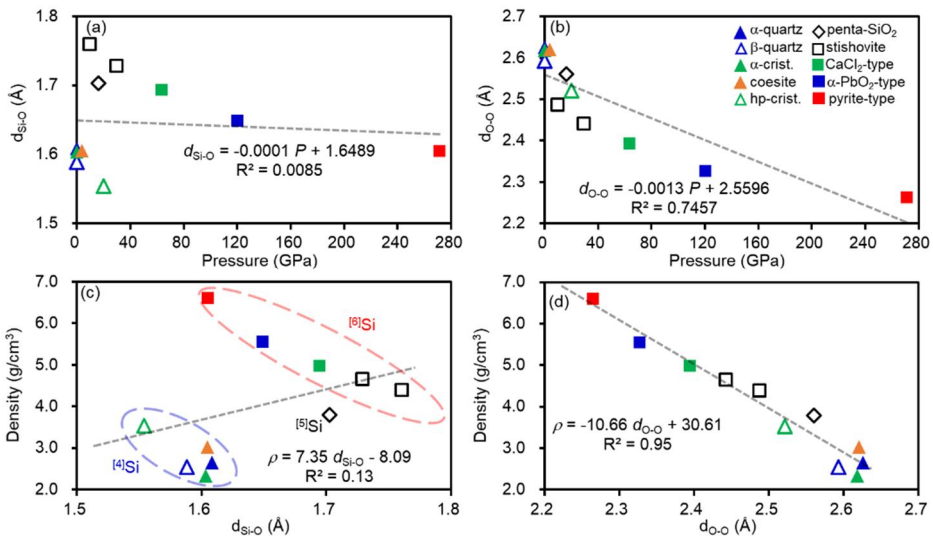

Figure 6-3. (a) Calculated *l*-resolved partial density of states (PDOS), for unoccupied states, of O atoms for the SiO_2 high-pressure polymorphs (α-quartz, β-quartz, α-cristobalite, coesite, hp-cristobalite, penta-SiO_2, stishovite, $CaCl_2$-type, α-PbO_2-type, and pyrite-type structures). The Gaussian-broadening full-width at half-maximum (FWHM) for PDOS is 0.02 Ry. Red, blue, and green solid lines refer to the unoccupied O *s*, *p*, and *d* states, respectively. The maximum PDOS intensity of each SiO_2 polymorph is presented at the left side of the figure. (b) Calculated O *K*-edge XRS spectra for the SiO_2 high-pressure polymorphs. The Gaussian-broadening FWHM for O *K*-edge XRS features is 0.5 eV. Site-resolved l-resolved PDOSs and O *K*-edge XRS features for the coesite and penta-SiO_2 structures are presented in Fig. 6-A2.

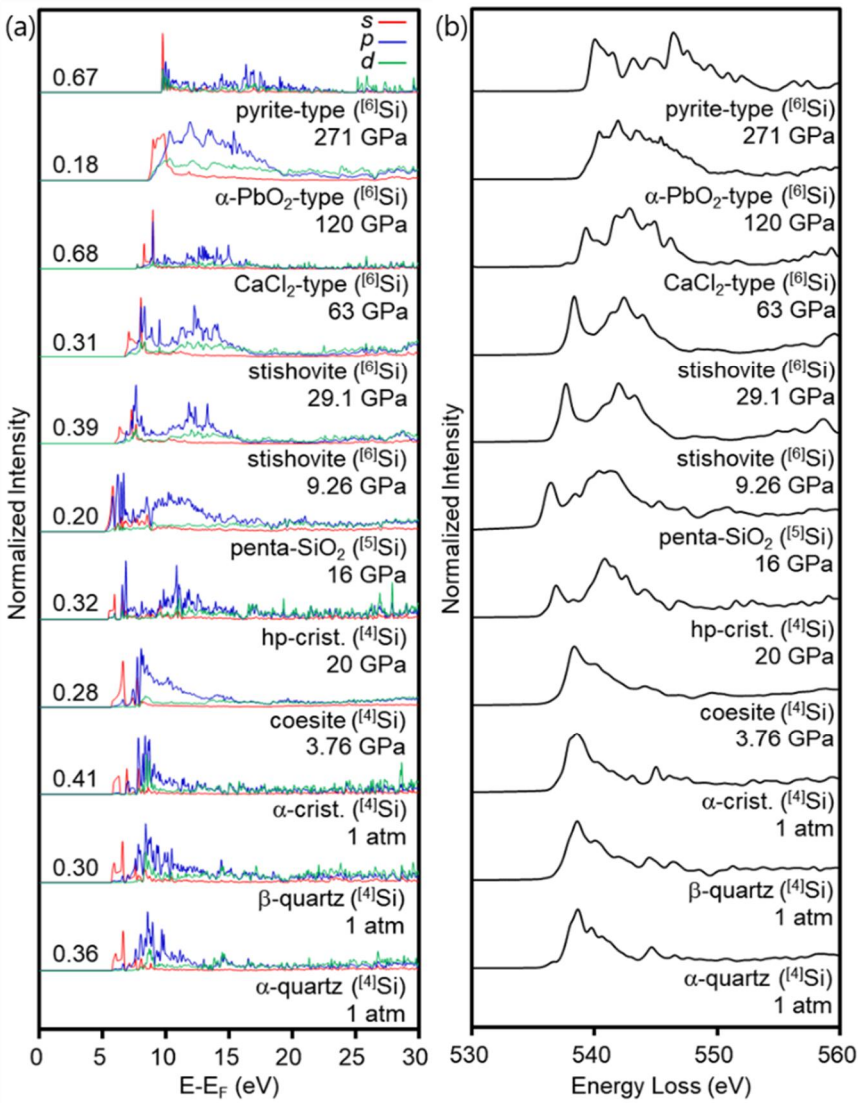
(a)
s
p
d
0.67
pyrite-type ([6]Si)
271 GPa
0.18
α-PbO2-type ([6]Si)
120 GPa
0.68
CaCl2-type ([6]Si)
63 GPa
0.31
stishovite ([6]Si)
29.1 GPa
0.39
stishovite ([6]Si)
9.26 GPa
0.20
penta-SiO2 ([5]Si)
16 GPa
0.32
hp-crist. ([4]Si)
20 GPa
0.28
coesite ([4]Si)
3.76 GPa
0.41
α-crist. ([4]Si)
1 atm
0.30
β-quartz ([4]Si)
1 atm
0.36
α-quartz ([4]Si)
1 atm
Normalized Intensity
0 5 10 15 20 25 30
E-EF (eV)
(b)
pyrite-type ([6]Si)
271 GPa
α-PbO2-type ([6]Si)
120 GPa
CaCl2-type ([6]Si)
63 GPa
stishovite ([6]Si)
29.1 GPa
stishovite ([6]Si)
9.26 GPa
penta-SiO2 ([5]Si)
16 GPa
hp-crist. ([4]Si)
20 GPa
coesite ([4]Si)
3.76 GPa
α-crist. ([4]Si)
1 atm
β-quartz ([4]Si)
1 atm
α-quartz ([4]Si)
1 atm
Normalized Intensity
530 540 550 560
Energy Loss (eV)

Figure 6-4. Band gap of the SiO_2 high-pressure polymorphs (α-quartz, β-quartz, α-cristobalite, coesite, hp-cristobalite, penta-SiO_2, stishovite, $CaCl_2$-type, α-PbO_2-type, and pyrite-type structures) with respect to the average Si-O bond lengths (a) and average O-O distances (b). Absorption threshold energies in the O *K*-edge XRS features of the SiO_2 high-pressure polymorphs with respect to the average Si-O bond lengths (c) and average O-O distances (d). The black dashed lines refer to the trend for all the SiO_2 polymorphs with the corresponding *linear* relationships. See details in the manuscript.

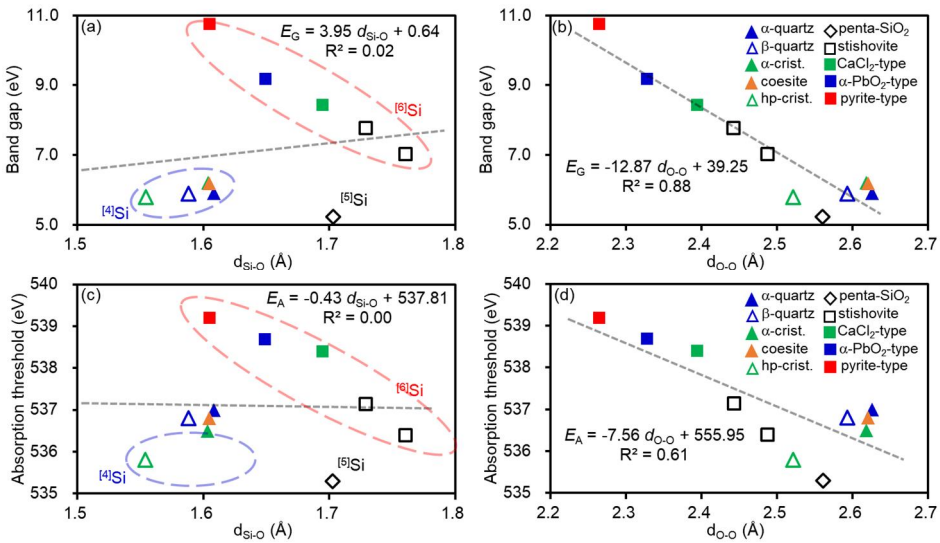

Figure 6-5. Densities of the SiO_2 high-pressure polymorphs (α-quartz, β-quartz, α-cristobalite, coesite, hp-cristobalite, penta-SiO_2, stishovite, $CaCl_2$-type, α-PbO_2-type, and pyrite-type structures) with respect to the absorption threshold energies in their O *K*-edge XRS features. The black dashed line refers to the trend for all the SiO_2 polymorphs, whereas the red dashed line is for the higher-pressure polymorphs only (hp-cristobalite, penta-SiO_2, stishovite, $CaCl_2$-type, α-PbO_2-type, and pyrite-type structures) with the corresponding *linear* relationships. See details in the manuscript.

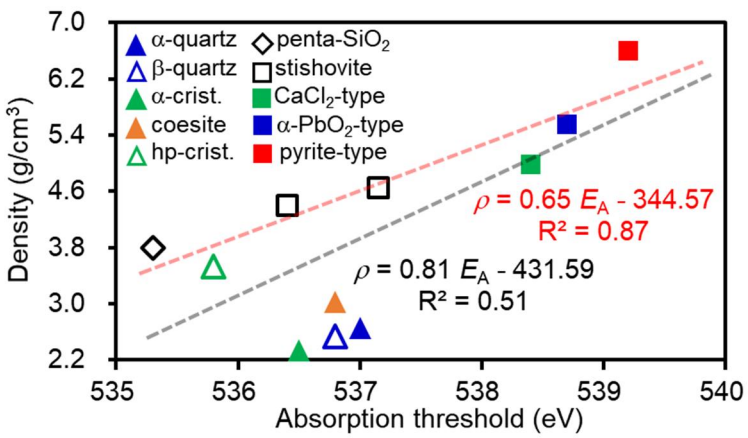

Appendix

l-resolved PDOSs of the SiO_2 high-pressure polymorphs

The results presented in Fig. 6-3(a) were calculated with applying the core-hole effects to the target O atom, and, thus, changes in the electronic structures in the valence region, such as the Si-O and O-O covalent characters, cannot be confirmed precisely. Therefore, the *l*-resolved PDOSs of the SiO_2 high-pressure polymorphs calculated without applying the core-hole effects, in an energy range from -30 to 30 eV, are presented here. Figure 6-A1 presents the *l*-resolved PDOSs of the SiO_2 high-pressure polymorphs in both the valence and conduction regions (from -30 to 30 eV). The PDOSs of the SiO_2 polymorphs with similar topologies around O atoms exhibit similar features, e.g. α-quartz, β-quartz, α-cristobalite, and coesite structures.

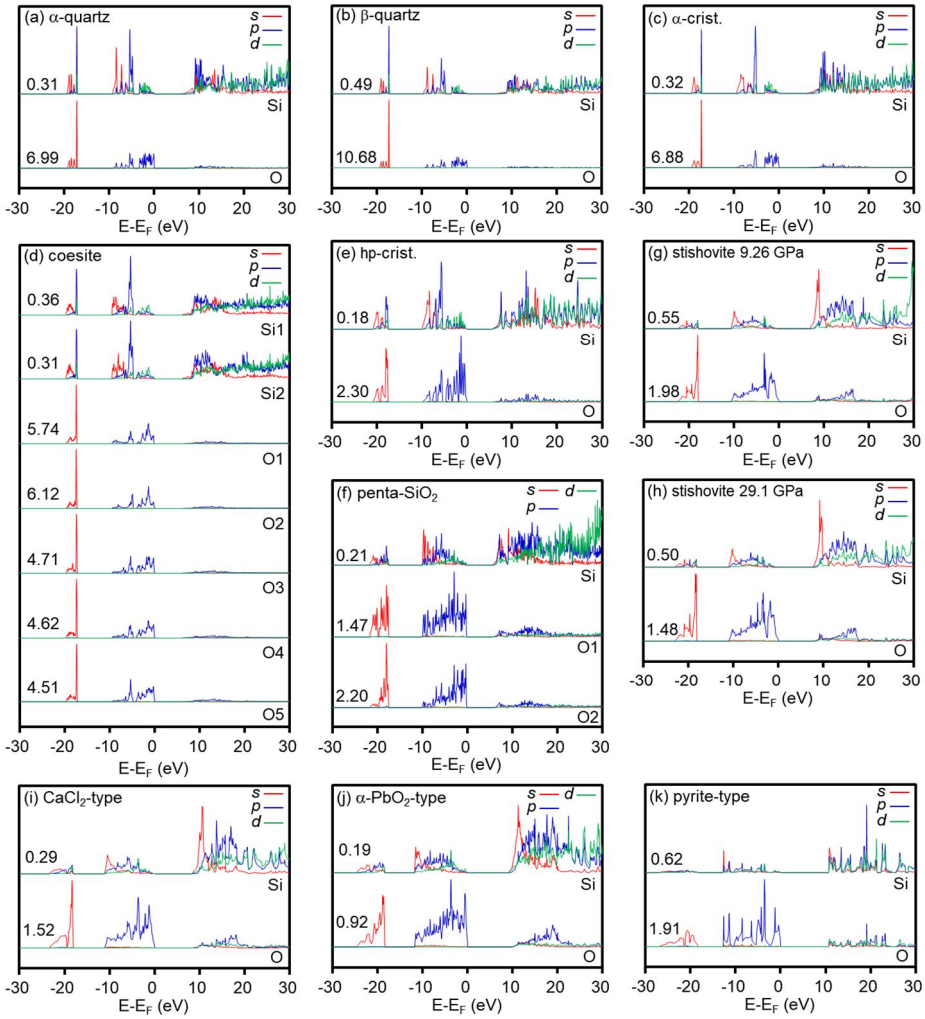

Figure 6-A1. Calculated *l*-resolved partial density of states (PDOS) for the SiO_2 high-pressure polymorphs as labelled: (a)α-quartz, (b) β-quartz, (c) α-cristobalite, (d) coesite, (e) hp-cristobalite, (f) penta-SiO_2, (g) stishovite at ~9.26 GPa, (h) stishovite at ~29.1 GPa, (i) $CaCl_2$-type, (j) α-PbO_2-type, and (k) pyrite-type structures. These results are calculated without applying the core-hole effects.

PDOSs and O K-edge XRS features of the coesite and penta-SiO_2 structures

Since the O atoms in the coesite (O1~O2) and penta-SiO_2 (O1~O2) structures exhibit symmetrically distinct oxygen sites, the O PDOSs and O *K*-edge XRS features of these distinct O atoms should be calculated separately. The results of the coesite and penta-SiO_2 structures, presented in Fig. 6-3(a) and Fig. 6-3(b), are obtained by taking into consideration the ratio of O atoms in the unit cells. Figure 6-A2 presents the site-resolved O PDOSs (the unoccupied O *s*, *p*, and *d* states) and the O *K*-edge XRS features of the SiO_2 high-pressure polymorphs.

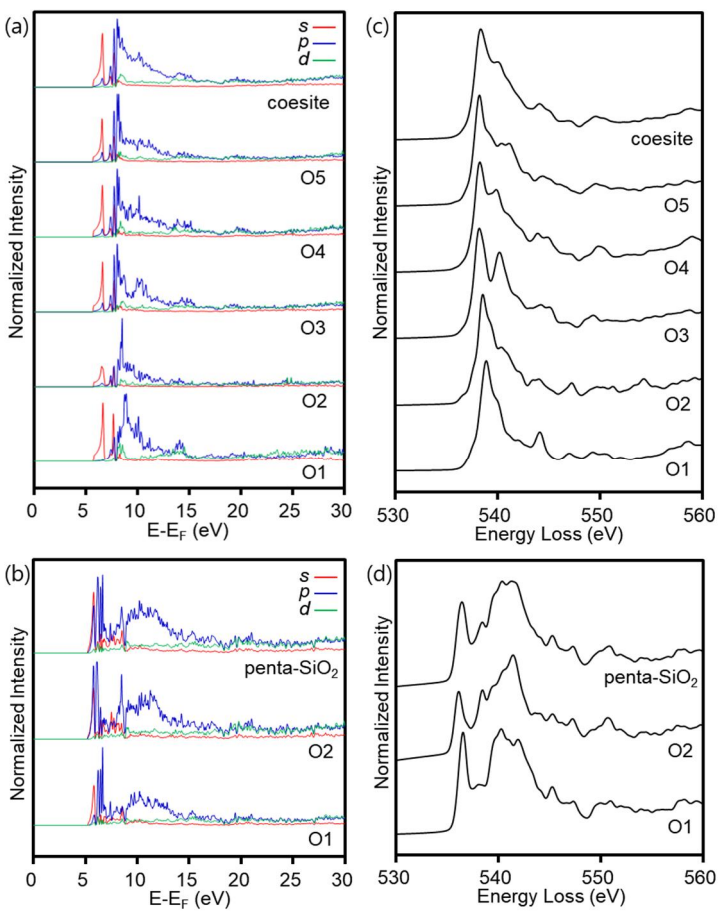

Figure 6-A2. Site-resolved O PDOSs (a) and O *K*-edge XRS spectra (b) of the coesite (O1~O5 distinct oxygen sites) and penta-SiO_2 (O1~O2 distinct oxygen sites) structures. The total O PDOSs and O *K*-edge XRS features obtained by taking into consideration the ratio of O atoms in the unit cell are presented in the top of each figure.

Pressure dependence of the densities of SiO_2 high-pressure polymorphs

Correlations between the local atomic structures around O atoms and densities of SiO_2 high-pressure polymorphs are well summarized in Fig. 6-2(a)~Fig. 6-2(d). However, the pressure dependence of the densities of SiO_2 high-pressure polymorphs is also one of the important to understand their atomic and associated elastic properties. Figure 6-A3 presents the correlation between the densities and the pressure conditions of the SiO_2 high-pressure polymorphs. Thus, the densities of SiO_2 high-pressure polymorphs with respect to their pressure conditions are presented here, and it exhibits a relatively clear *linear* relationship [ρ (g/cm^3) = 0.01*P* (GPa) + 3.32 (R^2 = 0.72)].

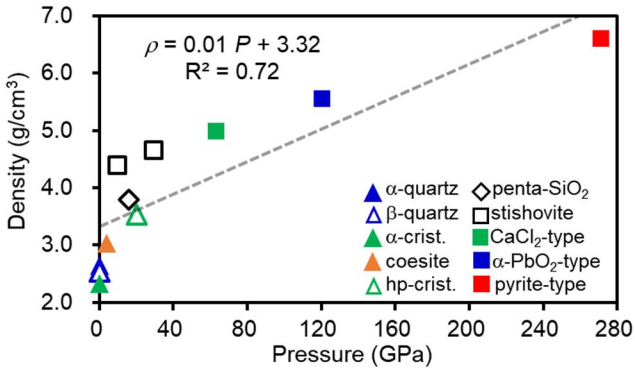

Figure 6-A3. Densities of the SiO_2 high-pressure polymorphs (α-quartz, β-quartz, α-cristobalite, coesite, hp-cristobalite, penta-SiO_2, stishovite, $CaCl_2$-type, α-PbO_2-type, and pyrite-type structures) with respect to the pressure conditions. The black dashed line refers to the trend for all the SiO_2 polymorphs with the corresponding *linear* relationship.

Spatial distribution of Si-O and O-O pairs

Since the characteristic double-peak-like excitation features were observed in the calculated O *K*-edge XRS spectra for some of SiO_2 polymorphs (e.g., hp-cristobalite, penta-SiO_2, stishovite structures) [Fig. 6-3(b)], I tried to reveal the correlation between the interatomic distances (Si-O bond lengths and the O-O distances) and the emergence of double-peak-like O *K*-edge XRS features of the SiO_2 high-pressure polymorphs. Figure 6-A4 presents the spatial distribution of Si-O and O-O pairs (partial radial distribution functions) of the SiO_2 high-pressure polymorphs. The double-peak-like O *K*-edge XRS features seem to be appeared in the SiO_2 polymorphs of which the nearest neighboring O atoms are in a distance of

less than ~2.5 Å, whereas the Si-O bond lengths do not present a strong correlation.

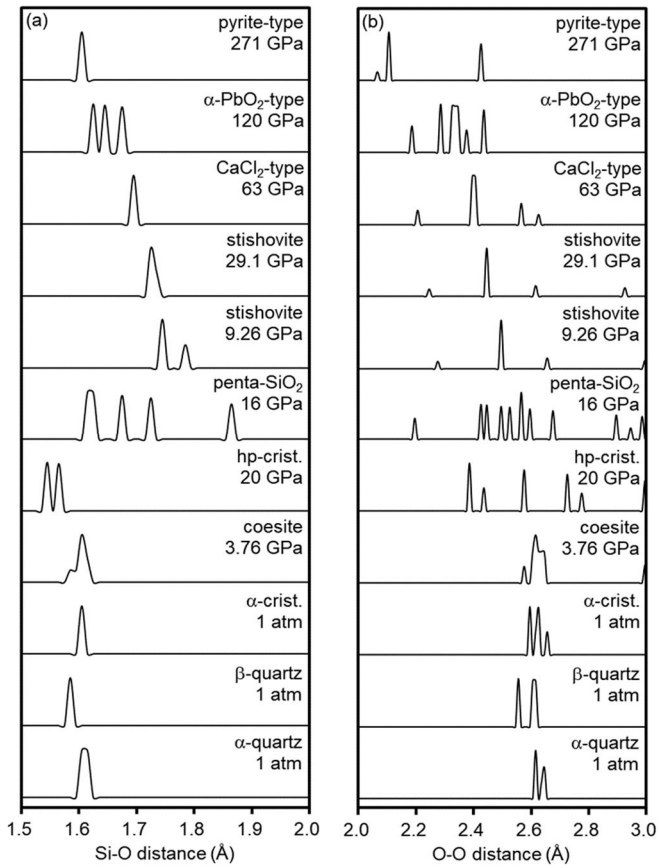

Figure 6-A4. Spatial distributions of Si-O and O-O pairs (partial radial distribution function) of the SiO_2 high-pressure polymorphs (α-quartz, β-quartz, α-cristobalite, coesite, hp-cristobalite, penta-SiO_2, stishovite, $CaCl_2$-type, α-PbO_2-type, and pyrite-type structures).

Band gap and absorption threshold energies

Since the O *K*-edge XRS features stem from the electronic excitation from the core-level state to the corresponding unoccupied states, the energy gap between the highest occupied state and the lowest unoccupied states, that is the band gap energy, should be strongly correlated with the absorption threshold energies in O *K*-edge XRS features of SiO_2 high-pressure polymorphs. Figure 6-A5 presents the correlation between the absorption threshold energies in O *K*-edge XRS features and the band gap energies of the SiO_2 high-pressure polymorphs. The band gap energies are estimated from the calculated total density of states of the SiO_2 high-pressure polymorphs without applying the core-hole effects.

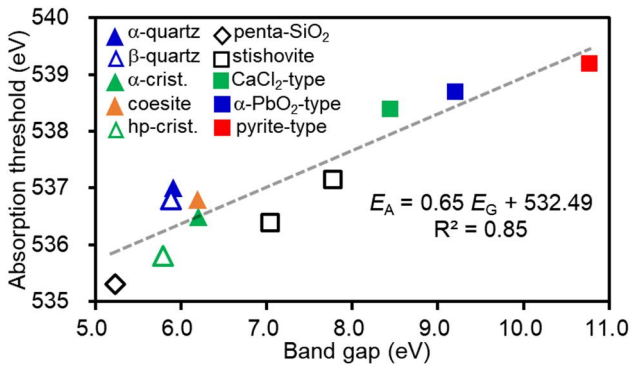

Figure 6-A5. The correlation between the absorption threshold energies in O *K*-edge XRS features and the band gap energies of the SiO_2 high-pressure polymorphs (α-quartz, β-quartz, α-cristobalite, coesite, hp-cristobalite, penta-SiO_2, stishovite, $CaCl_2$-type, α-PbO_2-type, and pyrite-

type structures). The black dashed line refers to the trend for all the SiO_2 polymorphs with the corresponding *linear* relationship.

Chapter 7.

Pressure-induced changes in Fe $L_{2,3}$-edge x-ray Raman scattering spectra of Fe-including oxides at high pressures: Insights from *ab initio* calculations

Yoo Soo Yi and Sung Keun Lee

This is the preliminary study of the pressure-induced changes in Fe $L_{2,3}$-edge spectra of Fe-including oxides, particularly FeO wustite structures. The aim of this study is confirming the possibility of calculating the pressure-induced changes in Fe $L_{2,3}$-edge XRS features of Fe-including oxides.

Introduction

The presence of Fe-including oxides near the core-mantle boundary (CMB), which stem from the dissolution of Fe from the outer core region, has been suggested in previous studies [82,83]. The x-ray Raman scattering (XRS) spectroscopy has been used to probe the element-specific local atomic structures, because the XRS features, and, thus, the local electronic structures, are determined from the short- to medium-range atomic structures around the target elements [65]. Thus, the Fe $L_{2,3}$-edge XRS features can provide the elements-specific electronic bonding structures, coordination environments, and oxidation states of Fe atoms [141]. In particular, the Fe $L_{2,3}$-edge XRS features of Fe-including oxides, such as almandine $Fe_3Al_2(SiO_4)_3$, andradite $Ca_3Fe_2Si_3O_{12}$, almandine-skiagite $Fe_3(Al_{1-x}Fe_x)_2[SiO_4]_3$, and skiagite-andradite $(Fe_{1-x}Ca_x)Fe_2[SiO_4]_3$, have been used to determine the Fe oxidation states (Fe^{2+} and Fe^{3+}) quantitatively [254]. As shown in the previous chapters, the *in situ* high-pressure XRS experiments has been used to reveal the topological changes around target element under compression from the pressure-induced changes in XRS features [64,65]. The XRS experiments also have been used to explore the noncrystalline high-z oxides: the Fe $L_{2,3}$-edge XRS features for the Fe oxidation state of Fe_2SiO_4 and $FeCO_3$ [66] and the Fe $M_{2,3}$-edge XRS features for the electron-spin-state of Fe atoms in FeS [179,207], Fe_2O_3, Fe_2SiO_4, $FePO_4$, and $FeAl_2O_4$ [180]. However, despite the enormous geological implications, the pressure-induced changes in Fe $L_{2,3}$-edge XRS features have not yet been explored systematically. I noted that the

crystallographic and electronic structures of FeO wustite structures at high pressures have been revealed in a previous study [255].

Recent advances in the *ab initio* calculations have provided the opportunity to explore the element-specific core-level excitation features, such as *K*- and $L_{2,3}$-edge excitation features, of crystalline and noncrystalline materials under high pressures. Thus, the aim of this study is establishing the direct correlation between the topological changes around Fe atoms and the changes in Fe $L_{2,3}$-edge XRS features of Fe-including oxides upon extreme compression using the *ab initio* calculations. For the purpose of this study, I have calculated the electronic structures and Fe $L_{2,3}$-edge XRS features for the FeO wustite structures at high pressures. I expect that probing changes in atomic and electronic structures, as well as Fe $L_{2,3}$-edge XRS features, of Fe-including oxides under high pressures would be helpful to improve our understanding about the evolution of mantle materials in the Earth's interior, particularly near the CMB. In further, the results of this study might be the guideline for the future *in situ* high-pressure XRS experiments for the Fe-including oxides at extremely high pressures.

Calculations

The density of states (DOS) and Fe $L_{2,3}$-edge XRS features of FeO wustite structures at high pressures have been calculated using the *ab* initio calculations based on the projector augmented wave (PAW) type pseudopotential method, i.e. CASTEP [78]. The reference structure of FeO

wustite was referred from the previous study [256], and the unit cell volume of this structure was defined as $1.0V_0$. Then, the unit cell volume of FeO wustite structure was compressed by $0.9V_0$, $0.8V_0$, $0.77V_0$, $0.73V_0$, $0.6V_0$, $0.57V_0$, $0.53V_0$, and $0.5V_0$.

Strongly correlated Fe 3*d* state (Hubbard U parameter)

The conventional GGA and LDA methods could not take into account the on-site Coulomb interaction. Thus, conventional GGA and LDA method have been failed to represent the electronic structures of Fe-oxides due to the presence of strongly correlated electrons of 3*d* state [257]. Recent previous studies, using the *ab initio* calculations, have suggested the presence of FeO_2 phases at extremely high pressures, while the FeO phases has been believed as the major Fe-oxides in the Earth's interior. In that study, the contribution of the on-site Coulomb interaction of Fe-oxides at high pressures, which can be adjusted by the Hubbard *U* parameter, has been revealed precisely. Thus, in this study, the diverse Hubbard *U* parameters were used to calculate the density of states (DOS) of FeO wustite structures. The FeO wustite, with the rocksalt structure, has been known as the Mott insulator (i.e., a class of materials that should be metal, but they are revealed to be insulators with the conventional band theories because of the strong electron-electron interactions in the Fe 3*d* state, the strong on-site Coulomb interaction), and, thus, applying the proper Hubbard *U* values can improve the precision of the calculated results. Therefore, in this study, diverse Hubbard *U* parameters were used to confirm the effects of Hubbard *U* parameter to the electronic structures, as well as the Fe spin-state transition, of the FeO wustite structures at high

pressures. In contrast, for the XRS calculations, the Hubbard U parameter of 5.0 eV was used, since U of 5.0 eV has been revealed to be appropriate for calculating the electronic structures and other properties of Fe-oxides, such as (Mg,Fe)O (Fe^{2+}), FeO (Fe^{2+}), FeO_2 (Fe^{2+}), and Fe_2O_3 (Fe^{3+}) [258].

Usually, the GGA method gives much better results than the LDA method for the system with the localized electronic structures. In further, in the higher-pressure region, the GGA method will be more reliable because of the delocalization of electronic states [259]. However, the strong on-site Coulomb interaction should be concerned to obtain the reliable results with considering the on-site electron-electron in the strongly correlated electronic states. Therefore, in this study, the GGA method are expanded with applying the Hubbard U potential (i.e., empirically modify the on-site Coulomb interaction), i.e. the GGA+U method.

Calculating the density of states

The PBE for solids (PBESOL) scheme was used as the exchange-correlation functional [194]. The plane-wave-cutoff energy of 990 eV was used. The number of irreducible k points was set to 60, i.e. the Monkhorst-Pack grid was 8×8×8. The All bands/EDFT scheme was used as the electronic minimizer for the self-consistent field (SCF) calculations. The orbital occupancy was not fixed with the parameters for empty band of 20% and smearing of 0.2 eV to enhance the convergence of SCF calculations. The SCF convergence criterion was set to 5.00×10^{-7} eV/atom. The Hubbard U parameters of 6.0, 5.0, 3.5, 2.5, 1.5 and 0.0 eV were used.

Calculating the Fe $L_{2,3}$-edge XRS features

Most of the Fe $L_{2,3}$-edge XRS features stem from the electronic transition from the occupied Fe 2*p* state to the unoccupied 3*d* state (i.e., 2*p*-3*d** transition). Thus, the core-hole effects should be applied to the Fe 2*p* state by removing a single occupation of Fe 2*p* state [260]. The Fe $L_{2,3}$-edge XRS features of the FeO wustite structures at high pressures have been calculated using the *ab initio* calculations based on the PAW-type pseudopotential method [78]. The PBE for solids (PBESOL) scheme was used as the exchange-correlation functional [194]. The plane-wave-cutoff energy of 630 eV was used. The number of irreducible *k* points was set to 63-1728, i.e. the Monkhorst-Pack grid were from 5×5×5 to 12×12×12. The SCF convergence criterion was set to 1.00×10^{-6} eV/atom. The parameters for empty band and smearing each were set to 20% and 0.2 eV, respectively. The Hubbard *U* parameter was set to 5.0 eV. The extended supercell structures of 2×2×2 (63 Fe and 62 O atoms) and 2×1×1 (23 Fe and 22 O atoms) were used to reduce the unexpected interactions from the mirror image of Fe atom, of which the electronic occupation of 2*p* state was modified to mimic the final-state of XRS process, due to the periodic boundary condition.

Results and discussion

Spin-state transition of Fe atom at high pressures

The spin state of Fe in the octahedral symmetry (O_h), which usually represents high-spin state [HS; S = 4 (ħ/2)], changes to the low-spin state

[LS; S = 0 (ħ/2)] with the crossover of crystal-field splitting (Δ) and spin-pairing (ε) energies upon compression. Since the FeO wustite structures at diverse pressure conditions were calculated, the pressure-induced Fe spin-state transition could be confirmed. In addition, the effects of Hubbard U parameters (6.0, 5.0, 3.5, 2.5, 1.5 and 0.0 eV) to the Fe spin-state transition of FeO wustite structures also could be revealed precisely. Figure 7-1 presents the Fe spin state of FeO wustite structures. The results in Fig. 7-1 present the complete spin-state transitions from HS to LS, particularly above U = 3.5 eV. Figure 7-2 presents the pressure-volume relationship of FeO wustite structures, which are estimated from the internal stress tensor. The results in Fig. 7-2 present the abnormal features near the spin-state transition threshold because the local electronic structures around Fe atoms are significantly affected by the Fe spin state. Figure 7-3 presents the pressure dependences of Fe spin state of FeO wustite structures. Whereas the estimated pressure values of FeO wustite structures present unexpected abnormal features near the transition threshold as revealed in Fig. 7-2, the spin-state-transition-threshold pressure seem to increase with increasing the Hubbard U parameter. Figure 7-4 presents the Fe spin-state density of FeO wustite structures with varying the volume of unit cell and the Hubbard U parameter, and figure 7-5 presents changes in the Fe spin-state density of FeO wustite structures with varying the pressure and Hubbard U parameter. Fig. 7-4 and Fig. 7-5 present the volume and pressure dependences of Fe spin state, as well as changes in spin-state-transition-threshold pressure, more systematically than the results presented in Fig. 7-1 and Fig. 7-3.

Calculated Fe $L_{2,3}$-edge XRS features

Figure 7-6 presents the calculated Fe $L_{2,3}$-edge XRS features of FeO wustite structures at high pressures (with the compressed unit cell structures). The Fe $L_{2,3}$-edge XRS feature present clearly distinguishable L_3- and L_2-edge features at lower- and higher-energy regions, respectively. The Fe L_3-edge features stem from the electronic transition from occupied 2*p* state of *J*=3/2 (the total angular momentum; *S*+*L*) to unoccupied 3*d* state, and the Fe L_2-edge features from the electronic transition from occupied 2*p* state of *J*=1/2 to unoccupied 3*d* state. The Fe L_2-edge features above ~720 eV present a significant shift to a higher-energy region upon compression, where the unit cell volume compressed by $0.73V_0$. The Fe L_3-edge features, near ~710 eV, do not present a significant shift to a higher-energy region upon compression, but their spectral features significantly change as revealed.

Future study

The effects of Fe spin-state-transition, Hubbard *U* parameter, structural transition to the Fe $L_{2,3}$-edge XRS features should be discussed to understand the pressure-induced changes in Fe $L_{2,3}$-edge XRS features of Fe-including oxides.

The effects of Fe spin-state-transition to the Fe $L_{2,3}$-edge XRS features

In the previous studies, the Fe *K*-edge features of Fe-including oxides, from the x-ray absorption spectroscopy (XAS), have been revealed

not to be sensitive to the Fe spin-state transition of Fe 3*d* state under high pressures [261]. In contrast, the Fe $L_{2,3}$-edge XRS features might be more strongly affected by the spin-state transition of Fe 3*d* state upon compression, because most of Fe $L_{2,3}$-edge XRS features stem from the Fe 2*p*-3*d** transition. Similar discussion about the significant changes in Fe $L_{2,3}$-edge features induced from the spin transition of Fe 3*d* state has been summarized in the previous studies [260]. The Fe $L_{2,3}$-edge x-ray emission spectroscopy (XES), which provide the electronic structures in the valence band, can be used to determine the spin-state transition of Fe atoms in the FeO wustite structures upon compression [262,263]. Therefore, the spin-state transition of Fe 3*d* state under high pressures should be precisely controlled to calculate the reliable Fe $L_{2,3}$-edge XRS features of Fe-including oxides.

The effects of Hubbard *U* parameters to the Fe $L_{2,3}$-edge XRS features

The electronic structures of FeO wustite structures, as well as the Fe spin state, are strongly affected by the Hubbard *U* parameters, to control the on-site Coulomb interaction. Thus, the Fe $L_{2,3}$-edge XRS features, which can provide the electronic bonding structures of Fe atoms, also would change with changing the Hubbard *U* parameter. Therefore, the effects of Hubbard *U* parameters to the Fe $L_{2,3}$-edge XRS features should be confirmed by calculating the Fe $L_{2,3}$-edge XRS features of FeO wustite structures with diverse Hubbard *U* parameters, whereas the results in Fig. 7-5 were calculated with the Hubbard *U* parameter of 5.0 eV.

The effects of phase transition to the Fe $L_{2,3}$-edge XRS features

In this study, the compressed FeO wustite structures, without further phase transitions upon compression. However, the FeO structure goes through the phase transition depending on the pressure- and temperature conditions [264]. Thus, probing the changes in Fe $L_{2,3}$-edge XRS features associated with the phase transition of FeO structures would be helpful to establish the correlation between the topological changes around Fe atoms and the evolution in Fe $L_{2,3}$-edge XRS features of Fe-including oxides at high pressures.

Pressure-induced magnetization of FeO wustite

The pressure-induced magnetization of FeO wustite structures have been reported in the previous studies using the Mössbauer spectroscopy [265,266]. Changes in the spin alignment of Fe atoms in the FeO wustite structures upon compression, i.e. the pressure-induced magnetization, would affect to their electronic structures and, thus, the Fe $L_{2,3}$-edge XRS features at high pressures. Therefore, the effects of pressure-induced magnetization should be accounted to calculate the Fe $L_{2,3}$-edge XRS features more precisely.

Fe $L_{2,3}$-edge XRS features of noncrystalline Fe-including oxides

Recent studies have suggested that the spin-state transition of Fe 3*d* state seem to be elusive in the Fe-including oxides [267]. Because the noncrystalline oxides go through the complicated and continuous structural changes upon compression, the correlation between the topological changes around Fe atoms and the evolution in Fe $L_{2,3}$-edge XRS

features of noncrystalline Fe-including oxides should be explored more systematically.

Figures

Figure 7-1. The Fe spin-state transition of FeO wustite structures with decreasing the volume of unit cell, from $1.0V_0$ to $0.5V_0$ as labelled. The Hubbard *U* parameters of 6.0, 5.0, 3.5, 2.5, 1.5 and 0.0 eV were used also as labelled.

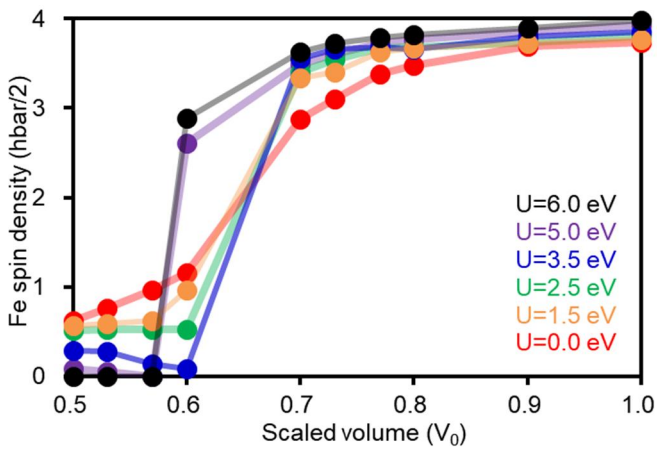

Figure 7-2. The pressure-volume relationship of FeO wustite structures explored in this study. The Hubbard *U* parameters of 6.0, 5.0, 3.5, 2.5, 1.5 and 0.0 eV were used as labelled.

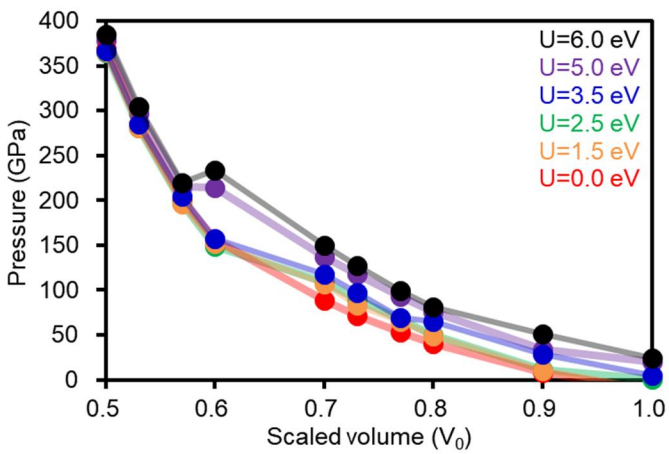

Figure 7-3. The pressure dependence of the Fe spin state of FeO wustite structures. The Hubbard *U* parameters of 6.0, 5.0, 3.5, 2.5, 1.5 and 0.0 eV were used as labelled.

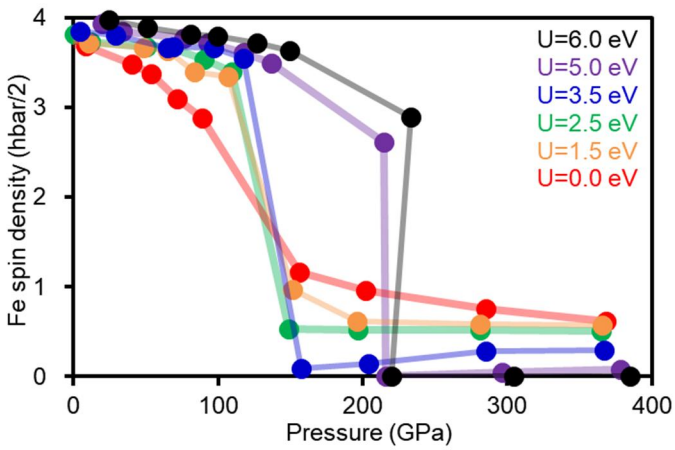

Figure 7-4. The Fe spin-state transition of the FeO wustite structures with decreasing the volume of unit cell. The Hubbard *U* parameters of 6.0, 5.0, 3.5, 2.5, 1.5 and 0.0 eV were used as labelled.

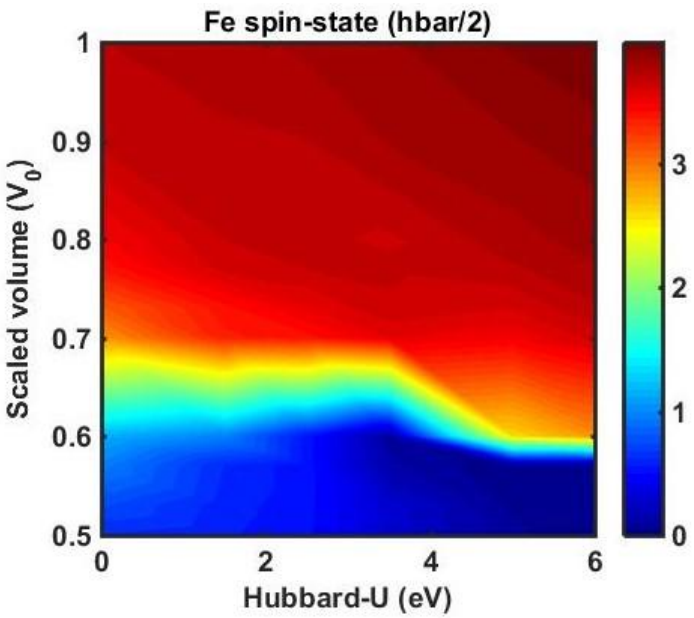

Figure 7-5. The Fe spin-state transition of the FeO wustite structures with decreasing the volume of unit cell. The Hubbard *U* parameters of 6.0, 5.0, 3.5, 2.5, 1.5 and 0.0 eV were used as labelled.

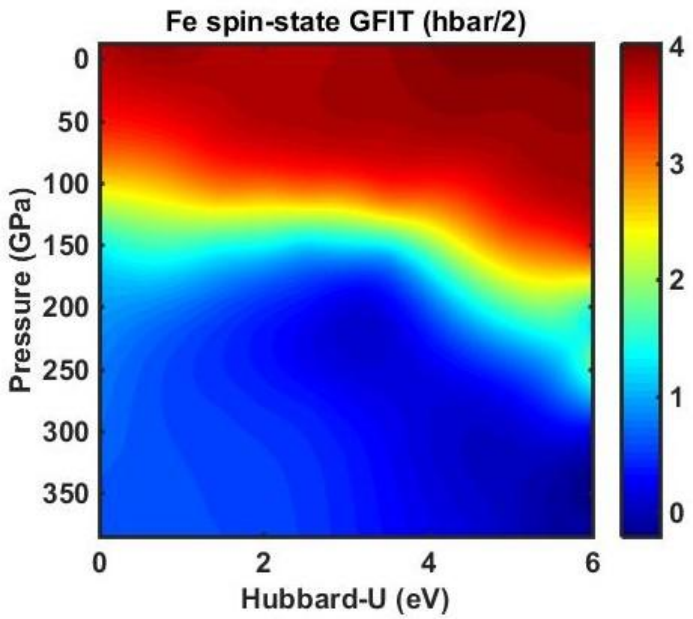

Figure 7-6. The calculated Fe $L_{2,3}$-edge XRS features of FeO wustite structures with different unit cell volumes ($1.0V_0$, $0.9V_0$, $0.8V_0$, $0.77V_0$, $0.73V_0$, $0.6V_0$, $0.57V_0$, $0.53V_0$, and $0.5V_0$).

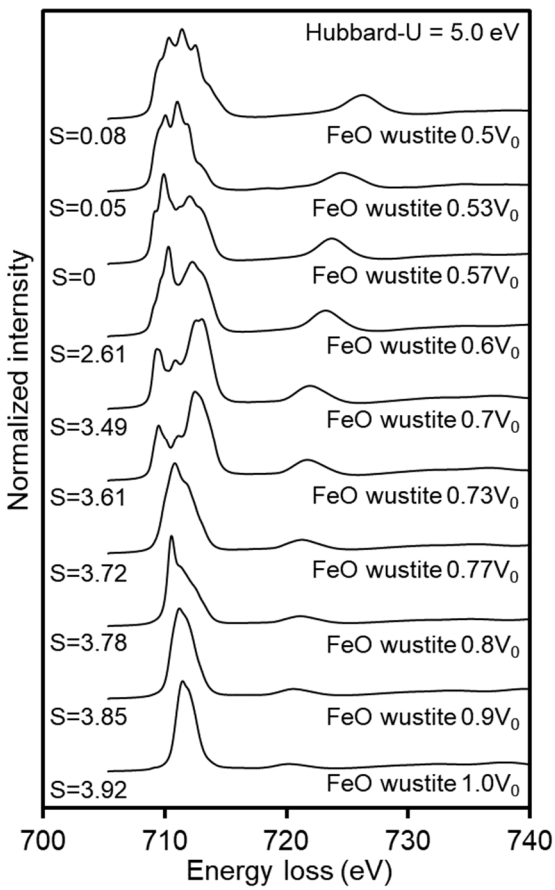

Chapter 8.

Chemical shielding and electric field gradient tensors of Li atoms in lepidolite structures: Insights from *ab initio* calculations

Yoo Soo Yi and Bum Han Lee

It will be submitted to *Minerals* (or other papers), in preparation

This study was conducted in collaboration with Dr. Bum Han Lee at Korea Institute of Geoscience and Mineral Resources (KIGAM). The calculations, results and analysis, part of results sections of the submitted paper were written by Yoo Soo Yi. Here, the introduction of this study, the structural information of lepidolite structures, the details of calculations, and the calculated results and analyses are presented.

Introduction

Lepidolite [$K(Li,Al)_3(Al,Si)_4O_{10}(F,OH)_2$] is one of phyllosilicate, and it is one of the well-known Li-bearing mineral [85]. In this study, I have tried to explore the atomic structures, detailed electronic structures, and the corresponding NMR parameters of two types of the Li-bearing lepidolite structures (1M- and $2M_2$-types) referred from the previous study [86]. Both lepidolite 1M and $2M_2$ structures consist of alternate layers of SiO_4-AlO_8-SiO_4 and K atoms. Some O atoms of the SiO_4-AlO_8-SiO_4 layer are substituted with the F atoms, and some Al of the SiO_4-AlO_8-SiO_4 layer also can be substituted with Li atoms. The Li atoms can be substituted into the symmetrically inequivalent M1 and M2 sites of the SiO_4-AlO_8-SiO_4 layer, and they can be distinguished as the Li-1 and Li-2 atoms. The previous study has revealed that most substituted Li atoms replace the Al atoms at the M1 site, as the occupation of Li atoms at the M1 site is 1.0 for both the lepidolite 1M and $2M_2$ structures . The Li atoms can be further substituted with the Al atoms at the symmetrically inequivalent M2 site, as the occupations of Li atoms at the M2 sites in the lepidolite 1M and $2M_2$ structures are 0.28 and 0.12, respectively [86]. Thus, four types of lepidolite structures have been used to calculate the NMR parameters of the Li atoms at the symmetrically inequivalent M1 (Li-1 atom) and M2 (Li-2 atom) sites: (1) the lepidolite 1M structure substituted with the Li-1 atom, (2) the lepidolite 1M structure substituted with the Li-1 and Li-2 atoms, (3) the lepidolite $2M_2$ structure substituted with the Li-1 atom, and (4) the lepidolite structures substituted with the Li-1 and Li-2 atoms.

The lepidolite structures substituted with the Li atoms should be relaxed to obtain the reliable and precise lattice topologies, because of the significantly different ionic sizes and charge occupations between the Al and Li atoms. The Mulliken charges, total energy values, and the NMR parameters of the lepidolite 1M and $2M_2$ structures have been calculated using CASTEP based on the projector augmented wave (PAW) type pseudopotential method [78]. The results of the lepidolite structures substituted with the Li-1 atom present considerable differences compared to the results of the lepidolite structures substituted with the Li-1 and Li-2 atoms simultaneously. The Mulliken charges of the O and F atoms around the M1 and M2 sites present significant changes associated with the furthers substitution of the Li atoms at the M2 site, as the Al-O/F bonds are disappeared. The total energy values of the lepidolite structures imply that the lepidolite structures substituted both with the Li-1 and Li-2 atoms are more stable than those substituted only with the Li-1 atom. The calculated NMR parameters for the Li-1 and Li-2 atoms in the lepidolite structures present considerable differences, implying that the Li atoms at the symmetrically inequivalent M1 and M2 sites would be resolvable through the ^{7}Li NMR experiments.

Calculations

In this study, the fine electronic structures around Li atoms and corresponding NMR parameters, such as the chemical shielding and electric field gradient tensors, have been calculated using the projected

augmented wave (PAW) type pseudopotential method implemented in CASTEP [78]. Details about the calculations for the NMR parameters of the lepidolite structures are summarized.

Crystal structures of the lepidolite

Lepidolite [$K(Li,Al)_3(Al,Si)_4O_{10}(F,OH)_2$] is in the mica group of phyllosilicate (layer silicate), and it is one of the well-known most-abundant Li-bearing mineral [85]. In this study, two lepidolite structures (1M-type and $2M_2$-type), which were referred from the previous study [86], have been used to calculate the NMR chemical shielding and electric field gradient (EFG) tensors of Li atoms. In the lepidolite structures, a layer of SiO_4-AlO_8-SiO_4 is alternatively arranged with a layer of K atoms, some O atoms of the AlO_8 are substituted with F atoms, and some Al atoms in the SiO_4-AlO_8-SiO_4 layer are substituted with Li atoms, in both the lepidolite 1M and $2M_2$ structures. Most of the substituted Li atoms replace the Al atoms at the M1 site, since the occupation of Li atoms at the M1 site is 1.0 for both the lepidolite 1M and $2M_2$ structures [86]. According to the previous study [86], the Li atoms can be further substituted with the Al atoms at the symmetrically inequivalent M2 site, as the occupations of Li atoms at the M2 sites in the lepidolite 1M and $2M_2$ structures are 0.28 and 0.12, respectively. The Li atoms, which are substituted with the Al atoms at the M1 and M2 sites, will be distinguished as the Li-1 and Li-2 atoms, respectively. Figure 8-1 presents the crystal structures of lepidolite 1M and $2M_2$ structures substituted with the Li atoms in the crystallographically inequivalent Al-O octahedral M1 (Li-1) and M2 (Li-2) sites. These crystal structures were visualized using VESTA [187]. As abovementioned, the

previous study for the lepidolite 1M and $2M_2$ structures [86] has revealed that the Li-2 atoms (the Li atom substituted with the Al atoms at the M2 site) share the atomic position of Al atoms at the M2 site. Thus, the NMR parameters of the Li atoms in the lepidolite structures have been calculated using the structures in which Al atoms at the M1 site are substituted with the Li atoms and the structures in which Al atoms at both the M1 and M2 sites are substituted with the Li atoms: (1) the lepidolite 1M structure substituted with the Li-1 atoms, (2) the lepidolite $2M_2$ structure substituted with the Li-1 atoms, (3) the lepidolite 1M structures substituted with the Li-1 and Li-2 atoms, and (4) the lepidolite $2M_2$ structures substituted with the Li-1 and Li-2 atoms. Each lepidolite structure was subjected to the geometry optimization prior to calculating the NMR chemical shielding and EFG tensors to obtain the precise and reliable NMR parameters as done in the previous studies for calculating the NMR parameters of the glutamic acid polymorphs [268] and SiO_2 polymorphs [269].

Geometry optimization

The results of calculated NMR chemical shielding and EFG tensors are considerably affected by changes in the fine electronic structures around the target nucleus [87,270]. Thus, the change in the atomic structures associated with the substitution of Li atoms is one of the most important factors to calculated the precise NMR parameters. For this reason, the geometry optimization calculations should be carried out for each lepidolite structure in prior to the NMR parameter calculations for each lepidolite structure. The Perdew-Berke-Ernzerhof scheme optimized for the solid (PBESOL) was used as the exchange-correlation functional to carry

out the geometry optimizations for the lepidolite structures [194]. The PAW-type ultrasoft pseudopotential (USP) scheme was used to describe the electronic interactions. The plane-wave-cutoff energy was set to 340 eV. The SCF convergence criterion for the total energy was 2×10^{-6} eV/atom. Only two inequivalent *k* points in the irreducible Brillouin zone was used for the self-consistent-field (SCF) calculations, since the single *Γ* point has been reported to be sufficient for the simple insulating oxides [68]. The smearing parameter, which indicates the broadening width of the occupied electronic states, was set to 0.2 eV to enhance the convergence of the SCF calculations. The Broyden-Fletcher-Goldfarb-Shanno (BFGS) algorithm was used for this geometry optimization [271]. The maximum values of force, stress, and atomic displacement applied to each atom were set to 0.03 eV/Å, 0.05 GPa, and 0.001 Å, respectively. The unit cell size of each lepidolite structure was fixed, so as not to change, during the geometry optimization calculations.

Calculating NMR chemical shielding and EFG tensors

The NMR chemical shielding (σ_{iso}, σ_{aniso}, η_{cs}) and EFG (C_q, η_Q) tensors of the Li atoms at the symmetrically inequivalent sites (Li-1 and Li-2 atoms) have been calculated using the optimized lepidolite structures. The NMR parameters have been calculated based on the gauge including projector augmented wave (GIPAW) method implemented in CASTEP [87,269,270]. The PBESOL method was used as the exchange-correlation functional [194]. The PAW-type ultrasoft pseudopotential with on the fly scheme, which calculates the pseudopotential for each SCF calculation step, should be used to calculate the NMR properties, not the conventionally

used ultrasoft pseudopotential (USP) and norm-conserving pseudopotential (NCP). The SCF convergence criterion for the total energy was set to 1×10^{-6} eV/atom. The smearing parameter was set to 0.2 eV. Since the NMR chemical shielding and EFG tensors are determined from the fine electronic structures around the target nucleus, the plane-wave-cutoff energy of 1000 eV, which is much larger than conventionally used 300-500 eV, was used to obtain the more accurate electronic wave functions. The number of inequivalent *k* points in the irreducible Brillouin zone was set to 48 and 45 for the lepidolite 1M and $2M_2$ structures, respectively. These input values each were determined after confirming the convergence of the NMR parameters; the number of inequivalent *k* points from 20 to 90 and the plane-wave-cutoff energy from 550 to 1200 eV. Finally, the reliable NMR parameters, which converge in less than 5%, have been presented in this study.

Results and discussion

The changes in the atomic structures, the Mulliken charges, the total energies, and the NMR parameters of the lepidolite structures associated with the substitution of the Li atoms with the Al atoms in the SiO_4-AlO_8-SiO_4 layer are discussed here.

Structural changes in the lepidolite due to the substitution of Li atoms

In the lepidolite structures explored in this study, the local atomic structures around the M1 (already occupied with the Li atoms; Li-1 atom)

and M2 sites significantly change due to the further substitution of the Li atoms with the Al atoms at the M2 site (Li-2 atom). Table 8-1 presents the structural characteristics of the lepidolite 1M and 2M2 structures substituted with either the Li-1 atom or the Li-1 and Li-2 atoms, after the geometry optimization calculations. I note that the space group of each lepidolite structure substituted with the L atoms, presented in Tab. 1, is slightly different from the results of the previous study because of the geometry optimization calculations [86]. Thus, the changes in the local atomic structures around the M1 and M2 sites can be confirmed through the comparison between the lepidolite structures substituted with the Li-1 atoms and those substituted with the Li-1 and Li-2 atoms.

In the lepidolite 1M structure, the average atomic distance of the Li-O/F octahedra with the Li-1 atom decreases by 0.80% (from 2.1215 to 2.1045 Å) but its volume increase by 0.97% (from 11.9259 to 12.0412 $Å^3$), due to the further substitution of the Li-2 atoms. The structural distortion of the Li-O/F octahedra with the Li-1 atom seemed to be relatively reduced; the quadratic elongation index (λ), which represents the structural distortion of the Li-O/F octahedron compared with the corresponding regular octahedron and, thus, the changes in the surrounding electric field gradient, decrease by 2.45% (from 1.0468 to 1.0212). The local atomic structures around the M2 site also significantly change due to the further substitution of the Li atoms, since the Al-O bonds are disappeared with the substitution of the Li atoms. The average atomic distance and volume of this octahedral site increase by 9.27% (from 1.9323 to 2.1115 Å) and 30.54% (from 9.3076 to 12.1499 $Å^3$), respectively. The λ decreases by 0.02% (from 1.0223 to 1.0221) implying the slightly reduced structural distortion in this

octahedral site due to the further substitution of Li-2 atoms. In the lepidolite $2M_2$ structures, the average atomic distance the Li-O/F octahedra with the Li-1 atom decreases by 0.33% (from 2.1261 to 2.1191 Å), but its volume increases 1.27% (from 12.1754 to 12.3305 $Å^3$), with the further substitution of the Li-2 atoms as in the lepidolite 1M structure. The λ index decreases 1.55% (from 1.0356 to 1.0195) implying the reduced structural distortion of the corresponding octahedral site. The local atomic structures around the M2 site, in this lepidolite $2M_2$ structure, also present significant changes due to the further substitution of the Li-2 atoms. The average atomic distance and volume of this octahedral site (M2) increase by 7.92% (from 1.9569 to 2.1119 Å) and 25.60% (from 9.7179 to 12.2061 $Å^3$), respectively. The λ decreases by 0.08% (from 1.0202 to 1.0194). These results of the geometry optimization calculations imply that the electric field gradient around the M1 and M2 sites and, thus, the fine electronic structures of the lepidolite structures can be affected by the further substitution of the Li atoms into the M2 site.

Calculated total energies for the lepidolite structures

Table 8-2 presents the changes in the total energy of the lepidolite 1M and $2M_2$ structures due to the further substitution of Li atoms at the M2 site (Li-2 atom). The presented energy values of the lepidolite structures are the Kohn-Sham energy (E_{KS}), the free energy (E_{TS}), and the corrected free energy approximated at 0 K ($E_{0.5TS}$). A smearing parameter was introduced to calculate the electronic structures of the lepidolite structures more efficiently. This smearing parameter adds the artificial electronic temperature effects to the electronic structure calculations for the lepidolite

structures. Thus, the E_{KS} obtained through the electronic structure calculations includes the disorder induced from the artificial electronic temperature (T), i.e. the Mermin entropy (S). The Mermin entropy is an effect manifested by the artificial electronic temperature, which affects how to fill the partially occupied electronic bands. The energy value including the effects of the artificial electronic temperature can be calculated with the free energy of E_{KS}-TS, as in Tab. 2 [272]. However, since the free energy of E_{KS}-TS is significantly affected by the smearing parameter (if T increases, the effects of the Mermin entropy also increases), averaging with E_{KS} would provide a better approximation to the energy at 0 K, i.e. the corrected free energy of E_{KS}-0.5TS [272]. The corrected free energies of the lepidolite 1M and 2M2 structures were compared according to the substitution state of the Li atoms; substitution only with the Li-1 atom or substitution with the Li-1 and Li-2 atoms. I should note that, in interpreting the results in Tab. 2, the calculated energy values of the lepidolite 1M and $2M_2$ structures cannot be compared directly because the numbers of atoms contained in their unit cells are different.

The calculated E_{KS}, E_{TS}, and $E_{0.5TS}$ for the lepidolite 1M structure substituted with the Li-1 atom were -15248.47, -15248.63, and -15248.55 eV, respectively. These energy values of the lepidolite structures considerably decrease with the further substitution of the Li atoms into the M2 site: The calculated E_{KS}, E_{TS}, and $E_{0.5TS}$ each decreases by ~1.11% from ~-15248 to ~-15402 eV as shown in Tab. 3. In the lepidolite $2M_2$ structure, the calculated E_{KS}, E_{TS}, and $E_{0.5TS}$ also decrease by ~0.95% with the further substitution of the Li-2 atoms. Since the lepidolite structures substituted with the Li-1 and Li-2 atoms are more stable than those substituted only with the Li-1 atom,

the results of this study are consistent in part with the previous study that has revealed the presence of the Li atoms at the symmetrically inequivalent M1 and M2 sites in the lepidolite 1M and $2M_2$ structures [86]. I note that the occupation of the Li atoms at the M2 sites in the lepidolite structures could be slightly larger than the results reported in the previous study (the occupations of the Li atoms at the M2 site in the lepidolite 1M and 2M2 structures are 0.28 and 0.12, respectively) [86], because it seems that the Li atoms prefer to be substituted into the M1 and M2 sites at the same time.

Calculated Mulliken charges for the lepidolite structures

The Mulliken population analysis have been carried out for the lepidolite structures using the linear combination of atomic orbital (LCAO) method implemented in CASTEP [78]. The results of the calculated Mulliken population gives the number of electrons occupied in each orbital, and it thus also can provide the Mulliken charge of each atom by comparing the original number of electrons in each orbital and the total Mulliken populations. Figure 8-2 presents the Mulliken charge of the Li (substituted into M1 and M2 sites), Al (M2 sites), O, and F atoms around the M1 and M2 sites in the lepidolite 1M and $2M_2$ structures (the Li-O/F and Al-O/F octahedral sites). I note that the Mulliken charges of these atoms in the lepidolite structures, in which Al atoms at the M1 site are already substituted with the Li atoms, considerably change, since Al atoms at the M2 site are further substituted with the Li atoms. Each Mulliken population of the Li-1 atom increases with the further substitution of the Li-2 atoms, and thus the Mulliken charge of the Li-1 atom change from +1 to +0.9 e in the lepidolite 1M structure and from +0.98 to +0.9 e in the

lepidolite $2M_2$ structure, respectively. The Mulliken charges of the O and F atoms around the M1 and M2 sites also decrease with the further substitution of the Li-2 atoms, since the Al-O/F bonds at the M2 sites are disappeared as the Al atom is replaced with the Li atom. These changes in the Mulliken charge of the Li-1 atoms, as well as the O and F atoms, associated with the further substitution of the Li-2 atoms, imply the considerable changes in the electric field gradient at the M1 and M2 sites along with corresponding NMR parameters.

Calculated NMR parameters for the lepidolite structures

Table 8-3 presents the calculated NMR parameters for the lepidolite 1M and $2M_2$ structures substituted with the Li atoms in the symmetrically inequivalent M1 (Li-1 atom) and M_2 (Li-2 atom) sites. The results in Tab. 3 present the chemical shielding tensor [the isotropic chemical shielding (σ_{iso}), the isotropic chemical shielding (σ_{aniso}), the asymmetry parameter (η_{cs})] and the EFG tensor [the quadrupolar coupling constant (C_Q) and the asymmetry parameter (η_Q)] of the Li atoms at the symmetrically inequivalent M1 and M2 sites in the lepidolite structures. The NMR parameters of the Li-1 atom in the lepidolite 1M structure substituted only with the Li-1 atom were calculated as following. The σ_{iso}, σ_{aniso}, and η_{cs} were -530.79 ppm, -1841.77 ppm, and 0, respectively; and the C_Q and η_Q were 4.18×10^{-3} MHz and 0.89, respectively. These NMR parameters of the Li-1 atom in the lepidolite 1M structure significantly change with the structural changes associated with the further substitution of the Li-2 atoms. The σ_{iso}, $\sigma_{aniso,}$ and η_{cs} increase by 620.72 ppm (from -530.79 to 89.93 ppm), 1837.38 ppm (from -1841.77 to -4.39 ppm), and 0.18

(from 0 to 0.18), respectively; and the C_Q and η_Q also change from 4.18×10^{-3} to -7.71×10^{-2} MHz and from 0.89 to 0.7, respectively. The chemical shielding and EFG tensors of the Li-2 atom in the lepidolite 1M structure substituted with the Li-1 and Li-2 atoms were obtained as following. The σ_{iso}, σ_{aniso}, η_{cs}, C_Q, and η_Q were 90 ppm, -4.03 ppm, 0.15, 4.47×10^{-2} MHz, and 0.68, respectively. In the lepidolite $2M_2$ structure, the NMR parameters of the Li-1 atom also present significant changes with the further substitution of the Li-2 atoms, as in the lepidolite 1M structure. The σ_{iso}, $\sigma_{aniso,}$ and η_{cs} decrease by -70.63 ppm (from 60.62 to -10.01 ppm), -270.41 ppm (from -54.77 to -325.18 ppm), and -0.11 (from 0.19 to 0.08), respectively; and the C_Q and η_Q also change from 1.67×10^{-1} to 3.67×10^{-2} MHz and from 0.09 to 0.89, respectively. The NMR parameters of the Li-2 atoms in the lepidolite $2M_2$ structure substituted with the Li-1 and Li-2 atoms were calculated as following. The σ_{iso}, σ_{aniso}, η_{cs}, C_Q, and η_Q were -13.86 ppm, -318.63 ppm, 0.12, 4.81×10^{-2} MHz, and 0.28, respectively. These changes in the NMR parameters of the Li-1 atom associated with the further substitution of the Li-2 atom are due to the changes in the local atomic structures around the M1 site (the volume of the Li-O/F octahedron at the M1 site increases while the λ decreases, see Tab. 1) and associated changes in the charge distribution (the Mulliken charge of the Li-1 atom adjacent to the M2 site decreases, see Fig. 8-2).

The calculated isotropic (σ_{iso}) and anisotropic (σ_{aniso}) chemical shielding for the Li atoms at the M1 (Li-1) and M2 (Li-2) sites in the lepidolite structures present differences about 0.07-6.5 ppm, and their quadrupolar coupling constants (C_Q) also present significant differences in both the lepidolite 1M (1.22×10^{-1} MHz) and $2M_2$ (1.13×10^{-2} MHz) structures.

These considerable differences in the calculated NMR parameters imply that the Li atoms at the symmetrically inequivalent sites in the lepidolite structures would be distinguishable using the NMR experiments, since the Li NMR experiments have been used to probe the local atomic structures, such as the coordination environments, of the diverse mixed-cation silicate glasses and inorganic matrixes [273-278]. The Li NMR experiments are carried out on the stable Li isotopes, i.e. ^{6}Li [I = 1, Q = ~-8×10^{-4} Barn, and the natural abundance of 7.4%] and ^{7}Li [I = 3/2, Q = ~-4×10^{-2} Barn, and the natural abundance of 92.58%] [279,280]. These ^{6}Li and ^{7}Li are quadrupolar nuclides and, thus, they would have complex interactions with the surrounding electric field gradient. The ^{6}Li (I = 1), which has a relatively small C_Q value, has been known to behave like the spin-1/2 elements because of its negligibly small quadrupolar splitting [280]. The high-resolution Li NMR spectrum thus would be better obtained from the ^{6}Li isotope rather than ^{7}Li isotope. However, the NMR experiments for the Li atoms are commonly carried out for the ^{7}Li isotope (I = 3/2, Q = ~-4×10^{-2} Barn) because of its enormously large natural abundance [281]. This makes it difficult to interpret the ^{7}Li NMR spectrum, because the conventional 1D magic angle spinning (MAS) experiments cannot completely remove the perturbation effects from the quadrupolar interactions. Therefore, the 2D multiple quantum magic angle spinning (MQMAS), which can significantly reduce the dipole-dipole and quadrupolar interactions [282], and the ^{7}Li-^{7}Li homonuclear correlation MAS experiments, which can establish the spatial correlations of spins [278,280], would be helpful to resolve the Li atoms located at the symmetrically inequivalent sites in the lepidolite structures.

Conclusion

The modern *ab initio* calculations have been used to interpret and predict the diverse spectroscopic results, such as the x-ray Raman scattering (XRS) [3,7] and nuclear magnetic resonance (NMR) [283,284], of the multi-component and complex crystalline and noncrystalline oxides. In this study, I have revealed the NMR parameters, i.e. the isotropic (σ_{iso}) and anisotropic (σ_{aniso}) chemical shielding and electric field gradient (EFG) tensors, of the Li-bearing lepidolite structures. The lepidolite structures, in which Al atoms at the M1 site are already replaced with the Li atoms (Li-1), present considerable structural changes due to the further substitution of the Li atoms with the Al atoms at the M2 site (Li-2). Since the calculated total energy values for the lepidolite structures reveal that the lepidolite structures substituted with the Li-1 and Li-2 atoms are more stable than those substituted only with the Li-1 atom, and, thus, the Li atoms can further replace the Al atoms at the M2 site. The Mulliken charges of the O and F atoms around the M1 and M2 sites present considerable decreases with the further substitution of the Li atoms at the M2 site implying the changes in the detailed electronic structures, such as the electric field gradient (EFG) and, thus, the corresponding NMR parameters. The calculated NMR parameters for the Li atoms at the M1 and M2 sites in the lepidolite structures present considerable differences in the chemical shielding and EFG tensors. This difference between the NMR parameters of the Li atoms at the symmetrically inequivalent sites suggests that the Li atoms at the M1 and M2 sites in the lepidolite structures would be resolvable through the 2D MQMAS and the ^{7}Li-^{7}Li homonuclear correlation

MAS NMR experiments. I believe that the current results, i.e. the theoretical approach have been used to explore the site-specific NMR parameters in the lepidolite structures, can shed light on probing the atomistic accounts of the NMR crystallography of the diverse multi-component and complex layer silicates.

Figures and Tables

Figure 8-1. Crystal structures of the lepidolite 1M and $2M_2$ structures. The Al atoms at the symmetrically inequivalent M1 and M2 sites (Al-O/F octahedral site) in the SiO_4-AlO_8-SiO_4 layer are substituted with the Li atoms (Li-1 and Li-2, respectively).

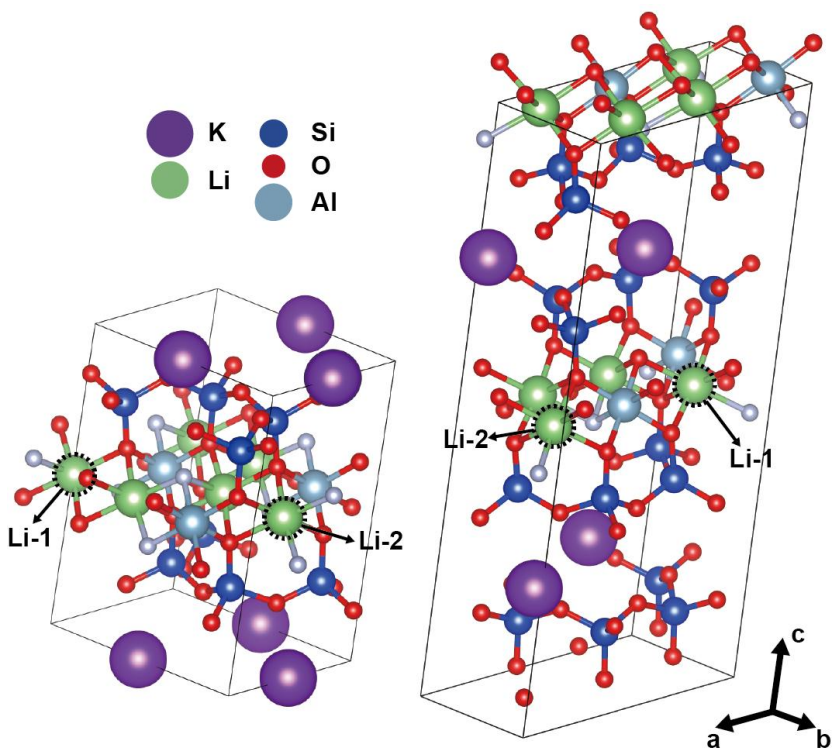

Figure 8-2. Mulliken charge distribution around the symmetrically inequivalent M1 and M2 sites. Mulliken charges are presented for the Li, Al, O, and F atoms of the SiO_4-AlO_8-SiO_4 layer in the lepidolite 1M and $2M_2$ structures substituted with the Li atoms at the M1 (Li-1) and M2 (Li-2) sites.

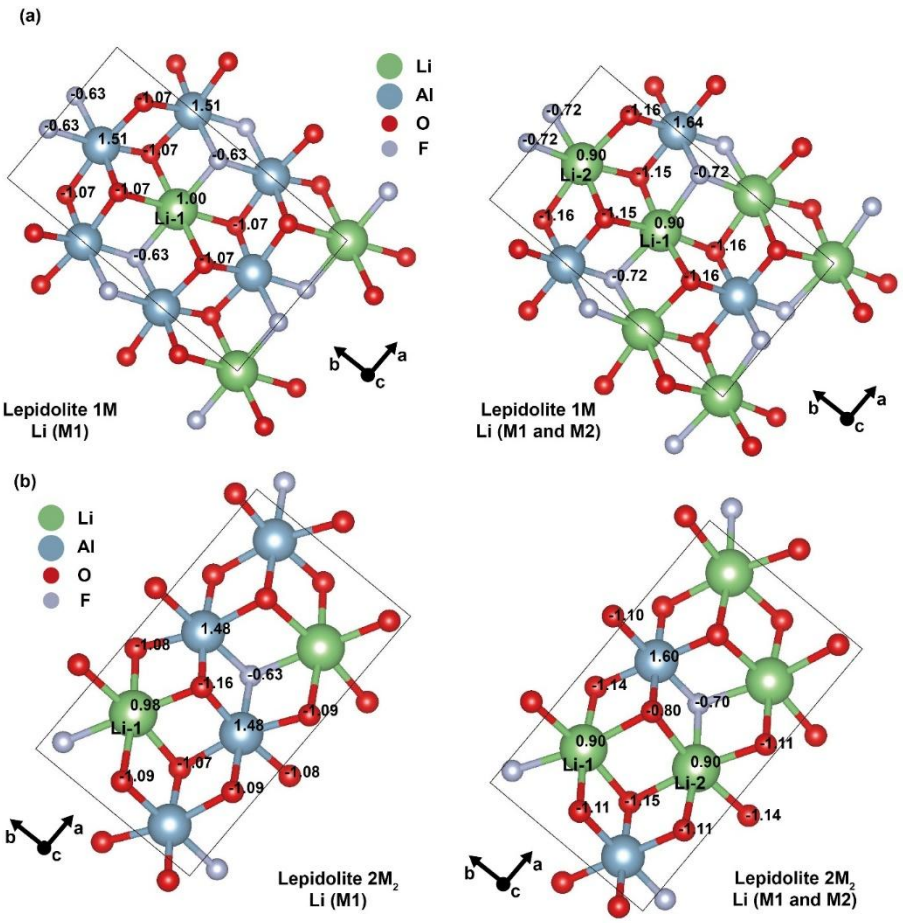

Table 8-1. Space groups, lattice parameters, and internal variables of the lepidolite 1M and $2M_2$ structures substituted with Li atoms at the symmetrically inequivalent M1 and M2 sites in the SiO_4-AlO_8-SiO_4 layer.

Structure			**Lepidolite 1M**		**Lepidolite $2M_2$**	
System			Monoclinic			
Space group			(12) C 2/m	(5) C 2	(9) C c	(9) C c
Substitution			Li (M1)	Li (M1/M2)	Li (M1)	Li (M1/M2)
Cell parameter	a (Å)		5.2090		9.0230	
	b (Å)		9.0110		5.1970	
	c (Å)		10.1490		20.1710	
	α, β (°)		90		90	
	γ (°)		100.7700		99.4800	
Li (M1) octahedron	Avg. dist. (Å)	Li-O	2.1922	2.1026	2.1304	2.1251
		Li-F	1.9800	2.1082	2.1044	2.0892
		Li-O/F	2.1215	2.1045	2.1261	2.1191
	V (Å^3)		11.9259	12.0412	12.1754	12.3305
	λ		1.0468	1.0212	1.0356	1.0195
Li (M2) octahedron	Avg. dist. (Å)	Li-O		2.1320		2.1167
		Li-F		2.0704		2.0881
		Li-O/F		2.1115		2.1119
	V (Å^3)			12.1499		12.2061
	λ			1.0221		1.0194
Al (M2) octahedron	Avg. dist. (Å)	Al-O	1.9315		1.9480	
		Al-F	1.9340		2.0015	
		Al-O/F	1.9323		1.9569	
	V (Å^3)		9.3076		9.7179	
	λ		1.0223		1.0202	

$\langle\lambda\rangle = \frac{1}{n}\sum_{i=1}^{n}\left(\frac{l_i}{l_0}\right)^2$; the quadratic elongation

The l_i is the center-to-vertex distance of the corresponding octahedron

The l_0 is the center-to-vertex distance of a regular octahedron of the same volume

Table 8-2. Total energy values of the lepidolite 1M and $2M_2$ structures substituted with Li atoms at the symmetrically inequivalent M1 and M2 sites.

Structure	Substituted sites	Energy (eV)		
		E_{KS}[(1)]	E_{TS}[(2)]	$E_{0.5TS}$[(3)]
Lepidolite 1M	M1	-15248.47	-15248.63	-15248.55
	M1 and M2	-15402.81	-15402.81	-15402.81
Lepidolite $2M_2$	M1	-29613.66	-29613.76	-29613.71
	M1 and M2	-29894.87	-29895.51	-29895.19

(1) E_{KS} is the final Kohn-Sham energy
(2) E_{TS} is the free energy including the electronic artificial temperature of smearing (T) and the Mermin entropy (S); E_{KS}-TS
(3) $E_{0.5TS}$ is the corrected free energy for approximation to the energy at 0 K; E_{KS}-0.5TS

Table 8-3. NMR chemical shielding and electric field grading (EFG) tensors of the lepidolite 1M and $2M_2$ structures substituted with Li atoms at the symmetrically inequivalent M1 and M2 sites.

Structure	Substituted sites	Atom	Chemical shielding tensor			EFG tensor	
			σ_{iso}(1)	σ_{aniso}(2)	η_{cs}(3)	C_Q(4)	η_Q(5)
Lepidolite 1M	M1	Li-1	-530.79	-1841.77	0	4.18×10^{-3}	0.89
	M1 and M2	Li-1	89.93	-4.39	0.18	-7.71×10^{-2}	0.7
		Li-2	90	-4.03	0.15	4.47×10^{-2}	0.68
Lepidolite $2M_2$	M1	Li-1	60.62	-54.77	0.19	1.67×10^{-1}	0.09
	M1 and M2	Li-1	-10.01	-325.18	0.08	3.67×10^{-2}	0.89
		Li-2	-13.86	-318.63	0.12	4.81×10^{-2}	0.28

(1) Isotropic chemical shielding (ppm); $\sigma_{iso} = (\sigma_{xx}+\sigma_{yy}+\sigma_{zz})/3$
(2) Anisotropic chemical shielding (ppm); $\Delta = \sigma_{zz}-\sigma_{iso}$
(3) Asymmetry parameter of chemical shielding tenso; $\eta_{cs} = (\sigma_{xx}-\sigma_{yy})/\Delta$
(4) Quadrupolar coupling constant (MHz); $C_Q = eQV_{zz}/h$;
V_{zz} is the largest component of the diagonalized EFG tensor,
Q is the nuclear quadrupole moment (Q_{Li} = -0.0401 Barn; ^{7}Li), and h is the Plank constant.
(5) Asymmetry parameter of electric field gradient tensor; $\eta_Q = (V_{xx}-V_{yy})/V_{zz}$

Appendix

Theoretical background

본 연구에서는 제 1 원리 양자계산을 이용하여 결정질 및 비결정질 SiO_2 와 $MgSiO_3$ 물질들의 전자구조와 O K-edge XRS 스펙트럼을 계산하였습니다. 상세한 내용은 이전 한국 광물학회에 출간한 논문들에 정리되어 있습니다 [285-287]. 하지만, 편의를 위하여 해당 논문의 이론적 배경 부분들을 발췌하였습니다. 특히, O *K*-edge XRS 스펙트럼의 정확한 결과를 얻기 위해서는 x-선 Raman 산란에 의해 나타나는 O 원자의 1*s* 정공(core hole)을 고려해야 한다. 이에 대한 내용은 최근에 제가 제 2 저자로 참여하여 출판된 광물학회의 논문에 상세하게 정리되어 있습니다 [287].

밀도 범함수 이론 (density functional theory)

본 연구에 이용된 양자화학계산은 물질을 구성하는 원자의 전자들의 상호작용을 기술하는 방법에 따라서 분류할 수 있으며, 대표적인 것으로는 대상 물질의 구성 원자로 이루어진 계의 기저 에너지(ground state energy)를 구할 때 모든 전자들을 계산에 포함하는 Hartree-Fock(HF) 방법론과 전자를 원자 주변에 퍼져있는 전자 밀도로 취급하는 밀도 범함수 이론(DFT; density functional theory)가 있다. HF 방법론의 경우 모든 전자들이 계산에 포함되어 계를 이루는 구성 원자의 숫자가 많아질수록 계산을 위한 많은 컴퓨팅 자원을 필요로 하게 된다. 이와 달리 DFT 는 전자들을 전자 밀도로 취급하여 n-전자 해밀토니안이 하나의 전자가 전자 밀도분포와 상호작용을 하는 단일-전자 해밀토니안으로 바뀌며 상대적으로 계산의 효율성이 높아져 많은 숫자의 원자를 계에 포함시켜야 하는 연구에 많이 이용되고 있다.

DFT 에서는 계를 구성하는 전자들이 정전기력에 의해서만 영향을 받고 서로 상호작용을 하지 않는다고 가정을 하고 해밀토니안을 기술한 다음, 전자의 파동함수에 의해서 나타나는 양자역학적인 교환-상관 상호작용(exchange-correlation interaction)에 의한 에너지를 교환-상관 퍼텐셜(exchange-correlation potential)에 근사하여 해밀토니안을 기술한다. DFT 의 해밀토니안은 Kohn-Sham 해밀토니안이라 불리며, 계의 전체 에너지는 상호작용하지 않는 전자들의 운동 에너지, 기준 전자와 원자핵들의 정전기력에 의한 에너지, 기준 전자와 주변 전자밀도와의 정전기력에 의한 에너지, 그리고 양자역학적 효과에 의한 교환-상관 에너지의 합으로 표현된다. 참고로 DFT 는 전자들의 교환-상관 상호작용이 모두 포함되어 있지만 전자들을 밀도 분포로 표현하여 교환-상관 에너지를 근사값으로 계산하는 반면에, 위에서 언급된 HF 방법론은 교환 상호작용에 의한 에너지만 해밀토니안에 포함되어 있지만 모든 전자들이 계산에 포함되어 교환 에너지를 구할 때 근사값을 취하지 않는다. 교환-상관 에너지는 DFT 의 해밀토니안에서 상호작용하지 않는 것으로 가정한 전자들에 대하여 양자역학적 효과에 의한 보정을 하기 위한 에너지 값으로서, 교환-상관 에너지의 교환 에너지는 전자 오비탈 파동함수의 반-대칭성(anti-symmetry)에 의한 Pauli 배타원리에서 나타나는 전자간의 반발(repulsion)로 나타나는 교환 상호작용에서 기인하며, 상관 에너지는 다른 스핀을 갖는 전자가 같은 오비탈을 채움으로써 나타나는 전자간의 반발에 의한 상관 상호작용에 기인하고 있다. 계의 구성 원자의 종류와 원자구조에 따라 그 값이 달라지는 교환-상관 에너지는 그 값이 전체 에너지에서 차지하는 비율은 작지만 띠 틈(band gap)과 같은 전자구조를 결정하는데 중요할 역할을 한다 [288-290].

밀 도 범함수 이론은 교환-상관 범함수를 표현하기 위해 이용하는 전자밀도의 정보(전자밀도 $\rho_{\uparrow\downarrow}$, 전자밀도의 기울기 $\nabla\rho_{\uparrow\downarrow}$, 전자밀도의 라플라시안 $\nabla^2\rho_{\uparrow\downarrow}$)에 따라 구분이 된다 [290]. 국소 밀도 근사(LDA; local density approximation) 방법론은 전자밀도의 분포를 기술할 때 교환-상관 범함수를 전자밀도에 대한 정보만으로 기술하는 것으로서 전하 분포가 급격하게 바뀌지 않는 금속이나 공유결합으로 이루어진 물질들을 기술하는데 주로 이용된다 [289]. 일반화된 기울기 근사(GGA; generalized gradient approximation) 방법론은 LDA 방법론과 달리 교환-상관 에너지의 더 정확한 근사를 위하여 전자밀도와 전자밀도의 기울기를 교환-상관 범함수를 표현하는데 이용하는 것이다 [289]. GGA 방법론에 의한 계산결과를 더 향상시키기 위하여 교환-상관 범함수를 기술하는데 전자밀도의 라플라시안을 추가적으로 이용하는 meta-GGA 방법론도 개발되었다 [291]. 본 연구에서는 GGA 방법론에 기반을 두고 있는 Perdew-Berke-Ernzerhof(PBE)-GGA 방법론을 고체 물질의 전자구조 계산에 최적화 한 PBEsol-GGA 방법론을 이용하여 양자화학계산을 수행하였다 [194,210]. 참고로 LDA 나 GGA 에 기반을 둔 방법론들은 Fe-산화물과 같이 국소화된 3*d*-오비탈(localized 3d-orbital)이 존재하는 강상관 전자계(strongly correlated electron system)에서는 *on-site* (intra-atomic) 전자-전자 상호작용에 의한 전자간의 반발력에 대한 정보가 포함되지 못하여 계산 결과에 오류가 발생한다. 이를 개선하기 위해 *on-site* 전자-전자 상호작용에 의한 반발 에너지를 변수화(Hubbard potential; U)하여 도입한 DFT+U(LDA+U, GGA+U) 방법론이 개발되었다 [292,293]. 이러한 것들 이외에도 B3LYP 와 같은 여러 접근 방법으로 만들어진 교환-상관 범함수들을 실험결과를 잘

재현하도록 조합하여 만들어진 복합 범함수(hybrid functional) 방법론도 이용되고 있다 [294].

ELNES 분석 이론

특정 원자에 대한 ELNES 스펙트럼은 x-선에 의한 전자 오비탈의 흡수에 수반되는 전자의 여기 현상으로 나타나기 때문에 대상원자 주변의 전자구조를 반영한다. 전자 여기 현상은 페르미 황금률(Fermi golden rule)을 따르며, 전이확률은 아래와 같다:

$$dW_{if} = \frac{2\pi}{\hbar}|\langle f|V|i\rangle|^2 dv_f \delta(E + E_i - E_f),\ \ dv_f = \frac{2m_e}{2\hbar} k_f dE d\Omega$$

여기서 'i' 와 'f'는 각각 전자의 초기 상태와 전이 이후의 파동함수, 'k_f'는 전이 이후의 파동함수의 파수벡터 (wave vector)이며, 'E_i' 와 'E_f'는 초기상태와 전이 이후 상태의 에너지를 뜻한다. '$\hbar$'와 'm_e'는 각각 플랑크 상수(Plank's constant)와 전자의 질량을 의미한다. 그리고, 'V'는 특정원자 주변의 전자구조로 인하여 발생하는 포텐셜로 원자구조에 따라 달라지는 값이다. 'Ω'는 특정원자에 산란된 광전자가 공간상에 퍼져나가는 입체각을 의미한다 [295,296]. 그리고 발생하는 광전자의 흐름은 다음의 식과 같이 정의된다:

$$d\sigma = \sum_{i,f} \frac{(2\pi)^3 m_e}{\hbar k_i} dW_{if}$$

그리고, x-선 라만 산란 실험에서 얻어지는 대상원자의 ELNES 스펙트럼은 아래의 식과 같은 DDSCS(double differential scattering cross section)을 통하여 구한다:

$$\frac{\partial^2\sigma}{\partial E\partial\Omega} = 4\left(\frac{e_0}{q}\right)^4 m_e^2 \frac{k_f}{k_i} S(\vec{q}, E)$$

위 식의 $S(\vec{q}, E)$ 는 dynamic form factor (DFF)로 전자의 전이확률과 유사한 형태를 가지며 아래의 식과 같이 주어진다.

$$S(\vec{q}, E) = \sum_{f,i} \left|\langle f|e^{i\vec{q}\cdot\vec{r}}|i\rangle\right| \delta\left(E + E_i - E_f\right)$$

본 연구에서는 양자계산을 이용하여 전자 오비탈의 초기상태와 여기상태의 파동함수를 구하고, 이로부터 대상원자의 DDSCS 와 ELNES 스펙트럼을 계산하였다(아래의 방법 참조).

양자계산을 이용한 결정의 전자구조 계산

양자계산은 양자역학의 이론을 이용하여 대상 물질의 원자구조에 따른 전자구조를 계산함으로써 물질의 다양한 물성과 실험의 결과를 예측하는 방법이다. 이 방법론의 핵심은 전자 오비탈을 파동함수(wave function)로 표현하고 시스템의 특성을 표현하는 해밀토니안 연산자(Hamiltonian operator)를 이용하여 전자구조와 에너지를 계산하는 것이다. 이때 해밀토니안 연산자를 표현하는 방법에 따라서 하트리-폭 근사법(Hartree-Fock approximation; HF), 배열 상호작용 (configuration interaction; CI) 방법, 몰러-플레셋 섭동 (Moller-

Plesset perturbation), 밀도범함수 이론 (density functional theory; DFT) 등으로 나뉘고, 전자 오비탈을 표현하기 위한 기저함수의 종류에 따라 가우스 함수 (Gaussian function), 직교 평면파 (orthogonal plane wave; OPW), 보충 평면파(augmented plane wave; APW)와 같이 분류할 수 있다[297-299]. DFT 를 기반으로 하는 많은 양자화학계산 방법론들은 원자구조에 따른 원자핵-전자 상호작용을 변수화하여 원자핵 부근의 전자구조를 간단하게 근사화시켜 계산을 수행하는 유사 퍼텐셜(pseudo potential) 방법론을 이용한다 [289]. 하지만 유사 퍼텐셜을 이용한 방법론은 원자핵 주변의 전자구조가 미리 계산되어 변수화 되어 있는 유사 퍼텐셜에 의하여 결정되기 때문에, 원자핵 주변 전자의 여기 현상을 이용한 XRS 실험의 ELNES 스펙트럼이나 원자핵 주변의 미세 전자구조에 의하여 결정되는 핵자기 공명(NMR; nuclear magnetic resonance) 스펙트럼에 대한 정보를 얻기 위해서는 대상 물질에 대하여 매번 원자핵 주변 전자에 수정을 가한 전자구조를 이용하여 유사 퍼텐셜을 구하거나 게이지 포함 프로젝터 보충파(GIPAW; gauge including projector augmented wave) 방법론과 같은 것을 도입해야 하는 어려움이 따른다 [270,300]. 이와 달리 본 연구에서 사용한 FP-LAPW 방법론은, 전자구조를 계산할 때 유사 퍼텐셜을 적용하지 않고 직접 원자핵-전자 상호작용에 대하여 계산을 수행하기 때문에, 유사 퍼텐셜을 사용하는 방법론들에 비하여 효율성은 떨어지지만 원자핵 주변의 전자구조를 잘 기술하여 물질의 ELNES 스펙트럼을 비롯한 원자 주변의 전자구조에 기인한 다양한 분광학적 특성을 예측하는데 매우 유용하다 [182,301].

본 연구에서는 LAPW 와 선형화 보충 평면파와 국소-오비탈 조합(augmented plane wave + local orbital: APW+lo)을 이용하여 대상의

전자분포를 표현하는 방법론을 이용하였다. LAPW 에서 전자 오비탈을 묘사하는 파동함수의 식은 아래와 같이 주어진다:

$$\phi_{K_n}(r) = \begin{cases} \sum_{lm} \left[A_{lm}^{K_n} u_l(r, E_l) + B_{lm}^{K_n} \dot{u}_l(r, E_l)\right] Y_{lm}(\hat{r}), & r < R_a \\ \Omega^{-\frac{1}{2}} \cdot e^{i(k+K_n)\cdot r}, & r \in I \end{cases}$$

$$\psi_K = \sum_n C_n \cdot \phi_{K_n}$$

위 식에 정리된 LAPW 는 원자핵 주변에서는 구면조화함수를 이용하고, 원자들 사이의 공간(interstitial region)에서는 평면파를 통하여 전자의 분포를 나타낸다. 그리고 APW+lo 방법에서 추가되는 국소-오비탈에 대한 파동함수는 아래의 식과 같이 주어진다:

$$\phi_{lm}^{Lo}(r) = \begin{cases} \left[A_{lm} u_l(r, E_l) + B_{lm} \dot{u}_l(r, E_{1,l}) + C_{lm} u_l(r, E_{2,l})\right] Y_{lm}(\hat{r}), & r < R_a \\ 0, & r \in I \end{cases}$$

위 식의 APW+lo 는 LAPW 에 국소-오비탈(local orbital)에 대한 정보를 추가하여 전자의 분포를 나타낸다. 위의 식에 나타나는 'ϕ_{K_n}'과 'ϕ_{lm}^{Lo}'는 결정 내부에서 'K_n'의 주기성을 갖는 특정원자 전자 오비탈과 국소-오비탈을 표현하는 분자-오비탈(molecular orbital)이며 원자핵 주변($r < R_a$)에서는 구면조화함수 'Y_{lm}'와 슈뢰딩거 방정식의 방사상 부분의 해(radial solution)인 'u_l'과 에너지의 변화량을 의미하는 '$\dot{u}_l$'로 표현되어 있다 (각 A_{lm}, B_{lm}, C_{lm} 는 구면조화함수에 따른 계수를 의미함). 그리고 DFT 의 콘-샴 방정식(Kohn-Sham equation)의 해인 'ψ_K'는 LAPW 와

APW+lo 기저함수들의 선형조합(linear combination)으로 주어진다[182,299,301].

Practical approach for solving the unexpected glitch when using WIEN2k

WIEN2k 를 이용하여 고압 환경에 놓인 지구물질의 전자구조 및 XRS 스펙트럼을 계산하는 과정에서 예상치 못한 문제가 발생할 수 있다. 특히, 다양한 규산염 물질들의 O *K*-edge XRS 스펙트럼을 계산하기 위해서는 타겟 산소 원자에 x-선 Raman 산란에 의하여 만들어진 O 원자의 1s 정공 (core hole)에 의한 전자구조의 변화를 고려해야 합니다. 이 과정에서 대상이 되는 O 원자 주변에 전하 밀도 분포에 변동(electronic charge density fluctuation)이 나타나게 되어, 전자-정공 효과(the core-hole effects)를 고려하지 않는 통상적인 전자구조 계산과는 달리 계산 과정에서 예상치 못한 에러가 발생하는 경우가 많습니다. 이러한 문제를 해결하기 위해서는 WIEN2k 에서 사용되는 여러 input 및 output 파일들의 흐름과 다양한 변수들에 대하여 상세한 정보가 필요합니다. 해당 내용들은 WIEN2k 의 user guide 에 잘 정리되어 있습니다 [302]. WIEN2k 를 사용하기 위해 알아야하는 기초적인 이론들과 각 모듈의 상세한 사용 방법들은 WIEN2k official website 의 text books 섹션에 업로드 된 자료들에 잘 정리되어 있습니다 (http://susi.theochem.tuwien.ac.at/reg_user/textbooks/). 다만, 해당 자료들은 매우 방대한 양의 내용을 다루고 있기 때문에, 이 곳에서는 편의를 위하여 WIEN2k 에 대한 기본적인 내용들을 user guide 에서 참조하여 정리하였습니다. 이뿐만 아니라 계산을 수행하면서 발생했던 문제들을 해결한 과정들도 정리하였습니다. 이 과정에서 여러 자료들이 참조되었습니다. 이 때문에, 정리하는 과정에서 참조했던 자료가

명확하게 명시되지 못할 수도 있습니다. 하지만, 모든 내용들은 WIEN2k user guide 와 official webpage 에 업로드 된 자료들을 참조하였습니다.

Generating the master input file

WIEN2k 를 이용하여 계산을 수행하기 위해서는 master input 파일이 필요합니다. 해당 파일은 case.struct 파일로, 이전 연구에서 얻어진 결정 구조 정보를 이용하여 직접 작성하거나 case.cif 파일에서 변환하여 만들 수 있습니다.

Generating case.struct file from conventional structure information file (case.cif and case.xyz)
One should prepare

One should prepare conventionally used crystal information file generated from other programs. In WIEN2k package, only two types of files can be converted using provided scripts.
#cif2struct case.cif
#xyz2struct case.xyz
After the converting process, one should renamed a title of each generated case.struct file. Predefined title of case.struct file is 'blebleble'.

Generating case.struct file using MAKESTRUCT_LAPW script
#makestruct_lapw
And then one should input the structural parameters such as space group, lattice parameters, number of inequivalent atoms, and atomic coordinate of each element.

Initialization

위의 과정을 통하여 만들어진 case.struct 파일을 이용하여 실질적인 전자구조 계산을 수행하기 위해서는 초기 전자구조와 전자구조 계산을 위한 세부적인 조건을 설정하는 초기화(initialization) 과정이 필요합니다. 이를 위해서는 다음과 같이 WIEN2k 의 모듈들을 순차적으로 실행시켜야 합니다. 그리고 그 과정에서 생성되는 각 모듈들의 input 파일에 정의된 중요한 변수들을 수정해야 정확한 전자구조와 O *K*-edge XRS 스펙트럼을 얻을 수 있습니다.

[SETRMT] – [NN] – [SGROUP] – [SYMMETRY] – [INSTGEN_LAPW] – [LSTART] – [KGEN] – [DSTART]

각 모듈의 역할을 WIEN2k user guide 의 97-103 페이지에 상세하게 기술되어 있습니다. 다만, 위에 정리된 WIEN2k 모듈의 목록은 WIEN2k 에서 기본적으로 제공하는 W2WEB 으로 불리는 GUI 가 아닌, 기본적으로 사용되던 CUI 기반으로 터미널에서 계산을 수행하는 경우를 기준으로 하고 있습니다. 위의 과정에서 정의를 해야 할 변수들은 다음과 같습니다.

Input file/Module	Parameters
SETRMT	Muffin-Tin radii
INSTGEN_LAPW	Core-valence separation energy (E_{CUT})
INSTGEN_LAPW	Exchange-correlation functional
case.inc	Core-electron occupation number
case.in1	LM expansion methods (LAPW, APW, and APW+lo, etc.) Energy window (Emin/Emax/number of bands) RK_{MAX}
case.in2	Interstitial charge density (valence charge) G_{MAX}
KGEN	Number of irreducible *k* points

SCF calculations without spin polarization

Initialization 단계가 종료된 이후에는 초기 전자구조와 interatomic potential 에 대한 정보가 얻어집니다. 정확한 전자구조를 얻기 위해서는 self-consistent field (SCF) 계산이 수행되어야 합니다. 해당 내용은 WIEN2k user guide 의 105-132 페이지에 상세하게 정리되어 있습니다. 일반적으로 규산염 물질은 unpaired spin 을 갖지 않기 때문에 spin polarization 계산이 필요하지 않습니다. 이 때문에 규산염 물질의 전자구조를 계산하기 위한 SCF 계산은 다음과 같이 상대적으로 간단한 과정을 거쳐 이루어집니다.

[LAPW0] – [LAPW1] – [LAPW2] – [LCORE] – [MIXER]

각 모듈에 대한 상세한 설명 역시 WIEN2k user guide 의 105-132 페이지에 정리되어 있습니다. Fe-including 산화물과 같이 unpaired spin 을 갖는 물질에 대한 계산을 수행하는 경우에는 up 과 down spin 에 대한 spin polarization 계산을 수행해야 하며, 해당 내용은 WIEN2k user guide 의 45 페이지에 정리되어 있습니다.

Analyzing the result of SCF calculation

SCF 계산을 수행한 이후 얻어지는 전자구조는 여러 output 파일들에 나눠 저장되며, case.scf 파일에 중요한 정보들이 요약됩니다. 해당 파일에 저장되는 정보들을 확인하기 위해서는 아래에 정리된 LABEL 들을 확인해야 합니다. 상세한 정보는 WIEN2k user guide 의 42 페이지에 상세하게 정리되어 있어, 아래의 표에 중요한 몇 가지 LABEL 들만 정리하였습니다.

#grep :LABEL case.scf*
:LABEL – properties :ENE – total energy (Ry) :DIS – charge distance between last two iterations ($\int \lvert \rho_n-\rho_{n-1} \rvert dr$). Good convergence criteria. :FER – Fermi energy (Ry) :GAP – Band gap energy (Ry and eV), provided you have a proper k-mesh
:LABEL – types of calculation :POT – Exchange-correlational potential used in this calculation :LAT – Lattice parameters in this calculation :VOL – Volume of unit cell :POSxx – Atomic positions for atom xx (as in case.struct file) :RKM – Actual matrix size and resulting RKMAX value :NEC – normalization check of electronic charge densities. If a significant amount of electrons is missing, one might have core states, whose charge density is not completely confined within the respective atomic sphere. In such a case the corresponding states should be treated as band states (using LOs).
:LABEL – properties using spin polarization calculation :MMTOT – total spin magnetic moment/cell :MMIxx – spin magnetic moment of atom xx. Note, that this value depends on RMT.

:CUPxx – spin-up charge (mixed) in sphere xx
:CDNxx – spin-down charge (mixed) in sphere xx
:NUPxx – spin-up charge (new, from lapw2+lcore) in sphere xx
:NDNxx – spin-down charge (new, from lapw2+lcore) in sphere xx
:ORBxx – orbital magnetic moment of atom xx (needs SO calculations and LAPWDM)
:HFFxx – hyperfine field of atom xx (in kGauss)

Calculating the density of states (DOS)

SCF 계산을 수행하여 얻어진 전자구조를 확인하기 위해서는 연구자가 직접 확인할 수 있는 band structure 나 density of states (DOS)를 그려야 합니다. 여기서는 DOS 를 그리는 과정에 대하여 정리하였습니다. DOS 는 WIEN2k 의 TETRA 모듈을 통하여 얻을 수 있으며, 이때 이용되는 input 파일은 CONFIGURE_INT_LAPW 스크립트를 이용하여 만들 수 있습니다. 상세한 내용은 WIEN2k user guide 의 180-183 페이지에 상세하게 정리되어 있습니다. 아래 테이블에는 SiO_2 α-quartz 에 대한 TETRA 의 input 파일입니다 (case.int).

Configuring case.int file

total 31 tot, s,p,PX,PY,PZ,d
(Calculate the total DOS of given system and the partial DOS of oxygen number 31 for s- and p-orbital) We have to modify the 'case.int' file by hand in hand to select the proper energy window and Gaussian broadening factor, etc.

case.int file

```
Quartz_3   #Title
0.000      0.0025     4.500      0.04       #Emin, DE, Emax, Gauss-Broad
8                                            #Number of DOS
0          1          Total
31         1          tot-O
31         2          s-O
31         3          p-O
...
31         7          d-O
```

TETRA 모듈이 정상적으로 실행되면 case.dos* 파일에 계산된 결과가 저장됩니다. 얻어진 결과는 간단하게 EXCEL 을 이용하거나 DOSPLOT2_LAPW 스크립트를 이용하여 그릴 수 있습니다. DOS 를 얻기 위한 전체적인 과정은 다음과 같습니다.

[INIT_LAPW] – [RUN_LAPW] – [X LAPW2 -QTL or X QTL] – [CONFIGURE_INT_LAPW] – [X TETRA] – [DOSPLOT2_LAPW]

DOS 를 얻기 위해서는 얻어진 전자구조로부터 *l*-resolved partial charge distribution 에 대한 정보를 계산해야 합니다. 이 과정은 LAPW2 -QTL 또는 QTL 모듈을 이용하여 수행할 수 있으며, 이 모듈들에 대한 설명은 WIEN2k user guide 의 122-126 과 167-170 페이지에 각각 상세하게 정리되어 있습니다.

Calculating the x-ray Raman scattering features

WIEN2k 에서 실제로 계산되는 것은 XRS 스펙트럼이 아닌 electron energy-loss spectroscopy (EELS) 이론을 기반으로 얻어지는 energy-loss near-edge structure (ELNES) 스펙트럼입니다. Low-q limit 에서의 XRS 스펙트럼은 x-ray absorption spectroscopy (XAS)나 EELS 에서 얻어지는 core-level excitation features 들과 유사한 정보를 제공하기 때문에, 본 연구에서 얻어지는 ELNES 스펙트럼들은 실험에서 얻어진 XRS 스펙트럼들과 비교되었으며, 논문에서는 WIEN2k 를 이용하여 계산된 ELNES 스펙트럼 결과들을 XRS 스펙트럼으로 칭하였습니다. 관련된 내용은 *in situ* high-pressure XRS experiments 에 대한 이전 리뷰에 상세하게 정리되어 있습니다 [64]. 규산염 물질의 O *K*-edge XRS 스펙트럼을 계산하기 위해서는 대상 O 원자에 전자-정공 효과를 적용해야 하고, 이 과정은 일반적인 전자구조 계산에 비하여 복잡합니다. 이를 간략하게 정리하면 다음과 같습니다 (터미널 환경에서 WIEN2k 실행했을 경우).

[Generating case.struct file with P1 supercell] – [INIT_LAPW without changing the symmetry of case.struct file] – [Modify the electronic configuration of the target atom/case.inc and case.in2c file] – [Re-run DSTART program] – [Run RUN_LAPW (SCF)] – [Remove the extra charge added to conduction band/case.in2c file] – [Re-run LAPW2 program] – [Prepare case.innes file] – [Re-run LAPW1 program (optional to calculate higher energy region)] – [Run QTL –TELNES] – [Run TELNES3] – [Modify case.inb] – [Run BROADENING]

ELNES 스펙트럼 계산에 이용되는 TELNES 3.0 모듈과 BROADENING 모듈은 WIEN2k user guide 의 173-180 과 138-139 페이지에 상세하게 정리되어 있습니다. 정확한 스펙트럼을 계산하기 위해서는 TELNES 3.0 모듈의 input 파일인 case.innes 파일에 중요한 변수들을 정확하게 정의해야 합니다. 기본적인 변수들에 대하여 아래의 표에 정리하였습니다.

Important parameters in case.innes file
selected values of important parameters used in this calculation Target atom: Mg (excitation: K-edge, n=0, l=0) Edge onset (Mg K-edge electron binding energy): 1307.3 eV Energy grid (calculated energy range; energy window): 0.0 ~ 35.0 eV Detector collection semi-angle: 5.0 mrad Microscope convergence semi-angle: 1.87 mrad Gaussian broadening parameter: 0.5 (a kind of experimental smearing factor) **Orientation sensitive calculation case** We have to define more parameters to calculate beam orientation sensitive ELNES spectrum of a given system. DETECTOR POSITION: qx qy (default: 0 0) QGRID: qmodus (U as defaults; U, L, and 1) ORIENTATION SENSITIVE: g1 g2 g3 (no default values, the Euler angle of incident beam orientation) **Another excitation (L-edge spectrum)** SELECTION RULE: type (default: d; d – dipole approximation; m, d, q, o, n, and 0-3) LSELECTION RULE: type (default: d)

WIEN2k 에서는 전자구조를 계산함에 있어 상대성 이론이 적용되기 때문에 특정 원자에 core hole 을 적용할 때 정확한 electronic state 를 확인하기 위해서는 일반적인 quantum number 뿐만 아니라 relativistic quantum number 를 확인해야 합니다. 아래는 case.inc 파일에서 정확한 electronic state 를 확인하기 위해서 필요한 relativistic quantum number 를 정리한 것입니다.

		$j = 1+s/2$		K		Max. occupation	
	l	Down	Up	Down	Up	Down	Up
***s* state**	0		1/2		-1		2
***p* state**	1	1/2	3/2	1	-2	2	4
***d* state**	2	3/2	5/2	2	-3	4	6
***f* state**	3	5/2	7/2	3	-4	6	8

I/O file flow in WIEN2k

WIEN2k 는 계산을 수행하는 과정에서 많은 input 및 output 파일들이 만들어지며 이로 인하여 내부적으로 I/O file 의 흐름이 매우 복잡하게 얽혀 있다. 계산을 수행하는 과정에서 예상치 못한 에러가 발생하는 경우에 이 흐름에 대하여 명확하게 이해하지 못하면 문제를 해결하는데 많은 어려움을 겪기 때문에 이러한 내용에 대하여 이해를 할 필요가 있습니다. 해당 내용은 WIEN2k user guide 의 33-38 과 43-48 페이지에 상세하게 정리되어 있습니다. 계산을 수행하는데 있어 중요한 변수들이 정의되는 input 파일이 사용되는 LAPW1 과 LAPW2 모듈과 XRS 스펙트럼 계산을 위해 사용되는 QTL 와 TELNES 모듈의 input 과 output 파일을 시각적으로 확인할 수 있도록 아래와 같이 정리하였습니다. Highlighted 된 파일들은 중요한 변수를 정의하는 input 파일들과 실제 계산의 결과가 저장되는 output 파일들입니다.

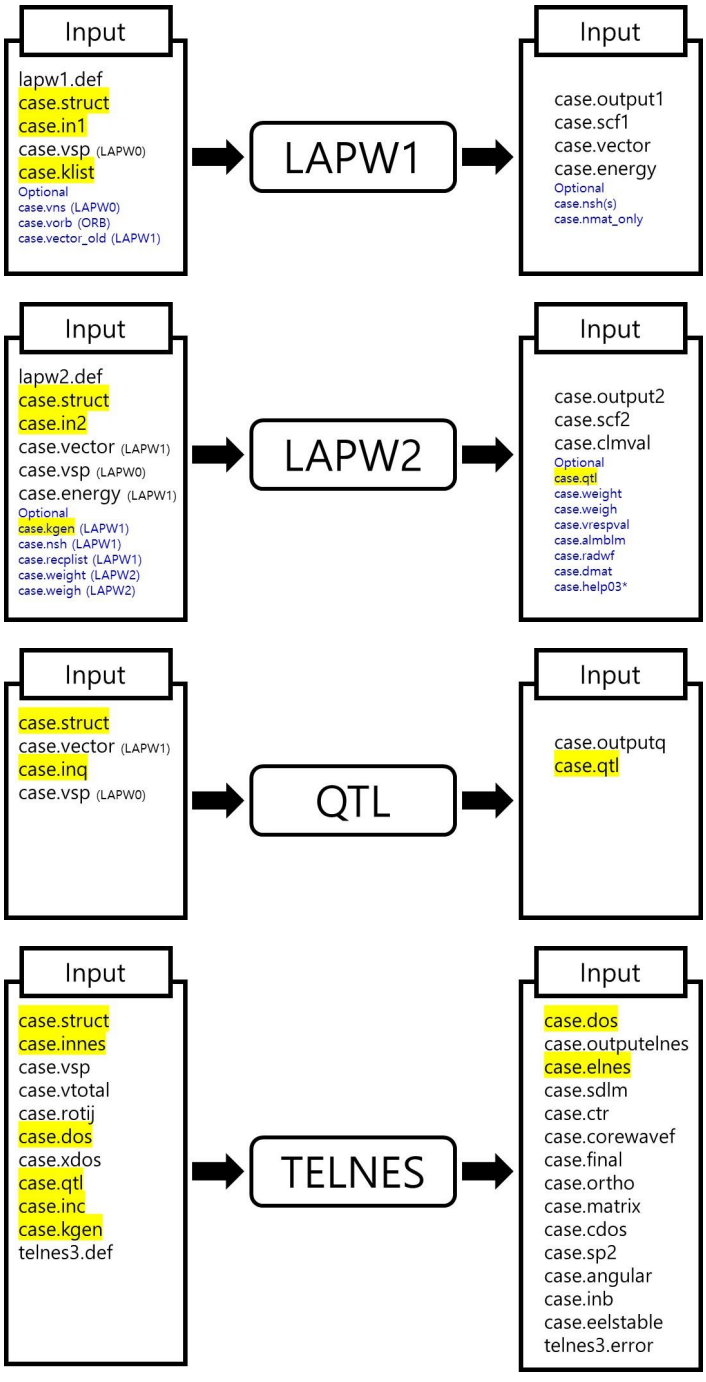

Trouble shooting

앞서 언급하였지만 WIEN2k 를 통하여 O *K*-edge XRS 스펙트럼을 계산하는 과정에 많은 오류가 발생하는데 기본적인 문제들의 해결 방법들은 WIEN2k user guide 의 219-223 페이지에 간략하게 정리되어 있습니다. 하지만, 전자-정공 효과를 적용하여 XRS 스펙트럼을 계산하는 과정에서 발생하는 오류는 일반적인 전자구조 계산과는 경우가 다르기 때문에 지금까지 연구를 수행하면서 발생한 문제들을 해결하는 과정을 정리하였습니다.

(Q1) Failure of SCF calculations in a few cycles

(A1) XRS 스펙트럼을 계산하는 과정에는 예측하지 못한 오류로 인하여 SCF 계산이 중간에 강제 종료되는 경우가 있습니다. 이런 상황이 발생하면, 기존에 계산되던 모든 결과 및 scratch 파일들을 삭제한 이후에 몇몇 중요한 변수들을 수정하여 initialization 과정을 다시 수행한 후 SCF 계산을 실행해야 합니다. 이런 과정을 거쳤는데도 SCF 계산이 계속 실패하는 경우에는 MIXER 의 설정을 변경하는 것도 하나의 방법입니다. MIXER 의 설정을 변경하는 경우는 다음과 같은 과정을 따르게 됩니다.

[#rm –f *broy*; rm –f *.scf] – [x dstart (-c/-up/-dn)] – [Modify 'case.inm' file: reducing MIXING factor] – [Restart SCF calculation]

(Q2) Segmentation fault in LAPW0 during the SCF calculations (RK_{MAX})

(A2) SCF 계산이 실패하는 경우에 어떤 모듈에서 문제가 발생하였는지 ERROR 파일에 해당 내용이 저장됩니다. 계산의 대상이 되는 구조가 100 개 이상의 원자를 포함하는 경우 RAM 용량이 부족하여 LAPW0

모듈에서 segmentation fault 에러 메시지가 나타나는 경우가 있습니다. 이때는 case.in1 파일에서 RK_{MAX} 값을 줄이는 것으로 계산에 이용되는 wave function 의 the number of coefficient 를 줄여 실제 이용되는 RAM 의 사용량을 조정해야 합니다. RK_{MAX} 값은 구성 원자의 종류에 따라 적당한 값이 정해져 있습니다. 해당 내용은 WIEN2k user guide 의 19 페이지에 정리되어 있지만, 편의를 위하여 아래 테이블에 RK_{MAX} 값의 기준을 정리하였습니다.

Elements	RK_{MAX}
proton (H)	$RK_{MAX} > 2.5$
sp elements	$RK_{MAX} > 5.0$ (oxygen in silicates)
d elements	$RK_{MAX} > 6.0$ (3*d* transition metals)
f elements	$RK_{MAX} > 7.0$

(Q3) Failure of SCF calculations due to the presence of the ghost bands

(A3) SiO_2 stishovite 구조의 O *K*-edge XRS 스펙트럼을 계산하는 과정에 SCF 계산이 지속적으로 실패하였습니다. STDOUT, lapw2.error, and case.scf2 파일을 확인하니 'QTL-B VALUE'와 관련된 ERROR 메시지를 확인할 수 있었습니다. 해당 내용은 계산이 진행되는 과정에서 GHOST BANDS (i.e., the spurious eigenvalues meaning unphysical results)가 나타났기 때문입니다. 해당 문제를 해결하기 위한 방법은 WIEN2k guide 의 220-223 페이지에 상세하게 정리되어 있습니다. 하지만, 이러한 문제가 발생하는 경우, core-hole effects 에 의하여 나타나는 rapid fluctuation of charge density 에 의하여 나타나는 것이기 때문에, user guide 에 제시된 방법 보다는 R_{MT} 값을 변경하고 the number of irreducible *k* points 의 값과, 계산되는 *k* points 를 변경하여 initialization 을 다시 수행하는 것으로 문제가 해결되었습니다. GHOST BANDS 가 나타나는 것이 rapid fluctuation of charge density 에 의한

것이기 때문에 electronic structure 가 계산되는 과정에서 실제 계산이 되는 k points 와 초기 전자구조를 변경하는 것으로 이러한 문제를 피해갈 수 있습니다. 해당 문제는 비결정질 $MgSiO_3$ 용융체의 전자구조를 계산하는 과정서도 발생했으며 동일한 방법으로 해결할 수 있었습니다.

(Q4) Warning message in LSTART, core-valence separation energy (E_{CUT})

(A4) WIEN2k 에서는 모든 electronic states 에 대한 계산을 모두 수행하기 때문에 core region 과 valence region 으로 구분하여 계산의 효율성을 높이게 됩니다. 이 과정에서 이를 구분하는 E_{CUT} 이 잘 정의되지 않으면 core leakage 에 의한 warning 메시지가 나타납니다. 이 경우에는 semi-core region 이 정의되어 leaked electron 의 계산이 수행됩니다. 이렇게 추가되는 과정으로 인하여 SCF 계산의 시간이 약간 길어집니다. 이를 피하기 위해서는 가능하면 잘 정의된 E_{CUT} 을 이용하여 semi-core region 이 정의되지 않게 해야만 합니다. 적당한 값의 E_{CUT} 을 사용하는 경우, SCF 계산 시간을 단축시킬 수 있다는 것도 확인하였습니다.

(Q5) Returning the cached RAM

(A5) 계산이 강제로 종료되거나 정상적으로 종료되더라도 사용 중이던 RAM 이 회수되지 않는 경우가 있습니다. 이 상황에서 많은 원자를 포함한 구조에 대한 계산을 수행하게 되면 RAM 부족으로 오류가 발생합니다. 이를 해결하기 위해서는 시스템을 재부팅하는 것이 간편한 방법이지만, 아래의 스크립트를 이용하여 간단하게 회수되지 못한 메모리를 회수하여 충분한 RAM 용량을 확보할 수 있습니다.

Returning cache memory to OS
#/bin/sync (1~3 times) #echo 0 > /proc/sys/vm/drop_caches (give the Kernel full control to the cache memory) #echo 1 > /proc/sys/vm/drop_caches (free page caches in cached memory) #echo 2 > /proc/sys/vm/drop_caches (free dentries and inodes in cached memory) #echo 3 > /proc/sys/vm/drop_caches (free page caches, dentries and inodes in cached memory) Alternatively, #/sbin/sysctl vm.drop_caches=3 ... Also, it could be added to crontab. #cd /etc/crontab And add this line to clear the cached memory every hour 0 * * * * root sync; echo 3 > /proc/sys/vm/drop_caches http://www.digitalinternals.com/unix/linux-clear-memory-cache/403/ The drop_caches file cannot be used to control the various kernel cache types (page cache, dentries, inodes, etc…). So, if you write 1 to the file to clear the page cache, you are not telling the kernel to disable the use of page cache anymore. You are just telling the kernel to clear the page cache at the instant. The kernel will start reclaiming the memory and build the page cache again after the call to drop the cache has been completed.

(Q6) Failure of calculating the density of states (TETRA)

(A6) 많은 숫자의 원자에 대한 partial density of states 를 한 번에 얻고자 case.int 파일을 만들면 TETRA 를 계산하는 과정에서 오류가 발생합니다. 원인을 찾지 못하여 많은 시행착오가 있었습니다. 하지만, 결국 TETRA 에서 DOS 를 계산하는 과정에서 한 번에 계산 가능한 partial DOS 의 숫자가 45 개로 제한되어 있기 때문이라는 것을 확인할 수 있었습니다. 개별적으로 100 개 이상의 원자를 포함하고 있는 구조의 total DOS 를 얻기 위해서는 각 원자들에 대하여 개별적으로 DOS 를 얻고, 얻어진 결과를 더해서 total DOS 를 얻을 수 있는 스크립트를 작성해야 합니다.

Published to Journal of
the Mineralogical society of Korea

Yoo Soo Yi and Sung Keun Lee, Quantum Chemical Calculations of the Effect of Si-O Bond Length on X-ray Raman Scattering Features for $MgSiO_3$ Perovskite, 2014, Journal of Mineralogical Society of Kore, 27(1), 1-15

Abstract

Probing the electronic structures of crystalline Mg-silicates at high pressure is essential for understanding the various macroscopic properties of mantle materials in Earth's interior. Quantum chemical calculations based on the density functional theory are used to explore the atomic configuration and electronic structures of Earth materials at high pressure. Here, we calculate the partial density of states (PDOS) and O *K*-edge energy-loss near-edge structure (ELNES) spectra for $MgSiO_3$ perovskite (Pv) at 25 GPa and 120 GPa using the WIEN2k program based on the full-potential linearized projected augmented wave (FP-LPAW) method. The calculated PDOS and O *K*-edge ELNES spectra for $MgSiO_3$ Pv show significant pressure-induced changes in their characteristic spectral features and relative peak intensity. These changes in spectral features of $MgSiO_3$ Pv indicate that the pressure-induced changes in local atomic configuration around O atoms such as Si-O, O-O, and Mg-O length can induce the significant changes on the local electronic structures around O atoms. The result also indicates that the significant changes in O *K*-edge features can results from the topological densification at constant Si coordination number. This study can provide a unique opportunity to understand the atomistic origins of pressure-induced changes in local electronic structures of crystalline and amorphous $MgSiO_3$ at high pressure more systematically.

Publication list

Sung Keun Lee, Sung Bo Lee, Sun Young Park, **Yoo Soo Yi**, and Chi Won Ahn, Structure of Amorphous Aluminum Oxide, 2009, Physical Review Letters, 103(9), 095501 (https://journals.aps.org/prl/abstract/10.1103/PhysRevLett.103.095501)

Sung Keun Lee, Sun Young Park, **Yoo Soo Yi** and Jaehyun Moon, Structure and Disorder in Amorphous Alumina Thin Films: Insights from High-Resolution Solid-State NMR, 2010, The Journal of Physical Chemistry C, 114(32), 13890-13894 (http://pubs.acs.org/doi/abs/10.1021/jp105306r)

Yoo Soo Yi and Sung Keun Lee, Local Electronic Structures of SiO_2 Polymorph Crystals: Insights from O *K*-edge Energy-Loss Near-Edge Spectroscopy, 2010, Journal of Mineralogical Society of Korea, 23(4), 403-411 (http://www.riss.kr/search/detail/DetailView.do?p_mat_type=1a0202e37d52c72d&control_no=9fba12879374bfc2ffe0bdc3ef48d419)

Yoo Soo Yi and Sung Keun Lee, Pressure-induced changes in local electronic structures of SiO_2 and $MgSiO_3$ polymorphs: Insights from *ab initio* calculations of O *K*-edge energy-loss near-edge structure spectroscopy, 2012, American Mineralogist, 97(5-6), 897-909 (https://www.degruyter.com/view/j/ammin.2012.97.issue-5-6/am.2012.3943/am.2012.3943.xml)

Sung Keun Lee, **Yoo Soo Yi**, George D. Cody, Kenji Mibe, Yingwei Fei, and Bjorn O. Mysen, Effect of Network Polymerization on the Pressure-Induced Structural Changes in Sodium Aluminosilicate Glasses and Melts: ^{27}Al and ^{17}O Solid-State NMR Study, 2012, The Journal of Physical Chemistry C, 116(3), 2183-2191
(http://pubs.acs.org/doi/abs/10.1021/jp206765s)

Se Yun Kim, Won Hyuk Suh, Jung Hoon Choi, **Yoo Soo Yi**, Sung Keun Lee, Galen D. Stucky and Jeung Ku Kang, Template-free synthesis of high surface area nitrogen-rich carbon microporous spheres and their hydrogen uptake capacity, 2014, Journal of Materials Chemistry A, 2(7), 2227-2232
(http://pubs.rsc.org/is/content/articlelanding/2014/ta/c3ta14030j#!divAbstract)

Yoo Soo Yi and Sung Keun Lee, Quantum Chemical Calculations of the Effect of Si-O Bond Length on X-ray Raman Scattering Features for $MgSiO_3$ Perovskite, 2014, Journal of Mineralogical Society of Kore, 27(1), 1-15
(http://www.riss.kr/search/detail/DetailView.do?p_mat_type=1a0202e37d52c72d&control_no=04466df86ff40192ffe0bdc3ef48d419)

Yoo Soo Yi and Sung Keun Lee, Atomistic origins of pressure-induced changes in the O *K*-edge x-ray Raman scattering features of SiO_2 and $MgSiO_3$ polymorphs: Insights from *ab initio* calculations, 2016, Physical Review B, 94(9), 094110
(https://journals.aps.org/prb/abstract/10.1103/PhysRevB.94.094110)

Hoon Khim, **Yoo Soo Yi**, and Sung Keun Lee, Probing the electronic structures and O *K*-edge x-ray Raman scattering excitation features of the SiO_2 polymorphs at high pressures: Practical aspects of the core-hole effects, 2017, Journal of Mineralogical Society of Kore, 30(2), 59-70

Yoo Soo Yi and Sung Keun Lee, Pressure-induced bonding transitions in $MgSiO_3$ melts: Insights from *ab initio* calculations of oxygen *K*-edge x-ray Raman scattering spectrum, *in preparation*

Yoo Soo Yi, Hoon Khim, Yong Hyun Kim, Sung Keun Lee, Pressure-induced changes in O *K*-edge x-ray Raman scattering features of SiO_2 high-pressure polymorphs: Implication for high-density SiO_2 melt and glass in the Earth's deep interior, *in preparation*

Yoo Soo Yi and Bum Han Lee, Chemical shielding and electric field gradient tensor of Li atoms in lepidolite structures: Insight from the *ab initio* calculations, *in preparation*

Conference list

The 4th Asian Conference on High Pressure Research (ACHPR) (2008.10)

Best Student Poster Presentation Reward

Title: Effect of composition on the pressure-induced coordination transformation in aluminosilicate glasses and melts: a view from solid-state ^{27}Al NMR spectroscopy

Author: **Yi Yoo Soo** and Lee Sung Keun

The 1st SNU-OSAKA Joint Symposium (2008.09)

Title: Effect of composition on the pressure-induced coordination transformation in aluminosilicate glasses and melts: a view from solid-state ^{27}Al NMR spectroscopy

Author: **Yoo Soo Yi** and Sung Keun Lee

International conference on high pressure science and technology (Joint of AIRAPT-22 and HPCJ-50) (2009.08)

Title: Effect of network modifying cation on pressure-induced structural changes in Na-aluminosilicate glasses and melts: high-resolution solid-state NMR study

Author: **Yoo Soo Yi** and Sung Keun Lee

2009 년도 광물학회 학술발표회 (2009.09)

Best Student Poster Presentation Reward

Title: Effect of network modifying cation on pressure-induced structural changes in Na-aluminosilicate glasses and melts: high-resolution solid-state

NMR study (with additional subject of ELNES simulation of Mg-silicates at high pressure)

Author: **Yoo Soo Yi** and Sung Keun Lee

2010 년도 광물학회 학술발표회 (2010.05)

Title: The Pressure-Induced Changes of Local Electronic Environments in Mg-silicates at High Pressure: Insights from First-Principle Calculations

Author: **Yoo Soo Yi** and Sung Keun Lee

2010 Gold Schmidt Conference (Earth, Energy, and the Environment) (2010.06)

Title: The Pressure-induced structural changes in Na-aluminosilicates and Mg-silicates at high pressure: insights from solid-state NMR and First-Principle calculations

Author: **Yoo Soo Yi** and Sung Keun Lee

2010 Western Pacific Geophysics Meeting (WPGM) (2010.06)

Title: Pressure-induced changes in atomic- and nanometer-scale structure of silicate glasses: solid-state NMR and First-Principle calculations

Author: **Yoo Soo Yi** and Sung Keun Lee

2011 년도 광물학회 학술발표회 (2011.09)

Title: Structure of alumina glass: A View from Al-27 NMR

Author: Sae Bom Ryu, Sun Young Park, **Yoo Soo Yi**, and Sung Keun Lee

2012 년도 광물학회 학술발표회 (2012.05)

Title: Pressure-induced changes in local electronic structure of $MgSiO_3$ perovskite and post-perovskite: Insight from *ab initio* calculations of O *K*-edge energy-loss near-edge structure (ELNES) spectroscopy

Author: **Yoo Soo Yi** and Sung Keun Lee

2012 년도 KIAS 전자구조학회 (2012.06)

Title: Pressure-induced changes in local electronic structure of SiO_2 and $MgSiO_3$ polymorphs: Insights from *ab initio* calculations of O *K*-edge energy-loss near-edge structure (ELNES) spectroscopy

Author: **Yoo Soo Yi** and Sung Keun Lee

2015 년도 광물학회 학술발표회 (2015.05)

Title: Quantum chemical calculations of local electronic structures and x-ray Raman scattering spectra for SiO_2 high pressures phases

Author: Hoon Khim, **Yoo Soo Yi**, and Sung Keun Lee

2016 년도 광물학회 학술발표회 (2016.05)

Title: Changes in electronic structures of $MgSiO_3$ melts under compression: Insights from the first principles calculations of O *K*-edge x-ray Raman scattering spectra

Author: **Yoo Soo Yi** and Sung Keun Lee

France Joint Workshop (2016.05)

Title: Dense silicates in Earth's interior: Insights from the first principles calculations of IXS spectra for crystalline and noncrystalline oxides at high pressures

Author: **Yoo Soo Yi** and Sung Keun Lee

2016 년도 KIAS 전자구조학회 (2016.06)

Title: Changes in local electronic structures of $MgSiO_3$ melts under compression: Insights from the first principles calculations of O *K*-edge x-ray Raman scattering spectroscopy

Author: **Yoo Soo Yi** and Sung Keun Lee

References

[1] S. K. Lee *et al.*, PNAS **105**, 7925 (2008).

[2] J. F. Lin *et al.*, Phys. Rev. B **75**, 012201 (2007).

[3] Y. S. Yi and S. K. Lee, Am. Miner. **97**, 897 (2012).

[4] M. Murakami, K. Hirose, K. Kawamura, N. Sata, and Y. Ohishi, Science **304**, 855 (2004).

[5] T. Iitaka, K. Hirose, K. Kawamura, and M. Murakami, Nature **430**, 442 (2004).

[6] Y. S. Yi and S. K. Lee, (2017).

[7] Y. S. Yi and S. K. Lee, Phys. Rev. B **94**, 094110 (2016).

[8] D. B. Ghosh, B. B. Karki, and L. Stixrude, Am. Miner. **99**, 1304 (2014).

[9] A. M. Dziewonski and D. L. Anderson, Phys. Earth Planet. Inter. **25**, 297 (1981).

[10] M. P. Panning, V. Lekić, and B. A. Romanowicz, J. Geophys. Res. Solid Earth **115**, n/a (2010).

[11] L. Stixrude, in *Treatise on Geophysics (Vol. 2 Mineral Physics)*, edited by S. Gerald (Elsevier, Amsterdam, 2007), pp. 7.

[12] J. M. Brown and T. J. Shankland, Geophys. J. Int. **66**, 579 (1981).

[13] G. R. Helffrich and B. J. Wood, Nature **412**, 501 (2001).

[14] S. H. Shim, Annu. Rev. Earth Planet. Sci. **36**, 569 (2008).

[15] T. Irifune and T. Tsuchiya, in *Treatise on Geophysics*, edited by S. Gerald (Elsevier, Amsterdam, 2007), pp. 33.

[16] J.-F. Lin, S. Speziale, Z. Mao, and H. Marquardt, Rev. Geophys. **51**, 244 (2013).

[17] B. Li, R. C. Liebermann, and D. J. Weidner, Science **281**, 675 (1998).

[18] E. Ito and E. Takahashi, J. Geophys. Res. Solid Earth **94**, 10637 (1989).

[19] K. Hirose, Rev. Geophys. **44**, RG3001 (2006).

[20] A. R. Oganov and S. Ono, Nature **430**, 445 (2004).

[21] T. Lay, in *Treatise on Geophysics 2nd Ed. (Vol. 1 Deep Earth Seismology)* (Elsevier, Oxford, 2015), pp. 683.

[22] P. J. Tackley, in *Treatise on Geophysics (Vol. 7 Mantle Dynamics)*, edited by S. Gerald (Elsevier, Amsterdam, 2007), pp. 437.

[23] S. Ono, E. Ito, and T. Katsura, Earth Planet SC Lett. **190**, 57 (2001).

[24] S. E. Kesson, J. D. F. Gerald, and J. M. G. Shelley, Nature **372**, 767 (1994).

[25] S. X. Saxena, L. S. Dubrovinsky, P. Lazor, and J. Hu, Eur. J. Mineral. **10**, 1275 (1998).

[26] E. Knittle and R. Jeanloz, Science **251**, 1438 (1991).

[27] K. Hirose, G. Morard, R. Sinmyo, K. Umemoto, J. Hernlund, G. Helffrich, and S. Labrosse, Nature **543**, 99 (2017).

[28] D. Andrault, G. Pesce, M. A. Bouhifd, B. N. Casanova, J. M. Hénot, and M. Mezouar, Science **344**, 892 (2014).

[29] D. Andrault, G. Fiquet, F. Guyot, and M. Hanfland, Science **282**, 720 (1998).

[30] B. B. Karki, M. C. Warren, L. Stixrude, G. J. Ackland, and J. Crain, Phys. Rev. B **55**, 3465 (1997).

[31] K. J. Kingma, R. E. Cohen, R. J. Hemley, and H. K. Mao, Nature **374**, 243 (1995).

[32] D. M. Teter, R. J. Hemley, G. Kresse, and J. Hafner, Phys. Rev. Lett. **80**, 2145 (1998).

[33] P. Cordier, D. Mainprice, and J. L. Mosenfelder, Eur. J. Mineral. **16**, 387 (2004).

[34] M. Murakami, K. Hirose, S. Ono, and Y. Ohishi, Geophys. Res. Lett. **30** (2003).

[35] Y. Kuwayama, K. Hirose, N. Sata, and Y. Ohishi, Science **309**, 923 (2005).

[36] F. González-Cataldo, S. Davis, and G. Gutiérrez, Sci. Rep. **6**, 26537 (2016).

[37] L. Wen and D. V. Helmberger, Science **279**, 1701 (1998).

[38] S. Rost, E. J. Garnero, Q. Williams, and M. Manga, Nature **435**, 666 (2005).

[39] Q. Williams and E. J. Garnero, Science **273**, 1528 (1996).

[40] J. A. Akins, S.-N. Luo, P. D. Asimow, and T. J. Ahrens, Geophys. Res. Lett. **31**, L14612 (2004).

[41] M. Murakami and J. D. Bass, P. Natl. Acad. Sci. U.S.A. **108**, 17286 (2011).

[42] T. Lay, E. J. Garnero, and Q. Williams, Phys. Earth Planet. Inter. **146**, 441 (2004).

[43] Q. Williams, J. Revenaugh, and E. Garnero, Science **281**, 546 (1998).

[44] M. Murakami and J. D. Bass, Phys. Rev. Lett. **104**, 025504 (2010).

[45] B. B. Karki, D. Bhattarai, and L. Stixrude, Phys. Rev. B **76**, 104205 (2007).

[46] L. Stixrude and B. Karki, Science **310**, 297 (2005).

[47] S. Baroni, S. de Gironcoli, A. Dal Corso, and P. Giannozzi, Rev. Mod. Phys. **73**, 515 (2001).

[48] S. R. Elliot, in *Physics of amorphous materials, 2nd Ed.* (Longman, 1990), pp. 186.

[49] C. Meade, R. J. Hemley, and H. K. Mao, Phys. Rev. Lett. **69**, 1387 (1992).

[50] T. Sato and N. Funamori, Phys. Rev. B **82**, 184102 (2010).

[51] S. Sugai and A. Onodera, Phys. Rev. Lett. **77**, 4210 (1996).

[52] A. C. Wright, J. Non-Cryst. Solids **179**, 84 (1994).

[53] S. Susman *et al.*, Phys. Rev. B **43**, 1194 (1991).

[54] W. Martin, G. Malcolm, K. Shinji, L. B. Craig, A. Jaakko, and G. T. Matt, J. Phys.: Condens. Matter **24**, 225403 (2012).

[55] N. Hiraoka, H. Fukui, and T. Okuchi, High Pressure Res. **36**, 250 (2016).

[56] V. L. Aksenov, M. V. Koval'chuk, A. Y. Kuz'min, Y. Purans, and S. I. Tyutyunnikov, Crystallogr. Rep. **51**, 908 (2006).

[57] E. F. Henry, C. B. Adrian, and S. S. Philip, Rep. Prog. Phys. **69**, 233 (2006).

[58] S. K. Lee, Y. S. Yi, G. D. Cody, K. Mibe, Y. Fei, and B. O. Mysen, J. Phys. Chem. C **116**, 2183 (2012).

[59] S. K. Lee, Solid State Nucl. Magn. Reson. **38**, 45 (2010).

[60] S. K. Lee, P. Natl. Acad. Sci. U.S.A. **108**, 6847 (2011).

[61] S. K. Lee, in *Advances in High-Pressure Techniques for Geophysical Applications*, edited by J. Chen *et al.* (Elsevier, 2011), p. 241.

[62] S. J. Gaudio, S. Sen, and C. E. Lesher, Geochim. Cosmochim. Acta **72**, 1222 (2008).

[63] W. B. Durham and D. C. Rubie, in *Properties of Earth and Planetary Materials at High Pressure and Temperature* (American Geophysical Union, 2013), pp. 63.

[64] J.-P. Rueff and A. Shukla, Rev. Mod. Phys. **82**, 847 (2010).

[65] S. K. Lee, P. J. Eng, and H.-k. Mao, in *Spectroscopic Methods in Mineralology and Materials Sciences*, edited by G. S. Henderson, D. R. Neuville, and R. T. Downs (Mineralogical Society of America, 2014), pp. 139.

[66] C. Sternemann and M. Wilke, High Pressure Res. **36**, 275 (2016).

[67] M. Wu, Y. F. Liang, J. Z. Jiang, and J. S. Tse, Sci. Rep. **2**, 398 (2012).

[68] H. Fukui, M. Kanzaki, N. Hiraoka, and Y. Q. Cai, Phys. Chem. Miner. **36**, 171 (2009).

[69] K. Hämäläinen and S. Manninen, J. Phys.: Condens. Matter **13**, 7539 (2001).

[70] W. Schulke, *Electron dynamics by inelastic X-ray scattering* (Oxford University Press 2007), Oxford series on synchrotron radiation, 7.

[71] R. J. Hemley, V. V. Struzhkin, R. E. Cohen, and G. Shen, in *Treatise on Geophysics (Second Edition)*, edited by G. Schubert (Elsevier, Oxford, 2015), pp. 313.

[72] Y. Meng *et al.*, PNAS **105**, 11640 (2008).

[73] H. Fukui, M. Kanzaki, N. Hiraoka, and Y. Q. Cai, Phys. Rev. B **78**, 012203 (2008).

[74] P. Blaha, Schwarz, K., Madsen, G., Kvasnicka, D and Luitz, J, WIEN2k, Techn. Univ. Wien, Austria, 2001.

[75] B. B. Karki and L. P. Stixrude, Science **328**, 740 (2010).

[76] B. B. Karki, D. Bhattarai, M. Mookherjee, and L. Stixrude, Phys. Chem. Miner. **37**, 103 (2010).

[77] N. P. de Koker, L. Stixrude, and B. B. Karki, Geochim. Cosmochim. Acta **72**, 1427 (2008).

[78] S. J. Clark, M. D. Segall, C. J. Pickard, P. J. Hasnip, M. J. Probert, K. Refson, and M. C. Payne, Z. Kristallogr. **220**, 567 (2005).

[79] M. R. Filip, G. E. Eperon, H. J. Snaith, and F. Giustino, Nat. Commun. **5** (2014).

[80] J. H. Lee, J.-H. Lee, E.-H. Kong, and H. M. Jang, Sci. Rep. **6**, 21687 (2016).

[81] Z. Ning *et al.*, Nature **523**, 324 (2015).

[82] W. L. Mao, H. K. Mao, V. B. Prakapenka, J. F. Shu, and R. J. Hemley, Geophys. Res. Lett. **33**, L12S02 (2006).

[83] W. L. Mao, G. Y. Shen, V. B. Prakapenka, Y. Meng, A. J. Campbell, D. L. Heinz, J. F. Shu, R. J. Hemley, and H. K. Mao, PNAS **101**, 15867 (2004).

[84] A. P. van Aken, B. Liebscher, and J. V. Styrsa, Phys. Chem. Miner. **25**, 323 (1998).

[85] R. A. H. a. J. Z. W. Deer, in *Introduction to the Rock-Forming Minerals* (Longman, London, 1966), p. 218.

[86] S. Guggenheim, Am. Miner. **66**, 1221 (1981).

[87] J. R. Yates, C. J. Pickard, and F. Mauri, Phys. Rev. B **76**, 024401 (2007).

[88] G. D. Price, *Mineral physics* (Elsevier, Amsterdam, 2007), Vol. 2.

[89] R. J. Hemley, *Ultrahigh-pressure mineralogy: physics and chemistry of the Earth's deep interior* (The mineralogical society of America, Washington,DC, 1998), Vol. 37.

[90] H. K. Mao and W. L. Mao, in *Treatise on Geophysics*, edited by S. Gerald (Elsevier, Amsterdam, 2007), pp. 231.

[91] E. Ohtani, A. Suzuki, R. Ando, S. Urakawa, K. Funakoshi, and Y. Katayama, in *Advances in High-Pressure Technology for Geophysical Applications*, edited by C. Jiuhua *et al.* (Elsevier, Amsterdam, 2005), pp. 195.

[92] A. R. Oganov, in *Treatise on Geophysics*, edited by S. Gerald (Elsevier, Amsterdam, 2007), pp. 121.

[93] A. R. Oganov, Y. M. Ma, A. O. Lyakhov, M. Valle, and C. Gatti, in *Theoretical and Computational Methods in Mineral Physics: Geophysical Applications*2010), pp. 271.

[94] W. L. Mao, H. K. Mao, W. Sturhahn, J. Y. Zhao, V. B. Prakapenka, Y. Meng, J. F. Shu, Y. W. Fei, and R. J. Hemley, Science **312**, 564 (2006).

[95] R. M. Wentzcovitch, Z. Q. Wu, and P. Carrier, in *Theoretical and Computational Methods in Mineral Physics: Geophysical Applications*2010), pp. 99.

[96] H. K. Mao, R. J. Hemley, Y. Fei, J. F. Shu, L. C. Chen, A. P. Jephcoat, Y. Wu, and W. A. Bassett, J. Geophys. Res. Solid Earth **96**, 8069 (1991).

[97] R. J. Hemley, H.-K. Mao, and R. E. Cohen, Rev. Mineral. Geochem. **37**, 591 (1998).

[98] L. Stixrude, R. E. Cohen, and R. J. Hemley, Rev. Mineral. Geochem. **37**, 639 (1998).

[99] C. T. Prewitt and R. T. Downs, Rev. Mineral. Geochem. **37**, 283 (1998).

[100] H.-K. Mao and R. J. Hemley, Rev. Mineral. Geochem. **37**, 1 (1998).

[101] R. Jeanloz and Q. Williams, Rev. Mineral. Geochem. **37**, 241 (1998).

[102] W. Xu, C. Lithgow-Bertelloni, L. Stixrude, and J. Ritsema, Earth Planet SC Lett. **275**, 70 (2008).

[103] F. de Groot, Chem. Rev. **101**, 1779 (2001).

[104] G. E. Brown, F. Farges, and G. Calas, Rev. Mineral. Geochem. **32**, 317 (1995).

[105] M. Wilke, F. Farges, P. E. Petit, G. E. Brown, and F. Martin, Am. Miner. **86**, 714 (2001).

[106] J. Stohr, *NEXAFS spectroscopy* (Springer, New York, 2003), 1 edn., Springer series in surface sciences, 25 p.^pp. 403.

[107] W. Y. Ching and P. Rulis, Phys. Rev. B **77**, 035125 (2008).

[108] S. Kostlmeier and C. Elsasser, Phys. Rev. B **60**, 14025 (1999).

[109] I. Tanaka and T. Mizoguchi, J. Phys.: Condens. Matter **21**, 104201 (2009).

[110] D. Cabaret, F. Mauri, and G. S. Henderson, Phys. Rev. B **75**, 184205 (2007).

[111] T. Mizoguchi, M. Yoshiya, J. Li, F. Oba, I. Tanaka, and H. Adachi, Ultramicroscopy **86**, 363 (2001).

[112] G. Duscher, R. Buczko, S. J. Pennycook, and S. T. Pantelides, Ultramicroscopy **86**, 355 (2001).

[113] M. Yoshiya, I. Tanaka, K. Kaneko, and H. Adachi, J. Phys.: Condens. Matter **11**, 3217 (1999).

[114] T. Mizoguchi, I. Tanaka, M. Yoshiya, F. Oba, and H. Adachi, J. Phys.: Condens. Matter **11**, 5661 (1999).

[115] I. Tanaka, J. Kawai, and H. Adachi, Solid State Commun. **93**, 533 (1995).

[116] C. Hebert, Micron **38**, 12 (2007).

[117] C. Hebert, J. Luitz, and P. Schattschneider, Micron **34**, 219 (2003).

[118] G. S. Henderson, D. R. Neuville, and L. Cormier, Chem. Geol. **259**, 54 (2009).

[119] F. Seifert, T. Sharp, B. Poe, and Z. Wu, Phys. Chem. Miner. **23**, 227 (1996).

[120] Z. Y. Wu, F. Seifert, B. Poe, and T. Sharp, J. Phys.: Condens. Matter **8**, 3323 (1996).

[121] L. A. J. Garvie, P. Rez, J. R. Alvarez, P. R. Buseck, A. J. Craven, and R. Brydson, Am. Miner. **85**, 732 (2000).

[122] S. K. Lee, P. J. Eng, H.-k. Mao, Y. Meng, M. Newville, M. Y. Hu, and J. Shu, Nat. Mater. **4**, 851 (2005).

[123] U. Bergmann, P. Wernet, P. Glatzel, M. Cavalleri, L. G. M. Pettersson, A. Nilsson, and S. P. Cramer, Phys. Rev. B **66**, 092107 (2002).

[124] S. K. Lee, P. J. Eng, H.-k. Mao, Y. Meng, and J. Shu, Phys. Rev. Lett. **98**, 105502 (2007).

[125] W. L. Mao *et al.*, Science **302**, 425 (2003).

[126] Y. Meng *et al.*, Nat. Mater. **3**, 111 (2004).

[127] Y. Q. Cai *et al.*, Phys. Rev. Lett. **94**, 025502 (2005).

[128] S. K. Lee, P. J. Eng, H.-k. Mao, and J. Shu, Phys. Rev. B **78**, 214203 (2008).

[129] P. Wernet *et al.*, Science **304**, 995 (2004).

[130] T. T. Fister, K. P. Nagle, F. D. Vila, G. T. Seidler, C. Hamner, J. O. Cross, and J. J. Rehr, Phys. Rev. B **79**, 174117 (2009).

[131] J. S. Tse, D. M. Shaw, D. D. Klug, S. Patchkovskii, G. Vanko, G. Monaco, and M. Krisch, Phys. Rev. Lett. **100**, 095502 (2008).

[132] U. Bergmann, P. Glatzel, and S. P. Cramer, Microchem J. **71**, 221 (2002).

[133] S. Aryal, P. Rulis, and W. Y. Ching, Am. Miner. **93**, 114 (2008).

[134] D. Cabaret, P. Sainctavit, P. Ildefonse, and A. M. Flank, Am. Miner. **83**, 300 (1998).

[135] Z. Y. Wu, G. Ouvrard, P. Gressier, and C. R. Natoli, Phys. Rev. B **55**, 10382 (1997).

[136] D. A. Eustace, D. W. McComb, and A. J. Craven, Micron **41**, 547 (2010).

[137] V. Krayzman, I. Levin, J. C. Woicik, D. Yoder, and D. A. Fischer, Phys. Rev. B **74**, 224104 (2006).

[138] J. J. Rehr, J. J. Kas, F. D. Vila, M. P. Prange, and K. Jorissen, Phys. Chem. Chem. Phys. **12**, 5503 (2010).

[139] K. Jorissen and J. J. Rehr, Phys. Rev. B **81**, 245124 (2010).

[140] J. J. Rehr and R. C. Albers, Rev. Mod. Phys. **72**, 621 (2000).

[141] H. Ikeno, I. Tanaka, L. Miyamae, T. Mishima, H. Adachi, and K. Ogasawara, Mater. Trans. **45**, 1414 (2004).

[142] T. Mizoguchi, I. Tanaka, M. Yoshiya, F. Oba, K. Ogasawara, and H. Adachi, Phys. Rev. B **61**, 2180 (2000).

[143] S. Kim, Y. Kim, J. Hong, I. Tanaka, and K. No, J. Appl. Phys. **97**, 073519 (2005).

[144] I. Tanaka, T. Mizoguchi, M. Yoshiya, K. Ogasawara, H. Adachi, S. D. Mo, and W. Y. Ching, J. Electron Microsc. **51**, S107 (2002).

[145] S. D. Mo and W. Y. Ching, Phys. Rev. B **62**, 7901 (2000).

[146] P. Rez, J. R. Alvarez, and C. Pickard, Ultramicroscopy **78**, 175 (1999).

[147] K. Schwarz, P. Blaha, and G. K. H. Madsen, Comput. Phys. Commun. **147**, 71 (2002).

[148] J. A. McLeod, R. G. Wilks, N. A. Skorikov, L. D. Finkelstein, M. Abu-Samak, E. Z. Kurmaev, and A. Moewes, Phys. Rev. B **81**, 245123 (2010).

[149] R. De Francesco, M. Stener, and G. Fronzoni, Surf. Sci. **605**, 500 (2011).

[150] N. A. Besley and F. A. Asmuruf, Phys. Chem. Chem. Phys. **12**, 12024 (2010).

[151] G. Fronzoni, R. Francesco, M. Stener, and M. Causa, J. Phys. Chem. B **110**, 9899 (2006).

[152] G. Fronzoni, R. De Francesco, and M. Stener, J. Phys. Chem. B **109**, 10332 (2005).

[153] K. Jorissen, University of Antwerp, 2007.

[154] H. Horiuchi, E. Ito, and D. J. Weidner, Am. Miner. **72**, 357 (1987).

[155] Y. Ohashi, Phys. Chem. Miner. **10**, 217 (1984).

[156] N. L. Ross, J. F. Shu, R. M. Hazen, and T. Gasparik, Am. Miner. **75**, 739 (1990).

[157] H. Horiuchi, M. Hirano, E. Ito, and Y. Matsui, Am. Miner. **67**, 788 (1982).

[158] G. Will, M. Bellotto, W. Parrish, and M. Hart, J. Appl. Crystallogr. **21**, 182 (1988).

[159] J. Luitz, M. Maier, C. Hebert, P. Schattschneider, P. Blaha, K. Schwarz, and B. Jouffrey, Eur. Phys. J. B **21**, 363 (2001).

[160] E. Tamura, J. van Ek, M. Fröba, and J. Wong, Phys. Rev. Lett. **74**, 4899 (1995).

[161] I. Davoli, E. Paris, S. Stizza, M. Benfatto, M. Fanfoni, A. Gargano, A. Bianconi, and F. Seifert, Phys. Chem. Miner. **19**, 171 (1992).

[162] A. V. Soldatov, M. Kasrai, and G. M. Bancroft, Solid State Commun. **115**, 687 (2000).

[163] T. Sharp, Z. Wu, F. Seifert, B. Poe, M. Doerr, and E. Paris, Phys. Chem. Miner. **23**, 17 (1996).

[164] J. R. Alvarez and P. Rez, Solid State Commun. **108**, 37 (1998).

[165] Y. L. Li and Z. Zeng, Int. J. Mod. Phys. C **20**, 1093 (2009).

[166] S. A. Cruz, C. Díaz-García, A. P. Pathak, and J. Soullard, Nucl. Instrum. Methods Phys. Res., Sect. B **230**, 46 (2005).

[167] J. A. Akins, S. N. Luo, P. D. Asimow, and T. J. Ahrens, Geophys. Res. Lett. **31**, L14612 (2004).

[168] E. Vanacore, F. L. Niu, and Y. L. Ma, Earth Planet SC Lett. **293**, 54 (2010).

[169] Y. Xu and K. D. Koper, Geophys. Res. Lett. **36**, L17301 (2009).

[170] J. L. Mosenfelder, P. D. Asimow, D. J. Frost, D. C. Rubie, and T. J. Ahrens, J. Geophys. Res. Solid Earth **114**, B01203 (2009).

[171] E. Ohtani, Chem. Geol. **265**, 279 (2009).

[172] K. D. Kwon, K. Refson, and G. Sposito, Phys. Rev. Lett. **100** (2008).

[173] L. W. Finger and R. M. Hazen, Rev. Mineral. Geochem. **41**, 123 (2000).

[174] G. Lelong, L. Cormier, G. Ferlat, V. Giordano, G. S. Henderson, A. Shukla, and G. Calas, Phys. Rev. B **85**, 134202 (2012).

[175] G. Lelong, G. Radtke, L. Cormier, H. Bricha, J. P. Rueff, J. M. Ablett, D. Cabaret, F. Gelebart, and A. Shukla, Inorg. Chem. **53**, 10903 (2014).

[176] B. J. A. Moulton, G. S. Henderson, H. Fukui, N. Hiraoka, D. de Ligny, C. Sonneville, and M. Kanzaki, Geochim. Cosmochim. Acta **178**, 41 (2016).

[177] S. K. Lee, S. Y. Park, H. I. Kim, O. Tschauner, P. Asimow, L. G. Bai, Y. M. Xiao, and P. Chow, Geophys. Res. Lett. **39**, 5, L05306 (2012).

[178] C. J. Sahle *et al.*, PNAS **110**, 6301 (2013).

[179] A. Nyrow, J. S. Tse, N. Hiraoka, S. Desgreniers, T. Buning, K. Mende, M. Tolan, M. Wilke, and C. Sternemann, Appl. Phys. Lett. **104**, 4, 262408 (2014).

[180] A. Nyrow *et al.*, Contrib. Mineral. Petrol. **167**, 13, 1012 (2014).

[181] M. Sugahara, A. Yoshiasa, Y. Komatsu, T. Yamanaka, N. Bolfan-Casanova, A. Nakatsuka, S. Sasaki, and M. Tanaka, Am. Miner. **91**, 533 (2006).

[182] K. Schwarz and P. Blaha, Comput. Mater. Sci **28**, 259 (2003).

[183] Y. P. Li and W. Y. Ching, Phys. Rev. B **31**, 2172 (1985).

[184] N. L. Ross and R. M. Hazen, Phys. Chem. Miner. **17**, 228 (1990).

[185] G. Fiquet, D. Andrault, A. Dewaele, T. Charpin, M. Kunz, and D. Hausermann, Phys. Earth Planet. Inter. **105**, 21 (1998).

[186] G. Fiquet, A. Dewaele, D. Andrault, M. Kunz, and T. Le Bihan, Geophys. Res. Lett. **27**, 21 (2000).

[187] K. Momma and F. Izumi, J. Appl. Crystallogr. **44**, 1272 (2011).

[188] S. K. Lee, Y. Fei, G. Cody, and B. Mysen, in *Advances in High-Pressure Technology for Geophysical Applications*, edited by C. Jiuhua *et al.* (Elsevier, Amsterdam, 2005), pp. 241.

[189] S. K. Lee, Y. S. Yi, G. D. Cody, K. Mibe, Y. Fei, and B. O. Mysen, J. Phys. Chem. C **116**, 2183 (2011).

[190] S. K. Lee, B. O. Mysen, and G. D. Cody, Phys. Rev. B **68**, 214206 (2003).

[191] S. K. Lee and E. J. Kim, J. Phys. Chem. C **119**, 748 (2014).

[192] S. K. Lee, H.-I. Kim, E. J. Kim, K. Y. Mun, and S. Ryu, J. Phys. Chem. C, 737 (2015).

[193] S. K. Lee and E. J. Kim, J. Phys. Chem. C **119**, 748 (2015).

[194] J. P. Perdew, A. Ruzsinszky, G. I. Csonka, O. A. Vydrov, G. E. Scuseria, L. A. Constantin, X. L. Zhou, and K. Burke, Phys. Rev. Lett. **100**, 136406 (2008).

[195] A. N. Chibisov, Tech. Phys. **58**, 692 (2013).

[196] G. S. Henderson, F. M. F. de Groot, and B. J. A. Moulton, in *Spectroscopic Methods in Mineralology and Materials Sciences*, edited by G. S. Henderson, D. R. Neuville, and R. T. Downs2014), pp. 75.

[197] P. L. Potapov, K. Jorissen, D. Schryvers, and D. Lamoen, Phys. Rev. B **70**, 045106 (2004).

[198] Z. J. Liu, X. W. Sun, X. M. Tan, Y. D. Guo, and X. D. Yang, Solid State Commun. **144**, 264 (2007).

[199] A. Sadao, *Properties of Group-IV, III-V and II-VI Semiconductors* (John Wiley & Sons Ltd, England, 2005).

[200] J. Phillips, Rev. Mod. Phys. **42**, 317 (1970).

[201] K. Hübner and V. Bashenov, Phys. Status Solidi B **77**, 473 (1976).

[202] C. Gatti, Z. Kristallogr. **220**, 399 (2005).

[203] J. Poater, M. Solà, M. Duran, and X. Fradera, Theor. Chem. Acc. **107**, 362 (2002).

[204] N. Christensen, S. Satpathy, and Z. Pawlowska, Phys. Rev. B **36**, 1032 (1987).

[205] O. Tschauner, C. Ma, J. R. Beckett, C. Prescher, V. B. Prakapenka, and G. R. Rossman, Science **346**, 1100 (2014).

[206] J. S. Tse *et al.*, J. Phys. Chem. C **118**, 1161 (2014).

[207] K. D. Kwon, K. Refson, S. Bone, R. Qiao, W.-l. Yang, Z. Liu, and G. Sposito, Phys. Rev. B **83**, 064402 (2011).

[208] B. B. Karki, Phys. Earth Planet. Inter. **240**, 43 (2015).

[209] J. T. K. Wan, T. S. Duffy, S. Scandolo, and R. Car, J. Geophys. Res. Solid Earth **112**, B03208 (2007).

[210] J. P. Perdew, K. Burke, and M. Ernzerhof, Phys. Rev. Lett. **77**, 3865 (1996).

[211] B. Leimkuhler, E. Noorizadeh, and F. Theil, J. Stat. Phys. **135**, 261 (2009).

[212] S. K. Lee, J. Phys. Chem. B **108**, 5889 (2004).

[213] S. R. Elliot, in *Physics of amorphous materials, 2nd Ed.* (Longman, 1990), pp. 268.

[214] M. H. Cohen, H. Fritzsche, and S. R. Ovshinsky, Phys. Rev. Lett. **22**, 1065 (1969).

[215] S. Hosokawa, H. Sato, K. Mimura, Y. Tezuka, D. Fukunaga, Y. Matsuzaki, and F. Shimojo, J. Phys. Soc. Jpn. **84**, 024605 (2015).

[216] H. Ünlü, Solid-State Electron. **35**, 1343 (1992).

[217] H. Fujihisa *et al.*, Phys. Rev. Lett. **97**, 085503 (2006).

[218] M. C. Wilding, C. J. Benmore, J. A. Tangeman, and S. Sampath, Europhys. Lett. **67**, 212 (2004).

[219] D. C. Presnall and T. Gasparik, J. Geophys. Res. B: Solid Earth **95**, 15771 (1990).

[220] J.-H. Parq, S. K. Lee, S.-M. Lee, and J. Yu, J. Phys. Chem. C **120**, 23152 (2016).

[221] R. Orbach, J. Non-Cryst. Solids **164**, 917 (1993).

[222] S. John, H. Sompolinsky, and M. J. Stephen, Phys. Rev. B **27**, 5592 (1983).

[223] S. Hunklinger, J. Phys. Colloques **43**, C9 (1982).

[224] S. Gelin, H. Tanaka, and A. Lemaitre, Nat. Mater. **15**, 1177 (2016).

[225] D. Caprion, P. Jund, and R. Jullien, Phys. Rev. Lett. **77**, 675 (1996).

[226] N. W. Ashcroft and N. D. Mermin, in *Solid State Physics* (Brooks Cole, New York, 1976), pp. 422.

[227] G. P. Francis and M. C. Payne, J. Phys.: Condens. Matter **2**, 4395 (1990).

[228] W. Haynes, *Handbook of Chemistry and Physics* (CRC Press, 2011), Vol. 92.

[229] M. I. Ojovan, J. Exp. Theor. Phys. **79**, 632 (2004).

[230] R. W. Godby, in *Unoccupied Electronic States: Fundamentals for XANES, EELS, IPS and BIS*, edited by J. C. Fuggle, and J. E. Inglesfield (Springer Berlin Heidelberg, Berlin, Heidelberg, 1992), pp. 51.

[231] E. Vella, F. Messina, M. Cannas, and R. Boscaino, Phys. Rev. B **83**, 174201 (2011).

[232] S. Arai, Y. Shimizu, and F. Gervilla, P. Jpn. Acad. B-Phys. **79**, 145 (2003).

[233] T. a. T. Tsuchiya, J., P. Natl. Acad. Sci. U.S.A. **108**, 1252 (2011).

[234] R. E. Cohen, High Pressure Res., 425 (1993).

[235] T. Tsuchiya, R. Caracas, and J. Tsuchiya, Geophys. Res. Lett. **31** (2004).

[236] A. N. Clark, C. E. Lesher, S. D. Jacobsen, and Y. Wang, J. Geophys. Res. Solid Earth **121**, 4232 (2016).

[237] J. F. Lin *et al.*, Phys. Rev. B **75** (2007).

[238] S. K. Lee, P. J. Eng, H.-k. Mao, Y. Meng, and J. Shu, Phys. Rev. Lett. **98**, 105502 (2007).

[239] S. K. Lee, P. J. Eng, H.-k. Mao, and J. Shu, Phys. Rev. B **78**, 214203 (2008).

[240] S. K. Lee, S. Y. Park, H.-I. Kim, O. Tschauner, P. Asimow, L. Bai, Y. Xiao, and P. Chow, Geophys. Res. Lett. **39**, L05306 (2012).

[241] K. Kihara, Eur. J. Mineral. **2**, 63 (1990).

[242] W. W. Schmahl, I. P. Swainson, T. Dove M, and A. Graeme-Barber, Z. Kristallogr. **201**, 125 (1992).

[243] R. J. Angel, C. S. J. Shaw, and G. V. Gibbs, Phys. Chem. Miner. **30**, 167 (2003).

[244] L. Huang, M. Durandurdu, and J. Kieffer, Nat. Mater. **5**, 977 (2006).

[245] J. Badro, D. M. Teter, R. T. Downs, P. Gillet, R. J. Hemley, and J.-L. Barrat, Phys. Rev. B **56**, 5797 (1997).

[246] T. Yamanaka, T. Fukuda, Y. Komatsu, and H. Sumiya, J. Phys.: Condens. Matter **14**, 10545 (2002).

[247] K. Momma and F. Izumi, J. Appl. Crystallogr. **44**, 1272 (2011).

[248] J. P. Perdew, A. Ruzsinszky, G. I. Csonka, O. A. Vydrov, G. E. Scuseria, L. A. Constantin, X. Zhou, and K. Burke, Phys. Rev. Lett. **100**, 136406 (2008).

[249] C. Hébert, Micron **38**, 12 (2007).

[250] K. Schwarz, J. Solid State Chem. **176**, 319 (2003).

[251] Y. Meng *et al.*, P. Natl. Acad. Sci. U.S.A **105**, 11640 (2008).

[252] A. R. Oganov, M. J. Gillan, and G. D. Price, Phys. Rev. B **71**, 064104 (2005).

[253] T. Sato and N. Funamori, Phys. Rev. Lett. **101**, 255502 (2008).

[254] P. A. van Aken, B. Liebscher, and V. J. Styrsa, Phys. Chem. Miner. **25**, 323 (1998).

[255] S. A. Gramsch, R. E. Cohen, and S. Y. Savrasov, Am. Miner. **88**, 257 (2003).

[256] R. W. G. Wyckoff, in *Crystal Structures* (Interscience Publishers, New York, 1963), pp. 85.

[257] A. Georges, L. de' Medici, and J. Mravlje, in *Annual Review of Condensed Matter Physics, Vol 4*, edited by J. S. Langer (Annual Reviews, Palo Alto, 2013), pp. 137.

[258] K. Persson, A. Bengtson, G. Ceder, and D. Morgan, Geophys. Res. Lett. **33**, L16306 (2006).

[259] Z. Fang, I. V. Solovyev, H. Sawada, and K. Terakura, Phys. Rev. B **59**, 762 (1999).

[260] P. S. Miedema and F. M. F. de Groot, J. Electron. Spectrosc. Relat. Phenom. **187**, 32 (2013).

[261] O. Narygina, M. Mattesini, I. Kantor, S. Pascarelli, X. Wu, G. Aquilanti, C. McCammon, and L. Dubrovinsky, Phys. Rev. B **79**, 174115 (2009).

[262] X. Wang and T. Tsuchiya, Am. Miner. **99**, 387 (2014).

[263] Z. Mao, J.-F. Lin, J. Yang, J. Wu, H. C. Watson, Y. Xiao, P. Chow, and J. Zhao, Am. Miner. **99**, 415 (2014).

[264] K. Ohta, K. Fujino, Y. Kuwayama, T. Kondo, K. Shimizu, and Y. Ohishi, J. Geophys. Res. Solid Earth **119**, 4656 (2014).

[265] A. P. Kantor, S. D. Jacobsen, I. Y. Kantor, L. S. Dubrovinsky, C. A. McCammon, H. J. Reichmann, and I. N. Goncharenko, Phys. Rev. Lett. **93**, 215502 (2004).

[266] I. Y. Kantor, C. A. McCammon, and L. S. Dubrovinsky, Journal of Alloys and Compounds **376**, 5 (2004).

[267] S. K. Lee, Am. Miner. **99**, 877 (2014).

[268] J. R. Yates, C. J. Pickard, M. C. Payne, R. Dupree, M. Profeta, and F. Mauri, J. Phys. Chem. A **108**, 6032 (2004).

[269] M. Profeta, F. Mauri, and C. J. Pickard, J. Am. Chem. Soc. **125**, 541 (2003).

[270] C. J. Pickard and F. Mauri, Phys. Rev. B **63**, 245101, 245101 (2001).

[271] J. D. Head and M. C. Zerner, Chem. Phys. Lett. **122**, 264 (1985).

[272] N. Marzari, D. Vanderbilt, and M. C. Payne, Phys. Rev. Lett. **79**, 1337 (1997).

[273] S. Y. Park and S. K. Lee, J. Am. Ceram. Soc. **99**, 3948 (2016).

[274] J. F. Stebbins, Solid State Ionics **112**, 137 (1998).

[275] F. Ali, A. V. Chadwick, G. N. Greaves, M. C. Jermy, K. L. Ngai, and M. E. Smith, Solid State Nucl. Magn. Reson. **5**, 133 (1995).

[276] R. Dupree, D. Holland, and M. G. Mortuza, J. Non-Cryst. Solids **116**, 148 (1990).

[277] Y. Lee, A. Woo, K. Sun Ryu, Y. Joon Park, B. Young Jung, J. Ho Lee, and K. Han, Solid State Ionics **175**, 311 (2004).

[278] P. Klein, J. Dedecek, H. M. Thomas, S. R. Whittleton, V. Pashkova, J. Brus, L. Kobera, and S. Sklenak, Chem. Commun. **51**, 8962 (2015).

[279] R. K. Harris, Chem. Soc. Rev. **5**, 1 (1976).

[280] M. J. Duer, in *Introduction to Solid-State NMR Spectroscopy* (Blackwell, 2004), pp. 116.

[281] M. H. Levitt, *Spin Dynamics: Basic of Nuclear Magnetic Resonance* (Wiley & Sons, Ltd, 2001).

[282] L. Frydman, in *Advances in NMR*, edited by R. K. H. David M. Grant (Wiley, 2002), pp. 262.

[283] S. K. Lee, H. N. Kim, B. H. Lee, H.-I. Kim, and E. J. Kim, J. Phys. Chem. B **114**, 412 (2010).

[284] B. H. Lee and S. K. Lee, Am. Miner. **94**, 1392 (2009).

[285] Y. S. Yi and S. K. Lee, JMSK **23**, 403 (2010).

[286] Y. S. Yi and S. K. Lee, JMSK **27**, 1 (2014).

[287] H. Khim, Y. S. Yi, and S. K. Lee, JMSK **30**, 59 (2017).

[288] M. C. Payne, M. P. Teter, D. C. Allan, T. A. Arias, and J. D. Joannopoulos, Rev. Mod. Phys. **64**, 1045 (1992).

[289] D. Marx, Hutter, J., Mod. Methods and Algorithms of Quantum Chem. **1**, 301 (2000).

[290] J. S. Tse, Annu. Rev. Phys. Chem. **53**, 249 (2002).

[291] Y. Zhao and D. G. Truhlar, J. Phys. Chem. A **110**, 13126 (2006).

[292] M. Cococcioni, in *Theoretical and Computational Methods in Mineral Physics: Geophysical Applications*, edited by R. Wentzcovitch, and L. Stixrude (Mineralogical Soc Amer, Chantilly, 2010), pp. 147.

[293] V. I. Anisimov, F. Aryasetiawan, and A. I. Lichtenstein, J. Phys.-Condes. Matter **9**, 767 (1997).

[294] A. D. Becke, J. Chem. Phys. **98**, 1372 (1993).

[295] D. J. Griffiths, *Introduction to Quantum Mechanics* (Prentice Hall, New Jersey, 2005), 2 edn., p.^pp. 480.

[296] J. L. McHale, *Molecular Spectrscopy* (Prentice Hall, New Jersey, 1999), 1 edn., p.^pp. 463.

[297] I. N. Levine, *Quantum Chemistry* (Prentice Hall, New Jersey, 2006), 5 edn., p.^pp. 739.

[298] C. Kittel, *Introduction to solid state physics* (Wiley, New York, 2004), 8 edn., p.^pp. 704.

[299] N. W. Ashcroft and N. D. Mermin, *Solid State Physics* (Brooks Cole, New York, 1976), p.^pp. 848.

[300] V. Milman *et al.*, Theochem-J. Mol. Struct. **954**, 22 (2010).

[301] D. J. Singh and L. Nordstrom, *Planewaves, pseudopotentials, and the LAPW method* (Springer, New York, 2006), 2nd edn., p.^pp. 134.

[302] P. Blaha, Schwarz, K., Madsen, G., Kvasnicka, D and Luitz, J, *User guide for Wien2k 10.1* (Inst. of Phys. and Theo. Chem. at Vienna Univ. of Tech., Vienna, 2010), p.^pp. 202.

Abstract of Korean

지구 내부에 존재할 수 있을 것이라 알려진 고밀도의 SiO_2 와 $MgSiO_3$ 가 많이 포함된 규산염 용융체는 맨틀 최하부에 존재하는 초-저속도층(ultralow velocity zone; ULVZ)이 나타나는 원인 중에 하나로 제안되어 왔습니다. 지구 내부에 존재하는 SiO_2 와 $MgSiO_3$ 가 많이 포함된 규산염 용융체의 압력 증가에 의한 탄성 특성 변화를 이해하기 위하여 SiO_2 와 $MgSiO_3$ 유리질 시료에서의 압력 증가에 의한 탄성파 전달 속도의 변화를 ~207 GPa 의 고압 환경까지 밝혀져 있습니다. 그리고 해당 연구들에서는 이와 같은 압력 증가에 의한 탄성파 전달 속도의 변화가 고배위수의 Si 원자의 형성과 연관이 있다고 제안되었습니다. 하지만, 비정질 SiO_2 와 $MgSiO_3$ 유리질 물질의 밀도 증가 과정과 이로 인한 전자구조 변화, 그리고 탄성 특성과의 상관관계가 명확하게 밝혀져 있지 않았습니다. 고압 환경에 놓인 비결정질 지구 물질의 원자 및 전자구조를 연구하기 위한 다양한 실험 방법들이 개발되어 사용되고 있지만, 고압 상태에 놓인 물질의 전자구조를 직접 관찰하여 그 기원이 되는 원자구조에 대한 정보를 유추하게 할 수 있는 것은 *in situ* 고압 x-선 Raman 산란(x-ray Raman scattering; XRS) 실험이 거의 유일합니다. XRS 실험은 특정 원자 주변의 전자구조를 밝혀 그 기원이 되는 국소 원자구조에 대한 정보를 제공할 수 있어, 압력 증가에 의한 지구물질의 전자구조의 변화를 분석하여 그 기원이 되는 원자구조의 변화에 대한 정보를 제공할 수 있습니다. 특히, 고압 환경에 놓인 결정질 및 비정질 SiO_2 및 $MgSiO_3$ 물질에 대한 연구는 압력 증가에 의한 O *K*-edge XRS 스펙트럼 변화를 분석하여 압력

증가에 의한 O 원자 주변의 국소 원자구조의 변화를 밝혀 압력 증가에 의한 규산염 및 Mg-규산염 지구물질의 원자구조 변화를 유추하는데 이용되어 왔습니다. 하지만 *in situ* 고압 XRS 실험을 통하여 고압 상태의 지구물질에 대한 연구를 수행하는 것에는 아직까지 많은 어려움이 있습니다. 이와 같은 실험적 한계와 어려움은 근래의 계산과학의 발달에 힘입어 제 1 원리 양자계산을 이용하는 것으로 일부 극복할 수 있습니다.

본 연구에서는 제 1 원리 계산을 이용하여 *in situ* 고압 XRS 실험으로 재현이 어렵거나 불가능한 고압환경에 존재하는 SiO_2 및 $MgSiO_3$ 의 고압 결정질 동질이상 물질들과 비결정질 $MgSiO_3$ 용융체의 전자구조 및 O *K*-edge XRS 스펙트럼을 계산하였습니다. SiO_2 및 $MgSiO_3$ 고압 결정질 동질이상 물질에서 나타나는 압력 증가에 의한 O *K*-edge XRS 스펙트럼 변화와 고압 상태의 SiO_2 결정질 물질에서 나타나는 특징적인 두 개의 피크가 압력 증가에 의하여 인접한 O 원자 간의 거리가 가까워지는 것과 연관이 있다는 것을 확인하였습니다. 그리고 비결정질 $MgSiO_3$ 물질에서 나타나는 압력 증가에 의한 O *K*-edge XRS 스펙트럼의 변화 또한 O 원자 주변의 원자 사이의 거리(특히, O-O 거리)와 상대적으로 강한 상관관계를 보여주고 있었습니다. 이와 같은 결과들은 SiO_2 와 $MgSiO_3$ 유리질 물질에서 나타나는 압력 증가에 의한 O *K*-edge XRS 스펙트럼의 변화가 고배위수의 Si 원자 형성보다는 인접한 O 원자 간의 거리 감소를 지시할 것이라는 의미합니다. 지금까지 얻어진 결과로부터 압력 증가에 의한 인접한 O 원자 간의 거리 감소가 결정질 및 비결정질 SiO_2 및 $MgSiO_3$ 물질의 전자구조에 큰 영향을 미친다는 것을 확인할 수 있었습니다. 비정질 산화물의 탄성 특성은 해당 물질의 짧은 거리 구조와 전자구조에 의하여 결정되기 때문에 압력증가에 의한 SiO_2 및 $MgSiO_3$ 유리질 물질의 탄성파 전달

속도 변화는 이전 연구에서 제시된 압력 증가에 의한 Si 원자의 배위수 변화보다는 인접한 O 원자 간의 거리 변화를 통하여 설명되어야 할 것입니다. 나아가서 본 연구의 결과는 실험적으로 접근이 어려운 환경에 놓인 지구물질의 다양한 성질, 실험의 결과에 대한 원자단위의 기원을 규명하여 지구내부에 존재하는 물질의 성질과 지구시스템의 진화를 이해하는 것에 있어 중요한 역할을 할 수 있을 것으로 기대하고 있습니다.